Optimization of Cellulose Nanocrystal Films for Optical and Micromechanical Applications

by

Partha Saha

A dissertation submitted to the Graduate Faculty of
Auburn University
in partial fulfillment of the
requirements for the Degree of
Doctor of Philosophy

Auburn, Alabama
May 5, 2018

Keywords: Cellulose nanocrystals, liquid crystal, planar ordering, aligned films, microelectromechanical systems

Approved by

Virginia A. Davis, Chair, Alumni Professor of Chemical Engineering
W. Robert Ashurst, Co-Chair, Uthlaut Family Endowed Associate Professor of Chemical Engineering
James Radich, Assistant Professor of Chemical Engineering
Michael Hamilton, Associate Professor of Electrical and Computer Engineering

Abstract

The objective of this research is to understand the effect of microstructural helix orientations and alignment in aqueous cellulose nanocrystals (CNC) dispersions and films on mechanical, optical, and surface properties for potential macroscale applications. The first part of this research involves understanding the effects of CNC dispersion concentrations, shear response, drying conditions, and surface anchoring to obtain controlled planar ordering of the cholesteric microstructures in films for photonic applications. CNC films with tunable selective reflections of visible spectra were fabricated, providing new insights into the spatial pitch defects previously reported in *lomaptera* beetles. The fundamental understanding of film fabrication provided insights into elucidating the governing parameters that control the cholesteric helix orientation and evolution of the planar microstructures. In the second part, the objective was to apply rheo-optics and 3D finite element modeling to monitor the shear response and relaxation dynamics of CNC mesogens after flow cessation. The dispersion rheology and rheo-optics results provided a better understanding of the CNC microstructures' response to flow alignment. The insight into the effects of dispersion concentration, shear response, and drying on uniaxial ordering guided the fabrication of microelectromechanical systems (MEMS) from shear aligned CNC films followed by micromechanical testing. The goal was to unwind the cholesteric microstructure into nematic and retain it in films to obtain the uniaxial CNC alignment for anisotropic (directional) device properties. The

micromechanical devices fabricated from aligned CNC films included mechanical strength testers (MSTs), residual stress testers (RSTs), cantilever beams arrays (CBAs), and doubly clamped beams (DCBs). These devices were tested to study macroscopic film properties including anisotropic elastic moduli, residual stress, fracture strength, and electrostatic actuation for potential specialty applications of CNC MEMS. This new paradigm of producing MEMS *via* low temperature processing of CNC derived from waste biomass provided the simplicity and tunability of fluid phase processing and enabled anisotropic mechanical properties within an order of magnitude of standard polysilicon devices. In the third part, CNCs' functionalization with cancer biomarkers was investigated for potential applications of CNC MEMS in biosensing. The compatibility of the CNC MEMS platform for multianalyte detection was researched based on the immobilization of the following cancer biomarkers: alpha fetoprotein (AFP), prostate specific antigen (PSA), and carcinoembryonic antigen (CEA) for liver, prostate, and ovarian cancer detection respectively. In summary, this research provides the fundamental insights on dispersion microstructures, shear alignment, and drying effects for tunable mechanical and optical properties in CNC films for macroscale applications.

Acknowledgments

Pursuing my Ph.D. has been a heartfelt journey and learning experience here at Auburn University. First of all, I thank department of Chemical Engineering at Auburn University for all the amazing opportunities and facilities. Second, I would like to acknowledge all the help, guideline, and support of my advisors Dr. Virginia A. Davis and Dr. W. Robert Ashurst; without their mentoring and expertise this journey would not have been possible. I also thank Dr. James Radich and Dr. Michael Hamilton for their support as my dissertation committee members. I thank Dr. Maria Soledad Peresin for her support as the outside reader of my dissertation. I also extend my gratitude to all of my group members and fellow researchers in both Davis and Ashurst labs for their support and making this journey enjoyable.

Last but not the least, I would acknowledge my father Mr. Dipak Saha, my mother Ms. Mamata Saha, and my wife Ms. Indira Bose, for their constant love, support, and encouragement to make this journey possible.

Table of Contents

Abstract ii

Acknowledgments iv

List of Figures x

List of Tables xxii

List of Equations xxiii

Chapter 1 Introduction 1

Chapter 2 Background 5

2.1 Cellulose Nanocrystals (CNC) 5

2.1.1 Structure of CNC 5

2.1.2 Preparation of CNC 7

2.1.3 Surface Modification of CNC 11

2.1.4 Morphology and Dimensions of CNC 13

2.1.5 Applications of CNC 14

2.2 Liquid Crystals 16

2.2.1 Types of Liquid Crystals 17

2.2.2 Lyotropic Liquid Crystal Phase Behavior 20

2.2.2.1 Onsager Theory 22

2.2.2.2 Stroobants-Lekkerkerker-Odjik Theory 25

2.2.3 Optical Signatures of Liquid Crystals 26

2.2.4 Rheological Signatures of Liquid Crystals 29

2.2.4.1 Local Maxima and Minima in Viscosity versus Concentration Curve 30

2.2.4.2 Three-region Behavior in Viscosity versus Steady Shear Curve 32

2.2.4.3 Sign Change of First Normal Stress Difference with Shear Rate 36

2.2.4.4 Long Oscillatory Transients after Start-up of Steady Shear Flow 37

2.2.4.5 Cox-Merz Rule is not Obeyed 39

2.3 Aqueous CNC Dispersions 40

2.3.1 Colloidal Stability of CNC 41

2.3.2 Phase Behavior of CNC Dispersions 43

2.3.3 Rheology of CNC dispersions 46

2.4 Fluid Phase Alignment of CNC 52

2.5 Dried CNC Films 54

2.5.1 Aligned CNC Films 55

2.5.2 Chiral Nematic CNC Films 62

Chapter 3 Experimental 67

3.1 Cellulose Nanocrystal Dispersion Preparation 67

3.2 Dispersion Drying and Film Preparation 67

3.3 Cellulose Nanocrystal Characterization 68

3.4 Microfabrication of CNC MEMS 71

3.4.1 Wafer Cleaning and Priming 71

3.4.2 Photoresist Coating 72

3.4.3 Pattern Transferring 72

3.4.4 Plasma Etching 73

3.4.5 Device Release and Drying 74

3.5 Characterization Methods 75

3.5.1 Optical Microscopy 75

3.5.2 Rheology 76

3.5.3 Microspectrophotometry 77

3.5.4 TGA-FTIR 77

3.5.5 Atomic Force Microscopy 78

3.5.6 Scanning Electron Microscopy 79
3.5.7 Goniometry 79
3.5.8 Micromechanical Testing 80
3.5.8.1 Nanoindentation 80
3.5.8.2 Mechanical Strength Testing 81
3.5.8.3 Residual Stress Testing 82
3.5.8.4 Phase Shifting Interferometry 84
3.5.9 Mechanical and Electrostatic Actuation 84
Chapter 4 Chiral Nematic CNC Films for Selective Reflection 86
4.1 Motivation 86
4.2 Dispersion Drying 89
4.3 Results 92
4.4 Conclusions 108
Chapter 5 Nematic CNC Films for MEMS Fabrication 109
5.1 Motivation 109
5.2 Sheared CNC Films 111
5.2.1 Fluid Phase Relaxation Dynamics after Shear Cessation 111

5.2.2 Directionally Aligned CNC Films for MEMS Fabrication 118

5.2.2.1 Microfabrication of CNC MEMS 120

5.2.2.2 Results 124

5.3 Conclusions 132

Chapter 6 Surface Modification of CNC for Biosensing 133

6.1 Motivation 133

6.2 Surface Modification of CNC 134

6.3 Results 139

6.3.1 Hydrolytic Stability of CNC films/CNC Cantilevers 139

6.3.2 Immobilization of Primary Antibody on the APTES Modified CNC Films .. 143

6.3.3 Antigen Detection on the Antibody Immobilized CNC APTES-GA Films ... 149

6.3.4 Mass Detection using Cantilever Beams Array (CBA) 154

6.4 Conclusions 158

Chapter 7 Conclusions 160

References 163

Appendix A-1

List of Figures

Figure 2.1. The structure of cellulose. The anhydroglucose unit is the monomer of cellulose where cellobiose is the dimmer. The cellulose chain has a direction, one end being a closed ring structure where the other being an aliphatic reducing end 5

Figure 2.2. A) Schematic of chain cross section showing unit cells of cellulose I_α (triclinic, dashed line) and I_β (monoclinic, solid line). B) Two possible inter-chain hydrogen bonding networks of $(110)_t$ and $(200)_m$ lattice planes proposed in literature 7

Figure 2.3. Schematic showing A) amorphous/disordered and crystalline/ordered regions in cellulose fiber and out of plane surface hydroxyl groups, B) hydrolytic cleavage of glycosidic bonds, C) nucleophilic substitution of hydroxyl groups during acid hydrolysis 9

Figure 2.4. Electron microscopic image of sulfuric acid hydrolyzed CNC 11

Figure 2.5. Scanning and transmission electron micrographs showing the different geometrical morphology of A) wood fibers, B) microcrystalline cellulose, C) microfibrillated cellulose, D) TEMPO nanofibrillated cellulose, E) wood CNC, F) tunicate CNC, G) algae CNC, and H) bacterial CNC 14

Figure 2.6. Schematic showing examples of A) thermotropic and B) lyotropic mesogens 18

Figure 2.7. Schematic showing Friedelian classes of liquid crystals: A) nematic, B) cholesteric, and C) smectic 19

Figure 2.8. Concentration regimes for rod-like molecules during phase transition. Adapted from Doi and Edwards 21

Figure 2.9. Polarized light microscopy of CNC suspensions at various concentrations at 25ºC. Scale bars are 50 µm 22

Figure 2.10. Diagrammatic representation of the excluded volume of two rod-like molecules, of length L and diameter d. γ is the angle between the long molecular axes . 23

Figure 2.11. Schematic representation of cellulose chain axis illustrating the refractive index parallel (extraordinary/slow axis) and perpendicular (ordinary/fast axis) to the crystal axis 27

Figure 2.12. Cross-polarized transmitted light microscopy of 2 wt. % poly(p-sulfo-phenyleneterephtalamide) solution in water 28

Figure 2.13. Michel-Levy birefringence chart showing correlation of LC film thickness, birefringence, and interference order. X and Y axes show order of interference (retardation) and sample thickness respectively. Diagonal lines represent material birefringence 29

Figure 2.14. Viscosity versus concentration plot for 50/50 copolymer of n-hexyl and n-propyl isocyanate (molecular weight 41000) in toluene at 25ºC 31

Figure 2.15. Decrease of maximum viscosity concentration of poly(ɤ-benzyl-glutamate) in m-cresol with increasing shear rate..... 32

Figure 2.16. Three regions of LC flow behavior originally proposed by Onogi and Asada 33

Figure 2.17. Schematic representation of the bulk LCs' structure under applied shear. (A) Piled polydomain system, (B) dispersed polydomain system, and (C) monodomain continuous phase..... 35

Figure 2.18. Shear viscosity and first normal stress difference versus shear rate for 17% PBLG (MW=350,000) in m-cresol (circled triangles are negative N_1)..... 37

Figure 2.19. The long transient oscillatory response of 7.6 vol. % (6 wt. %) single-walled carbon nanotubes in 102% sulfuric acid to start-up shear flow at a 5 s^{-1}shear rate 39

Figure 2.20. Cox-Merz rule is not obeyed by a lyotropic LC which is 7.6 vol. % SWNTS in superacids. Triangles: dynamic viscosity η*versus frequency ω, Squares: steady shear viscosity η versus shear rate..... 40

Figure 2.21. A) Photograph of CNC dispersions of various concentrations in water under the cross-polarized light environment (Adapted from Honorato-Rios et al.[8]). Cross-polarized transmitted light microscopic images of B) 3 wt. % (isotropic) and C) 7 wt. % (biphasic) dispersions..... 41

Figure 2.22. Plots showing zeta potential and size of CNC with added electrolyte concentrations of A) Na^+ and B) Ca^{2+} counterions 43

Figure 2.23. A) Schematic showing the chiral nematic ordering, n is the nematic director perpendicular to the chiral nematic or cholesteric axis, p indicates half pitch; length that is covered when director rotates 180º about the cholesteric axis, B) cross-polarized transmitted light microscopy of CNC cholesteric alignment, on the image blue and orange arrows are basically helix and director directions respectively. Oblate shape CNC birefringent liquid crystalline domains are suspended in an isotropic matrix of suspension, C) schematic of twisted morphology illustrating tighter packing at an angle, D) schematic showing ionic envelope developed surrounding the sulfonated CNC rod, due to the physical twist of the rods envelope of surrounding counter ions is also twisted 44

Figure 2.24. Schematic representation of bacterial CNC rods A) before and B) after the NaCl addition to screening out the charged layers 46

Figure 2.25. Steady shear and complex viscosity with increasing concentrations of sulfonated CNC from A) cotton (H_2O suspension)[124] and B) wood (D_2O suspension at 1 s^{-1} shear rate) 47

Figure 2.26. Steady shear viscosity versus shear rate plots showing the three-region behavior of A) cotton linter CNC for concentrations of 1.2 (black dots), 1.7 (hollow squares), and 2.7 (solid triangles) wt. % and B) cotton CNC of 6.99 vol. % at four different temperatures..... 48

Figure 2.27. Steady shear viscosity and order parameter versus shear rate plots of CNC dispersed in deuterium oxide showing three-region behavior for concentrations of 3.83 (hollow purple circles), 4.5 (hollow orange triangles), 5.16 (hollow blue squares), and 5.83 vol. %(hollow red diamonds)..... 49

Figure 2.28. Cox-Merz rule comparison for the aqueous sulfonated CNC dispersions for different concentrations of A) 6.3 (biphasic) and B) 12.1 (liquid crystalline) vol. %. The open and solid symbols denote the steady shear and complex viscosities respectively. .. 50

Figure 2.29. Linear viscoelastic properties of sulfonated CNC dispersions showing A) storage modulus (G′), B) loss modulus (G″), and C) ratio of G″ to G′ or tanδ. Dispersion concentrations shown on the plots are 17.3 (red solid diamonds), 14.5 (blue solid squares), 12.6 (black stars), 12.1 (orange solid triangles), 10.4 (purple solid circles), 9.03 (red open diamonds), 7.69 (blue open squares), 6.30 (orange open triangles), and 5 (purple open circles) vol. % 51

Figure 2.30. Cross-polarized transmitted light microscopic images of sulfonated CNC dispersions after shear (flow direction is up). Scale bars are 100 µm[196]. 53

Figure 2.31. Schematic of experimental setup showing the convective-shear assembly of fluid phase CNC..... 56

Figure 2.32. AFM height image of CNC film prepared on a charged gold substrate using 4.5% dispersion at a withdrawal speed of 8.4 cm/h. The withdrawal direction is down to up..... 56

Figure 2.33. Cross-polarized transmitted light microscopic images showing optical contrast (OC) in shear aligned CNC films using concentrations of A) 11.6 vol. % (liquid crystalline) and B) 15.8 vol. % (gel). C) and D) are same images of films in A) and B) respectively rotated 45º to the cross-polarized position. Scale bars are 100 µm 58

Figure 2.34. Polarized transmittance spectra and images of CNC films fabricated from 11.6 vol. % (liquid crystalline) concentration. Dispersion wet thickness is varied as A), B) 50

(0º and 45º), C) 100, D) 150, and E) 200 µm. The colors in the transmitted spectra correspond to the colors observed in these films. Scale bars are 50 µm 59

Figure 2.35. Mechanical properties of CNC/PEO films using flocculated and non-flocculated scheme. A) Young's modulus, B) tensile strength, and C) toughness. Dark gray and light gray refer to parallel and perpendicular to flow direction. The error bars are standard errors of each set of films 61

Figure 2.36. A) SEM and B) TEM images showing the 90º and an oblique cross-section of CNC films. Inset (a) shows the progression of nanocrystals from parallel to perpendicular orientation to the cross-section and oblique cross-section on Teflon plate reveals the arc like morphology of image showing the 90º and an oblique cross-section of CNC films. Inset (a) shows the progression of nanocrystals from parallel to perpendicular orientation to the cross-section and oblique cross-section on Teflon plate reveals the arc like morphology of the rods 63

Figure 2.37. Reflection colors and spectra for CNC films obtained from 2.7 wt. % dispersion subjected to sonication energy of A) 750 J/g, B) 1:1 ratio of 750 J/g to 2250 J/g, and C) 2250 J/g. Reflection is normal to the film surface. Scale bar is 1 cm. A (square), B (triangle), C (diamond), 1490 J/g (cross) 64

Figure 2.38. Reflectance spectra of different domains of chiral nematic CNC and their correlation to SEM scanning of the cross-sections. A) Left-handed circularly polarized light reflectance image showing digital colors of the domains. B), C), and D) reveal the cross sections SEM of selected spots on A as b, c, and d (white circles), respectively. E-F show the corresponding reflectance spectra. The solid black lines are curve fits the spectra using Berreman's 4 x 4 matrix method 65

Figure 3.1. AFM height scan of CNC on a mica surface. 69

Figure 3.2. Plots showing the size distributions of CNC based on AFM. 70

Figure 3.3. Schematic showing HMDS priming reaction 72

Figure 3.4. Schematic showing the sessile-drop contact angle system; θ is the contact angle. 80

Figure 3.5. Photograph showing the custom-built probe station for micromechanical testing of CNC MEMS 82

Figure 3.6. Photograph showing the set-up for micro-manipulator developed to actuate the CNC mechanical strength tester (MST)..... 82

Figure 3.7. Schematic of the released residual stress tester (RST) showing A) tensile and B) compressive residual stress in the MEMS structural devices. θ is the line angle measured using microscopic imaging 83

Figure 4.1. Schematic showing different orientation directions of the chiral nematic helix, A) planar: standing helix in the z-direction, 360° rotation of n shown as pitch P, B) homeotropic: helix parallel x-direction along the substrate, and C) focal conic: helices tilted in both directions..... 87

Figure 4.2. Photograph, schematic, and optical micrograph showing A) drying set up, B) CNC dispersion on microscope slide with a coverslip on the top, C) directions of capillary drag and orbital shear, and D) stitched composite image comprised of an array of 20 x 2 individual images (14 arrays in total) of a dried CNC films from a 6.5 wt. % (4.2 vol. %) dispersion sandwiched between a microscope and coverslip slide..... 90

Figure 4.3. Cross-polarized transmitted light micrographs showing A) 2.0 wt. %/1.3 vol. % (isotropic), B) 6.5 wt. %/4.2 vol. % (biphasic), and C) 8.0 wt. %/5.1 vol. % (liquid crystalline) dispersions of CNC. Scale bars are 50 µm 91

Figure 4.4. Cross-polarized reflected light micrographs showing planar chiral nematic domains of CNC in dried films using A) isotropic (2 wt. %/1.26 vol. %), B) biphasic (6.5 wt. %/4.15 vol. %), and C) liquid crystalline (8 wt. %/5.14 vo l %) dispersion concentrations. All scale bars are 100 µm. Each image is a total of 1.4X1.1 mm field of view..... 93

Figure 4.5. Steady shear viscosities of liquid crystalline and biphasic aqueous CNC (Na^+ as counterion) dispersions at 10 ˚C. 94

Figure 4.6. Cross-polarized reflected light micrographs showing a stitched image of A) distinct planar regions across the CNC film between the coverslip and glass substrate. It also illustrates variable shapes and sizes of planar domains shown from left to right in B) Region 3L, C) Region 2, D) Region 1, where domains were subjected to variable shear, and E) Region 3R, where domains were subjected to even higher shear resulting fingerprints or non-planar ordering. All scale bars are 100 µm. 96

Figure 4.7. Cross-polarized micrographs showing uniform reflectance colors of A) blue, B) green, and C) red, in planar domains with slight transition colors of green, orange, and green, respectively. Scale bars are 50 µm. 98

Figure 4.8. Cross-polarized reflected micrograph showing the evolution of the helix orientation in a CNC film obtained using 6.5 wt. % (4.15 vol. %) dispersion. Arrows indicate the relative directions of shear and capillary flow. Scale bar is 50 µm. 100

Figure 4.9. Cross-polarized reflected micrographs showing the effect of surface anchoring on planar orientation, CNC film dried in water vapor saturated environment assisted by orbital shear with a coverslip A) off and B) on during drying. Scale bars are 100 µm…..102

Figure 4.10. Microscopic images of CNC planar domains using A) left-handed and B) right-handed circularly polarized reflected light 104

Figure 4.11. Selective reflectance spectra using circularly polarized light showing A) single-peak, and B) double-peak reflection from planar domains of CNC film using both left handed circularly polarized (LCP), and right handed circularly polarized (RCP) light, C) selective reflection micrograph under LCP illumination, D) transmission of RCP light over the same planar domains, E), F) cross polarized reflected micrographs showing selected planar domains giving reflectance spectra of both single-peak (1, 2, and 3) and double-peak (4, 5, and 6). 105

Figure 4.12. Scanning electron microscope (SEM) images of cross sections of CNC films showing A) chiral nematic layers viewed at 90° cross section, B) uniform parallel arc-like morphology of planar ordering viewed at oblique cross section, C) constant pitch and D) spatially varying pitch within a planar domain, E) line defect due to change of chiral nematic layers number, and F) tilted domain next to planar ones. Dome shaped topography on the surface of the film is attributed to beam damage. Scale bars are 1 μm. 107

Figure 5.1. Cross-polarized transmitted light microscopic images showing the relaxation texture of 8 wt. % (5.14 vol. %) CNC dispersion after shear cessation at different times. Shear cell gap was 50 μm. 113

Figure 5.2. Cross-polarized transmitted light microscopic images showing the relaxation texture of 8 wt. % (5.14 vol. %) CNC dispersion after shear cessation at different times. Shear cell gap was 500 μm. 114

Figure 5.3. Cross-polarized transmitted light microscopic images showing the relaxation texture of A) - D) 8 wt. % (5.14 vol. %) and E) - H) 7 wt. % (4.5 vol. %) CNC dispersions after shear cessation at 0 and 10 minutes. 116

Figure 5.4. 3-D simulation based on finite element analysis showing cholesteric microstructure at equilibrium. x, y, and z are the flow, vorticity, and shear directions. R, θ, and U are parameters associated with concentration, chirality, and elastic constants of the system. 118

Figure 5.5. Cellulose Nanocrystal (CNC) Films. Transmitted cross-polarized and scanning electron microscopic images of dried CNC films produced from aqueous dispersions. Arrows indicate shear direction. A) The signature cholesteric texture in film cast without shear from 6.5 wt. % (4.2 vol. %) CNC. B) Crack formation along the shear direction in a film made using 8.9 wt. % (5.6 vol. %) CNC and a 1000 s^{-1} shear rate. C) The absence of cracking in the film made using 6.5 wt. % CNC and a 100 s^{-1} shear rate. D) The crack free aligned film obtained using the same process of C followed drying at 80 °C for 20 minutes followed by desiccation. E) SEM micrograph of the cross section of D, the inset shows the better uniaxial alignment of CNCs at the drying surface compared to near the substrate. 120

Figure 5.6. Photograph and cross-polarized reflected light optical microscopy images showing the whole substrate and steps involved in photolithographic fabrication scheme for CNC MEMS. A) A 4″ diameter wafer substrate with shear dried CNC film onto the photoresist CNC MEMS pattern on it. B) Shear aligned and dried CNC film on a patterned photoresist layer using a Si substrate. C) The same CNC film of A) after E-beam deposition of 10 nm thick Ti/TiO_2 layer. D) After creating the device pattern using a second photoresist layer achieved by photoresist coating, drying, UV exposure through an aligned mask, and developing. E) Etched out device profiles after using inductively coupled plasma etching, white and black areas indicate the etched film and the residual photoresist on the device patterns respectively. F) Released devices after washing off the residual photoresist layers using acetone followed by IPA rinsing. G) The higher magnification image of a released MST after critical point drying. Scale bars are 100 μm. 123

Figure 5.7. Representative micrographs of freestanding CNC MEMS after release. A) Interferograms on a cantilever beam array (CBA). B) A doubly clamped beam (DCB) array with 30 μm wide beams with lengths ranging from 100–300 μm. C) An optical micrograph showing a residual stress tester (RST) with a 300 μm distance between supporting beams connected to I-shaped beam before release. D) The same RST after release; the counterclockwise rotation is due to the compressive residual stress in the structural CNC film and indicates the device was functional and freestanding……..125

Figure 5.8. Reflected light microscopic images showing the effect of the stress gradient developed in 300 μm long CNC cantilevers and doubly clamped beams (DCBs). Arrows indicate the shear alignment direction. A) The parallel CNC alignment on 2 μm thick beam showing stress induced deflection. B) Perpendicular CNC alignment on a 2 μm thick beam, the image distortion is due to the downward beam curvature and curling of the end. C) Parallel CNC alignment on 4 μm thick beam. D) Perpendicular CNC alignment on a 4 μm thick beam. E) and F) Doubly clamped 4 μm thick, 300 μm long beams with parallel CNCs' alignment resulted in intact beams, but perpendicular CNC alignment resulted in cracking of 300 μm long beams. Scale bars are 100 μm. 127

Figure 5.9. Cross-polarized reflected light microscopy images showing tunable optical properties in CNC cantilever arrays resulting from birefringence. Arrows indicate the applied shear direction A) 2 μm thick devices and B) 4 μm thick devices. Uniform colors, A) blue and B) yellow at 45° stage rotation, indicate alignment of CNC along beam long

axis. Dark spots are due to local orientation of domains in a slightly different direction. Scale bars are 50 µm. 127

Figure 5.10. Micromechanical property analysis of CNC MEMS devices. A) Load versus deflection curve of 100 µm long, 30 µm wide and 2 µm thick DCB showing deflection distance until hits the substrate, triangle shows the selected linear region used to extract the slope needed for elastic modulus calculation following linear elastic beam theory B) elastic modulus of 2 µm and 4 µm thick CNC DCBs showing anisotropic mechanical properties in both parallel and perpendicular alignment direction of nanomaterials to the beams' long axis, C) Change in X and Y position of MST shuttle (4 µm thick) during mechanical actuation upon applied voltage on an open loop piezo assisted micromanipulator, the suspended shuttle was pushed towards X direction until 60 µm long fracture beams on both sides fractured giving the breaking length for fracture strength calculation, and D) deflection profiles of gold sputter coated CNC cantilever beam (500 µm long, 30 µm wide and 4 µm thick) due to electrostatic actuation by applying DC voltage. 131

Figure 6.1. Different bonding modes of APTES on a substrate 135

Figure 6.2. Schematic showing the APTES surface chemistry for antibody immobilization on CNC. 136

Figure 6.3. Picture showing the set up for fluid phase APTES modification of CNC dispersions..... 137

Figure 6.4. Photograph showing A) CNC film made from APTES modified dispersion and B) regular CNC film after two hours submersion in DI water. 139

Figure 6.5. Cross-polarized A) reflected and B) transmitted light microscopic images showing sheared CNC film made from APTES modified dispersion. 140

Figure 6.6. Graphs showing static water contact angles (WCA) on APTES modified CNC films. A) Water contact angle versus time for APTES modified CNC dispersion made films and regular CNC film, B) WCA after post film modification with varying APTES

concentrations, and C) WCA of 10 wt.% APTES modified post CNC film with varying reaction time..... 142

Figure 6.7. Reflected light optical microscopic image of APTES modified CNC CBA after submersion in water followed by air drying. 143

Figure 6.8. Thermograms showing thermal degradation of CNC films in the air with increasing temperature after surface modification steps using APTES (black line), APTES-GA (orange line), APTES-GA-antiAFP (green line), and APTES-GA-antiAFP-AFP (light blue line). 145

Figure 6.9. FTIR spectra showing different absorbance peaks associated with each step of surface modification of CNC films using APTES, GA, anti-AFP, and AFP antigens... 146

Figure 6.10. AFM height images (3D) and corresponding roughness averages after surface modification of CNC..... 147

Figure 6.11. Fluorescence optical microscopic images showing the presence of Alexa 350 (blue fluorophore) tagged with AFP antibody attached to CNC-APTES-GA surface under A) DAPI, B) FITC, and C) TRITC filters..... 148

Figure 6.12. Fluorescence optical microscopic images showing the presence of Alexa 488 (green fluorophore) and Alexa 555 (red fluorophore) tagged with PSA and CEA antibodies respectively, attached to CNC-APTES-GA surface under A), D) DAPI, B), E) FITC, and C), F) TRITC filters. 149

Figure 6.13. Graphs showing average intensity measured after control films fluorescence measurement for A) AFP, C) PSA, and E) CEA antibodies and after positive experiments in presence of corresponding antigen solutions of B) AFP, D) PSA, and C) CEA. 150

Figure 6.14. Graphs showing average intensity measured after control films fluorescence measurement for A) AFP, C) PSA, and E) CEA antibodies and after positive experiments

in the presence of corresponding antigen solutions and secondary antibody exposures of B) AFP, D) PSA, and F) CEA antibodies. 153

Figure 6.15. Photograph showing freestanding CNC cantilevers used as AFM tips. Beams are 500 μm long. 155

Figure 6.16. Resonance frequencies of A) 500 μm and B) 300 μm long CNC cantilevers. 156

Figure 6.17. Cross-polarized reflected microscopy showing arrays of CNC cantilevers A) before and B) after the AFP antigen detection..... 157

Figure 6.18. Plots showing PSI based height profiles of CNC cantilevers before (CBA1, 2, 3, 4) and after (CBA1, 2, 3,4) the AFP antigen detection..... 158

List of Tables

Table 2.1. CNC particle size and morphology based on different sources of cellulose. .. 13

Table 2.4 Flow aligned CNC films order parameter and mechanical properties. CNC-1 is CNC film with low pH, CNC-n with neutral pH, A (axial) refers to the parallel to flow/shear direction, and T (transverse) refers to perpendicular to the flow direction. The numbers in brackets are the standard deviation 57

Table 4.1. Measured full pitch using optical spectra and SEM 106

Table 5.1. Tabulated micromechanical properties for CNC MEMS devices (shear alignment along long directions). Column 2, elastic modulus based on indentation was derived for 100 μm long DCBs. Column 3, residual stress was derived for RSTs with 300 μm distance between supporting beam arms. Column 4, fracture strength was derived for MST with 60 μm long and 6 μm width fracture beams. Notation; w (width), t (thickness), m (slope of force versus deflection curve), θ (angle of rotation), d (distance between supporting beams), δ_f (distance traveled by shuttle to fracture), L_c (distance between shuttle and corresponding anchored stopper). 129

List of Equations

Equation 2.1 Excluded volume 23

Equation 2.2 Order parameter 24

Equation 2.3 Isotropic to biphasic transition, Onsager 24

Equation 2.4 Biphasic to liquid crystalline transition, Onsager 24

Equation 2.5 Volume fraction to weight fraction 24

Equation 2.6 Isotropic to biphasic transition, SLO 26

Equation 2.7 Biphasic to liquid crystalline transition, SLO 26

Equation 2.8 Effection diameter of rod 26

Equation 2.9 Debye length 26

Equation 2.10. Birefringence 27

Equation 2.11 Phase difference 28

Equation 2.12 Optical contrast 58

Equation 2.13 Bragg's law 62

Equation 4.1 Selective reflection 87

Equation 4.2 Cholecteric pitch 96

Equation 6.1 Resonance frequency 154

Chapter 1 Introduction

The objective of this research was to understand how the fluid phase microstructural alignment of lyotropic cellulose nanocrystals (CNC) affects the anisotropic mechanical and optical properties of macroscopic films. Cellulose is the most abundant natural polymer on earth with an estimated biomass production of 1.5 trillion tons per year[1,2]. Since its discovery in 1838 by French chemist Anselme Payen, cellulose and its derivatives have been the heart of a multitude of industries including pulp and paper, textiles, food, and pharmaceuticals[3]. Cellulose fibers consist of two repeating regions; amorphous and crystalline. It took more than a century to realize the importance of cellulose crystallites' role on the shear piezoelectricity in wood, reported by Bazhenov in 1950[4]. Later, Marchessault *et al.*[5] extracted the anisotropic rigid crystalline parts of cellulose which are reffered to as cellulose nanocrystals (CNC). CNC are lightweight and have excellent mechanical strength. CNC dispersions also exhibit lyotropic liquid crystalline phase behavior that enable fluid phase ordering and scalability. Therefore, as a renewable building blocks CNC instigated the era of cellulosic biomass based anisotropic nanomaterials for advanced applications[5]. Due to excellent elastic (150 GPa) and tensile moduli (7 GPa), most of the studies have focused on CNCs' use as the reinforcing agent in polymer nanocomposites. However, advanced nanoscale properties of CNC were realized more recently due to discovery of its chiral microstructure in early 1990's by Revol *et al.*[6] Since then CNC have been considered as the nanoscale building blocks for advanced macroscale mechanical and optical applications. Due to the increasing demand for smart products from biodegradable and non-petroleum based renewable sources, there has been a growing research interest on CNC to obtain engineered high performance materials[7].

Many studies have focused investigating the effects of different alignment techniques (*i.e.,* electric, magnetic, and mechanical shear) on liquid crystalline CNC dispersions to realize individual CNCs' high mechanical strength in films[2-8]. However, issues such as macroscopically controlled ordering, shear induced cracking, complex drying, and relaxation dynamics are not yet fully understood[7,8]. On the other hand, achieving the predictable ordering of CNC microstructures has been an area of active research for controlled and uniform optical properties (*i.e.,* selective reflection of light). Most of the studies have focused on air dried CNC dispersions, reporting uniform photonic domains on the lateral scale of only a few tens of microns[9]. The effects of initial dispersion concentration, drying conditions, and surface anchoring are yet to be adequately investigated to obtain uniform optical properties for advanced applications including mirrorless lasing, security encryption, and broadband selective reflectors[9-11].

The research goal of this dissertation was to test the hypothesis that CNC dispersions can be processed into films with tailored mechanical and optical properties. In particular, the research focused on producing microelectromechanical systems (MEMS) and selective reflectors for photonic applications. In addition, the objective was to understand the relationship between CNC cholesteric microstructures and processing that would enable controlled macroscale properties. Initially, the planar alignment of CNCs' cholesteric microstructure on macroscopic optical properties was investigated. The surface anchored CNC films were fabricated in a humid environment using orbital shear. The combined effects of slow drying, mechanical shear (below the unwinding threshold), and anchoring were studied using cross-polarized reflected optical microscopy, scanning electron microscopy, and spectrophotometry. Thus, a fundamental understanding of the

effects of dispersion microstructure, concentration, shear response, and drying conditions was developed for tunable optical properties by retaining macroscopic planar microstructure in films.

Next, to obtain uniform nematic alignment, the unwinding of CNCs' cholesteric microstructures was investigated. The objective was to demonstrate CNCs' intrinsic mechanical strength on macroscale films with alignment dependent properties. First, the relaxation dynamics of the CNC dispersions after shear cessation was explored using rheo-optics. A combined approach of relaxation experiments and 3-D finite element modeling was performed to understand the post shear relaxation dynamics. Results from this study provided the insights into drying window to retain the nematic CNC microstructures in films. Drying of mechanically sheared CNC dispersions was then adapted for an optimized MEMS microfabrication platform. The properties of the resulting films were controlled by several parameters including the initial dispersion concentration, wet thickness, shear rate, substrate roughness, and drying kinetics. Optimization of these parameters alleviated the well documented difficulties with CNC films' cracking during drying. Layout system designs for CNC MEMS and photolithographic fabrication methodology were developed for CNC films blade coated onto a patterned photoresist layer on a 100 mm diameter silicon substrate. The proper tuning of the lithography processes led to the successful fabrication of multiple CNC MEMS enabling micromechanical testing and actuation. Results based on nanoindentation, microscopy, as well as mechanical and electrostatic actuation, revealed controlled directional mechanical and optical properties in CNC MEMS.

In summary, the highlights of this dissertations provide new insights of CNC dispersion drying to obtain uniform selective reflection (on lateral length scales up to 1

mm) and MEMS type microdevices with a new material platform. An outline of this dissertation is described in the following sentences. Chapter 2 provides an extensive literature background on CNCs' structure, preparation, phase behavior, microstructural response to shear or rheology, and applications. Chapter 3 provides detailed information on instrumentation and techniques used in this research. Chapter 4 presents the insights on the effect of dispersion concentration, drying conditions, and surface anchoring on uniform selective reflection of circularly polarized light. Also, it provides information on the defect microstructure mimicking the defects found in natural photonic materials (*i.e., lomaptera* beetles). Chapter 5 discusses the complete unwinding of the cholesteric CNC microstructure into aligned 2 - 4 micron thick CNC films. It provides new insight into the importance of initial dispersion concentration to alleviate cracking resulting in successful microfabrication of CNC MEMS. To the best of the author's knowledge, this is the first study showing successful fabrication of multiple MEMS devices from this renewable forest product using conventional lithography microfabrication. Nanoindentation based elastic modulus of ~60 GPa shows the individual CNCs' excellent mechanical properties were largely achieved in macroscale freestanding devices. In summary, this chapter shows the potential for a paradigm shift of material platform for future MEMS research using renewable and biodegradable CNC nanomaterials. Chapter 6 discusses the proof of concept of the surface modified CNC films and microdevices for detecting cancer biomarkers. It presents the results on the hydrolytic stability of CNC films achieved *via* silane chemistry followed by immobilization of three different antibodies and antigens specific to the liver, prostate, and ovarian cancers. Finally, Chapter 7 summarizes the conclusions of this research.

Chapter 2 Background

2.1 Cellulose Nanocrystal (CNC)

2.1.1 Structure of CNC

Cellulose Nanocrystals (CNC) are anisotropic rigid nanomaterials derived from the most abundant natural polymer on earth, cellulose[12]. Cellulose is the main macromolecular constituent of plant cell walls and is produced by a range of natural organisms including some bacteria, algae, fungi, and even by animals like tunicate[13]. The native cellulose polymer consists of linear glucan chains with repeating (1→4)-β-glucopyranose/anhydro-D-glucose units as shown in **Figure 2.1** (The dimmer of anhydro-D-glucose units is referred as cellobiose)[14].

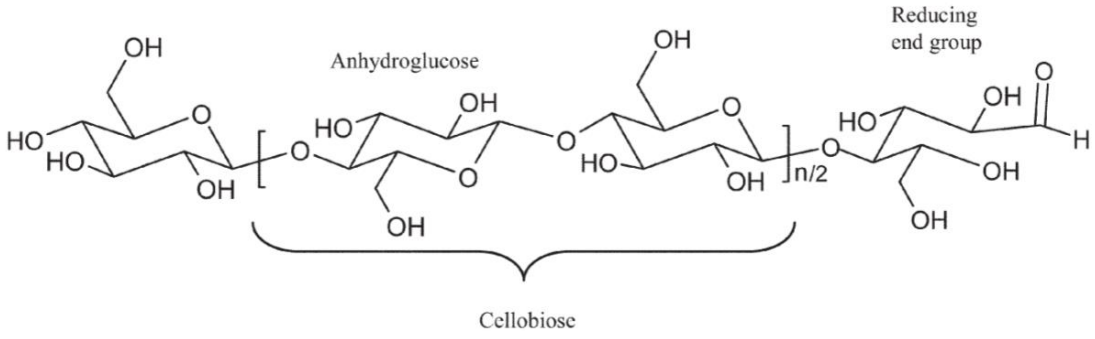

Figure 2.1. The structure of cellulose. The anhydroglucose unit is the monomer of cellulose where cellobiose is the dimmer. The cellulose chain has a direction, one end being a closed ring structure where the other being an aliphatic reducing end[14].

The complex supramolecular structure of cellulose has been a subject of debate for years. However, four different polymorphs of cellulose are known to exist especially in living plant cells; cellulose I, II, III, IV. The plant cellulose fibers have repeated crystalline

or ordered regions and amorphous or disordered regions that were first realized by X-ray investigation Ranby *et al.* back in 1951[15]. During biosynthesis, intermolecular hydrogen bonds and van der Waals attractions between adjacent molecules promote parallel stacking of cellulose chains. On the other hand, intra and inter-chain hydrogen bonding give rise to high axial stiffness making cellulose a stable polymer (crystalline region)[7]. Among other polymorphs, cellulose I has the highest axial stiffness or rigidity[16] and has two crystalline structures; triclinic (I_α) and monoclinic (I_β) (**Figure 2.2**)[7]. These two types can coexist, and their proportions may depend on the source of the cellulose[13,17,18]. The I_α is the dominating polymorph in algae and bacteria, whereas I_β is the dominating one in plant cellulose[19-21]. In both of these orientations, CNC unit cells have almost identical molecular arrangements exhibiting three principal lattice planes illustrated as 1, 2, and 3 in **Figure 2.2A**. The corresponding lattice planes (1, 2, and 3) for Iα and Iβ are $(110)_t$, $(010)_t$, and $(100)_t$ and $(200)_m$, $(110)_m$, and $(1\bar{1}0)_m$, respectively. As hydroxyl groups are equatorial to the cellulose chain plane, the most prevalent intra- and inter-chain hydrogen bonding is observed in $(110)_t$ and $(200)_m$ (labeled as hydrogen bonding planes in **Figure 2.2A**). Two possible networks for the hydrogen bonding have been proposed[22] as shown in **Figure 2.2B** and **C**. As illustrated, the interchain hydrogen bond network is dominated by O_3-H·····O_5 bond configuration. However, the intra-chain network configuration out of $(110)_t$ and $(200)_m$ planes is still in less consensus in cellulose community[7,22].

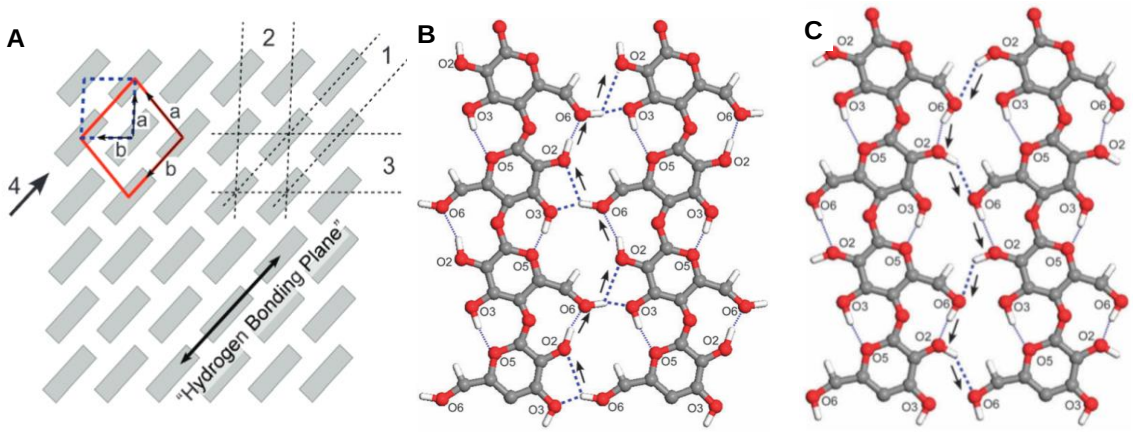

Figure 2.2. A) Schematic of chain cross section showing unit cells of cellulose I_α (triclinic, dashed line) and I_β (monoclinic, solid line). B) Two possible inter-chain hydrogen bonding networks of $(110)_t$ and $(200)_m$ lattice planes proposed in literature[7].

2.1.2 Preparation of CNC

The conversion of cellulose fibers to cellulose nanocrystals is a two-stage isolation process. The first stage is the pretreatment and homogenization of the source material which depends on the type of the cellulose source. As an example, plant and wood sources require pretreatments for partial or complete removal of hemicellulose, lignin, *etc*. (matrix material) and isolation of cellulose fibers[7]. The second stage is required to separate the purified cellulose materials and crystalline components of it. Among other approaches, three basic second stage separation processes are in practice to produce cellulose nanocrystals (CNC)[23-27]. These are mechanical treatment[23,25,28,29], acid hydrolysis[23,25,30], and enzymatic hydrolysis[23,25]. Any of these methods can be used to get CNC from the purified cellulose fiber/fibrils. However, to obtain the desired particle morphology, several of these methods can be applied in sequence[7,30].

When native cellulose is treated with strong acids, the less ordered regions are preferentially disintegrated compared to the crystalline regions (**Figure 2.3A**). The preferential isolation is attributed to the differences in the kinetics of the hydrolysis between disordered and ordered domains of cellulose[30]. Nevertheless, it is hypothesized that disordered/amorphous regions are more regularly distributed along the microfibers and therefore more susceptible to the acid attack. In an acid environment, through a water-induced reaction, protonation of the glucosidic oxygen takes place followed by dissociation of glucosidic bonds (hydrolytic cleavage) of the amorphous regions (**Figure 2.3B**). In addition, deprotonation and nucleophile formation of the acid molecules trigger the protonation of out of plane -OH groups on cellulose surface resulting in nucleophile substitution and condensation[30]. As a result, acid hydrolyzed cellulose turns into a colloidal suspension of cellulose crystallites[5,6,31,32]. As sulfuric acid is commonly used, nucleophilic substitution of the out of plane -OH groups is achieved by anionic sulfur ester groups as shown in **Figure 2.3C**.

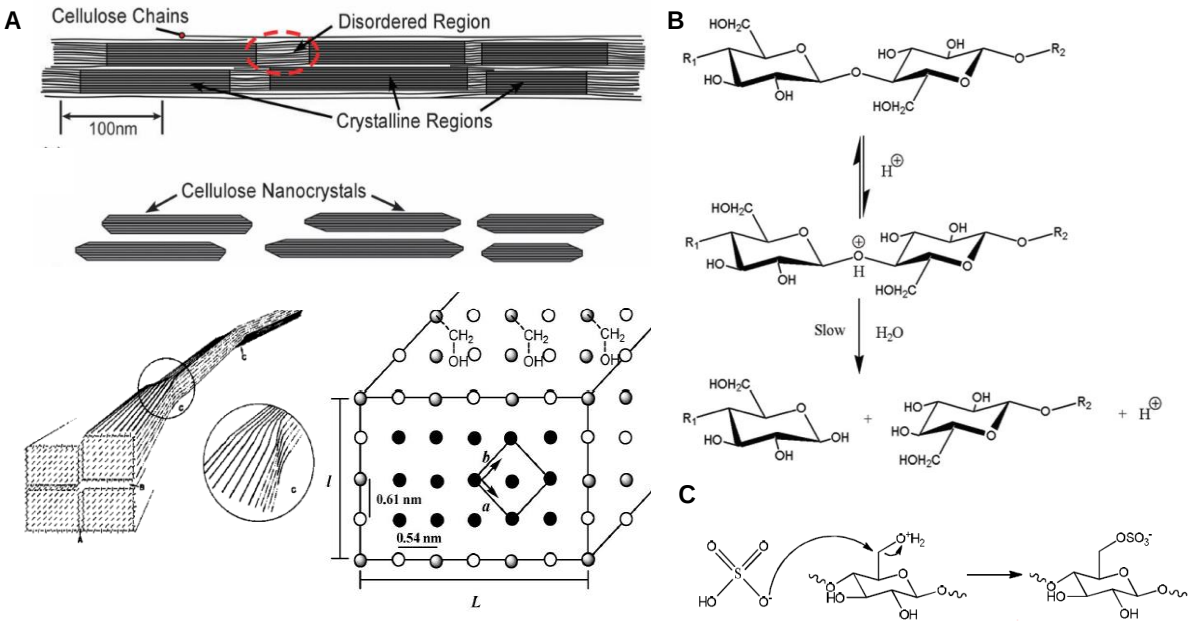

Figure 2.3. Schematic showing A) amorphous/disordered and crystalline/ordered regions in cellulose fiber and out of plane surface hydroxyl groups, B) hydrolytic cleavage of glycosidic bonds, C) nucleophilic substitution of hydroxyl groups during acid hydrolysis[7,30].

Depending on the presence of the surface charges, acid hydrolyzed CNC dispersions' stability behavior changes. Sulfuric acid hydrolyzed CNC dispersions are readily dispersible in polar media showing electrostatic stability due to the presence of sulfate ions on the surface[5,6,31-33]. In contrast, hydrochloric and phosphoric acid hydrolyzed CNC dispersions lack stability and tend to aggregate because of not having any surface charges[5,6,31,32,34,35]. Depending on the process conditions, the post separation CNC properties may vary significantly. Along with the type of the native cellulose source, hydrolysis conditions can affect crystal properties such as size, aspect ratio, the degree of sulfation/surface charge density, and the potential to form cholesteric liquid crystals[36-38]. Acid species (sulfuric, hydrochloric, phosphoric, and maleic acid[39]), acid concentration,

acid-to-cellulosic fiber ratio[30], agitation, reaction temperature, and reaction time greatly affect the resulting CNC dispersion colloidal stability, liquid crystalline phase and flow behavior, and optical or mechanical properties.

The production of CNC colloidal dispersion by acid hydrolysis was first reported by Ranby *et al*. in 1949[40]. Cellulose fibers were boiled in 2.5 N sulfuric acid for 1 - 8 hours followed by repeated washing and centrifugation in distilled water. Based on X-ray and electron diffraction analysis Ranby *et al.*[41] concluded that acid hydrolysis resulted in rod-like particles having the same dimensions as the crystalline regions of the cellulose fibers (**Figure 2.4)**. Next, Marchessault *et al.* hypothesized that the colloidal stability of CNC dispersions can be attributed to repulsive forces from the sulfate half esters introduced to the cellulose surface during hydrolysis[32]. This was further confirmed by the presence of 1% to 2% sulfur in freeze-dried CNC followed by electrophoresis showing the presence of negative charge particles. Since then specific protocols have been established for acid hydrolysis of cellulose from various sources including cotton[37,42], ramie[43-45], hemp[46], flax[47,48], wheat straw[49], bleached softwood and hardwood[34,38], bacterial cellulose[50-52], and Tunicates[53-55]. Dong *et al.* refined the hydrolysis conditions for cotton fibers by varying the temperature and time keeping the sulfuric acid concentration constant at 64 (w/v) with cellulose to acid ratio of 1:8.75 (g/ml)[37]. The optimum reaction temperature was reported as 45 ºC, producing a yield of 44% after 1 hour of reaction followed by quenching with cold DI water.

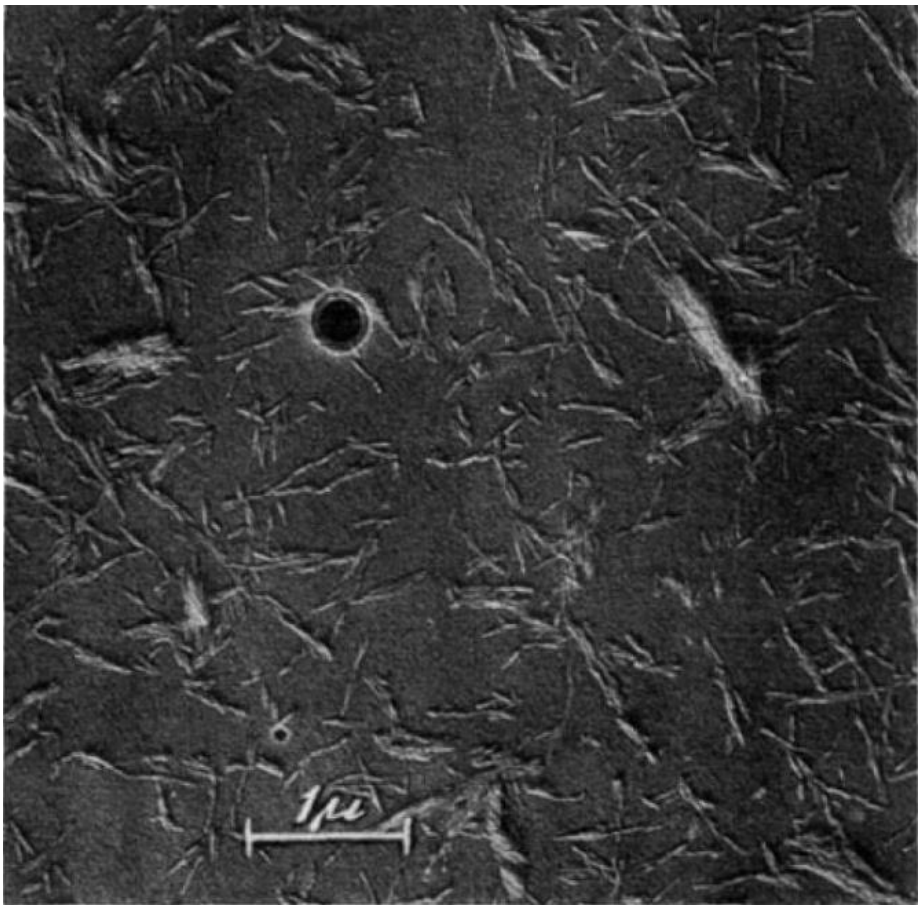

Figure 2.4. Electron microscopic image of sulfuric acid hydrolyzed CNC[41].

2.1.3 Surface Modification of CNC

Because of the abundance of -OH groups at the CNC surface, chemical modification with different moieties has been attempted including silylation, oxidation, etherification, esterification, and polymer grafting[30]. In addition, non-covalent modification by adsorbing surfactants and polymer coating has been performed to alter CNC surface properties. Besides, the tunable surface energy of CNC has been obtained especially for non-polar dispersion and hydrophobic matrix for composites without altering the rod-like morphology[56,57]. Heux *et al.* introduced a surfactant based non-covalent approach using

mono-and di-esters of phosphoric acid bearing alkyl phenol tails[56]. Small angle neutron scattering (SANS) study further revealed the formation of a thin surfactant coating of 15 Aº on CNC which improved its dispersibility in a non-polar solvent[58]. Both anionic and non-ionic based surfactants have been reported by Bondeson *et al*. and Kim *et al*., respectively, for CNC dispersion in poly(lactic acid) (PLA) and polystyrene based composite fibers[58-61]. Araki *et al.* first reported a (2,2,6,6-Tetramethylpiperidine-1-oxyl)-mediated or TEMPO mediated oxidation scheme of hydrochloric acid hydrolyzed CNC to promote polymer grafting[62]. Even after grafting of polymer chains, a homogeneous aqueous dispersion was obtained without any change of morphological and crystalline properties of the native CNC rods. However, the TEMPO-oxidized CNC have been mainly used to convert the hydroxymethyl groups to their carboxylic form as reported by De Nooy *et al.*, Montanari *et al*., and Habibi *et al*., showing the same integrity of post surface treatment morphological properties[63,64]. The cationization of CNC was also reported *via* nucleophilic addition of the alkali-activated -OH groups to the epoxy moiety of epoxypropyl trimethyl ammonium chloride (EPTMAC)[65]. In addition to the strategies above, esterification and silylation have been reported by several research groups. CNC with this functionalization have excellent dispersion properties in organic solvents which eventually improved the stiffness and ductility of CNC in nanocomposite[66-71]. Recently, Orelma *et al*. extended the TEMPO mediated carboxymethylated cellulose approach for biomolecular detection converting the -COOH groups to amine-reactive esters followed by avidin-biotin linkages[72,73].

2.1.4 Morphology and Dimensions of CNC

Cellulose nanocrystals are three-dimensional rigid rod-like parallelepipeds, and their geometrical dimensions (length *L*, width *w*) can follow a broad spectrum depending on the native cellulose source and reaction conditions[7,30]. As shown in **Table 2.1**, depending on the sources CNC can have cross-sectional morphologies of a square, parallelogram, rectangle, and cylinder[38,74-77].

Table 2.1. CNC particle size and morphology based on different sources of cellulose[7].

	Particle size					
Particle Type	Length (μm)	Width (nm)	Height (nm)	Cross-Section	Crystallinity[a] (%)	Iβ (%)
WF and **PF**	>2000	20–50 (μm)	20–50 (μm)	—	43–65	—
MCC	10–50	10–50 (μm)	10–50 (μm)	—	80–85	—
MFC	0.5–10's	10–100	10–100	—	51–69	10–66
NFC	0.5–2	4–20	4–20	—	—	—
CNC	0.05–0.5	3–5	3–5	Square	54–88	68–94
t-CNC	0.1–4	~20	~8	Parallelogram	85–100	76–90
AC					>80%	
(Valonia)	>1	~20	~20	Square	—	36–42
(Micrasterias)	>1	20–30	5	Rectangular	—	—
BC					65–79	
(Acetobacter)	>1	30–50	6–10	Rectangular	63	3–27
(Acetobacter)[b]	>1	6–10	6–10	Square	—	53
Cellulose II	Filament	—	—	Cylindrical	27–43	—

[a] Degree of crystallinity relative to cellulose. [b] Chemical addition during culturing.

In addition to morphology, the crystallinity of cellulose also varies depending on the source. The cellulose nanocrystals derived from tunicate exhibit the highest crystallinity index; this can be attributed to their higher aspect ratio (length over height) and higher fraction of the triclinic crystal structure[75,78] (**Table 2.1**). **Figure 2.5** shows the scanning and transmission electron microscopy images illustrating different morphologies of CNC. These morphological variations are attributed to various factors including the inherent variability of the biological synthesis process of cellulose in different sources

(statistical variability of cellulose crystals), crystal extraction process conditions, and differences in the measurement techniques used[7].

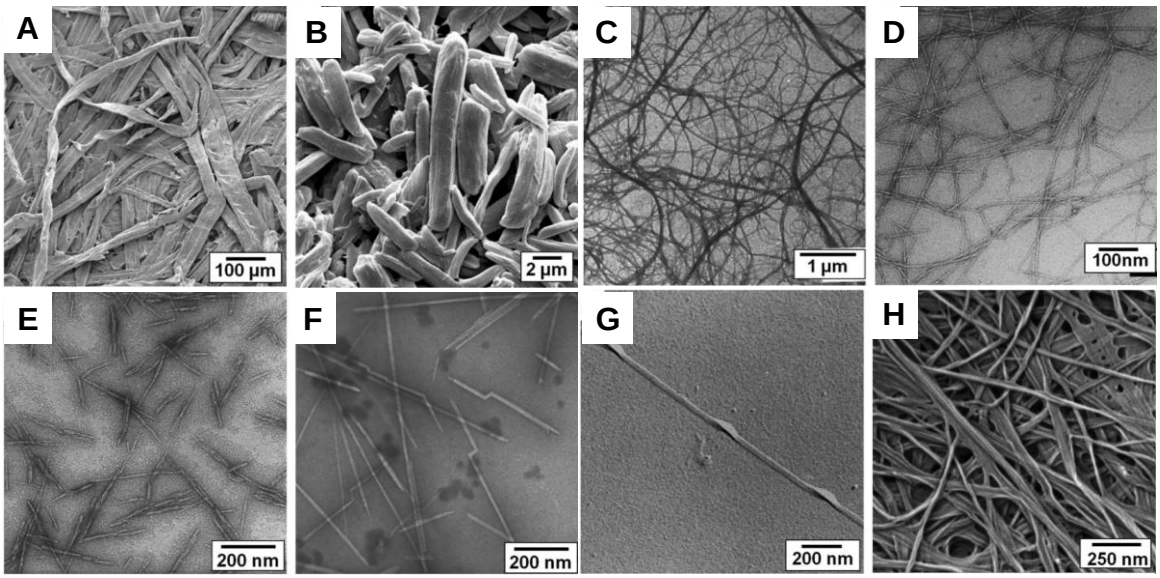

Figure 2.5. Scanning and transmission electron micrographs showing the different geometrical morphology of A) wood fibers, B) microcrystalline cellulose, C) microfibrillated cellulose, D) TEMPO nanofibrillated cellulose, E) wood CNC, F) tunicate CNC, G) algae CNC, and H) bacterial CNC[79-82].

2.1.5 Applications of CNC

Due to extraordinary mechanical and birefringent crystal characteristics, in recent years, CNC are drawing interests as a renewable nature-based nanomaterial[11,83,84]. However, realizing the intrinsic nanomaterial properties has been a challenge for researchers to manifest controlled properties on macroscopic length scales[85]. CNCs' biocompatibility, high elastic modulus (~150 GPa), low thermal expansion coefficient, optical transparency and anisotropy, negative diamagnetic anisotropy, and tunable surface chemistry have driven a broad range of applications including composites, security papers, wound

dressings and medical implants, and microstructural devices and sensors[86-89]. Shopsowitz *et al*. used CNCs' helical ordering to template inorganic sol-gel precursors such as tetramethyl orthosilicate and 1, 2-bis (trimethoxysilyl) ethane using ambient drying conditions[90-94]. Removal of CNC from the composite films using calcination showed excellent control over the optical iridescence which was proposed for photonic band gap applications. Following the footsteps of this research by MacLachlan team, helical silica[90], organosilica[93], TiO_2[92], metal nitride/carbon composites[95] and carbon have also been explored by other researchers using CNC templates. The transfer of CNCs' optical response to inorganic templates may further be realized in cholesteric-based mirrorless lasing in future[10,96]. Other than photonic applications, helical CNC templated mesoporous material can also be used for supercapacitors, transistors, and sensors[94]. Imprinting CNCs' photonic properties has also been investigated for thermosetting polymers. Giese *et al.* have reported CNC-melamine-urea-formaldehyde composites with tunable optical iridescence for photonic smart coating applications. Also, helical ordering CNC of alone has been used for optical sensors[97], decorative coatings[98], encryption in banknotes[99], circular dichroism with plasmonic nanoparticles[100], and scattering based light shutters[101]. Besides optical properties, CNCs' mechanical features have also been explored for reinforced mechanical performances in polymer composites[50,102-106], BioMEMS[107], biomedical devices[105], energy storage devices and sensors[108-111], and aerogels[110,112,113]. For all these macroscale applications of CNC, the fundamental understanding of fluid phase processing is very critical. Hence, rheology and phase behavior of lyotropic liquid crystalline microstructure of CNC has also been the major area of research interests[114-116].

2.2 Liquid Crystals

In 1888, the discovery of double melting points of cholesterol benzoate by Prague scientist Friedrich Reinitzer marked the birth of liquid crystal science[83]. Liquid crystals are an intermediate state of matter with the fluidity of a liquid and the order of a crystal or solid. Any entity, organic (with flat chain molecules) or inorganic (rods, plates, disks *etc.*) can form liquid crystals if two requirements are fulfilled. One is the shape anisotropy, and another is the rigidity of the macromolecule or inorganic entity. In the initial decades after its inception, liquid crystal science remained a purely academic interest; mainly shared between physicists and chemists[83]. In 1920, Friedel classified the three major types of liquid crystals as nematic, chiral nematic (cholesteric), and smectic. Afterward, in 1936 Bawden *et al.* reported a lyotropic liquid crystalline system based on rod-like tobacco mosaic viruses (TMV)[117]. However, it was 1949, when Onsager proposed the first theoretical model based on statistical thermodynamics[114]. In 1956, another competitive model was proposed by Flory, widely known as the lattice model[115]. It took almost 88 years since the discovery of this science until the liquid crystals found its way in display devices in 1976[116]. Then, 1970 - 1990 was more about the development of the application science based on aligned fibers spun from rod-like polymer liquid crystals. Until 1990 only a fewer than 20 different inorganic liquid crystal systems were discovered compared to thousands of organic liquid crystal polymers (LCPs). For almost 50 years, Florys' lattice model was more commonly used than Onsager's' due to its compatibility for semiflexible lower aspect ratio systems like LCPs. However, with a boom of nanotechnology science, a renewed interest was realized in inorganic liquid crystals, which perfectly followed Onsager's hard rod model.

Since the revolutionary invention of liquid crystal displays (LCD), this single application strongly dominated the advancement of liquid crystal science for quite a long time. Academic liquid crystal science has, in contrast, shown other stimulating trends of liquid crystal research on optics, nano/micro manipulation, novel composites, and biotechnology. Besides soft matter science, liquid crystals also overlap with polymers, colloids, and nanomaterials. Other than display technology, high strength DuPont Kevlar is another example of liquid crystals' application for engineered materials[118].

2.2.1 Types of Liquid Crystals

There are two primary types of liquid crystals: thermotropic and lyotropic. Small molecules (or other building blocks capable of forming liquid crystals referred as mesogens) with a rigid core and flat ring structure (gives shape anisotropy) can be the constituents of thermotropic liquid crystals[83]. Their phase transitions result from changes in temperature. Temperature drives the phase transition from crystalline ordered phase to biphasic (T_m or melting temperature) and from biphasic to isotropic liquid/disordered (T_c or clearing temperature). Thermotropic liquid crystals are made of individual molecules, and no further solvent molecule species is required. In addition to anisometry, thermotropic mesogens' rigidity is a combination of a stiff core (linear or circularly arranged aromatic rings) and flexible terminal chains (generally aliphatic hydrocarbons) as shown in **Figure 2.6A**[83]. On the other hand, lyotropic liquid crystals consist of macromolecular building blocks with shape anisotropy dispersed in a solvent. Phase transitions in a lyotropic liquid crystal are driven by the change of mesogens' concentration in the solvent. Lyotropic

mesogens can form from a micelle of amphiphilic molecules (non-polar tails and polar heads), amphiphilic lipids (phosphor, glycol, and sphingolipids found in body cell membranes), amphiphilic block copolymers, and non-amphiphilic macromolecules shown in **Figure 2.6B**[83]. Also, the lyotropic mesogens can be particles such as viruses or inorganic rods, plates, and disks in colloidal suspension[117,119].

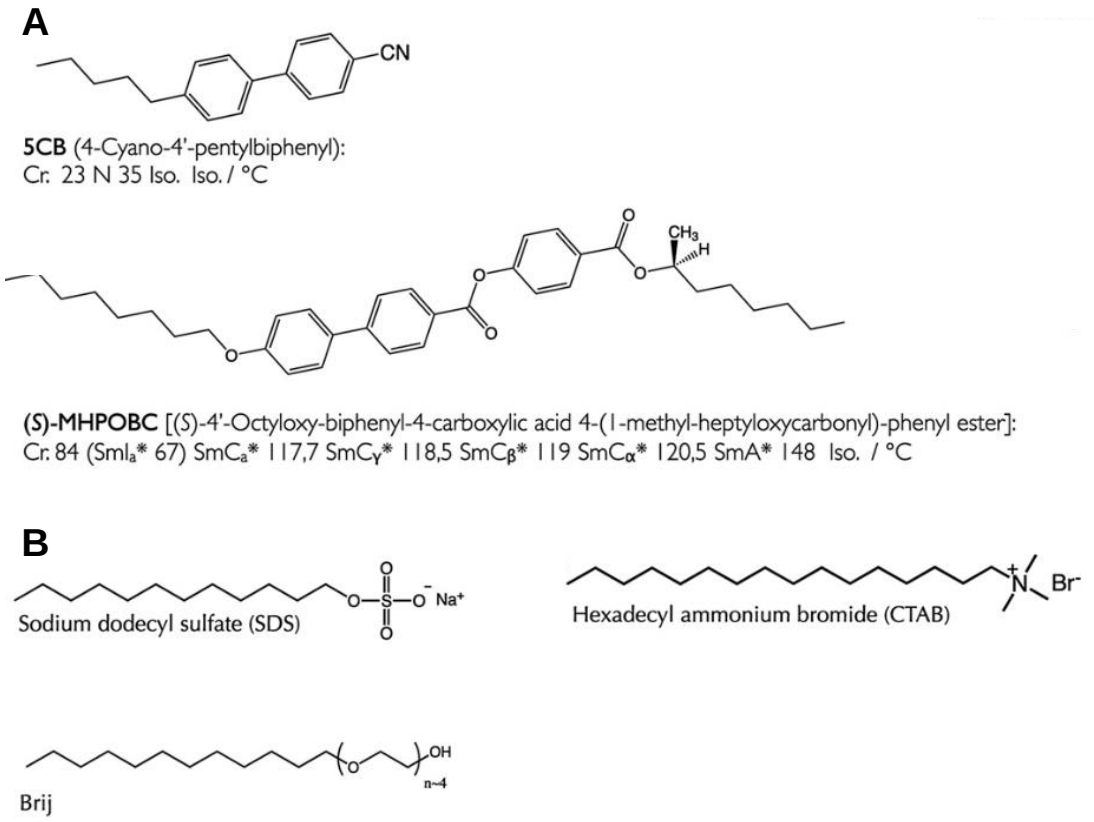

Figure 2.6. Schematic showing examples of A) thermotropic and B) lyotropic mesogens[83].

Under these two main categories, three basic liquid crystalline microstructures were classified by Friedel[120] back in 1920. These are defined as (i) nematic, (ii) cholesteric (chiral nematic), and (iii) smectic. Nematic is the simplest type with long range orientational order of the rod-like molecules or mesogens, but no positional order. In a

nematic class of liquid crystals, anisotropic macromolecules are locally oriented along a director called **n** as shown in **Figure 2.7A**.

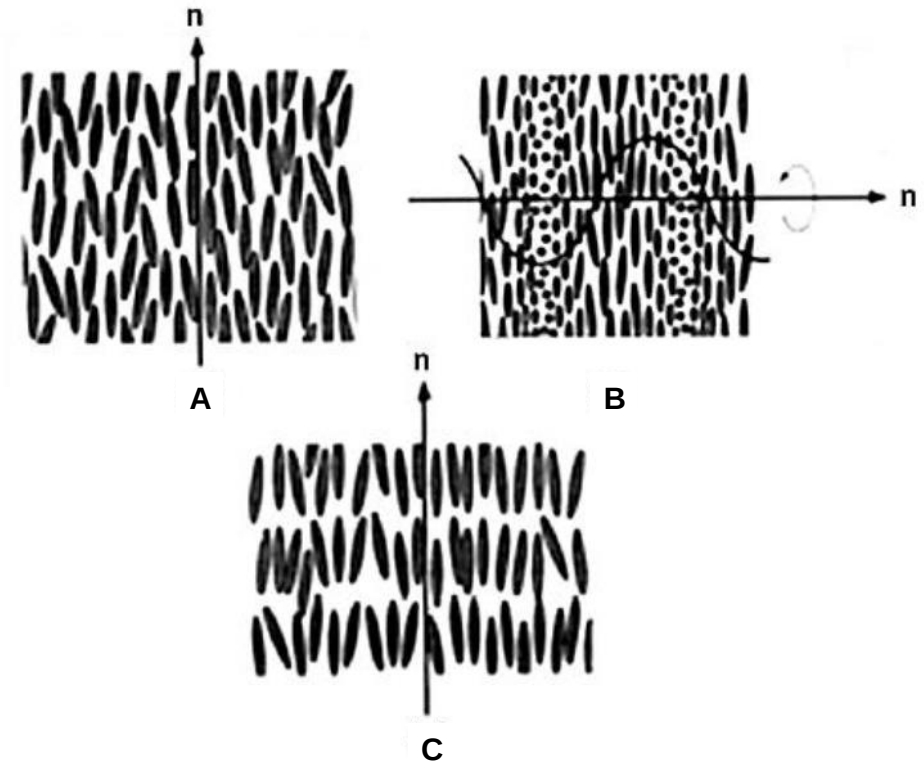

Figure 2.7. Schematic showing Friedelian classes of liquid crystals: A) nematic, B) cholesteric, and C) smectic[120].

In cholesteric or chiral nematic ordering, the nematic microstructures are slightly twisted along an axis perpendicular to the director **n**. That axis associated with cholesteric microstructure is termed as a helical director or helix as shown **Figure 2.7B**. **Figure 2.7C** shows the smectic microstructure where both long range orientational and positional order can be observed. In smectics, the degree of positional order may vary, and molecules can interchange their position from one layer to another. Within the layers, the molecules can be aligned perpendicular to the layers forming smectic type A or SmA. They can also be inclined at an angle forming smectic C or SmC. The concentration driven phase behavior

of lyotropic crystals mainly depends on the aspect ratio of mesogens. The rest of the dissertation will focus on lyotropic mesogens because CNC exhibit such phase behavior.

2.2.2 Lyotropic Liquid Crystal Phase Behavior

According to Onsager (1949), Flory (1956), and Doi-Edwards (1986) theories, the phase behavior of lyotropic liquid crystals can be pictured as a series of different regimes with increasing concentrations: dilute, semidilute, isotropic concentrated, biphasic, and liquid crystalline[114,115,121]. The following discussion will be focused on lyotropic rods since CNC are rod-like nanomaterials. As shown in **Figure 2.8**, in dilute regime the rod-like mesogens are far away from each other and exhibit Brownian motion. The rods can freely rotate and translate without any interaction with neighboring rods. In the dilute regime, the number concentration of Brownian rods can be predicted as $v < 1/L^3$ where L is the length of the rod and v is the number concentration of rods ($v\pi d^2L/4$ is the volume fraction of rods). The rotation is inhibited in the semidilute regime ($1/L^3 < v < 1/dL^2$), but the rods still can translate[122]. However, both rotation and translation get inhibited in the isotropic concentrated regime and rods are trapped in a straw-like volume as illustrated by the schematic in **Figure 2.8**. In this regime, rods tend to vibrate in a fixed volume about their axis before they transition into the biphasic regime. At a critical concentration of Φ_I the system enters into the biphasic regime where two phases of randomly oriented rods (isotropic) and ordered rods (liquid crystalline) co-exist in equilibrium. Further increasing concentration results in an increased portion of liquid crystalline phase; more rods will enter the ordered phase from the isotropic phase. At a second critical concentration Φ_{LC},

the whole system will transition into a single phase liquid crystalline regime. In summary, the phase behavior of rods with increasing concentration can be ascribed to loss of rotational entropy which is compensated by the gain of translational entropy due to alignment. Hence, alignment or ordering is thermodynamically favored. The concentration range of Φ_I to Φ_{LC} depends on both the aspect ratio (length/diameter) distribution of the rods and solvent quality (energetic interactions between rods and solvent)[123].

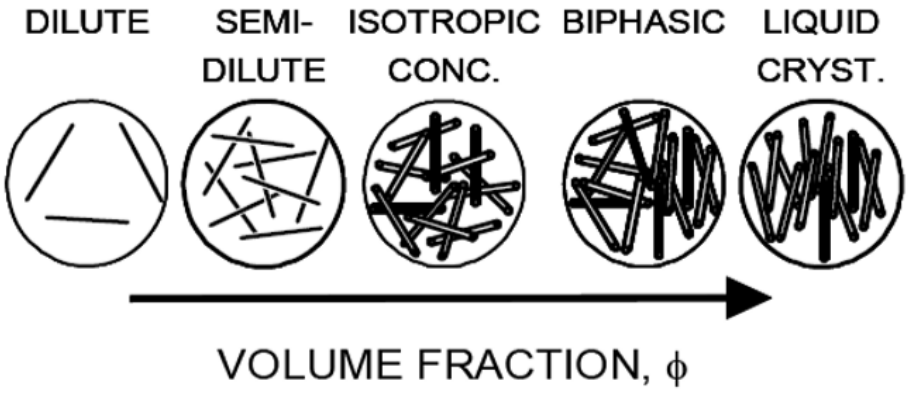

Figure 2.8. Concentration regimes for rod-like molecules during phase transition. Adapted from Doi and Edwards[122].

Lyotropic dispersions' phase behavior can be characterized by cross-polarized optical imaging and rheology of the bulk dispersions. Ureña-Benavides *et al.* investigated the phase behavior of lyotropic CNC using polarized microscopy and rheology[124]. **Figure 2.9** shows the onset of the biphasic regime at 5.0 vol. % (Φ_I) where the droplets of ordered CNC (white striped) appeared in a continuous matrix of isotropic CNC (black background) phase. As the concentration increased, the bright birefringence of the ordered phase increased to 9.9 vol. % (Φ_{LC}) where the whole system turned into a single liquid crystalline phase showing birefringence colors of aligned liquid crystalline domains of CNC[124]. At

even higher concentration (14.5 vol. %), CNC dispersion transitions in to gel phase indicated by the whitish texture under cross-polarized microscopy.

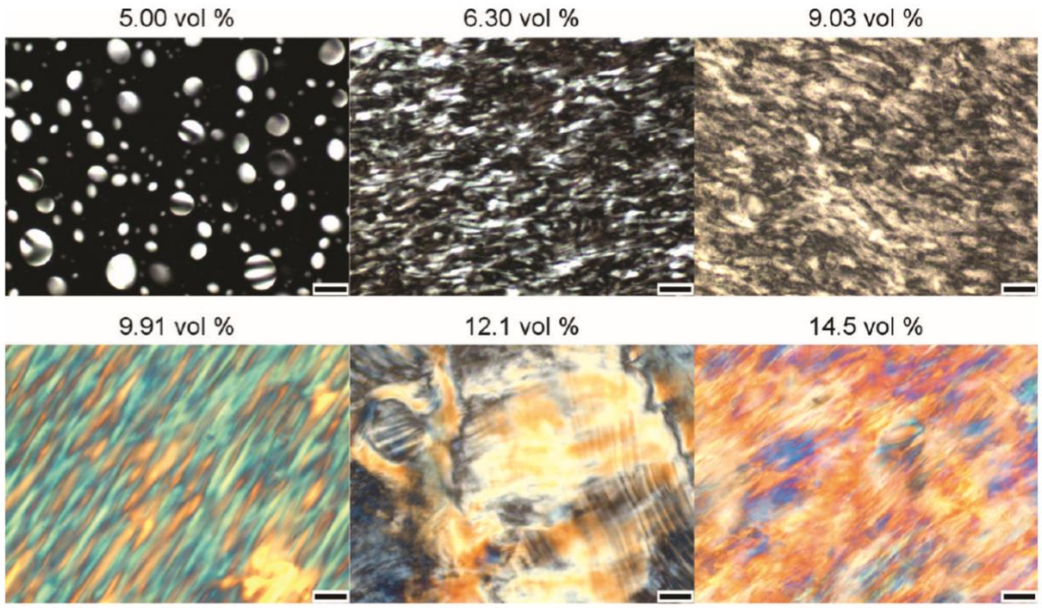

Figure 2.9. Polarized light microscopy of CNC suspensions at various concentrations at 25ºC. Scale bars are 50 μm[124].

2.2.2.1 Onsager Theory

Onsager (1949) theory is considered to be historically significant for understanding the phase behavior of liquid crystals with concentration as it was the first theoretical model developed based on hard repulsion between tobacco mosaic viruses (TMV)[114]. The theoretical approximation of this model is based on the basic idea of excluded volume interactions between hard rod-like molecules in a given volume. As hard rod-like molecules cannot interpenetrate, the excluded volume of adjacent rods would exclude the center of mass of any other rod from this particular region as shown in **Figure 2.10**.

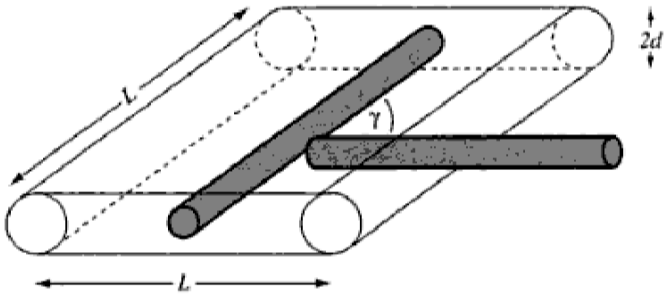

Figure 2.10. Diagrammatic representation of the excluded volume of two rod-like molecules, of length L and diameter d. γ is the angle between the long molecular axes. Adapted from Donald *et al.*[120]

The excluded volume of two spherocylinders with specific orientations can be calculated using the following equation:

$$V_{exclu} = 2L^2 d|sin(\gamma)| + 2\pi d^2 L + \frac{4}{3}\pi d^3 \qquad 2.1$$

where L is the length, d is the diameter, and γ is the relative angle between two rods. For rods with higher aspect ratios. When the spherocylinders have large aspect ratio, the equation is approximated as $V_{exclu} \approx 2L^2 d|sin(\gamma)|$. Hence, the excluded volume will be maximized if the angle between two rod-like molecules long axis is also maximum or $\gamma = 90^{\circ}$ and minimum for $\gamma = 0^{\circ}$. In other words, the excluded volume will be minimized if two rods transform from perpendicular to parallel orientations. As a consequence, liquid crystalline phase formation attributed to reduced free volume is caused by increasing translational entropy over the loss of orientational entropy due to parallel alignments of rod-like molecules[120,125]. The following equation gives the parameter that describes the degree of molecular orientations in nematic liquid crystals:

$$S = \frac{3}{2}\langle cos^2\theta \rangle - \frac{1}{2} \qquad 2.2$$

where *S* is orientational order parameter, θ is the angle between the rod and nematic local director **n**, and the brackets "< >" denote an average over all the rods. For a completely isotropic phase, S is 0, while for a complete nematic ordering or parallel orientation of rod-like molecules S is 1. Hence, the orientation order parameter for a liquid crystal phase will always be less than 1. The Onsager theory considered monodisperse hard rods in an athermal solvent. In addition, the equation of free energy interaction of rigid rods was truncated at second virial coefficient. As a result of Onsager's prediction, the phase boundaries of the biphasic chimney for monodispersed spherocylinders are following:

$$\Phi_I = \frac{3.34\ d}{L} \qquad 2.3$$

$$\Phi_{LC} = \frac{4.49\ d}{L} \qquad 2.4$$

where *L* is the length and d is the diameter of the rods. Here, Φ_I and Φ_{LC} are phase transition volume fractions of anisotropic mesogens. The volume fraction can be directly converted into weight fraction by the following equation:

$$w = \frac{mass\ of\ rods}{mass\ of\ rods + mass\ of\ solvents} = \frac{\rho_r V_r}{\rho_s V_s + \rho_r V_r} = \frac{\phi}{\rho_{rel} + (1 - \rho_{rel})\phi} \qquad 2.5$$

where V_r and V_s are the rod and solvent volumes, ρ_r and ρ_s are the rod and solvent densities, and ρ_{rel} is the density ratio (ρ_s/ρ_r). In an ideal solution, Onsager theory works best for very long rod-like mesogens with an aspect ratio (*L/d*) higher than 100[126]. Also, in a dilute regime where only pairwise excluded volume interactions can be approximated[125]. However, in a real system other factors may play a crucial role on the breadth of the

biphasic boundaries including polydispersity, the flexibility of the rod-like molecules, depletion interaction, sedimentation, and the balance between short-range electrostatic repulsion and long-range van der Waals attractive interactions[120,127]. A later extension of the Onsager model considering attractive interactions[128] and polydispersity[127] enabled it to be applied to other non-ideal systems as well. Stroobants-Lekkerkerker-Odjik (SLO) further considered the effect of charged rod-like systems on phase behavior into account which can be applied for sulfonated cellulose nanocrystal dispersion in water.

2.2.2.2 Stroobants-Lekkerkerker-Odjik Theory

As an extension of Onsager theory, Stoobants-Lekkerkerker-Odjik (SLO) theory predicts the biphasic boundaries for charged rod-like or polyelectrolyte systems; a full explanation of the underlying assumptions and limitations of the theory can be found in the original reference[129]. In brief, they demonstrated that for a system with excess monovalent electrolyte, the effect of electrostatic repulsion on phase separation could be understood. According to SLO, the presence of anionic or cationic charges on the rods surface have a two-fold impact. First, due to the charge and presence of associated counterions, there is an increase in the effective diameter of the rods D_{eff}. Second, a twisting factor h that accounts for the preferred orthogonal orientation of the charged rods. According to Odjik, the co-existing concentrations of the rods in the biphasic region can be obtained by the following equations[130]:

$$C_I = 3.290[(1 - 0.675h)b]^{-1} \quad 2.6$$

$$C_{LC} = 4.191[(1 - 0.730h)b]^{-1} \quad 2.7$$

where $b = \frac{\pi}{4} L^2 D_{eff}$ and $h = \left(\kappa D_{eff}\right)^{-1}$. The effective diameter and Debye length κ^{-1} of a charged rod system can be measured using following equations:

$$D_{eff} = D + \kappa^{-1}\left(ln\left(2\pi {v_{eff}}^2 Q \kappa^{-1} e^{-\kappa D}\right) + 0.7704\right) \quad 2.8$$

$$\kappa^{-1} = \sqrt{\frac{\epsilon_r \epsilon_o k_B T}{2 N_A e^2 I}} \quad 2.9$$

where v_{eff} is the effective linear charge density of rods, Q is the Bjerrum length (7.14 A^o in water). ϵ_r and ϵ_o are the relative and absolute permittivity constants, k_B is the Boltzmann constant, and T is the temperature. N_A is the Avogadro's number and I is the ionic strength.

2.2.3 Optical Signatures of Liquid Crystals

Whether long chain polymers or inorganic particles, liquid crystalline macromolecules exhibit birefringence. Due to their shape anisotropy, liquid crystalline mesogens possess two distinct refractive indices along parallel and perpendicular to their long axis of the anisotropic structure. Therefore, depending on the ordering of their long axes, liquid crystals can split the polarized light in two directions. One along the slow axis or long mesogen axis (extraordinary ray) and another is in the fast axis or short mesogen axis (ordinary ray). Orthogonally split slow and fast polarized lights encounter phase difference (due to the retardation of light) and when they come out of the liquid crystal material they

tend to interfere with each other. If they are allowed to pass through another polarizer, depending on the nature of the interference (constructive or destructive), birefringence colors appear. Hence, the difference between two refractive indices is termed as birefringence of that liquid crystalline polymers[131] Δn:

$$\Delta n = n_e - n_o \qquad 2.10$$

where n_e and n_o are the extraordinary and ordinary axes refractive indices of rod-like polymers. For example (**Figure 2.11**), two different refractive indices are reported for rod-like wood cellulose nanocrystals along and perpendicular to the anisotropic axis; the extraordinary (n_e) and ordinary (n_o) refractive indices of 1.595 and 1.534, respectively.

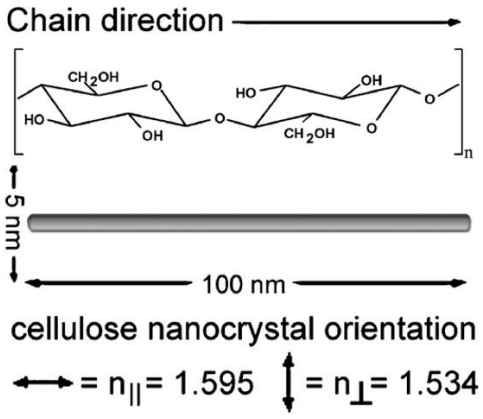

Figure 2.11. Schematic representation of cellulose chain axis illustrating the refractive index parallel (extraordinary/slow axis) and perpendicular (ordinary/fast axis) to the crystal axis[132].

When a monochromatic polarized light propagates through the homogeneously aligned nematic rods with a polarization angle of $0 < \theta < \pm 90^{o}$ to **n,** the extraordinary and ordinary ray of the outgoing light will experience a phase difference[133] δ:

$$\delta = \frac{2\pi d \Delta n \sin^2 \theta}{\lambda} \qquad 2.11$$

where d is the sample thickness, θ is the polarization angle to **n**, and λ is the wavelength of monochromatic polarized light. Due to this phase contrast of polarized light, birefringence induced interference textures can be observed using cross-polarized transmitted microscopy of liquid crystalline polymers. The typical birefringence texture attributed to the spontaneous nematic ordering of poly(p-sulfo-phenyleneterephtalamide)[134] (sulfo-PPTA) in water can be observed under polarized light microscopy as shown in **Figure 2.12**. The birefringence also reveals a polydomain texture; white and gray spots indicate the local ordering of **n** in 45° and 0° directions with respect to polarizers respectively. Depending on the order of interference birefringence texture of ordered mesogens' can also be colorful. Birefringence induced interference colors depend on ordering, retardation, and thickness of the sample. **Figure 2.13** show the Michel-Levy[135] chart illustrating the relation of material birefringence, sample thickness, and retardation of elliptically polarized lights to obtain different interference colors under cross polarized microscopy.

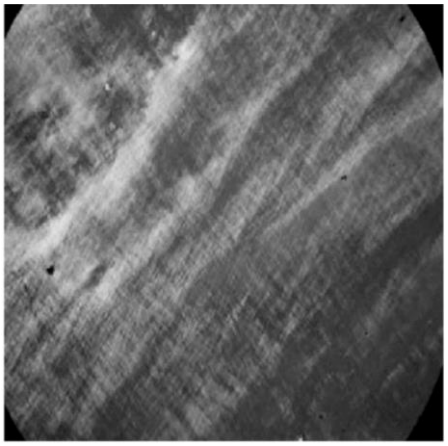

Figure 2.12. Cross-polarized transmitted light microscopy of 2 wt. % poly(p-sulfo-phenyleneterephtalamide) solution in water[134].

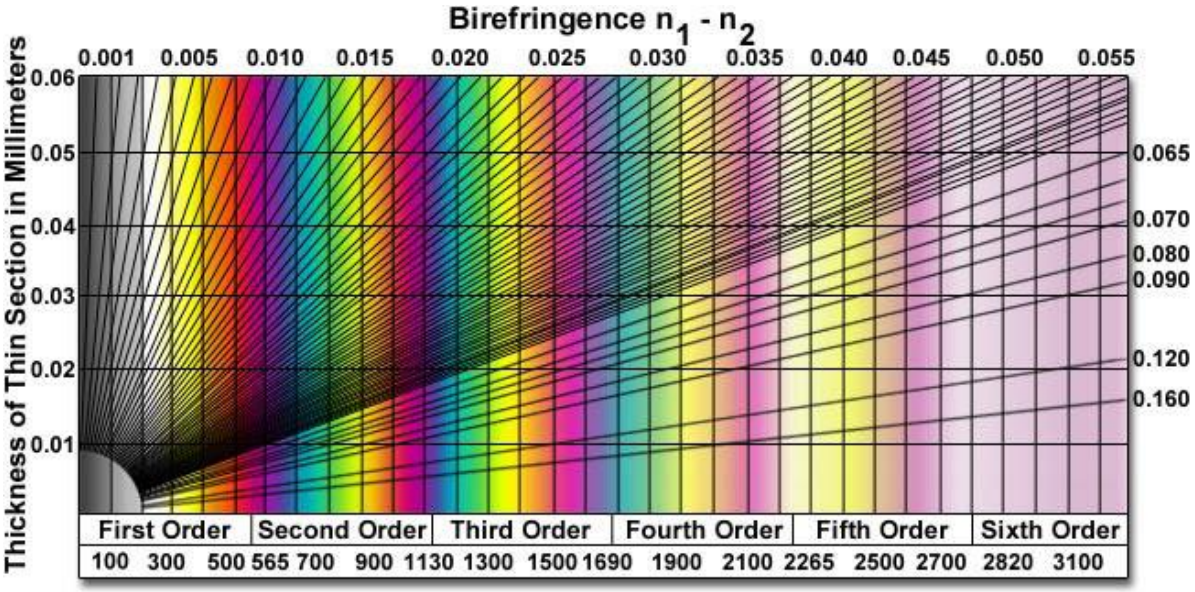

Figure 2.13. Michel-Levy birefringence chart showing correlation of LC film thickness, birefringence, and interference order. X and Y axes show order of interference (retardation) and sample thickness respectively. Diagonal lines represent material birefringence[135].

2.2.4 Rheological Signatures of Liquid Crystals

In addition to investigating the flow and deformation under stress, rheology can also probe liquid crystals (LC) phase behavior and microstructures. Rheological characterization of microstructural alignment due to shear, temperature, and mesogen concentration can provide insights into effects of fluid phase processing for the macroscopically ordered materials (e.g., in films or fibers or composites). The rheology of liquid crystalline polymers (LCPs) is different than conventional polymers. Therefore, the comparison of rod-like (*i.e.,* CNC) LCs' rheological signatures with model LCPs is a great tool to understand the flow behavior of lyotropic LC systems. Such model LCPs with rheological signature studied include hydroxypropyl cellulose[136,137] (HPC), poly (γ benzyl-L-glutamate)[138,139] (PBLG), and poly (γ benzyl glutamate) or (PBG)[140,141]. The interplay of

molecular interactions and conformation, shear flow, and orientation or relaxation state enables nematic LC to exhibit signature rheology behavior which can be summarized as follows[137,140]:

- Local maxima and minima of steady shear viscosity versus concentration curve
- Three-region steady shear viscosity versus shear rate curve
- Sign change of first normal stress difference with increasing shear rate
- Long oscillatory transients after start-up of steady shear flow
- Cox-Merz rule is not obeyed

2.2.4.1 Local Maxima and Minima in Viscosity versus Concentration Curve

A non-monotonic relationship between the steady shear viscosity and concentration is one of the key rheology features of lyotropic nematic LC. This behavior was originally reported by Hermans *et al*.[142] which was later supported by Papkov *et al*.[143] for poly-p-benzamide LCP. At the low shear rate, the viscosity of LC goes through a sharp maximum in the biphasic regime followed by a sharp drop until around the biphasic to liquid crystalline transition volume fraction. In addition, the magnitude of this maximum decreases with increasing shear rate[125]. The concentration associated with the shoulder (before reaching the maxima) is typically proved as the transition concentration for isotropic to biphasic regime.[144-146] As shown in **Figure 2.14** for 50/50 copolymer of n-hexyl and n-propyl isocyanate in toluene, when the biphasic system (> 20 v/v %) is predominantly isotropic, the viscosity tends to increase with increasing concentrations. However, with the increase of anisotropic phase in equilibrium with the isotropic matrix due to parallel alignment of

rod-like polymers less shear stress is required to flow aligned the LC. Hence, the steady shear viscosity goes down with increasing concentrations. As the increase in translational entropy compensates for the loss of rotational entropy, due to the relative ease of anisotropic macromolecules sliding past each other in a partially ordered state than a complete isotropic state sharp decrease in viscosity is encountered.

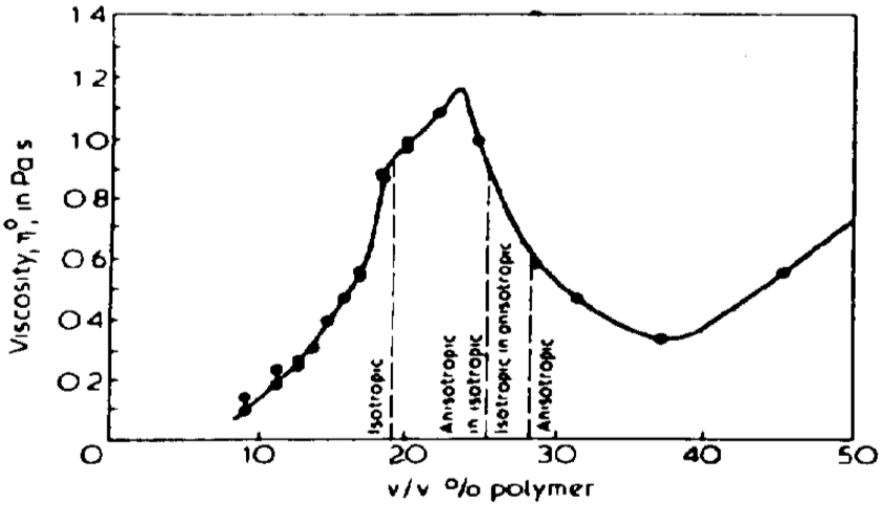

Figure 2.14. Viscosity versus concentration plot for 50/50 copolymer of n-hexyl and n-propyl isocyanate (molecular weight 41000) in toluene at 25ºC[145].

Typically, a fully liquid crystalline phase would be indicated by the local viscosity minima. Then, the viscosity increases again after the liquid crystal to gel transition; due to the extensive packing of rod-like molecules it takes more stress to flow orient the system. The average order parameter along the flow direction is increased from the maxima to the minima for a range of concentrations. Importantly, it is expected that the effect of shear orientation would be to ease the formation of ordered phase[144]. Therefore, the node of maximum viscosity will be approached faster with increasing shear rate. This behavior can be observed explicitly in **Figure 2.15**, where another LCPs was investigated by Kiss *et*

al.[147] As shown, the concentration of maximum viscosity of the poly(ɤ-benzyl-glutamate) in m-cresol decreases with an increasing shear rate which is in agreement with the observation reported by Hermans *et al*.[142]

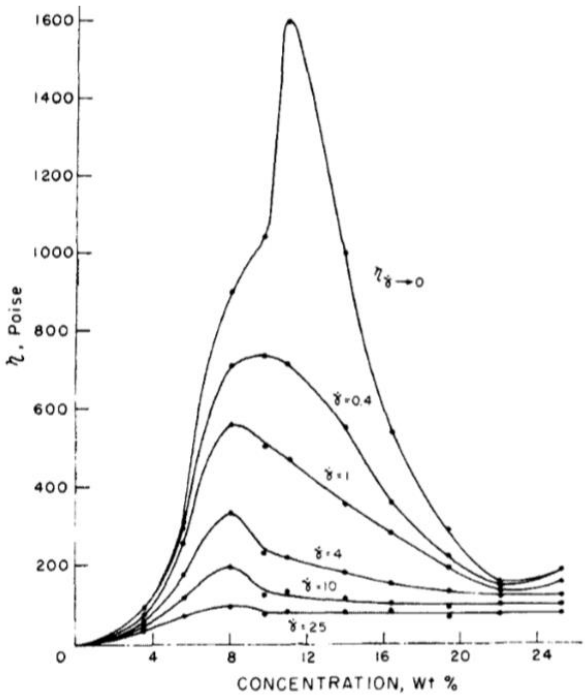

Figure 2.15. Decrease of maximum viscosity concentration of poly(ɤ-benzyl-glutamate) in m-cresol with increasing shear rate[144].

2.2.4.2 Three-region Behavior in Viscosity versus Steady Shear Curve

Three-region flow curve initially proposed by Onogi *et al.*[148] is used as a framework to discuss the rheology characterization of LCPs. Pochan *et al.*[149] also reported the similar flow curve with a different interpretation earlier for a cholesteric mesophase system which set the basis for the rheo-optics study of other kind of LC. As shown in **Figure 2.16**, the three-region flow curve of LCPs consists of two shear thinning (region I and III) and one Newtonian plateau (region II). Depending on the availability of lower shear rates data, it

could be hard to ascertain region I. However, depending on other evidence including yield stress and history-dependent rheology, the existence of three distinct regions have been confirmed for multiple LC systems[148,150-152]. Nevertheless, the shear thinning behavior at low shear stress has been the most complex and least understood rheology behavior of LC[153].

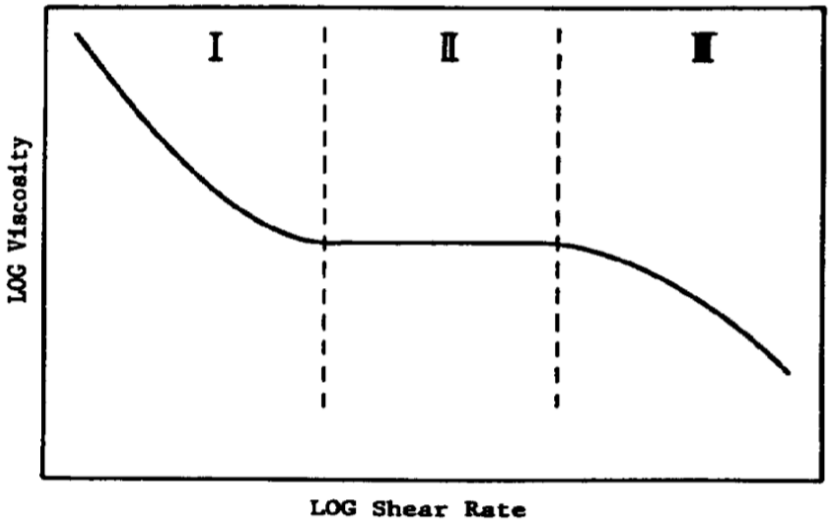

Figure 2.16. Three regions of LC flow behavior originally proposed by Onogi and Asada[148].

Three distinct mechanisms regarding microstructural changes in the region I have been proposed as discussed below:

- As reported by Fisher and Fredrickson *et al.*, due to a competition of molecular orientation at the boundary and in the shear field, the low shear rate dependent viscosity is observed[154]. According to this mechanism, the yield stress would be the static stress required to impose an equilibrium director field along the flow

direction from the globally random but uniform directors of the polydomain system[154,155].

- A second mechanism assumes the LC as a pile of domains before the stress is applied. It attributes the yield stress to "plastic flow of the piled domains" associated with the texture change of liquid crystals. This proposal was analogous to the findings reported by Horn and Kleman *et al.*[156]
- As opposed to the first two, the third mechanism refers the yielding behavior as a result of phase separation. For various reasons mainly related to the chemistry, some LC may undergo phase separation thereby giving rise to the yield stress behavior commonly observed in colloidal dispersion systems[157].

Kulichikhin *et al.*[158] reported an order of magnitude higher yield stress in the polyp-benzamide system (for the region I) in an initially homeotropic ordered (molecules perpendicular to the wall) state compared to planar ordering (molecules parallel to the wall) of molecules. This finding agrees with the proposed first mechanism. Based on the rheo-optics study of LCPs by Onogi *et al.*[148,159], the plastic flow of polydomains mechanism was reinforced. As shown in **Figure 2.17**, the initial pile of domains with globally random directors undergoes plastic deformation causing yielding at a very low shear rate (**Figure 2.17A** to **B** corresponds to the region I flow). The monodomain continuous phase texture can only be obtained at higher shear rates where all the directors tend to face the imposed flow direction (**C**).

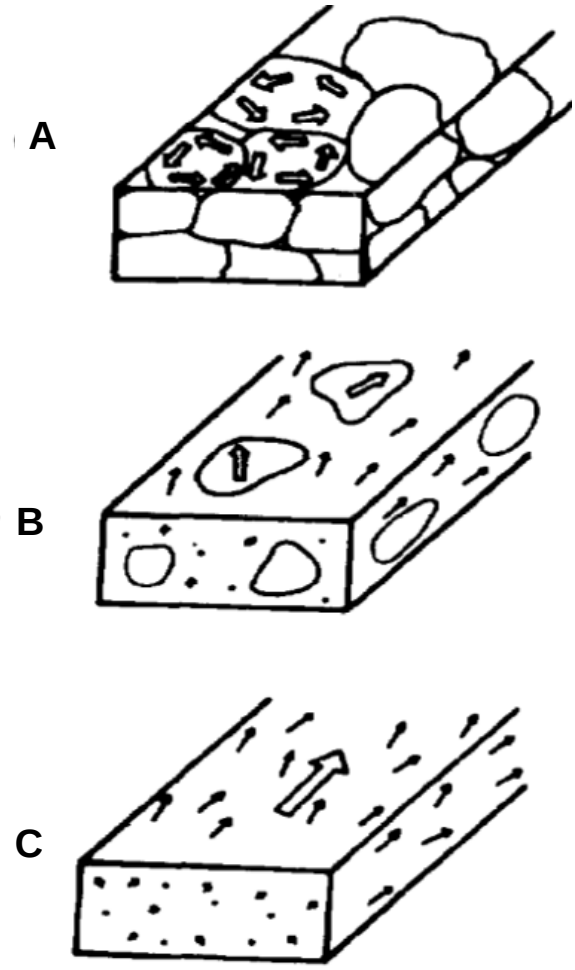

Figure 2.17. Schematic representation of the bulk LCs' structure under applied shear. (A) Piled polydomain system, (B) dispersed polydomain system, and (C) monodomain continuous phase[148].

Cogswell *et al.*[160] and Wissbrun *et al.*[153] independently found the evidence of phase separation and shear history dependency of yield stress in the region I flow behavior. Due to lack of elastic recovery especially in heterogeneous LC, the steady state rheology measurements become sensitive to shear and thermal history for both lyotropic and thermotropic systems[158]. In summary, the material history is essential and can be responsible for the change of microstructure of liquid crystal systems. If the structure of some sort is already induced it may affect the yield stress and shear thinning behavior of

region I. In effect, the disruption of intrinsic microstructure may cause the elimination of region I completely[153]. However, for lyotropic nematic LC, region I is also believed to be associated with the director "tumbling" of the anisotropic phase[146,161]. For a lyotropic cholesteric system, the region I mechanism is even less well understood as the helix director flow alignment to nematic director flow alignment is very complicated. At the low shear rate, region I of some cholesteric LCPs like hydroxypropyl cellulose show diffraction characteristics of the chiral nematic phase while the chiral structure is unwound at higher shear somewhere in region II[125,162].

Region II or "Newtonian Plateau" followed by another shear thinning region III are the other standard features for LC. These can be observed even for isotropic solutions of flexible or rigid polymers[144,146,153]. However, Davis *et al*. reported a very narrow plateau between two shear thinning regions for inorganic nanorods or single-walled carbon nanotubes (SWNT) in superacids[161]. For thermotropic LCPs, region II is attributed to wagging, kayaking, or log rolling of rod-like molecules along the flow direction[163,164]. For cholesterics, region II is where the chiral structure is reported to be unwound as observed for HPC and cellulose nanocrystal systems[162,165]. The second shear thinning region or region III is attributed to individual rod alignment along flow direction resulting in a monodomain of nematic mesophase[153].

2.2.4.3 Sign Change of First Normal Stress Difference with Increasing Shear Rate

The first normal stress difference, $\tau_{11} - \tau_{22}$, is the total normal thrust of flow measured at a given shear rate[144]. **Figure 2.18** shows the first normal stress difference N_1 changing

signs with increasing shear rate for a lyotropic nematic LCP originally reported by Kiss *et al*. in 1978[144]. Since this first evidence of negative N_1, several other LCPs were reported to show two sign changes in N_1. At lower shear rates N_1 is positive and increases with shear rate which can be associated with director tumbling. At the intermediate shear rate, N_1 suddenly drops and changes sign to negative due to director wagging which may cause low molecular ordering. At even higher shear rate, N_1 becomes positive again which is attributed to flow alignment of rods[125,166]. This sign change of N_1 can directly be compared with three distinct viscosity versus shear rate regions as shown in **Figure 2.18**.

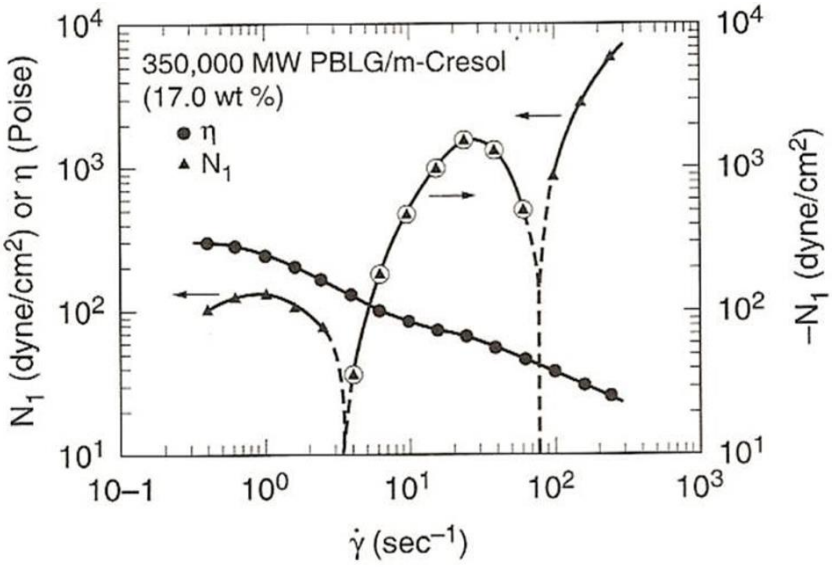

Figure 2.18. Shear viscosity and first normal stress difference versus shear rate for 17% PBLG (MW=350,000) in m-cresol (circled triangles are negative N_1)[125].

2.2.4.4 Long Oscillatory Transients after Start-up of Steady Shear Flow

Another remarkable feature of LC is the long oscillatory transients in shear flow observed before reaching the steady state. Typically, more than 100 shear units (product of shear rate

and time) is required to reach the steady state of lyotropic LC[146]. In contrast, for isotropic and ordinary polymer solutions, a few shear units may be sufficient[167]. **Figure 2.19** shows the long transient oscillatory response of 7.6 vol. % single-walled carbon nanotubes dispersion in superacids to the start-up of steady shearing at 5 s^{-1}; reported by Davis *et al*.[161] The response can be characterized by a broad peak followed by damped oscillations. After a few damped oscillations, the amplitude falls below the noise fluctuation resulting in a steady-state value of stress[168]. Both the shear stress τ and first normal stress difference N_1 oscillate for at least 100 shear units before they reach a steady profile[161]. The periodic oscillations at steady state can be processed with a scaling law to reduce all the data at different shear rates to a single curve, by plotting the reduced stress (stress over stress at steady state) versus total shear deformation (shear units)[168,169]. In region II of viscosity versus shear rate plot, the oscillation period is fairly regular and inversely proportional to the shear rate[146]. Hence, when transient response at different shear rates (of region II) are plotted against shear deformation, the maxima and minima of the oscillation will typically overlap.[168,169] In summary, the result of start-up shear flow exhibits a long transient damped periodic behavior of shear stress. This behavior (resting time affects the oscillation peaks) is governed by both shear deformation and shear rate[168].

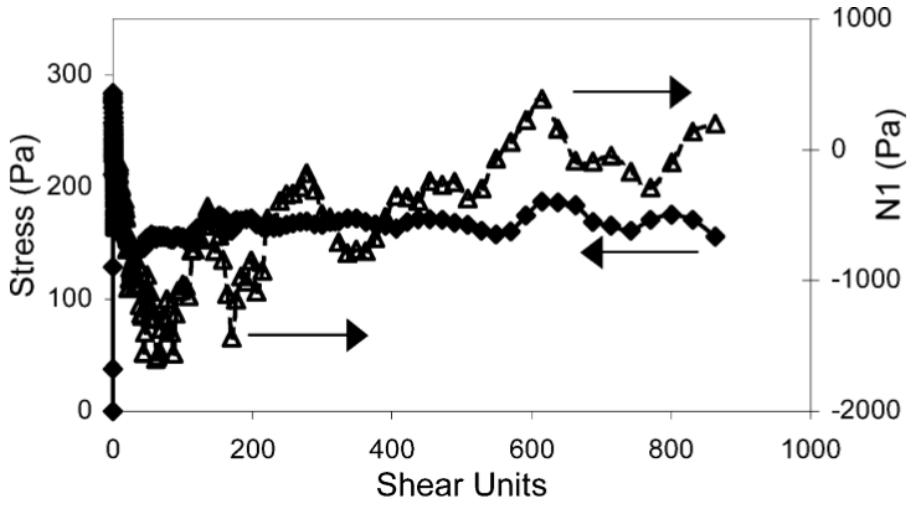

Figure 2.19. The long transient oscillatory response of 7.6 vol. % (6 wt. %) single-walled carbon nanotubes in 102% sulfuric acid to start-up shear flow at a 5 s^{-1}shear rate[161].

2.2.4.5 Cox-Merz Rule is not Obeyed

According to Cox-Merz rule, the complex viscosity $\eta^*(\omega)$, a linear viscoelastic material property, equals to steady shear viscosity $\eta(\dot{\gamma})$ at equal values of angular frequency ω (s^{-1}) and shear rate $\dot{\gamma}$ (s^{-1}). The first molecular theory, successfully predicting this rule for the monodisperse polymer was proposed by Marrucci *et al.* in 1996[170,171]. Later, it was extended for a polydisperse system using convective constraint release mechanism by Mead *et al*[172,173]. In contrast to ordinary polymers, the Cox-Merz rule is not obeyed by LC. LC having a complex deformation dependent microstructure fails to follow this empirical rule and hence, steady and dynamic viscosities do not exhibit the same behavior as a function of shear rate and frequency[167,168,174,175]. **Figure 2.20** shows an example of lyotropic SWNTS dispersion in 102% sulfuric acid. At a given frequency and shear rate the dynamic and steady viscosities do not equal, not obeying the Cox-Merz rule[161].

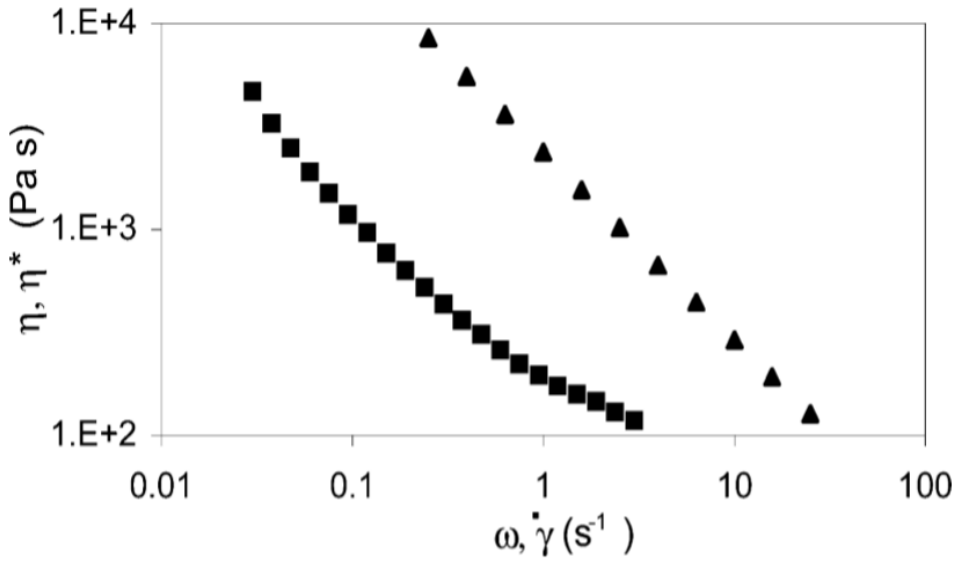

Figure 2.20. Cox-Merz rule is not obeyed by a lyotropic LC which is 7.6 vol. % SWNTS in superacids. Triangles: dynamic viscosity η*versus frequency ω, Squares: steady shear viscosity η versus shear rate γ[161].

2.3 Aqueous CNC Dispersions

Because of having negative half sulfate esters on the surface, CNC can easily be dispersed in polar solvents like water. CNC dispersions in water can have a translucent texture under ambient light, but cross-polarized light and microscopy reveal the isotropic or liquid crystalline regime of various concentrations. As shown in **Figure 2.21A**, the aqueous sulfonated CNC dispersion with Na^+ counter ions phase transitions from isotropic (3 wt. %) to biphasic (4 wt. % to 9 wt. %) and then to fully liquid crystalline (10 wt. % or above) regimes. The anisotropic phase birefringence can be observed under cross-polarized light[176]. **Figure 2.21B** and **C** show the cross-polarized microscopic images of isotropic (3 wt. %) and biphasic (7 wt. %) dispersions, respectively, revealing the fingerprints of cholesteric microstructure associated with the anisotropic phase of CNC.

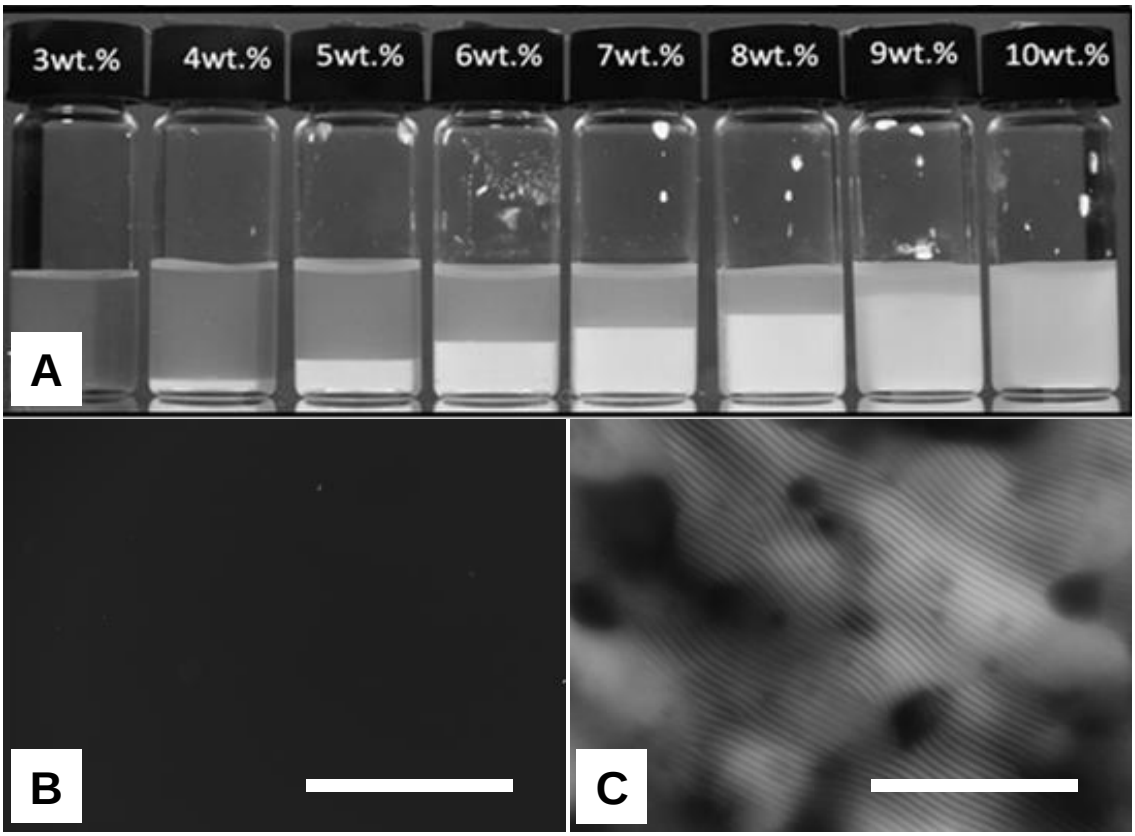

Figure 2.21. A) Photograph of CNC dispersions of various concentrations in water under the cross-polarized light environment (Adapted from Honorato-Rios *et al.*[8]). Cross-polarized transmitted light microscopic images of B) 3 wt. % (isotropic) and C) 7 wt. % (biphasic) dispersions.

2.3.1 Colloidal Stability of CNC

As for other colloidal dispersions, the zeta potential (ζ) indicates the colloidal stability of CNC in water[177,178]. It is the electrical potential at the interfacial electric double layer of the CNC rods at the slipping plane relative to any point of in the bulk fluid away from the interface[179]. Using electrophoretic light scattering, for a 0.01 wt. % sulfonated CNC (with H^+ counterions), a zeta potential of -40.4 ± 1.7 mV was reported by Lin *et al.*[179] Interestingly, the post sulfation technique resulted in better colloidal stability with a zeta potential of -66.1 ± 1.5 mV. However, the colloidal stability, phase separation, and

cholesteric microstructure are sensitive to the nature of the counterion present in the suspension[180]. A decrease in electric double layer owing to the added electrolyte (NaCl) can increase the chiral interactions resulting in a decrease of the cholesteric pitch of the CNC microstructure[31,52]. On the other hand, Dong *et al*. and de Souza *et al*. reported an increase of critical concentration for ordered phase formation due to increased ionic strength upon added inorganic electrolytes[37,181]. For organic electrolytes, the phase transition concentration increases (in general), with increasing counterion size attributed to the interplay of hydrophobic and steric interactions[182]. Nevertheless, the colloidal stability of CNC dispersion decreases with increasing either monovalent (Na^+) or bivalent (Ca^{2+}) counterion concentrations. Above a certain concentration of Na^+, the zeta potential decreases dramatically as reported by Araki *et al*.[51] and Boluk *et al*.[183] Recently, Zhong *et al*.[180] also reported the similar behavior with dynamic light scattering based size probing of CNC with added electrolyte concentrations. As shown in **Figure 2.22A** and **B**, for both Na^+ and Ca^{2+} counterions, zeta potential decreases dramatically for CNC dispersion. For bivalent counter ions like Ca^{2+}, the stability decrease is more pronounced which can be attributed to the bridging effect. For both monovalent and bivalent counterions, there is a steady plateau nanomaterial size plots (**Figure 2.22A** and **B**) up to the threshold of the added electrolyte concentrations. Then there is a sharp increase in the size of CNC with increasing electrolyte attributed to floc or aggregate formation. The colloidal stability of sulfonated CNC dispersion may also be affected due to temperature change. A drastic change of temperature is recognized to cause desulfation and release of sulfuric acid from the surface of CNC reported by Beck *et al*.[184] The colloidal stability may also depend on the post-hydrolysis treatment of CNC as trapped hydronium ions on the rods' surface tend

to facilitate aggregation. In this case, mild sonication treatment after the hydrolysis reaction is believed to improve the colloidal stability by breaking those aggregates releasing the trapped counter ions[88].

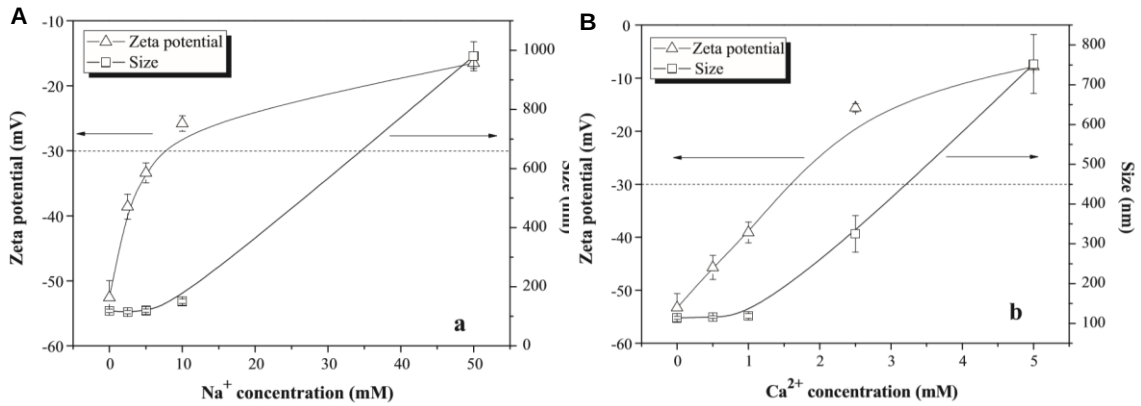

Figure 2.22. Plots showing zeta potential and size of CNC with added electrolyte concentrations of A) Na^+ and B) Ca^{2+} counterions[184].

2.3.2 Phase Behavior of CNC Dispersions

Rod-like CNC can exhibit liquid crystalline phase behavior upon increasing volume fraction[185]. CNCs' liquid crystalline ordering induces macroscopic birefringence texture which was first observed by Marchessault *et al*. using cross-polarized light microscopy[5]. The CNC rods in a dilute dispersion are randomly oriented forming an isotropic phase. At a sufficiently high dispersion concentration the CNC can form a chiral nematic or cholesteric liquid crystal phase[5,6,31,32]. In CNCs' cholesteric ordering, the nematic layers are left-handedly rotated along an axis perpendicular to **n**. This axis is termed as the helical axis or cholesteric axis as shown in Figure **2.23A**. When **n** completes a full rotation of 360º, the covered distance is considered as the pitch P. **Figure 2.23A** illustrates the half pitch

(p). The chiral nematic pitch can easily be observed using cross-polarized microscopy as shown in **Figure 2.23B**. Two white stripes (birefringent layers) and two black stripes are indicative of the cholesteric pitch P.

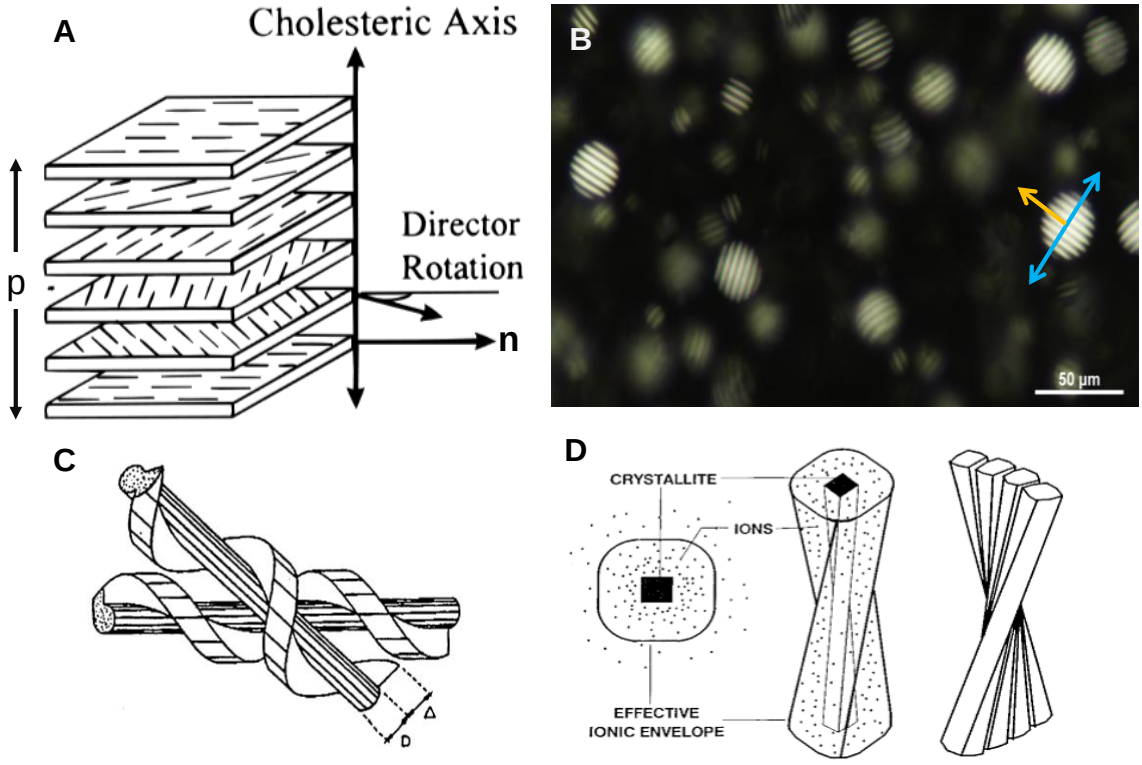

Figure 2.23. A) Schematic showing the chiral nematic ordering, n is the nematic director perpendicular to the chiral nematic or cholesteric axis, p indicates half pitch; length that is covered when director rotates 180º about the cholesteric axis[31], B) cross-polarized transmitted light microscopy of CNC cholesteric alignment, on the image blue and orange arrows are basically helix and director directions respectively. Oblate shape CNC birefringent liquid crystalline domains are suspended in an isotropic matrix of suspension, C) schematic of twisted morphology illustrating tighter packing at an angle proposed by Orts *et al.*[33], D) schematic showing ionic envelope developed surrounding the sulfonated CNC rod, due to the physical twist of the rods envelope of surrounding counter ions is also twisted[33].

The chiral nematic ordering is due to the intrinsic chiral interaction between CNC rods. In 1976 Straley *et al.*[186] proposed that the source of the chiral assembly is directly attributed to the packing of screw-like rods. Later, Orts *et al.*[33] used small angle neutron

scattering (SANS) and reported that CNC rods pack tighter along the chiral axis than in the nematic planes perpendicular to it. As shown in **Figure 2.23C**, screw-like CNC rods' threads within each other can fit tightly resulting in cholesteric ordering. That was in agreement with Straley's hypothesis as well. Interestingly, the physical twist in CNC rods may impose a twist in the electric double layer surrounding the rods as shown in **Figure 2.23D**. In between two nematic layers, the presence of the electric double layers and lubricating media (*i. e.* water) play an important role in terms of defining the pitch or the chiral interaction. With increasing concentration, more rods pack together changing these ionic envelopes' thickness, resulting in smaller pitch and higher chiral interactions. However, the importance of negative sulfate charges on the surface for chiral nematic orientation is still a debated issue. Among all the different types of CNC functionalizations, only sulfonated CNC dispersions in water exhibits chiral microstructure[65,162]. For example, CNC generated from hydrochloric acid hydrolysis do not give rise to the chiral nematic orientation as they are uncharged rods[65]. But interestingly, some recent studies on polymer grafting[62] and surfactant coating[56] of sulfonated CNC have provided the compelling evidence of chiral microstructure even though the negative sulfate charges were fully masked. More supporting evidence was reported by Araki *et al.* where nematic to chiral nematic ordering of bacterial CNC dispersion was achieved by only introducing electrolytes to it[51]. In this case, a morphological change was encountered. Due to the screening of surface charges, twisted rod geometry was recovered resulting in chiral nematic ordering as shown in **Figure 2.24**. **Figure 2.24A** illustrates the bacterial CNC rods with surface charges on it. It shows the effective particle shape which is non-chiral attributing to the repulsion by surface charges extending to long-range. **Figure 2.24B**

illustrates the affected particle shape which is twisted or chiral rod after adding NaCl. NaCl decreases the long-range repulsion in aqueous media recovering the twisted morphology which supports the theory of chiral rod geometry that gives rise to chiral nematic ordering in CNC dispersions.

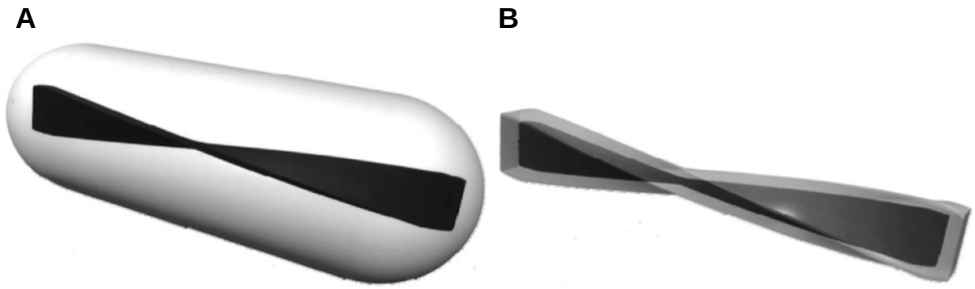

Figure 2.24. Schematic representation of bacterial CNC rods A) before and B) after the NaCl addition to screening out the charged layers[51].

2.3.3 Rheology of CNC dispersions

The rheological understanding of CNC is still evolving[159,189,191]. CNC do not show all the rheological signatures associated with lyotropic liquid crystals as reported by some recent rheological studies performed on aqueous CNC suspension obtained from different sources[162,185,187]. For example, no viscosity maxima and minima in the steady shear viscosity versus concentration graph was found. The sulfonated cotton CNC (with H^+ counterions) in water exhibit a monotonic increase of steady shear viscosity with concentration for a range of shear rates (**Figure 2.25A**), reported by Ureña-Benavides *et al.*[124] Similar behavior was observed by Haywood *et al*. for sulfonated wood CNC (with Na^+ counterions) dispersion in deuterium oxide (**Figure 2.25B)**[162]. Unlike the LCPs, no local maxima in the biphasic region or minima at biphasic to liquid crystalline region were observed. Instead, a very small decrease in liquid crystalline viscosity was observed upon

increasing concentration[33,124,188] (**Figure 2.25A**). However, the average order parameter tends to decrease at liquid crystalline to gel transition concentration where viscosity reaches a plateau (**Figure 2.25B**).

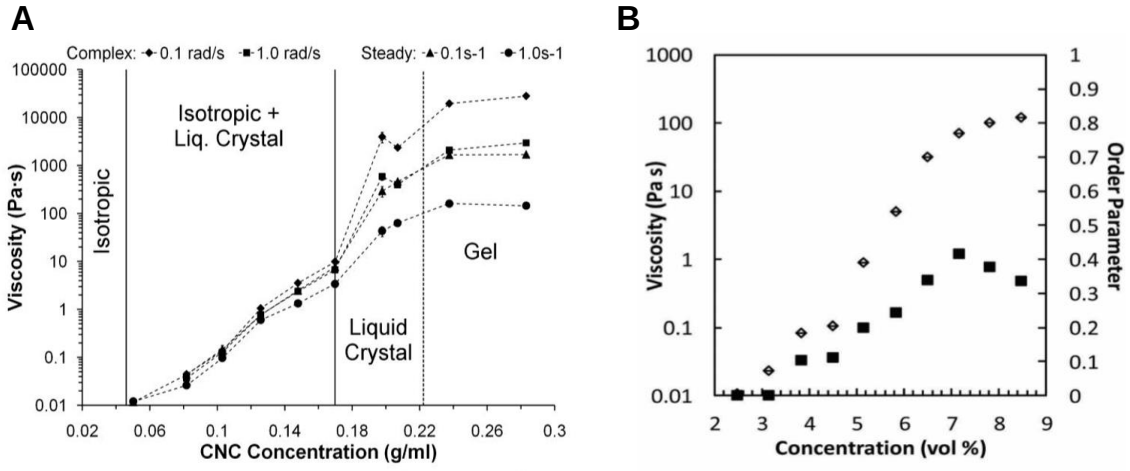

Figure 2.25. Steady shear and complex viscosity with increasing concentrations of sulfonated CNC from A) cotton (H_2O suspension)[124] and B) wood (D_2O suspension at 1 s^{-1} shear rate)[162].

CNC dispersions exhibit three region steady shear viscosity behavior. However, this behavior deviates from classical polymer lyotropic liquid crystals. Orts *et al*. reported the three-region behavior of liquid crystalline CNC obtained from black spruce bleached Kraft pulp[33]. Using SANS, they showed that region I was observed at very low shear rates where domains tend to flow; attributing to the shear thinning behavior. At higher shear rates cholesteric domains are broken up, and the chiral microstructure is unwound resulting in a Newtonian plateau[185]. At even higher shear rates second shear thinning behavior is encountered where individual CNC rods tend to flow align and nematic ordering is achieved. CNC rods with higher aspect ratio were found to achieve higher order parameters around the onset of region III. The orientation of the rods in the flow direction, as suggested

by neutron scattering, decreases the drag force. Therefore, dispersion viscosity goes down with increasing shear rate[33]. Similar behavior was observed for CNC extracted from cotton linter. As reported by Lima *et al.* (**Figure 2.26A**), three-region behavior was observed for three different concentrations of 1.2, 1.7, and 2.7 wt. %[54]. Ureña-Benavides *et al*. also observed this behavior for cotton CNC at four different temperatures, but only for biphasic dispersions concentration (below 6.99 vol. %) as shown in **Figure 2.26B**[124].

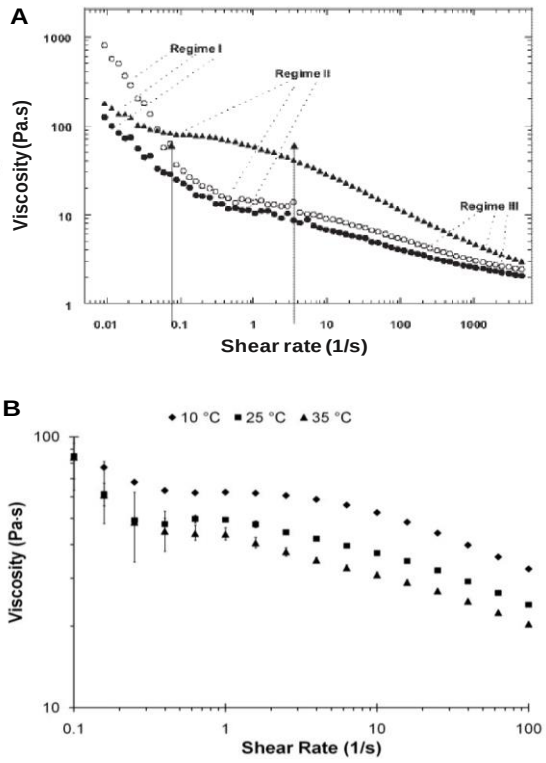

Figure 2.26. Steady shear viscosity versus shear rate plots showing the three-region behavior of A) cotton linter CNC for concentrations of 1.2 (black dots), 1.7 (hollow squares), and 2.7 (solid triangles) wt. % and B) cotton CNC of 6.99 vol. % at four different temperatures[54,124].

The three region behavior appears to be elusive for fully liquid crystalline concentration of CNC which was similarly reported by Bercea *et al.*[189] This anomaly of the liquid crystalline CNC in contrast to other LCPs is attributed to the "electroviscous

effect" of polydisperse charged rods though not fully understood. According to this effect, when the charged particles are sheared both the deformation and overlapping of the electric double layer contribute to the low shear rate viscosities[190]. This electroviscous contribution decreases with increasing ionic strength. However, this complex behavior is not fully understood and depends on suspensions' concentration as well. Recently, another SANS study by Haywood *et al*. showed the three-region behavior for biphasic wood CNC dispersion in deuterium oxide using average order parameter[162]. As shown in **Figure 2.27A** and **B**, for a range of biphasic CNC dispersions more prominent three-region boundaries were observed based on order parameter compared to the steady shear viscosity with increasing shear rate. As an example, the viscosity versus shear rate plot of 5.83 vol. % only shows a shear thinning behavior. However, the SANS order parameter versus shear rate plot distinctively illustrates the three separate regions within the same shear rate range. (**Figure 2.27B**).

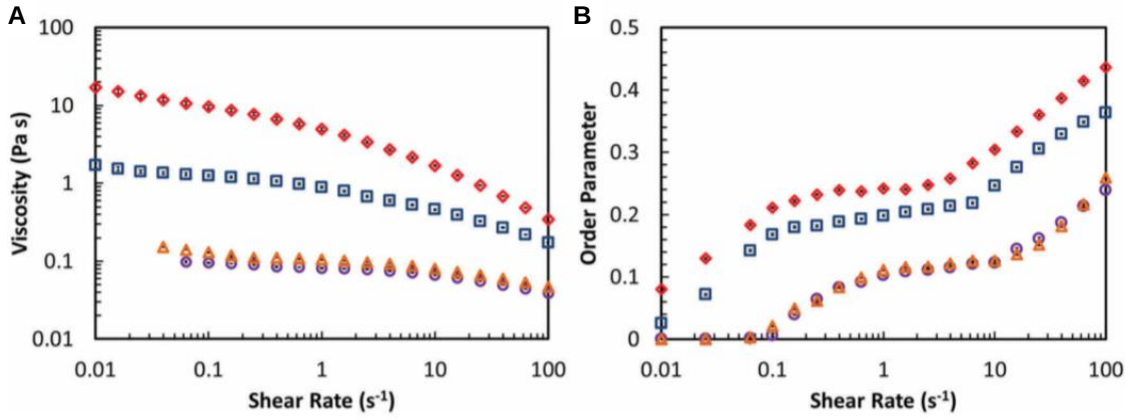

Figure 2.27. Steady shear viscosity and order parameter versus shear rate plots of CNC dispersed in deuterium oxide showing three-region behavior for concentrations of 3.83 (hollow purple circles), 4.5 (hollow orange triangles), 5.16 (hollow blue squares), and 5.83 vol. %(hollow red diamonds)[162].

Sulfonated CNC dispersions also do not obey the Cox-Merz rule. As shown in **Figure 2.28**, for the same frequency and shear rate the steady and dynamic viscosities are not equal. The biphasic concentration (6.3 vol. %, **Figure 2.28A**) showed more deviation from Cox-Merz rule at high shear rate/frequencies (10-100 s^{-1}) compared to low shear rate (0.1-1 s^{-1}). However, for a fully liquid crystalline sample (12.1 vol. %, **Figure 2.28B**), the deviation was observed for the entire range of shear rate/frequency. This behavior can be attributed to the presence of isotropic phase in biphasic dispersions[124,161].

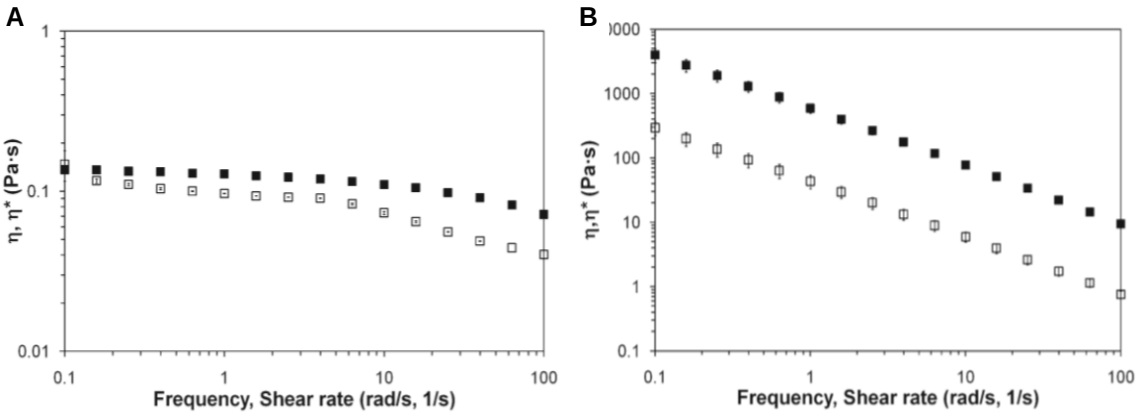

Figure 2.28. Cox-Merz rule comparison for the aqueous sulfonated CNC dispersions for different concentrations of A) 6.3 (biphasic) and B) 12.1 (liquid crystalline) vol. %. The open and solid symbols denote the steady shear and complex viscosities respectively.

In addition to steady shear rheology, the dynamic response of CNC microstructure has also been investigated by several researchers[124,185,188]. From the dynamic response or frequency sweep, the linear viscoelastic properties of CNC microstructure with increasing concentration can be probed as shown in **Figure 2.29**. The storage modulus G′, loss or viscous modulus G″, and tangent of the phase angle or $\tan\delta = G''/G'$ were investigated by Ureña-Benavides *et al.* for a range of CNC concentrations of isotropic, biphasic, liquid

crystalline, and gel regimes[124]. The samples with concentrations of 10.4 vol. % (highest concentration on the biphasic regime) and lower showed predominantly viscous fluid behavior with a $\tan\delta > 1$. For 12.1 vol. % and above, the elastic behavior was dominant ($\tan\delta < 1$). However, there is a dependency of G′ on ω until 14.5 vol. %. At 14.5 vol. %. G′ was constant with frequency indicating liquid crystal to gel transition.

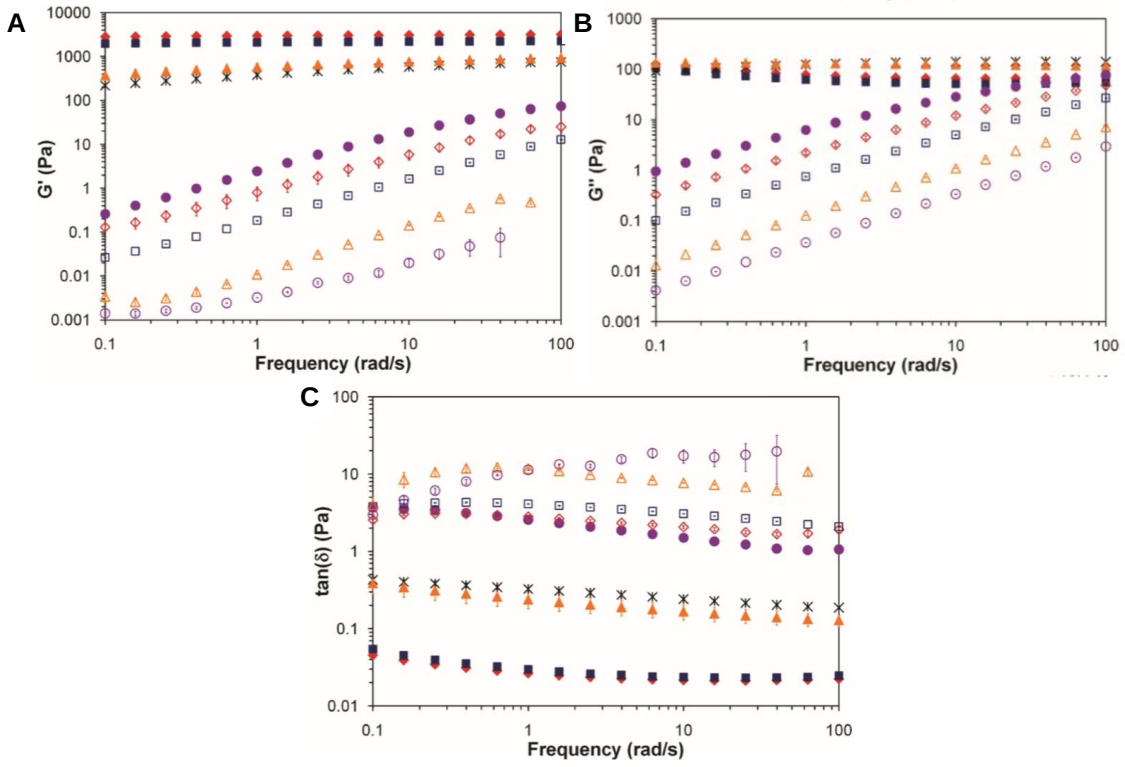

Figure 2.29. Linear viscoelastic properties of sulfonated CNC dispersions showing A) storage modulus (G′), B) loss modulus (G″), and C) ratio of G″ to G′ or tanδ. Dispersion concentrations shown on the plots are 17.3 (red solid diamonds), 14.5 (blue solid squares), 12.6 (black stars), 12.1 (orange solid triangles), 10.4 (purple solid circles), 9.03 (red open diamonds), 7.69 (blue open squares), 6.30 (orange open triangles), and 5 (purple open circles) vol. %[124].

In addition to sulfonated CNC dispersions, the rheological investigation has been performed for non-charged (CNC derived using hydrochloric acid) system as well[191,192]. Due to lack of surface charges, poor inter-particle stability was encountered, and thixotropic behavior was reported for hydrochloric acid derived CNC suspensions[35,191,192]. This behavior can be associated with inter-particle flocs that break under applied shear[185]. Interestingly, hydrochloric acid derived non-charged rods exhibit lower intrinsic viscosity than sulfuric acid derived charged CNC systems which can be attributed to the so-called "electroviscous effect"[193,194].

2.4 Fluid Phase Alignment of CNC

To manifest the exquisite functional properties of CNC as nanomaterial building blocks, understanding fluid phase alignment and relaxation dynamics is very critical. Initially, Orts *et al.* and Ebeling *et al*. reported the fluid phase alignment investigation of CNC using SANS[33,195]. Recently, Sabet *et al.* and Haywood *et al.* reported new insights into the fluid phase alignment of CNC using rheo-optical investigations[185,196]. Haywood *et al.* observed the quiescent CNC microstructures (**Figure 2.30 A, F,** and **K**) using transmitted cross-polarized microscopy as a function of concentration. The birefringent concentric systems of spheres in the biphasic (6.98 vol. %) concentration changed into fully developed fingerprints in the 11.60 vol. %, or fully liquid crystalline concentration. The random brightly colored regions of 15.8 vol. % CNC dispersion can be attributed to gel formation. Upon shear, the discrete liquid crystalline domains started to break up (**Figure 2.30B**) elongating in the flow direction. Up to 1 s^{-1} shear, the isotropic domains were visible with elongated anisotropic domains (with remnants of the bullseye pattern). Around $10s^{-1}$, a

marked difference in birefringent texture was observed (**Figure 2.30D**) which is attributed to the alignment of isotropic phase in the biphasic CNC suspension. At even higher shear (100 s^{-1}) the CNC rods became completely flow aligned and had a uniform interference color all over the sample (nematic texture, **Figure 2.30E**). As there are no isotropic rods in a fully liquid crystalline sample (11.6 vol. %), the fluid phase alignment of CNC upon increasing shear (0.1-100 s^{-1}) can be correlated with the change of interference color order which depends on the ordering of rods. With increasing shear rate, the striped texture becomes less prominent. At the intermediate shear rates the band textures attributed to unwinding of the chiral microstructure (**Figure 2.30G - I**) were observed followed by a very uniform texture at 100 s^{-1} (**Figure 2.30J**).

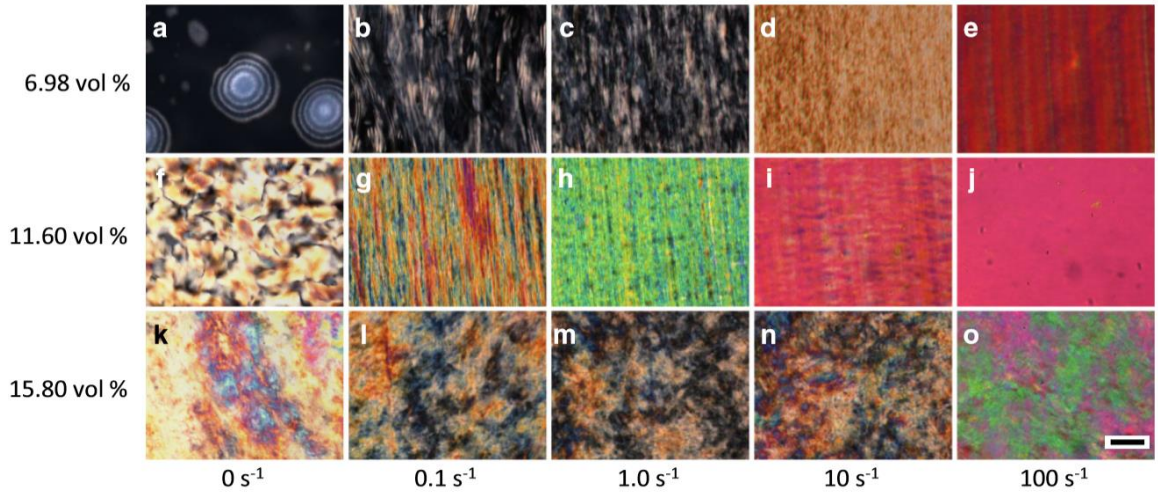

Figure 2.30. Cross-polarized transmitted light microscopic images of sulfonated CNC dispersions after shear (flow direction is up). Scale bars are 100 µm[196].

In contrast to the biphasic and fully liquid crystalline suspensions, the birefringence colors remained unchanged upon increasing shear for the gel (15.8 vol. %). At 100 s^{-1} there was a shift of interference texture indicating increased domain size with insignificant local

ordering. However, the higher shear rate may be enough to break the gel structure and align rods into a monodomain nematic texture. Both Geng *et al*. and Kiss *et al.* reported the fluid phase orientation behavior for cholesteric microstructures for HPC and PBLG[147,150,197].

2.5 Dried CNC Films

The intrinsic chiral nematic microstructures of CNC dispersion can be retained in dried films to obtain photonic properties. On the other hand, they can be unwound using shear resulting in nematically aligned rods in transperent films. However, issues like non-uniformities, thickness variation due to capillary effect, and cracking have been the main concerns to realize individual CNC rods properties in films. In 1992, Revol *et al*. observed the retention of the chiral microstructure of CNC dispersion in an air-dried film[6]. Later on, Pan *et al.* reported a detailed investigation on the effect of ionic strength, dispersion concentration, drying temperature, and magnetic field (external stimuli) on the chiral microstructure of CNC in films[198]. On the other hand, the unwinding of chiral microstructure to obtain nematic liquid crystal ordering in films have also been approached using mechanical shear and electric field[196,199-201]. However, the addition of counterions screens out the electric double layer followed by more chiral interaction of rods with negative sulfate groups. Hence, CNCs' chiral nematic pitch decreases which enables tunable optical properties in films.

2.5.1 Aligned CNC Films

The theoretical and experimental (using Raman spectroscopy) Young's modulus of individual CNC are 168[202] and 150[203] GPa respectively. Due to this high mechanical strength, CNC have been used in various nanocomposites including polyurethane[48] and polyvinyl acetate[43,107]. There has also been interest in producing uniaxially aligned pure CNC films for directional optical, thermal, and mechanical properties[11,85,198,199,204]. Unlike magnetic and electric field alignment, mechanical shear is inherent in almost all fluid phase manufacturing processes[187]. Hence, this dissertation focuses on the shear induced alignment only. Using a convective shear technique, Hoeger *et al*. first reported aligned CNC films and looked into the effect of dispersion concentration, withdrawal speed, and type of substrate material[204]. As shown in **Figure 2.31**, a CNC dispersion was drop cast on a solid support and then sheared using a withdrawal plate. The shear rate was controlled by controlling the withdrawal speed and gap of the plate from the top of the substrate. It was reported that the unidirectional ordering of CNC resulted from the balance of many forces including hydrodynamic (drag or shear), surface tension (capillary), electrostatic, and Brownian interactions[204]. Higher dispersion concentrations, with greater intrinsic microstructural CNC ordering, resulted in better macroscopic alignment upon shear and drying (**Figure 2.32**). In addition, a gold substrate with positive surface changes resulted in better nematic ordering. **Figure 2.32** shows the CNC alignment in an AFM height scan of a film made using this method.

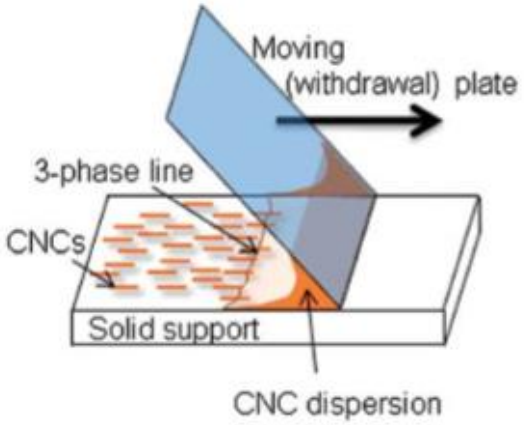

Figure 2.31. Schematic of experimental setup showing the convective-shear assembly of fluid phase CNC[204].

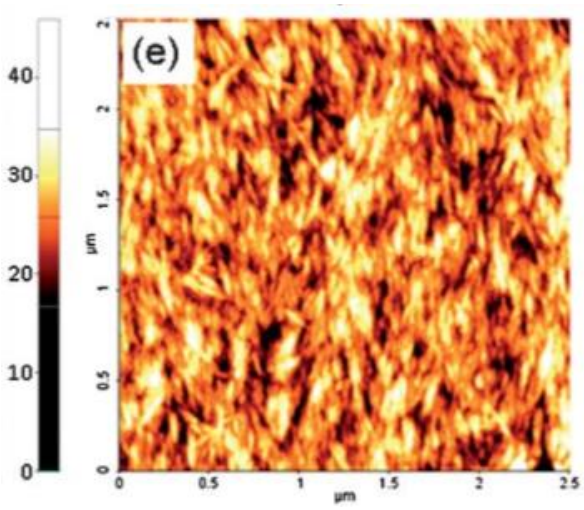

Figure 2.32. AFM height image of CNC film prepared on a charged gold substrate using 4.5% dispersion at a withdrawal speed of 8.4 cm/h. The withdrawal direction is down to up[204].

Recently, the effect of dispersion pH and shear rate on the ordering of CNC have been investigated on flow aligned films and compared against randomly aligned CNC films by Reising *et al*[199]. Films cast from a suspension concentration slightly below the gel transition were investigated for the order parameter and mechanical properties. Anisotropic

mechanical properties were reported for both parallel and perpendicular directions of the shear as shown in **Table 2.4**. Based on Hermans order parameter, they found an increased ordering with increasing the shear rate and pH. The maximum order parameter of S = 0.53 was achieved for neutral pH and 100 s^{-1} shear rate exhibiting excellent anisotropic mechanical properties. For the axial and transverse direction of the flow aligned CNC films, elastic moduli of 31.5 and 7.0 GPa were reported, showing excellent control of mechanical shear to obtain nematically ordered CNC films.

Table 2.4 Flow aligned CNC films order parameter and mechanical properties. CNC-1 is CNC film with low pH, CNC-n with neutral pH, A (axial) refers to the parallel to flow/shear direction, and T (transverse) refers to perpendicular to the flow direction. The numbers in brackets are the standard deviation[199].

CNC neat film properties.													
Samples	**Suspension Concentration** (wt%)	**S**	**Density** (g/cm³)	**Film**									
				E (GPa)		σ_f (MPa)		ε_f (%)		**WF** (MJ/m³)	
				A	**T**	**A**	**T**	**A**	**T**	**A**	**T**
CNC-I Unsheared	1.3	0.04	1.43 (0.11)	14.9 (1.4)	--	70 (29)	--	0.6 (0.3)	--	0.26 (0.19)	--
10 s^{-1}	10.3	0.27	xx	21.6 (0.2)	8.5 (1.4)	61 (21)	45 (12)	0.3 (0.1)	0.7 (0.2)	0.13 (0.09)	0.18 (0.11)
100 s^{-1}	10.3	0.36	1.55 (0.02)	23 (2.1)	7.2 (0.7)	49 (8)	46 (11)	0.4 (0.4)	0.9 (0.3)	0.10 (0.04)	0.21 (0.11)
CNC-n 100 s^{-1}	7.5	0.53	1.55 (0.02)	29.7 (1.2)	6.7 (0.2)	77 (10)	48 (2)	0.3 (0.1)	0.9 (0.2)	0.12 (0.04)	0.23 (0.04)
CNC-n w/ heat 100 s^{-1}	7.5	0.53	1.55 (0.02)	31.5 (0.5)	7.0 (0.8)	70 (6)	36 (13)	0.2 (0.03)	0.6 (0.3)	0.09 (0.01)	0.18 (0.04)

Interestingly, Haywood *et al*. reported better order parameters and optical properties on aligned CNC films using the same shear rate[200]. However, Haywood *et al.* used the liquid crystalline concentrations in contrast to gel as reported by Reising *et al*.[199] Haywood *et al.*[196] measured the ordering based on optical contrast which can be obtained using the following equation:

$$OC = \frac{I_{max} - I_{min}}{I_{max} + I_{min}} \qquad 2.12$$

where I_{max} and I_{min} is the intensity measured at 45º and 0º position with respect to the cross-polarized set up using transmitted polarized light. Using this technique, optical contrasts of 0.96 and 0.50 were reported (**Figure 2.33**) for 11.6 (liquid crystalline) and 15.8 (gel) vol. % dispersions of CNC. The monodomain texture with excellent optical uniformity was found using liquid crystalline dispersions not to gels. This was attributed to the higher viscosity in the gel[187,196]. However, periodic cracking was observed upon dying parallel to the flow alignment direction. Haywood *et al.*[196] also reported a critical thickness of 250 µm; above this thickness a polydomain texture was observed in the shear dried film.

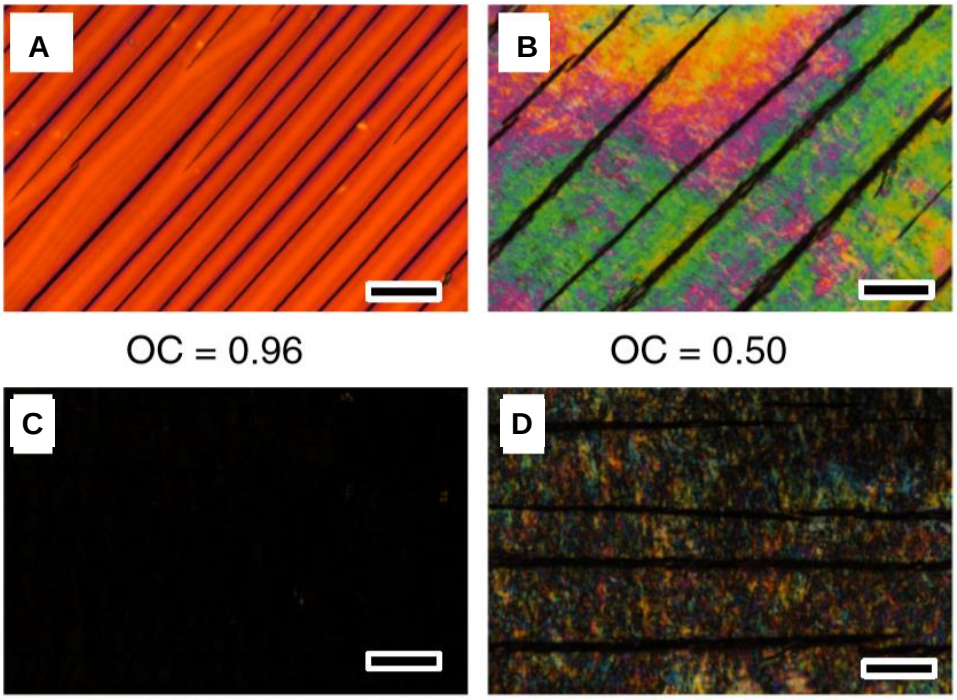

Figure 2.33. Cross-polarized transmitted light microscopic images showing optical contrast (OC) in shear aligned CNC films using concentrations of A) 11.6 vol. % (liquid crystalline) and B) 15.8 vol. % (gel). C) and D) are same images of films in A) and B) respectively rotated 45º to the cross-polarized position. Scale bars are 100 µm[196].

Though cracking was prevalent, the uniform birefringence colors were reported which can be tuned by both the degree of ordering and thickness of the films[196]. **Figure 2.34** shows the visible spectra of four different films obtained from 11.6 vol. % liquid crystalline dispersion concentration. The 50 µm wet thickness resulted in a dried film of 6 µm showing first order gray color under cross-polarized transmitted light. With increasing dried thicknesses of 12, 17, and 23 µm (wet thicknesses of 100, 150, and 200 µm), the interference colors advanced to first order orange, second-order blue, and second order yellow respectively. The interference colors demonstrate that the uniaxially aligned CNC film thickness can readily be used to tune the optical properties with tunable the spectral bandwidth.

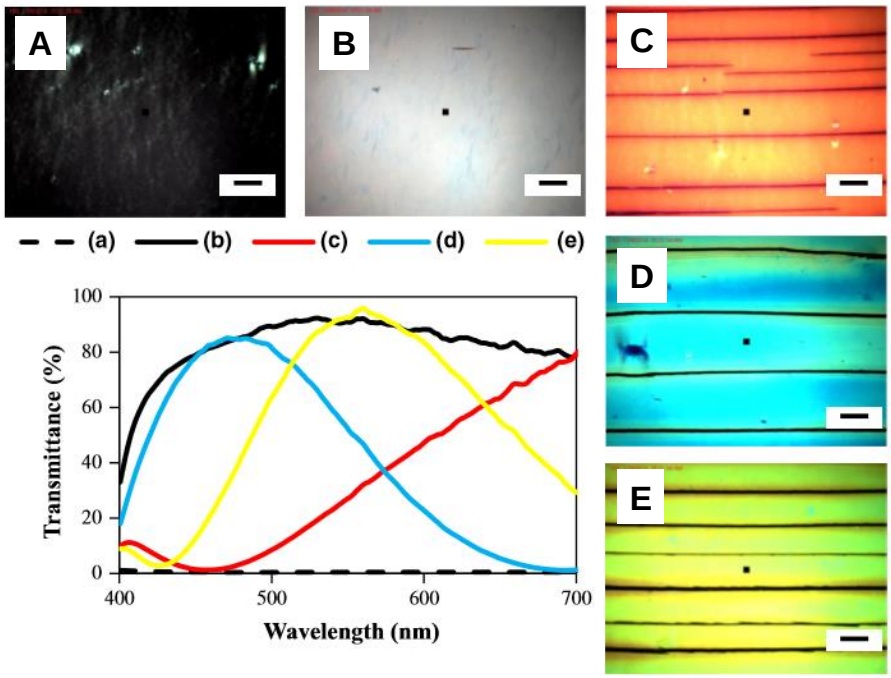

Figure 2.34. Polarized transmittance spectra and images of CNC films fabricated from 11.6 vol. % (liquid crystalline) concentration. Dispersion wet thickness is varied as A), B) 50 (0º and 45º), C) 100, D) 150, and E) 200 µm. The colors in the transmitted spectra correspond to the colors observed in these films. Scale bars are 50 µm[196].

In another work, Passantino *et al*.[103] investigated the effects of polyethylene oxide (PEO), flocculation (using hydrochloric acid), and the combination of both on the critical cracking thickness and mechanical properties of shear aligned CNC film. Using 2.6 - 5.2 s^{-1} shear rate, the CNC/PEO (87/13 wt. %) films (50 - 100 µm dry thickness) were sheared with and without the flocculation scheme with hydrochloric acid [103]. PEO with different molecular weights (MW) of 100k, 1M, and 8M was used and the effects on optical and mechanical properties were analyzed. **Figure 2.35** shows the summary of mechanical properties obtained using tensile testing of the composite films (CNC/PEO) with and without flocculation. The flocculation consistently resulted in crack-free shear dried CNC/PEO films compared to all combinations of CNC/PEO films alone. In addition, flocculation increased the critical cracking thickness to greater than 100 µm. However, the mechanical anisotropy observed in pure CNC film was not obtained in flocculated composite films[103]. In contrast, the mechanical properties (Young's modulus, tensile strength, and toughness) of pure CNC and non-flocculated CNC/PEO films showed significant anisotropy which agreed with optical properties (**Figure 2.35)**[103]. However, the plasticizing effect of PEO was evident as there was a decrease of mechanical properties in the composite films relative to pure CNC. With the addition of 100000, 1M, and 8M PEO, the reduction of Young's modulus was about 25%, 35%, and 19% for CNC aligning in parallel directions, and 59%, 72%, and 76% in perpendicular directions respectively.

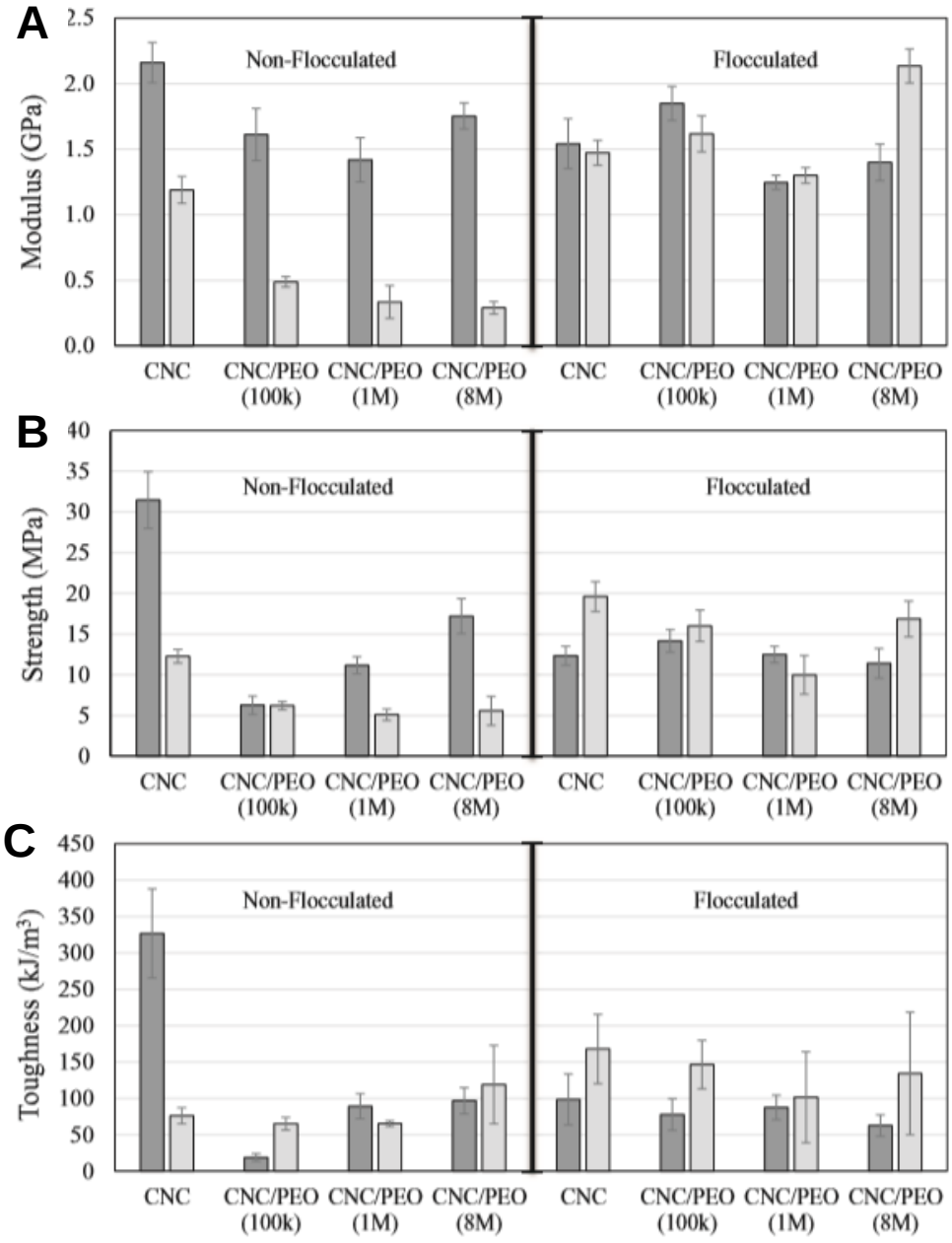

Figure 2.35. Mechanical properties of CNC/PEO films using flocculated and non-flocculated scheme. A) Young's modulus, B) tensile strength, and C) toughness. Dark gray and light gray refer to parallel and perpendicular to flow direction. The error bars are standard errors of each set of films[103].

2.5.2 Chiral Nematic CNC Films

In 1992 Revol *et al.*[6] described how the cholesteric liquid crystalline microstructure of CNC dispersion could be preserved in a solid film. Upon slow evaporation of water, the solid CNC film was obtained, and the oblique cross-section was imaged using transmission electron microscopy. Later, Gray *et al.*[86] also observed the chiral nematic CNC microstructures in concentrated dispersions and polymer melts of many cellulose derivatives. However, to date, only left-handed helicoids have been observed for CNC films; these were first reported by Giasson *et al.*[205] in 1988. When the axis of the helicoid is perpendicular to the film surface, planar ordering is observed. In this case, the film cross section reveals a quasi-layered structure; showing nanocrystals progressing parallel to perpendicular to cross-section[86] (**Figure 2.36A**). However, a cross-section with an oblique angle to the helicoidal axis reveals arc-like morphology. **Figure 2.36B** shows the left-handed arc-like morphology found in cholesteric CNC microstructures[205]. The regularly spaced lines shown in **Figure 2.36A** correspond to half of the pitch (p). When the chiral nematic pitch is on the order of the wavelength of visible light, the iridescent visible colors are reflected following Braggs law:

$$\lambda = nP \sin\theta \qquad 2.13$$

where λ is the wavelength of reflected light, n is the average refractive index of cellulose nanocrystals (1.56[206]), P is the pitch, and θ is the angle between the film surface and incident light. The reflection band of CNC films can be tuned by modifying the dispersions' ionic strength, surface charge density, and aspect ratio/length of the rods[88]. The change of

periodic spacing thickness due to any external stimuli, *i.e*., humidity, can change the reflection colors as well[207].

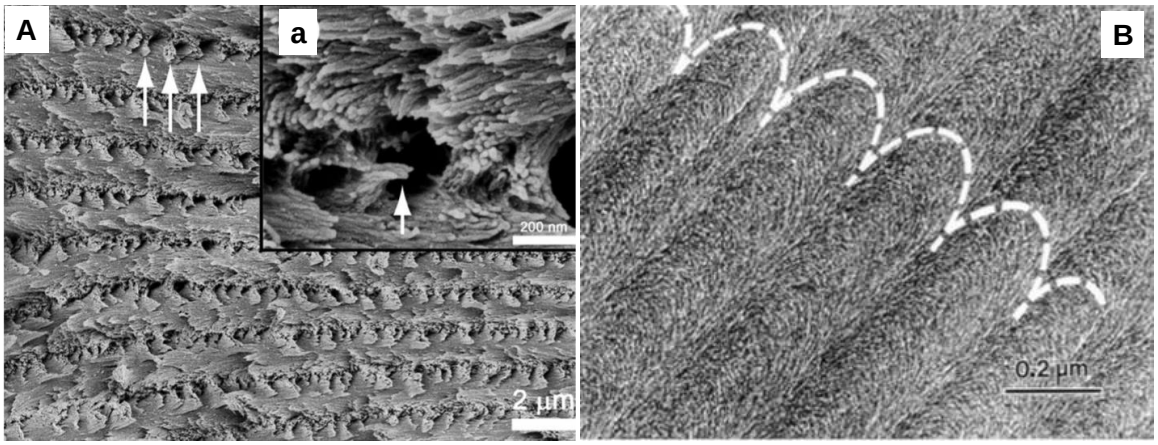

Figure 2.36. A) SEM and B) TEM images showing the 90º and an oblique cross-section of CNC films. Inset (a) shows the progression of nanocrystals from parallel to perpendicular orientation to the cross-section and oblique cross-section on Teflon plate reveals the arc like morphology of image showing the 90º and an oblique cross-section of CNC films. Inset (a) shows the progression of nanocrystals from parallel to perpendicular orientation to the cross-section and oblique cross-section on Teflon plate reveals the arc like morphology of the rods[86,205].

Beck *et al*. reported the effect of ultra-sonication energy on the tuning of reflection colors of CNC films[88]. As the applied sonication energy to CNC suspension increases, a red shift in the reflection color was observed owing to increased pitch. As shown in **Figure 2.37A** and **C**, sonication energies of 750 J/g and 2250 J/g on 2.7 wt. % (1.7 vol. %) CNC dispersions resulted in blue and orange reflectance respectively. A 1:1 mixture ratio of both of these sonicated dispersions was also drop cast and dried which resulted in a film with green reflectance (**B**). Interestingly, a separate dispersion (sonicated for 1490 J/g energy, half of the summation of previous two sonication energies) dried film also exhibited the same green reflectance as shown in **Figure 2.37** reflectance spectra. These findings

indicate that the sonication treatment effects are such that the self-assembly properties follow a rule of mixtures.

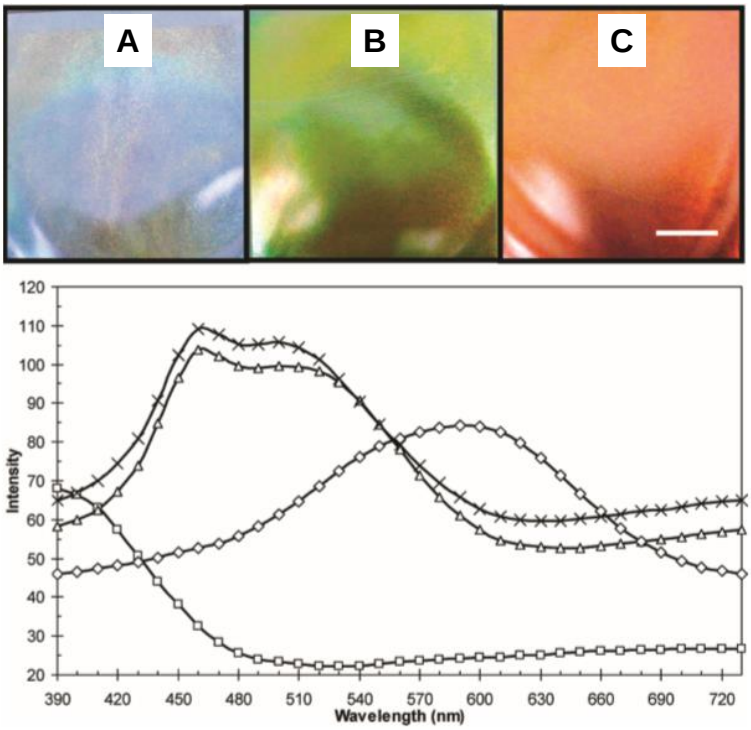

Figure 2.37. Reflection colors and spectra for CNC films obtained from 2.7 wt. % dispersion subjected to sonication energy of A) 750 J/g, B) 1:1 ratio of 750 J/g to 2250 J/g, and C) 2250 J/g. Reflection is normal to the film surface. Scale bar is 1 cm. A (square), B (triangle), C (diamond), 1490 J/g (cross).

Recently, Dumanli *et al*. reported the thinnest chiral nematic CNC films to date with thicknesses from 1.0 to 1.3 μm[9]. The air-dried 4 wt. % (2.5 vol. %) CNC dispersion on a polystyrene Petri dish resulted in films with a radial color variation (blue to red from center to edge). Interestingly, the center part with the weakest reflection colors happens to have the complete planar ordering, revealing the digitalized colors. Circularly cross-polarized light revealed a polydomain texture of CNC domains with specific reflectance colors as shown in **Figure 2.38**. Optical reflectance spectra were obtained for the selected

areas of interest followed by the cross-section SEM of the same spots. **Figure 2.38** shows the cross-sections revealing the different numbers of quasi-layers with corresponding reflectance spectra using both left (solid) and right-handed (dot) circularly polarized light[9]. Only the left-handed circularly polarized light reflected back which agreed with the spectra. In addition, the pitch measured from optical spectra peak was directly compared to the pitch measured by SEM. They were consistent with each other.

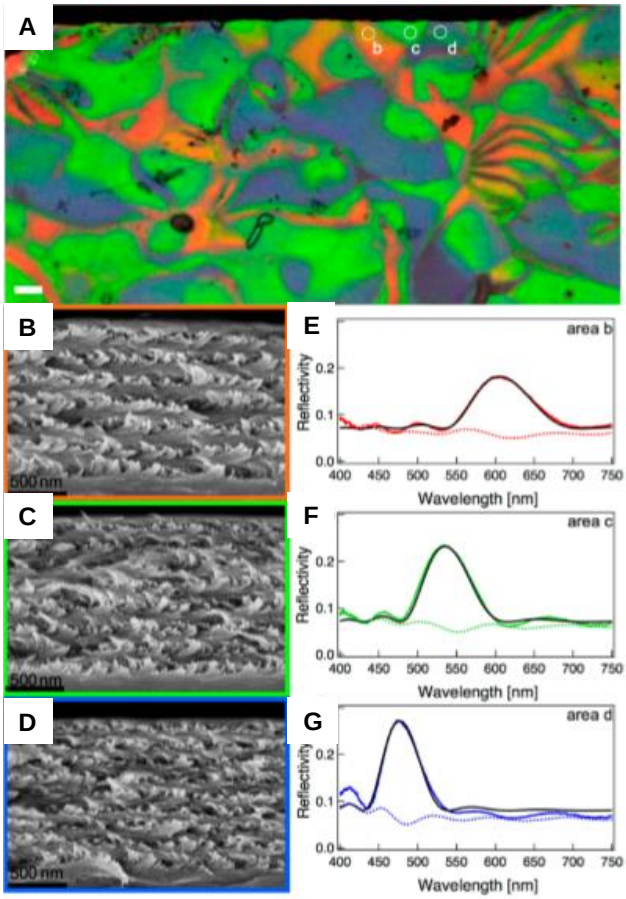

Figure 2.38. Reflectance spectra of different domains of chiral nematic CNC and their correlation to SEM scanning of the cross-sections. A) Left-handed circularly polarized light reflectance image showing digital colors of the domains. B), C), and D) reveal the cross sections SEM of selected spots on A as b, c, and d (white circles), respectively. E-F show the corresponding reflectance spectra. The solid black lines are curve fits the spectra using Berreman's 4 x 4 matrix method[9].

As uniform optical properties of CNC films depend on the uniformity of the planar orientation, there has been research interest in improving the control over helix orientation during drying. Recently, Park *et al*. reported the effect of rotational shear and initial dispersion concentration to enhance the uniformity of the reflectance colors[85]. By varying the rotational speed, they were able to investigate the unwinding threshold of the helical microstructure during drying. The optimization of the rotational speed and initial suspension concentration resulted in CNC films with very uniform pitch throughout the film. However, the presence of homeotropic ordering (fingerprints) and domain size of a few tens of microns were reported which are the subjects of future research. This work formed part of the foundation for the research presented in this dissertation.

Chapter 3 Experimental

3.1 Cellulose Nanocrystal Dispersion Preparation

Sulfonated cellulose nanocrystal aqueous suspensions (11.8 wt. %/7.7 vol. %) containing 1.2 wt. % sulfur (according to product specification) with Na^+ as the counter ion were procured from U.S. Forest Products Laboratory (FPL), and supplied by University of Maine process development center (Batch no-2015-FPL-077 CNC). The as-received cellulose nanocrystal suspensions were dispersed to the desired concentrations using ultrapure water (purified using Thermo Scientific Auto Dispenser, Millipore water, pH 6.5, conductivity 0.95 µS/cm at 23.3 °C). The dispersions were then vortex mixed for 10 minutes followed by overnight bottle rolling. The bottle rolled dispersions were allowed to rest for at least 1 hour before drop casting, or rheo-optics, or shear alignment, to make sure no bubbles were present.

3.2 Dispersion Drying and Film Preparation

For drying CNC dispersions using surface anchoring (Chapter 5), a 75 mm x 25mm microscope glass slide (substrate) and 22 mm x 22 mm coverslip (anchoring surface) were cleaned with acetone and DI water and air dried. This was followed by further cleaning with air plasma (300 mTorr, 100 watts, 1 min) for ultra-cleaning. The microscope slide was placed inside a polystyrene Petri dish; 200 - 300 µL (concentrations ranged 2 – 8 wt. %) of the dispersion was then dropped onto the slide with a spatula. Water drops were added to the surrounding area using a micropipette, and the lid was closed. Then, the closed Petri dish was placed on an orbital mixer (VWR Standard Analog Shaker, set speed 60 rpm) for

15 minutes to pre-shear the dispersion. After that, the lid was opened, and the coverslip was placed on the cast dispersion. The lid was put back again and left for 24 hours drying (under a relative humidity of 98% at 22 °C).

For obtaining the shear dried films, CNC dispersions were drop cast on the substrate of interest (*i.e.*, silicon wafer, glass slide, photoresist, etc.) followed by mechanical shear, using a Gardco (Pompano Beach, FL) Microm II film applicator. The sheared dispersion was immediately placed into a convection oven maintaining 80 °C temperature for 20 minutes followed by 24 hours desiccation. For hydrolytic stability test free standing CNC, films were fabricated using the same shear technique. However, a Teflon mold was used with groves on it to peel off the freestanding films easily.

3.3 Cellulose Nanocrystal Characterization

Based on atomic force microscopy (AFM) measurements (height scan, **Figure 3.1**), CNCs' average height, width, and length were 5.5 nm (standard deviation 1.3), 46.7 nm (standard deviation 8.5), and 160.8 nm (standard deviation 47.3), respectively (based on 100 individual CNC count, batch number 2015-FPL-077, **Figure 3.2**). The width measurements included blind tip estimation (using Gwyddion's) to deconvolute the shape of the particles from the geometry of the tip.

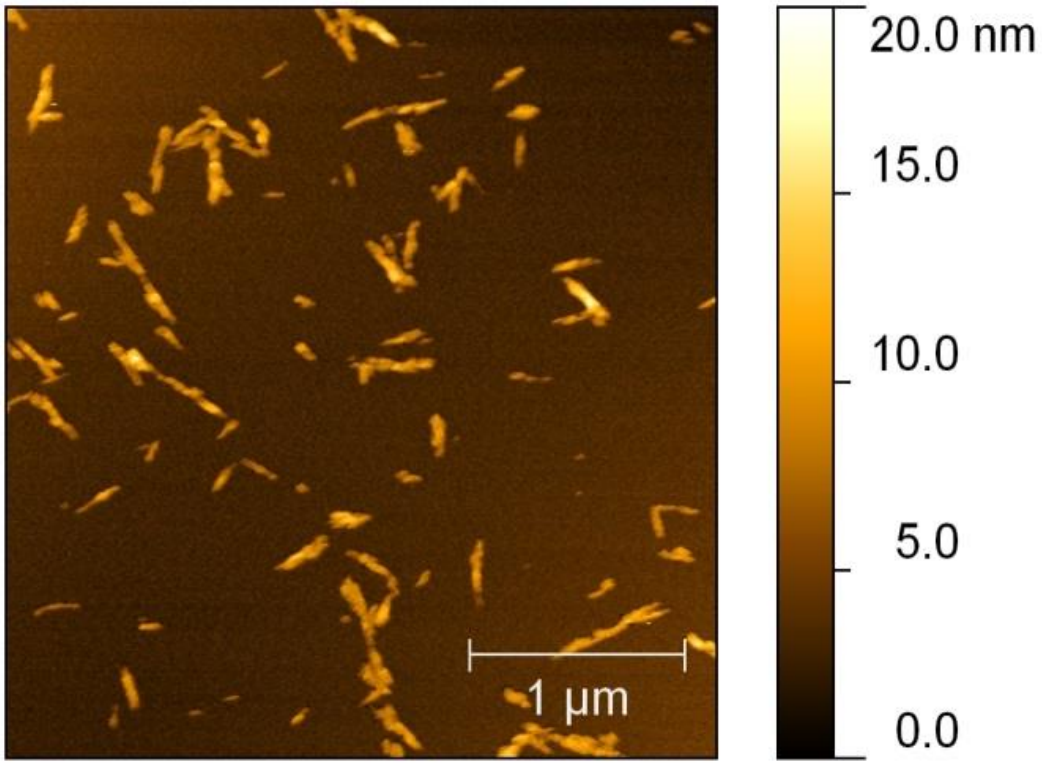

Figure 3.1. AFM height scan of CNC on a mica surface.

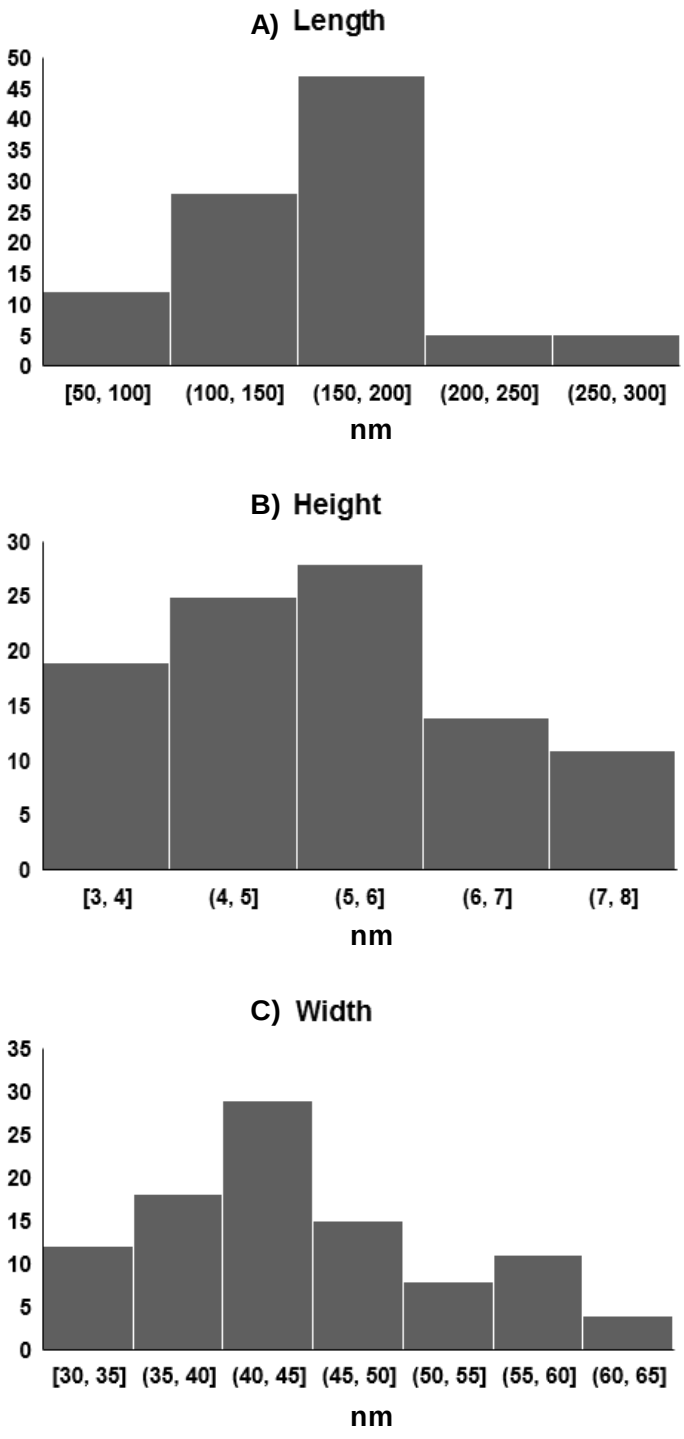

Figure 3.2. Plots showing the size distributions of CNC based on AFM.

3.4 Microfabrication of CNC MEMS

3.4.1 Wafer Cleaning and Priming

As the first step to CNC MEMS fabrication, test silicon wafers of 100 mm (4″) diameter were cleaned in acetone. Next, the wafer was rinsed with DI water followed by N_2 drying. The wafer was then kept in a convection oven for 20 minutes at 150 ºC (dehydration bake) followed by ambient cooling in a dry environment. The dehydration bake is useful in volatilizing organic contaminants cleaning the substrate. However, the surface silicon atoms bond strongly with a monolayer of water forming silanol groups (SiOH). An adhesion promoter was used to chemically react with surface silanol and replace the -OH group with an organic functional group as shown in **Figure 3.3**. Unlike the –OH groups, organic functional groups exhibit better adhesion to the photoresist. Hexamethyl disilizane (HMDS) was used as the adhesion promoter to the photoresist. The cleaned wafer was subjected to HMDS vapor for 10 minutes in a closed glass chamber. The application of adhesion promoter is called the priming of the wafer before photoresist coating. For the proposed methodology, HMDS priming was done right after the dehydration bake so that the elevated temperature of the wafer surface promotes the chemical reaction of silanol removal. The priming was done for 10 minutes only to avoid HMDS overexposure which can cause poor adhesion.

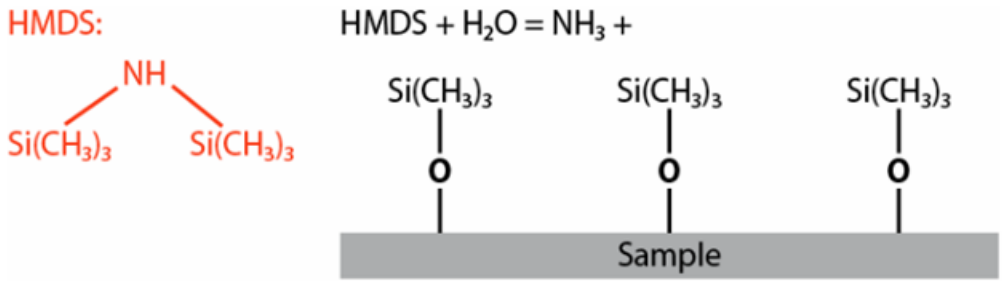

Figure 3.3. Schematic showing HMDS priming reaction[208].

3.4.2 Photoresist Coating

The photoresist is a light-sensitive organic material that is used to create a pattern on a surface. In case of a positive photoresist, the light-sensitive material is degraded by light followed by dissolving in the developer solution. An image reversal positive photoresist AZ5214E (UV sensitivity h-line, 310 - 420 nm) was spin coated on HMDS coated silicon substrate (100). Using a ramp of 500 rpm^{-1} and rpm of 2500 the photoresist was spin coated for 30 seconds followed by a hot plate drying at 110 ˚C for 1 min, resulting in a photoresist thickness of 2 µm.

3.4.3 Pattern Transferring

The pattern transfer of the CNC MEMS devices was done using designed masks. Using the anchoring mask, the resist layer was UV exposed (UV400) and developed with a potassium-based developer AZ400K (1-part developer to 3 parts water). The exposed photoresist part was washed off with DI water followed by N_2 drying. In the next step, a wafer with an anchor pattern of photoresist AZ5214E was treated with air plasma at 500

mTorr and 100 Watts for 1 min. After plasma treatment, the water contact angle of the patterned surface decreased from 53˚ to 17˚ facilitating the wettability of the aqueous CNC dispersions. Afterward, the CNC dispersion was sheared and dried onto the anchor photoresist layer using a Gardco (Pompano Beach, FL) Microm II film applicator. The sheared dispersion was placed into a convection oven maintaining 80 ˚C temperature for 20 minutes followed by 24 hours desiccation. Next, a 10 nm thin layer of Ti/ TiO_2 was E-beam (PVD) deposited on the CNC film to improve the adhesion of the second photoresist layer to the film (HMDS does not work as the resist adhesion promoter to CNC). This was followed by spin coating of the second photoresist layer, AZP4620. In a convection oven, the wafer was heated at 70 - 80 ^{0}C for 10 minutes to cure the second photoresist layer onto Ti/TiO_2 coated CNC film. After sufficient cooling, the dry photoresist was UV exposed similarly as before, except a device mask was used to create the device pattern. After developing and drying, some parts of the Ti/TiO_2 coated CNC film were covered with the second photoresist layer with the actual structural pattern of the MEMS devices.

3.4.4 Plasma Etching

Etching is considered to be the third key process used in micromachining. Like pattern transferring using lithography, etching is also an essential technique for fabricating MEMS[209]. The three-dimensional geometry of micromechanical devices is defined by this process[210]. The etching process, in general, can be classified into two categories: wet etching and dry etching. The etch type can further be classified as either isotropic or anisotropic etching process. As initially invented for silicon MEMS, isotropic etching is usually accomplished using hydrofluoric (HF) acid solutions or HF buffered with

ammonium fluoride (NH_4F)[211]. Anisotropic or directional etching is done using a plasma process using oxygen (O_2), sulfur hexafluoride (SF_6), and/or the various ratio of fluorocarbons (CF_4, C_4F_8, etc.)[212]. However, this mechanism may vary due to physical removal of the material or crystal planes[210]. For the directional mechanism, chemical reactions with plasma radicals are followed by removal of reaction products which is tuned by plasma environment including pressure, electrode power, and chemistry of it. In this research, the windows (the uncovered area by resist) of the Ti/TiO_2 coated CNC film were plasma etched to shape the structural CNC MEMS. The 10 nm Ti/TiO_2 film was etched out first, applying inductively coupled plasma (ICP-STS AOE) using CF_4. Along with induction coil power (500 watts), a platen power (300 watts) was applied at 20 - 40 mTorr pressure and 20 sccm flow rate to obtain anisotropic etching. Afterward, the Ti/TiO_2 free CNC film was plasma etched using O_2 plasma using same plasma conditions with a flow rate of 40 sccm. Cross-polarized reflected light microscopy was used to confirm the completeness of etching.

3.4.5 Device Release and Drying

After the completion of plasma etching, the 4″ wafer with the CNC MEMS was diced into small pieces using the diamond cutter. Next, the diced portions of the wafer with devices were submerged into 99.99% pure isopropyl alcohol (IPA), and then acetone was slowly added to wash off the residual photoresist layers (residual from both the surface of the devices and anchoring layer beneath it). The devices were released by dissolving the anchor photoresist layer followed by rinsing in 99.99% IPA. The released devices submerged in

IPA solution were carefully transferred (keeping an IPA film on the die) to a critical point dryer (CPD) chamber filled with IPA as well. Thus, the devices were carefully removed from the short alcohol solution and placed in a high-pressure chamber without exposing them to the liquid-vapor interface[213]. Next, the high-pressure chamber was sealed, and the IPA solution present inside is completely displaced with liquid carbon dioxide (CO_2) and taken outside the chamber by purging. Then, the chamber was first isothermally pressurized up to a pressure higher than the critical pressure of CO_2 (1400 psi) followed by isobaric heating up to a temperature higher than the critical temperature of CO_2 (32 ˚C). At equilibrium, this pressure and temperature transform the liquid CO_2 into a supercritical fluid. In the following step, the supercritical CO_2 was slowly vented out of the chamber until the pressure of the chamber reduced to atmospheric pressure. The venting of CO_2 from the high-pressure chamber is performed isothermally to ensure that the physical state of the CO_2 present inside the chamber never crosses the vapor-liquid line[213]. After the high-pressure chamber was completely vented, it was opened, and the dried freestanding MEMS devices were removed[214] and then placed in a desiccation chamber before testing.

3.5 Characterization Methods

3.5.1 Optical Microscopy

Transmitted cross-polarized optical microscopy was used to image the dispersion microstructures of CNC with varying concentrations. The onset of the biphasic and liquid crystalline phases in the aqueous CNC dispersions were observed around 4.8 and 8.0 wt. % (3 and 4.8 vol. %), respectively. Cross-polarized reflected light microscopy was used to

image the chiral nematic films with different helix orientation. In addition to film imaging, the optical microscopy was also used to obtain the residual stress in CNC MEMS and investigate the optical anisotropy of the birefringent devices. A Nikon (Melville, NY), Eclipse 80i microscope with imaging workstation and Nikon Elements, was used to capture all of the cross-polarized reflected light micrographs using 10X/0.30 and 20X/0.45 LU Plan Fluor objectives. The camera used was a Nikon DS-Ri2. All the fluorescence microscope images were acquired using an inverted Nikon Eclipse Ti microscope fitted with an Andor Luca S camera. For the average intensity measurement, all the fluorescence images were analyzed using ImageJ software, version 1.48q (NIH).

3.5.2 Rheology

In this research, the steady shear rheology was primarily used to determine the viscosity of CNC dispersions using an Anton Paar MCR301 rotational rheometer. For each concentration, the steady shear viscosity versus the shear rate plot was generated using 0.01 - 100 s^{-1} shear rate range. Before that, a startup flow test was done for each concentration at 0.01 s^{-1} to determine the time to reach the steady state. Oscillatory measurements were also performed within the linear viscoelastic (LVE) region from $\omega = 0.1$ - 100 rad/s. The LVE was obtained using an amplitude sweep at a constant frequency of 5 - 50 rad/s depending on the CNC concentration. For the biphasic to gel CNC concentrations (5 - 12 wt. %), the cone and plate (CP50) and parallel plate (PP50) geometries were used. However, for the isotropic concentrations (<5 wt. %), due to torque limit of the rheometer

the Mooney-Ewart fixture was used. Multiple geometries were used for some concentrationss and temperatures to test for fixture related artifacts.

3.5.3 Microspectrophotometry

Microspectrophotometry was used to obtain the left and right-handed circularly polarized light spectra of the planar CNC domains. CRAIC 2020 UV-Vis/Fluorescence Microspectrophotometer was used to get the selective reflection (using 75 W Xenon reflectance power supply) spectra of the chiral nematic planar domains. A UV-vis-NIR polarizer with a quarter wave plate retardation was used to obtain the circularly polarized light.

3.5.4 TGA-FTIR

Thermogravimetric analysis (TGA) is used to investigate the thermal decomposition behavior of a material with temperature. On TGA, the mass of the sample is monitored as a function of temperature while it is subjected to a controlled temperature environment. In addition to thermal analysis, TGA can also be used to determine the dispersion concentration or concentration of a certain component in a mixture. The TGA used in this research was a TA Instruments (New Castle, DE) TGA Q50. It has a high precision balance with a platinum pan for sample loading. The balance is enclosed in a small furnace which can be purged with either inert gas or air. In this study, TGA was performed to determine the CNC dispersion concentrations and thermal decomposition analysis of surface modified CNC with silane and glutaric anhydrides (Temperature ranged 25 – 700 ˚C). The

TGA can also be coupled with Fourier transformed infrared spectroscopy (FTIR) to identify the chemical composition of thermally decomposed products. In this research TGA-FITR or FTIR were used to analyze the thermal decomposition products of sulfonated CNC films and surface modified films with APTES, and glutaric anhydride conjugated primary antibodies and antigens. The FTIR used in this research was a Thermo Scientific (Waltham, MA) Nicolet iS 10 FTIR. The TGA was connected to the FTIR by a heated flow line with TGA-IR interface. A gas flow cell was equipped with the FTIR with an oven to prevent the condensation of the decomposition gases.

3.5.5 Atomic Force Microscopy

A Pacific Nanotechnology Nano-R SPM (Model O-020-0002) atomic force microscope (AFM) was used in non-contact mode, to determine the size distribution of the CNC. The tips that were used for the AFM scan were made of Si with 10 nm radius of curvature. Approximately 10 μL of 0.05 vol. % CNC dispersion was drop cast onto a freshly cleaved mica surface. Then the dispersion was allowed to sit for 5 min followed by air drying, leaving behind adsorbed CNC on the surface. Each 3 μm X 3 μm area scan was acquired at a scan speed of 0.2 Hz with a 1024 × 1024-pixel resolution. An image of the tip was obtained using a porous aluminum standard surface. Gwyddion's blind tip estimation algorithm was used to deconvolute the shape of the particles from the geometry of the tip. In addition, AFM scanned height image was processed using Gwyddion to determine the root mean square (RMS) roughness of the CNC films.

3.5.6 Scanning Electron Microscopy

A JEOL (Peabody, MA) JSM-7000F Field Emission Scanning Electron Microscope was used for scanning electron microscopy (SEM) analysis using both 10 - 15 kV electron beam voltage. Prior to SEM, the plasma based gold sputtering was applied to the CNC films using a PELCO SC-6 SPU system run by argon (0.08 millibar pressure was used for plasma sputter). SEM was used to image the CNC films' cross-sections to investigate the macroscopic alignment of the rods. Also, SEM was used to image the microfabricated CNC MEMS and the film thickness of sheared dried films.

3.5.7 Goniometry

The static water contact angle measurements were done using a goniometer to determine the wettability of photoresist surfaces before casting and shearing the CNC dispersions for the MEMS fabrication. In addition, APTES modified CNC films' hydrophobicity was characterized based on the initial water contact angle of the film surface. The contact angle is the interior angle θ, measured between the wetted surface and sessile droplet as shown in **Figure 3.4**. γ_{lv}, γ_{sl}, and γ_{sv} are liquid-vapor, solid-liquid, and solid-vapor interfacial tensions, respectively. If it is a droplet of water, surfaces with θ above 90° is considered to be hydrophobic in nature. The water contact angles were measured using a ramé-hart Instrument Co. (Succasunna, NJ, Model 200-00-115) standard goniometer. The measurement reproducibility of this instrument is $\pm 2°$. The setup was equipped with a CCD digital camera, a backlight source, movable sample stage, and a water injection

syringe calibrated to drop liquid in a controlled manner (4 μL) on the solid surface. The analysis of the droplet image and contact angles were done using DROPimage software.

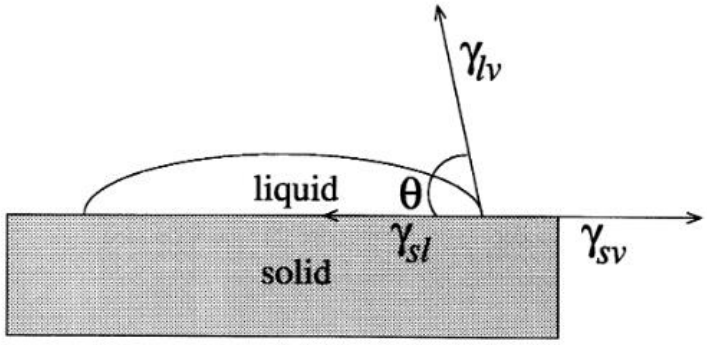

Figure 3.4. Schematic showing the sessile-drop contact angle system; θ is the contact angle[215].

3.5.8 Micromechanical Testing

3.5.8.1 Nanoindentation

Nanoindentation is used for extracting material properties at the nanoscale/microscale. In this research, the nanoindentation based load versus displacement profile of CNC doubly clamped beams was obtained to determine the elastic modulus of 2 and 4 micron thick MEMS devices. An MTS Nanoindenter XP was used to press the doubly clamped beams using 0.5 mN load at 0.05 mN/s loading rate. In this work, a Berkovich indenter tip was used to run all the tests. This is a three-sided pyramid-shaped tip which is typically made of diamond due to its high elastic modulus (~1050 GPa) and low Poisson's ratio. The Berkovich tip with a tip radius <10nm was set for 10 nm/s surface approach velocity. A surface approach distance was set at 1200 nm with 180 s peak load time. As a required input to the software, a Poisson's ratio of 0.3 was used for CNC.

3.5.8.2 Mechanical Strength Testing

The mechanical strengths of the CNC MEMS devices were tested on a custom-built Probe station. The station is equipped with a long-working-distance, incoherent light interference microscope like that reported by Sinclair *et al*.[216] The station is mounted on a vibration isolation table (Newport Electronics, Inc., ST Series) that dampens the noise associated with the ground vibrations. The Mitutoyo M Plan Apo objectives (10X - 100X) were used as the objective lens in the microscope. A green LED (λ_{max} of 525 nm, Nichia corp.) was used as the light source with a monochromator that transmits 532 nm as the illumination source. The probing system is also equipped with a charge-coupled device (CCD)-IRIS camera (Sony, XCD-SX910) to collect digital images as shown in **Figure 3.5**. In addition, the station contains six probe modules that are used to establish the mechanical and electrical contacts with the MEMS devices. A micro-manipulator integrated with the module was used to determine the fracture strength of the CNC MEMS devices. The micro-manipulator consists of coarse and fine manipulators as shown in **Figure 3.6**. The coarse manipulator is a micropositioner (Model # S - 926) procured from Signatone. It was used to hold the fine manipulator and to position the probe tip. The tip was used to push the CNC mechanical strength testers (MST) for actuation, with a controlled movement. The open-loop piezo module (Melles Griot, travel range is 0 - 30 µm and operating voltage are 0 - 100 V) was used to generate the force to push the central shuttle. The probe tip was electrically grounded using the “bypass” connection. This test enabled the central shuttle to be displaced in extremely small, precise, and equal nanometer-scale steps. This actuation process of CNC MST of the test platform was executed using a scripting environment called MEMScript reported by Ansari *et al*.[213]

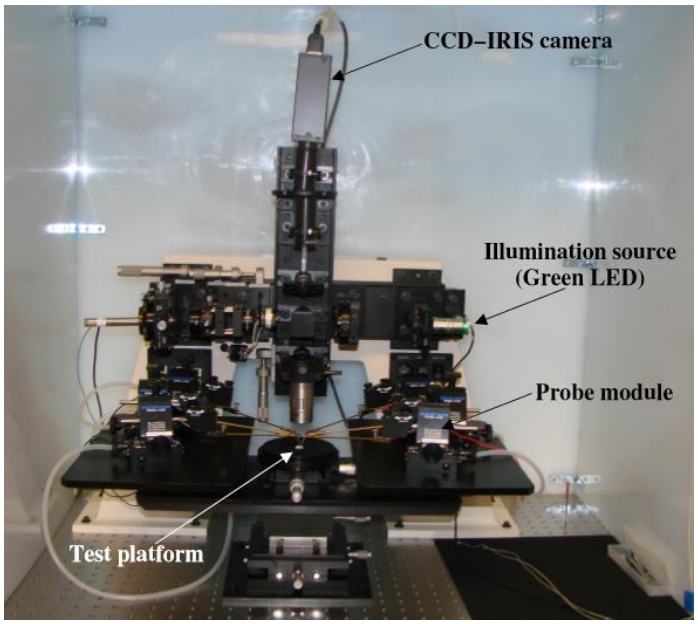

Figure 3.5. Photograph showing the custom-built probe station for micromechanical testing of CNC MEMS[213].

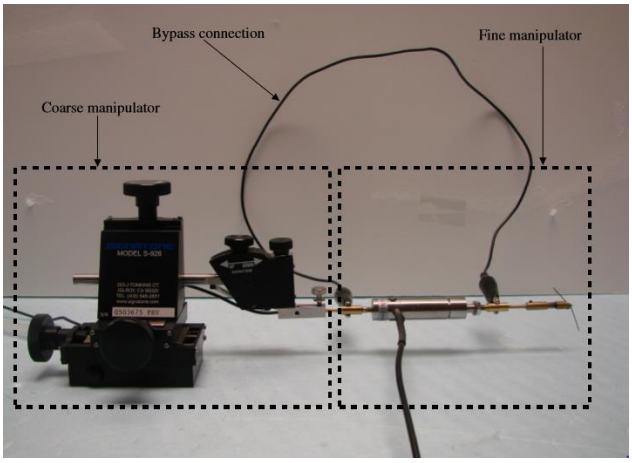

Figure 3.6. Photograph showing the set-up for micro-manipulator developed to actuate the CNC mechanical strength tester (MST)[213].

3.5.8.3 Residual Stress Testing

A Nikon (Melville, NY), Eclipse 80i microscope with imaging workstation and Nikon Elements, was used to determine the residual stress developed in released CNC MEMS.

The residual stress testers (RST) were optically imaged after release using the reflected light using 10X/0.30 and 20X/0.45 LU Plan Fluor objectives. The camera used in this experiment was a Nikon DS-Ri2. All the captured images were processed with Nikon elements software to determine the angle of rotation of the I shaped beam of the RST. Using the line angle technique, all the angles were obtained in degrees and then converted in radians to obtain the developed residual stress in CNC MEMS (**Figure 3.7**).

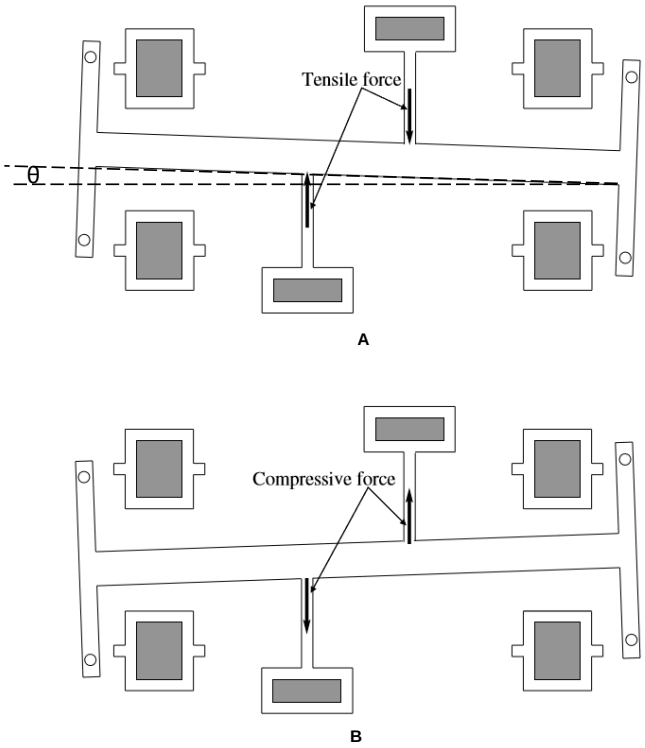

Figure 3.7. Schematic of the released residual stress tester (RST) showing A) tensile and B) compressive residual stress in the MEMS structural devices. θ is the line angle measured using microscopic imaging[213].

3.5.8.4 Phase Shifting Interferometry

Phase shifting interferometry (PSI) is an optical testing technique that requires the collection of interferograms at optical phase difference using definite phase steps. The PSI technique in this research was used to obtain the height profiles of freestanding CNC cantilevers. In addition, 2-dimensional PSI scanning was performed for height profile analysis of cantilevers upon electrostatic actuation. PSI was also required to determine the fracture strength via actuation of CNC MST using MEMScript. The interference microscope was equipped with a green LED (with λ_{max} of 525 nm, monochromated at 532 nm) and Mitutoyo M Plan Apo 10X objective. The light beam was split into two beams using a beam splitter/prism. One beam was projected in the same direction to a polished surface of silicon (8 mm X 8 mm, Si (100)) and another was deflected at 90º, projected towards the test platform. The reflecting polished silicon was equipped with a closed-loop PZT actuator (PI, PZT model #PZ-70E, LVPZT controller model # E-610.SO) which was considered as the reference surface. The MEMScript controlled small phase steps were executed using the PZT actuator, and real-time frames were captured using a charge-coupled device (CCD)-IRIS camera (Sony, XCD-SX910). The collection of frames were also controlled using the MEMScript and used for obtaining the interferograms[213].

3.5.9 Mechanical and Electrostatic Actuation

The CNC cantilever arrays fabricated in this research were actuated both manually and electrostatically. For the manual actuation, a sharp tungsten probe tip (Signatone SE-SMS) equipped with the probe module was used to push the cantilever surface. The manual force

using a module regulator was applied to bring the cantilever surface in contact with the underlying silicon surface. Then the tip was progressively moved over the beam followed by retraction. This test used to investigate the in-plane stiction between CNC and silicon test wafer surface. The obtained height profile with a crack length can be used to obtain the apparent work of adhesion of the in-plane surface. On the other hand, a different probe tip (SE-20T) with the module system was used to actuate the CNC cantilevers electrostatically. One tip was placed on the test pad next to the beam fixed end, and another was in contact with the test silicon wafer surface. The DC voltages applied to the tip was connected with the gold sputter coated CNC cantilevers. A digital-to-analog converter (DAC) was used to control the command using the MEMSscript. The input signal was amplified using a high-voltage amplifier (TEGAM, 2350S). With increasing voltage, the deflection of cantilevers towards the test surface became more significant followed by the relaxation of the structure due to elastic restoration. Right after the actuation, the beams were scanned using 2D PSI technique to capture the height profiles using the MEMSsript command window.

Chapter 4 Chiral Nematic CNC Films for Selective Reflection

4.1 Motivation

CNC extracted from biomass using sulfuric acid hydrolysis readily form chiral nematic liquid crystalline phases in water, and there is considerable interest in using this phase behavior to produce films with tunable photonic properties such as selective reflection. Depending on the source, the width and length of CNC vary from 3 - 20 nm and 50 - 1000 nm respectively[6,7]. Although CNC are not truly cylindrical, they generally follow the lyotropic phase behavior associated with rigid rods above a critical concentration they form chiral nematic (cholesteric) liquid crystals. Retention of the CNC's microstructural ordering during drying results in photonic films (Figure A1) whose optical properties depend on the helix orientation and pitch[30,198]. In the chiral nematic phase, local orientation of the CNC rods is defined by the director **n**, which rotates in a left-handed helical fashion resulting in slightly skewed nematic layers[86,217]. The helix direction is perpendicular to the director **n**. The distance that **n** travels to complete a full (360 °) rotation is known as the pitch (P) which decreases with increasing chiral interaction during drying. Depending on the direction of helix alignment, chiral nematic ordering can be classified into three distinct categories: planar (helix perpendicular to film surface), homeotropic (helix parallel to film surface revealing fingerprints under cross-polarized light), and focal conic (tilted helix or helix in both directions), shown in **Figure 4.1**[218]. Circularly polarized light with the same handedness as the cholesteric CNC is reflected as a single color; the wavelength of maximum reflection λ_{max} is related to the helical pitch P by described by Braggs' formula[219,220]:

$$\lambda_{max} = n_{av} P sin\theta \qquad 4.1$$

where n_{av} is the average refractive index of the crystalline material (1.56 for CNCs[206]), and θ is the angle of incident circularly polarized light with respect to the film surface. Obtaining uniform selective reflection requires achieving planar alignment over macroscopic areas.

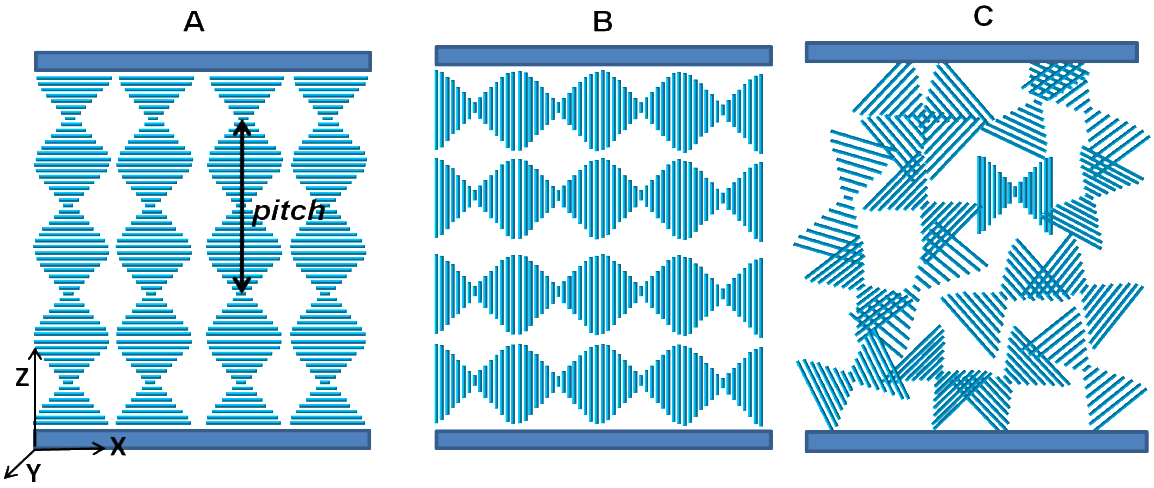

Figure 4.1. Schematic showing different orientation directions of the chiral nematic helix, A) planar: standing helix in the z-direction, 360° rotation of n shown as pitch P, B) homeotropic: helix parallel x-direction along the substrate, and C) focal conic: helices tilted in both directions.

Several researchers have shown that dried CNC films can display remarkable photonic properties including Bragg reflection and circular dichroism[97,100]. This microstructure induced photonic property makes CNC films excellent potential photonic materials for optical sensing, including security papers, selective reflectors, templates for plasmonic nanomaterials, and decorative films[90,97,98]. However, achieving uniform helix ordering and pitch over large areas remains a challenge. Nonuniformities between isotropic

and anisotropic phases in biphasic dispersions, shear associated with film casting and gelation during drying all impair the ability to achieve the uniform helix orientation required for selective reflection of a single color from large areas[11,221]. Typically photonic properties are limited by the size of the planar domains, which typically vary from a few microns to several tens of microns[9]. In addition, poor control over the helix orientation during drying gives rise to defect-rich, mosaic-like domains that are typically observed in air-dried CNC films. Hence, improved planar domain size, control over the pitch (photonic color), and insights into spatial helix defects are matters of great importance for macroscopic optical properties of photonic CNC films.

Recently, Park *et al.* reported that circular shear flow during drying of liquid crystalline CNC dispersions facilitated planar anchoring and uniform photonic properties on length scale on the order of 50 microns[85]. In another work, Dumanli *et al.*[9] reported more distinct colors in different domains with sizes on the order of 10 μm. However, the effects of dispersion concentration and processing on the uniformity of helix orientation and associated optical properties across a film are not yet fully understood. In addition, while there have been many recent advances in understanding the role of defects in photonic materials[222] such as *lomaptera* beetles[223] and *pollia condensata* fruits[224], there is relatively little understanding of helical defects in CNC films. Line defects in CNC have been attributed to varying pitch in adjacent domains[9], but the defects arising from pitch variation within the cross-sections of individual domains have not been addressed.

This research investigated the individual and combined effects of concentration, orbital shear, surface anchoring, and drying conditions. The evolution of helix orientation and pitch during drying and the microstructure and properties of the solid films were

investigated using a combination of polarized optical microscopy, reflectance spectroscopy, and scanning electron microscopy (SEM). Slow drying of CNC dispersions anchored between two glass surfaces on an orbital mixer in a water vapor-saturated environment (relative humidity 98%, at 22 °C) resulted in films with large planar domains on the order of a few hundred microns in length. Some of these domains exhibited the biomimetic property of double-peaked reflectance spectra such as that seen in *lomaptera* beetles[223]. This optical property was the result of variations in chiral nematic pitch within the films' cross-section and, to the best of the author's knowledge, has not previously been reported in CNC films.

4.2 Dispersion Drying

A drop of CNC dispersion was placed on a microscope slide and covered with a (22 mm x 22 mm) glass coverslip placed in a water vapor-saturated (relative humidity 98% at 22°C) environment (**Figure 4.2**). The humid environment was created using water droplets in a closed Petri dish (**Figure 4.2A**). This assembly was allowed to dry for 24 hours on an orbital mixer moving between 50 and 80 rpm. The process created a combination of slow capillary flow (toward the edges of the sample) and orbital flow through the slow drying rate and applied motion of the orbital mixer (**Figure 4.2C**). With increasing mixer speed, the domains became smaller. However, films made at 50 rpm exhibited more color variation with each domain than films made at 60 rpm. Therefore, 60 rpm was chosen for the remainder of the experiments. **Figure 4.2D** shows a mosaic cross-polarized reflected light microscopy image of a film prepared from a 6.5 wt. % (4.2 vol. %) dispersion. The center of the film was predominantly isotropic as expected based on both coffee ring

formation due to capillary flow, and the limited shear resulting from the lower velocity at the center of the mixer. The inhomogeneities from left to right are attributed to the mixer not being perfectly level and the rotation path not being completely uniform or circular (Figure A2).

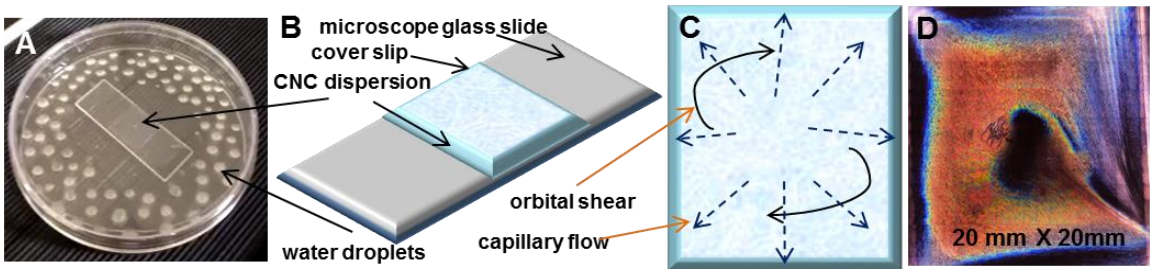

Figure 4.2. Photograph, schematic, and optical micrograph showing A) drying set up, B) CNC dispersion on microscope slide with a coverslip on the top, C) directions of capillary drag and orbital shear, and D) stitched composite image comprised of an array of 20 x 2 individual images (14 arrays in total) of a dried CNC films from a 6.5 wt. % (4.2 vol. %) dispersion sandwiched between a microscope and coverslip slide.

To understand the effects of the initial dispersion concentration, cross-polarized optical micrographs were compared for films prepared from a 2.0 wt. % (1.3 vol. %) isotropic, 6.5 wt. % (4.2 vol. %) biphasic, and 8.0 wt. % (5.1 vol. %) liquid crystalline dispersion (**Figure 4.3**). As described in the seminal work by Park *et al.*[18], drying results isotropic of biphasic dispersions results in the formation of new chiral nematic domains (tactoids) at random locations within the continuous isotropic phase. Since each of these new domains can potentially adopt any helix orientation, Park *et al*. hypothesized that drying fully liquid crystalline dispersions would eliminate the possibility of forming new liquid crystalline domains with random helix orientations[11]. They further showed that minimizing the interfacial tension by applying orbital shear; tactoids could be distorted in such a way that facilitates the perpendicular helix to the interfaces. Thus, cholesteric helix

can be guided to the short axis of the ellipsoidal or elongated tactoids setting **n** tangential to the interfaces.

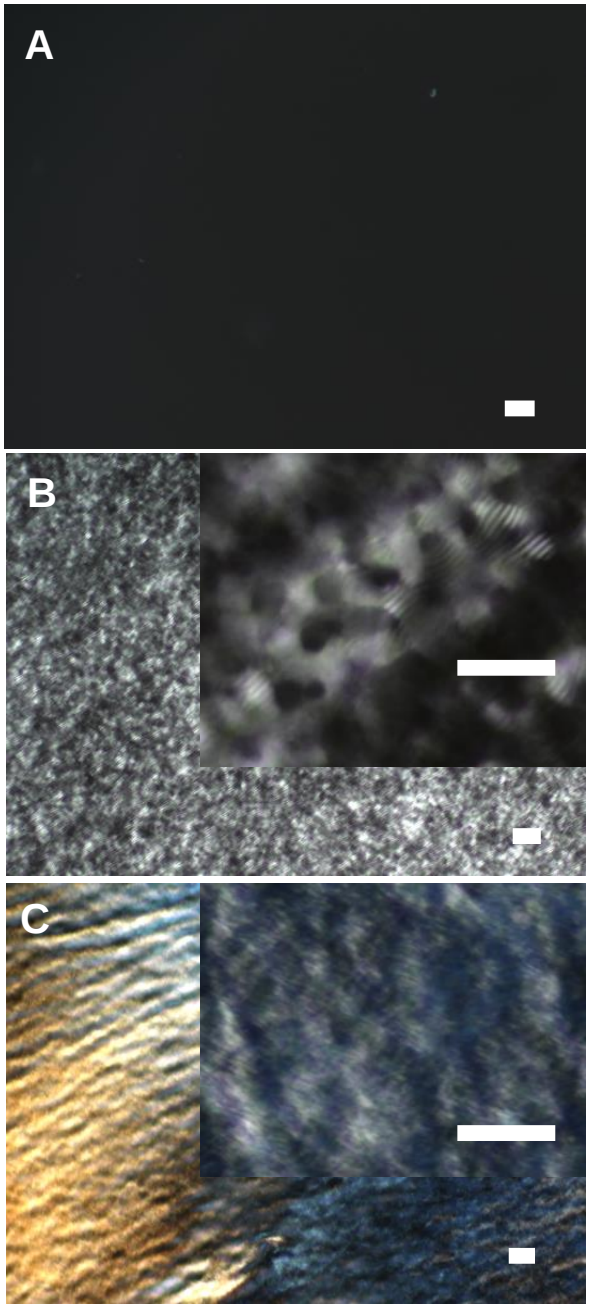

Figure 4.3. Cross-polarized transmitted light micrographs showing A) 2.0 wt. %/1.3 vol. % (isotropic), B) 6.5 wt. %/4.2 vol. % (biphasic), and C) 8.0 wt. %/5.1 vol. % (liquid crystalline) dispersions of CNC. Scale bars are 50 μm.

4.3 Results

Figure 4.4A shows the images of CNC films obtained from isotropic dispersions (2 wt. %, 1.26 vol. %) using the drying scheme shown in **Figure 4.2A**. Dot-shaped smaller domains surrounded by islands of elongated planar domains were observed showing distinct reflectance colors. Some of the dot-shaped domains had a striped texture which is attributed to fusion defects between liquid crystalline domains or tactoids in a phase coexistence regime. As the isotropic dispersion dries, the growing tactoids coalesce or fuse with each other followed by bending, folding, and elongation of the cholesteric layers[225]. Under ambient drying conditions, two fused tactoids may never merge into a single uniform tactoid, possibly due to slow relaxation of CNCs. **Figure 4.4B** shows a CNC film obtained from a biphasic dispersion (6.5 wt. %, 4.2 vol. %). Despite some defects, this film revealed large bands of planar domains with uniform reflectance colors that spanned the 1.4 mm wide field of view. In contrast to Park *et al*., films from the liquid crystalline dispersion (8 wt. %, 5.1 vol. %) showed the smallest domains (**Figure 4.4C**). This difference could be due to a combination the longer drying time enabling more time for annealing defects between newly formed tactoids and the higher concentration required for liquid crystalline phase formation of the CNC used in the present research (8.0 vs. 4.8 wt. %). While the viscosities of the samples used in Park *et al.* are not known, the viscosities of the 8 wt. % liquid crystalline samples of commercial CNC (with Na^+ counter ions) are at least two orders of magnitude higher than the 8.0 wt. % made in our lab (with H^+ counterions). Park *et al*.[18] described the similar extraction process of CNC without counter ion exchange using NaOH. Therefore, these higher viscosities may have retarded annealing of defects between the tactoids.

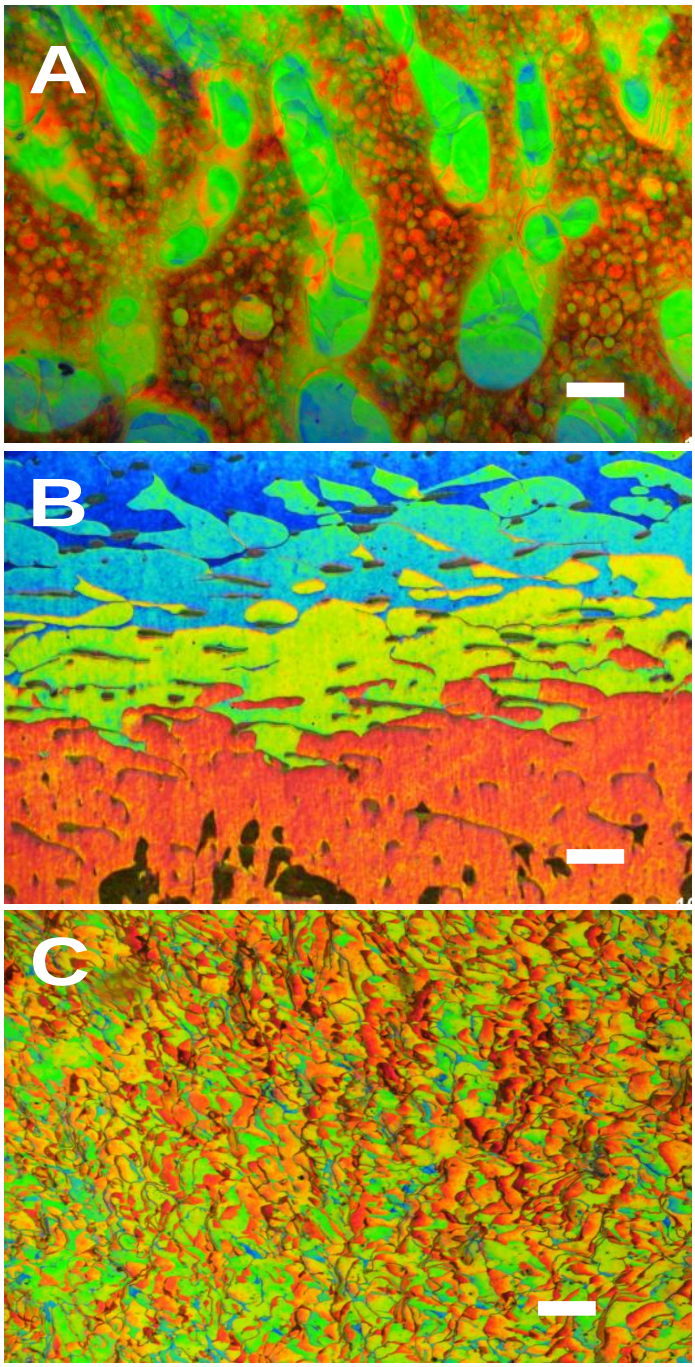

Figure 4.4. Cross-polarized reflected light micrographs showing planar chiral nematic domains of CNC in dried films using A) isotropic (2 wt. %/1.26 vol. %), B) biphasic (6.5 wt. %/4.15 vol. %), and C) liquid crystalline (8 wt. %/5.14 vo l %) dispersion concentrations. All scale bars are 100 µm. Each image is a total of 1.4X1.1 mm field of view.

In addition, the low shear (0.01 sec^{-1}) viscosity of aforementioned liquid crystalline dispersion (8.0 wt. %) increases by at least one order of magnitude compared to the biphasic dispersion (6.5 wt. %) as shown in **Figure 4.5**. As mentioned before, the biphasic CNC dispersion showed the signature three-region behavior, where the liquid crystalline exhibited a Newtonian plateau followed by shear thinning behavior. This increased viscosity resulted in less mobility of CNC in liquid crystal than biphasic dispersions resulting in smaller planar domains in the dried films.

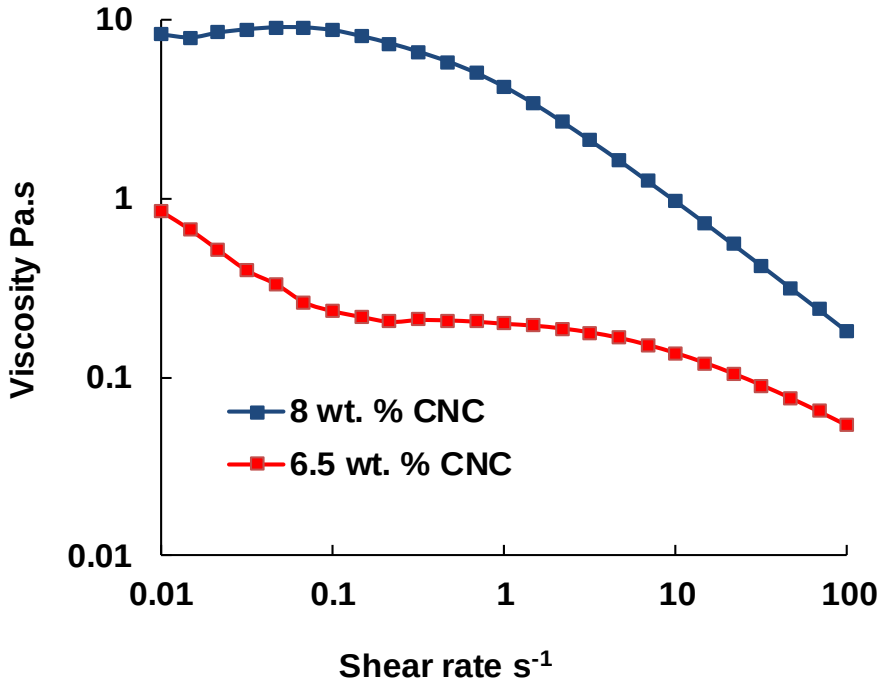

Figure 4.5. Steady shear viscosities of liquid crystalline and biphasic aqueous CNC (Na^+ as counterion) dispersions at 10 ˚C.

The order of magnitude increased viscosities from biphasic to liquid crystalline dispersions was also reported by Ureña-Benavides *et al.*[124] for cotton CNC (H^+ as counterion). We hypothesize that the reduced mobility resulting from the higher viscosity and elastic modulus in the liquid crystalline regime impedes achieving long range uniform

helix orientation. In addition, the higher initial concentration of the dispersion reaches the gel transition and associated kinematic arrest at shorter drying time limiting the long range planar ordering. In contrast to more viscous liquid crystalline CNCs, lower concentration and lower viscosity biphasic dispersions can achieve longer range ordering due to the combination of greater mobility and longer times for rearrangement before the kinematic arrest. In the following paragraphs (unless mentioned) results will be discussed for the CNC films obtained from the biphasic dispersion (6.5 wt. %).

A strip from the stitched micrograph shown in **Figure 4.2D** is shown in **Figure 4.6A**. Based on the size, shape, and uniformity of reflectance colors, this film strip can be divided into three regions of broadband reflectance colors, starting from violet to deep red. From the near center to the edge, variation in the film thickness (Figure A3) associated with the variation of reflectance colors was observed. The center of the film did not show any reflectance due to a sub-micron thickness of the film having no planar ordering. This thickness variation in the CNC film is attributed to capillary drag known as coffee ring effect during the drying of colloidal dispersions.[11,226] Region 3L displayed the most elongated planar domains showing striped areas of blue and green reflection colors mainly, shown in **Figure 4.6B**. Some of the domains revealed a subtle change in reflectance colors such as yellowish green in a green domain shown in **Figure 4.6B**. This subtle change could be associated with variation of pitch along the vertical direction or a slight variation of the planar angle. This will be discussed based on optical spectra and SEM later. In Region 2, the film thickness was rather uniform as indicated by the uniform reflectance colors (**Figure 4.6C**). Due to higher thickness than Region 3, the reflectance colors in Region 2 varied from yellow to red. Towards the center, domains became less elongated where they

were subjected to milder orbital shear. The further away from the center, the smaller the domains became as the domain size, and shear rate are inversely proportional[218].

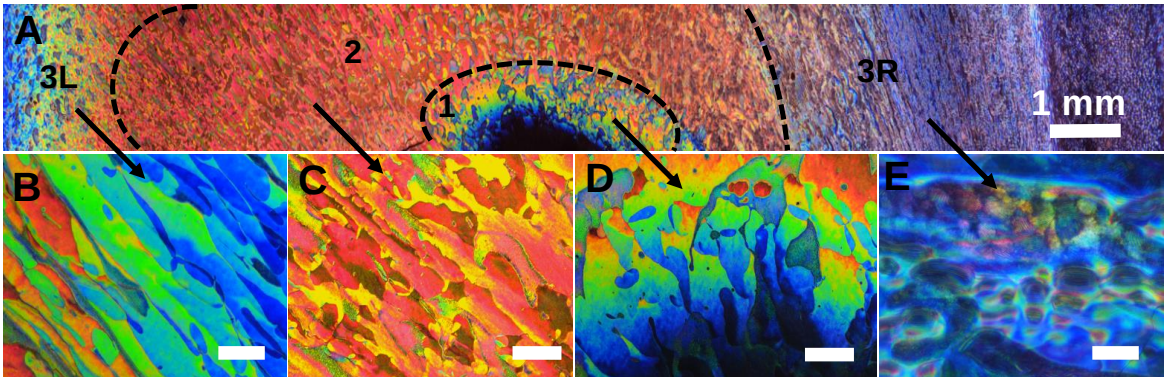

Figure 4.6. Cross-polarized reflected light micrographs showing a stitched image of A) distinct planar regions across the CNC film between the coverslip and glass substrate. It also illustrates variable shapes and sizes of planar domains shown from left to right in B) Region 3L, C) Region 2, D) Region 1, where domains were subjected to variable shear, and E) Region 3R, where domains were subjected to even higher shear resulting fingerprints or non-planar ordering. All scale bars are 100 µm.

Figure 4.6D shows the largest macroscopic domains resemble the "Grandjean" texture reported previously in planar thermotropic liquid crystals[218,227]. In this Region, the significant change in thickness near the center caused a red shift in reflectance colors. The pitch (P) increased from near center to edge of Region 1 (blue to orange) due to increasing film thickness (d) according to this following relation[228]:

$$P = \frac{2d}{N} \qquad 4.2$$

With increasing thickness (d), the number of chiral layers (N, periodic spacing indicating half of the pitch in the dried film) typically decreases (lateral direction), resulting in planar domains with a shift of reflectance colors. However, the number of chiral layers may also vary even if the thickness remains constant. **Figure 4.6E** shows Region 3R, had

a completely different texture than 3L. As the dispersion was confined to a square geometry (shape of the coverslip) and subjected to a right-handed orbital shear, this part of the dispersion experienced a higher shear rate. Therefore, Region 3R mainly shows the focal conic and homeotropic ordering of the helix indicated by fingerprints (Figure A4). However, cross-polarized reflected colors of these domains from Region 1, 2, and 3L, did not change upon rotation of the film meaning no strong birefringence was induced by the optical axis of the homeotropic helix (Figure A5).

Interestingly, some of the areas in Region 2 showed clusters of domains with uniform reflectance colors which spanned areas of 0.2 - 0.4 mm^2, shown in **Figure 4.7**. A single reflectance color was found to be dominant indicating well-controlled pitch. For blue clusters, bleached green was the second reflective color meaning elusive transition of the pitch among some of the neighboring domains (**Figure 4.7A**). The same observation was found for green (with the orange transition) and deep red (with green transition) clusters as shown in **Figure 4.7B and C**, respectively. However, though the overall colors remained uniform, there were clear disclinations between adjacent domains. These line defects are attributed to non-integer changes in the number of layers N between the domains; these non-integer changes are incomplete half-turns of the director $\mathbf{n}$[229].

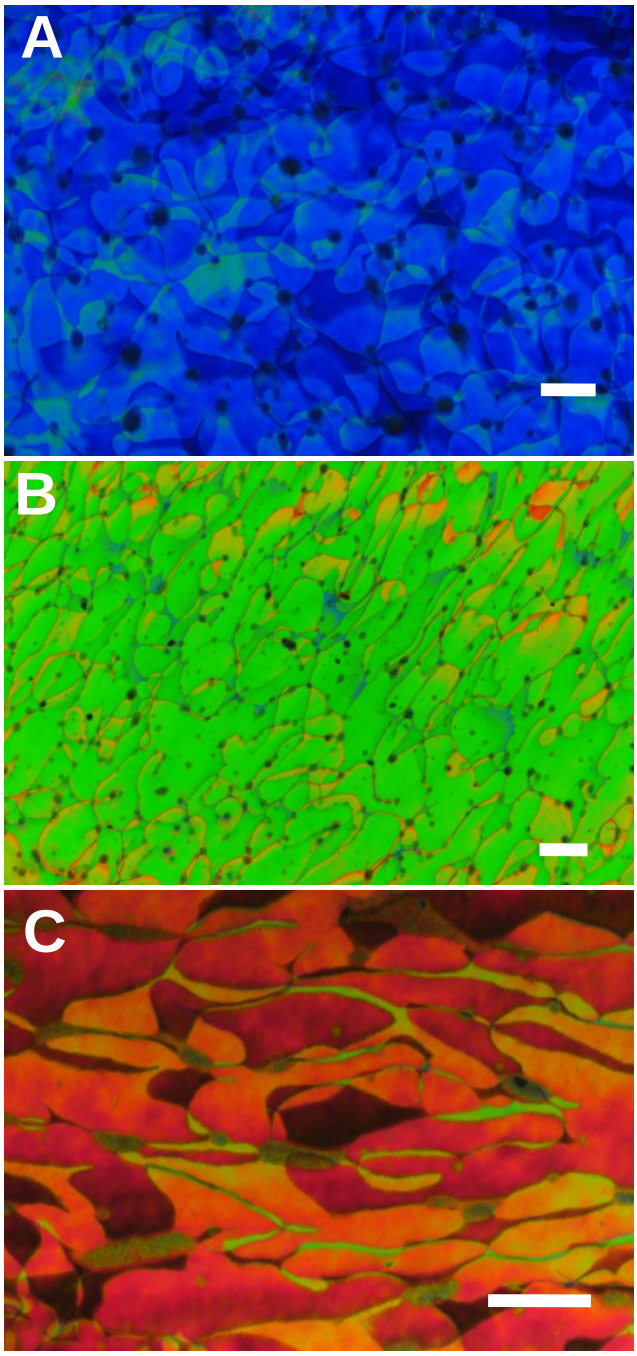

Figure 4.7. Cross-polarized micrographs showing uniform reflectance colors of A) blue, B) green, and C) red, in planar domains with slight transition colors of green, orange, and green, respectively. Scale bars are 50 μm.

Films produced using the scheme shown in **Figure 4.2** did not exhibit the typical coffee ring effect observed for open surface drying of colloid dispersions, including CNC dispersions[230]. For a CNC drop dried on a surface with contact line pinning, the higher evaporation rate at the edge results in capillary flow of the CNC to the edge of the drop and a thick iridescent ring in the dried film[231]. This affects not only the alignment of the nanocrystals at the edge, but also the helix alignment in the rest of the drop cast dispersion.[9] Drying in a water vapor saturated environment effectively slowed down the capillary flow, allowing more time to the helix ordering before the kinetic arrest of the microstructure.[8] Thus, this drying scheme allowed more time for the liquid crystalline domains to achieve planar ordering. We hypothesized that the interplay of weakened capillary flow and orbital shear may have enabled vertical helix orientation while the coverslip surface pinned the nematic directors of the adjacent liquid crystal domains at the dispersion coverslip interface. To confirm this hypothesis, the evolution of the vertical helix during drying was investigated using cross-polarized reflected light microscopy. A biphasic CNC dispersion sandwiched between the slide and coverslip was taken out from the water vapor saturated environment after two hours of slow drying. Then, the dispersion was left out to dry under ambient conditions (relative humidity 10 % at 22°C). Because of the slow drying followed by fast drying, some of the chiral nematic domains were trapped in between horizontal and vertical helix orientations displaying a tilted helix transition. As shown in **Figure 4.8**, fingerprints, tilted helix, and planar alignment were all observed in close proximity (circled areas). This kind of helix transition was previously observed by Zola *et al*. for thermotropic liquid crystals in the presence of a rubbed anchor surface[232].

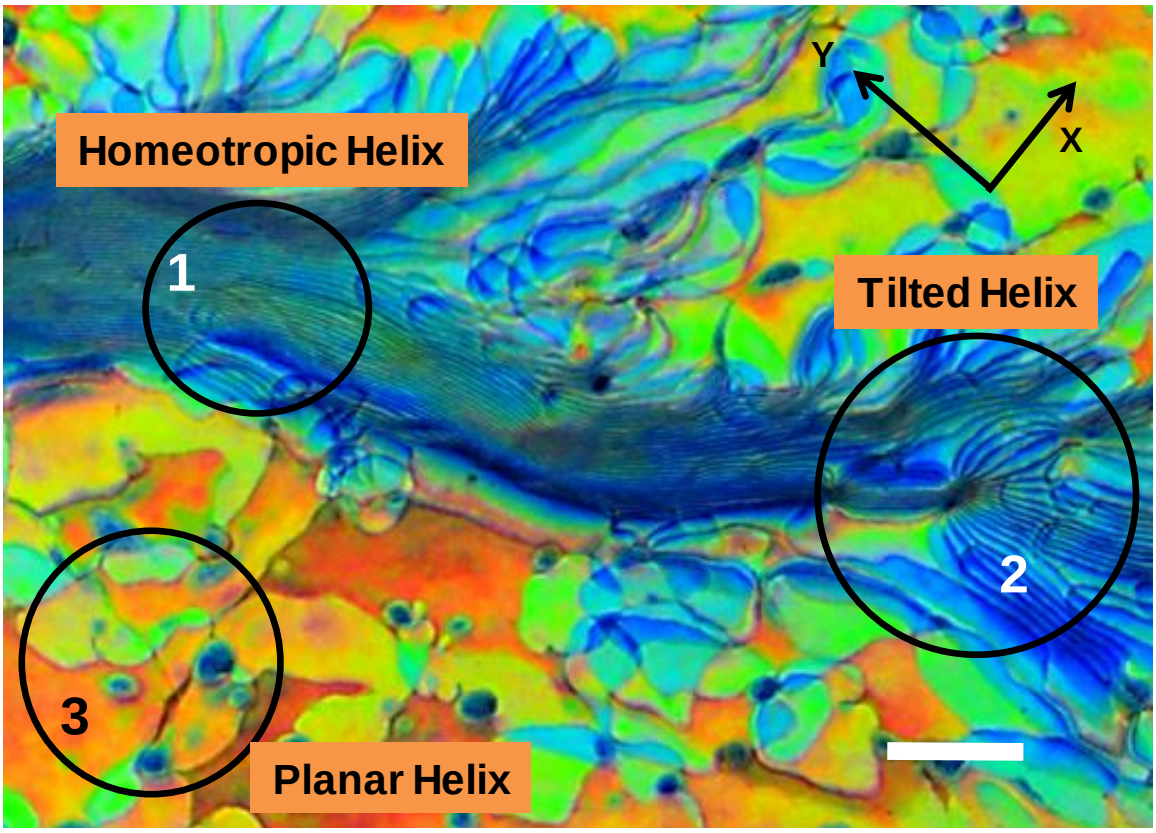

Figure 4.8. Cross-polarized reflected micrograph showing the evolution of the helix orientation in a CNC film obtained using 6.5 wt. % (4.15 vol. %) dispersion. Arrows indicate the relative directions of shear and capillary flow. Scale bar is 50 µm.

The microstructures of dispersions dried with and without a coverslip on the apparatus shown in **Figure 4.2** were compared. The isotropic dispersion (2.0 wt. %) was chosen for study because films from isotropic dispersions have the most nonuniformities[11]. During drying, tactoids (droplets of anisotropic phase dispersed in isotropic phase) form, evolve, and merge resulting in small planar domains with random mosaic defects[18]. **Figure 4.9** shows the difference in the optical texture with and without top surface anchoring to a coverslip. Without the coverslip (**Figure 4.9A**), there are many mosaic defects and fingerprints textures resulting from parallel helix ordering to the substrate. Helices far away

from vertical assembly with random orientation on the substrate plane were observed; exhibiting reflection of different colors. However, with the coverslip (**Figure 4.9B**), the film had dot-shaped planar domains with subtle mosaic defects. The similarity of the regular dot-shaped planar domains' appearance (also shown in **Figure A1B** and **A5I**) to cholesteric blue phase defects is an interesting subject for future investigation. The marked differences between **Figures 4.9A** and **4.9B** show that two surface anchoring (slide and coverslip) has a significant effect on CNC ordering during drying. This effect may be partially due to interactions with the dispersion and glass surfaces, but is likely to primarily be the result of preventing evaporation from, and skin formation on, the top surface, which is known to limit microstructural uniformity by locking everything into a glassy state[11,221]. However, the shape anisotropy of rod-like CNC causes them to parallelly align to the microscope coverslip and slide. Therefore, the helix will tend to be orthogonal to the surfaces during drying and favor a planar texture. The detailed study to understand the effects of slow drying, dispersion concentrations, orbital shear, and surface anchoring was done based on cross-polarized reflected light microscopy. These results with brief discussion can be found in Appendix Figure A6-A13.

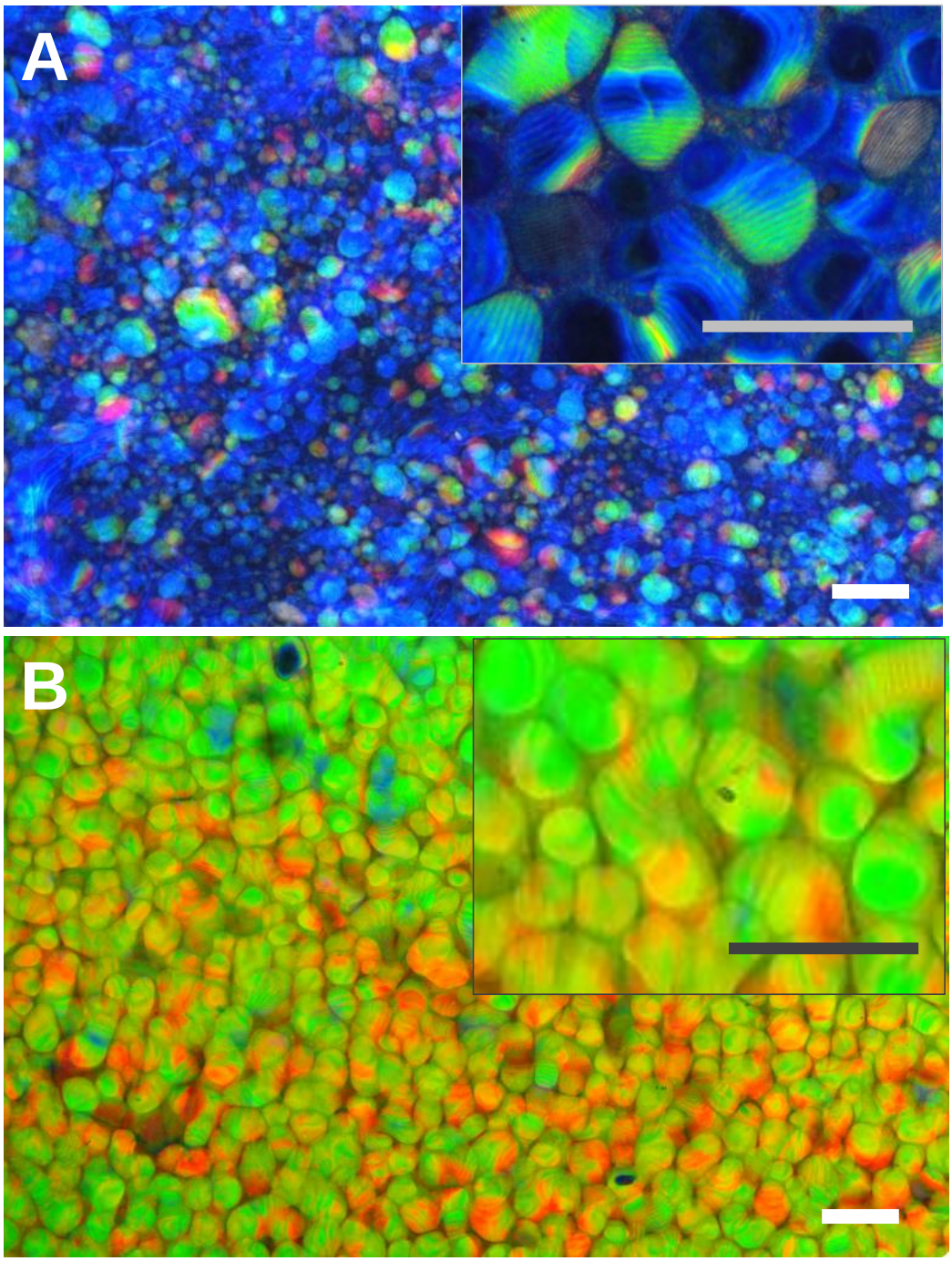

Figure 4.9. Cross-polarized reflected micrographs showing the effect of surface anchoring on planar orientation, CNC film dried in water vapor saturated environment assisted by orbital shear with a coverslip A) off and B) on during drying. Scale bars are 100 µm.

Figure 4.10A shows the micrograph under LCP light showing reflection by the planar domains (using 0^{o} incident angle of illumination). The same domains transmitted the RCP light due to opposite handedness of chiral nematic ordering, shown in **Figure 4.10B**. **Figure 4.11A** and **B** show the selective reflectance spectra that were observed using both left-handed circularly polarized (LCP) and right-handed circularly polarized (RCP) reflected light on the selected domains with blue, green, and orange colors. **Figures 4.11C** and **D** show the selected areas of domains for spectral analysis. As shown in **Figures 4.11A** and **B**, areas like 1, 2, and 3 were found to exhibit single-peak reflectance spectra. As expected, cross-polarized reflectance micrographs of those spots (1, 2, and 3) showed the uniformity of colors. On the other hand, areas like 4, 5, and 6 showed a subtle change of reflectance colors within a domain. The double-peak LCP reflection spectra (**Figure 4.11B**) with a narrow trough were observed for these types of domains (i.e., green with yellowish green). Interestingly, similar kind of double-peak reflectance spectra has been recently reported in a biological photonic material such as Lomaptera beetles by Carter *et al.*[223] Two possible variations in a planar chiral nematic ordering can give rise to double-peak spectra. First, the cholesteric microstructures with variable half-pitch (throughout the film's cross section) cause an abrupt change to the periodic modulation of the refractive indices. Therefore, a sudden phase jump at the interface of cholesteric stacking with different half-pitch takes place, causing twist defects in films[222,233]. The shape and width of the double-peak reflection bands depend on the birefringence and maximum and minimum values of the half-pitch. Second, any discontinuity between cholesteric stacking even with constant half-pitch, may also cause twist defect mode resulting in double-peaks[233]. Different shapes of the double-peak bands are attributed to different phase jumps

caused by twist defects (**Figure 4.11B**). To the best of the authors' knowledge, this is the first report of such a narrow photonic stop band defect in CNC photonic films, resolved by LCP. Interestingly, Ličen *et al.* reported a thickness dependent variation of cholesteric half-pitch using Fast Fourier Transformation spectra; illustrated by multiple peaks associated with periodic variation[234]. Photonic CNC films with such twist band defects can have potential use in advanced applications including narrow band optical filters, displays, and low-threshold mirrorless lasing[233,235,236].

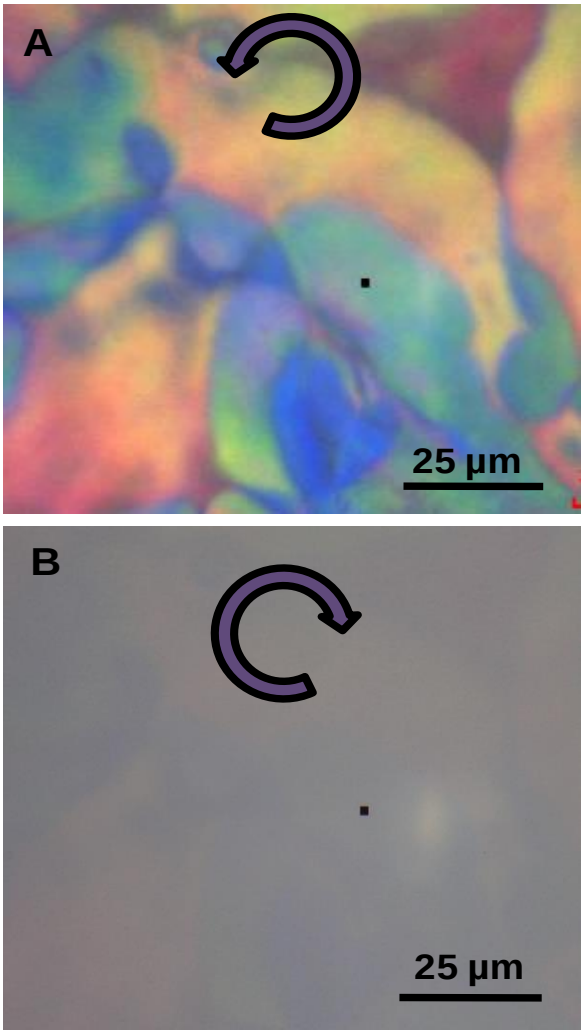

Figure 4.10. Microscopic images of CNC planar domains using A) left-handed and B) right-handed circularly polarized reflected light.

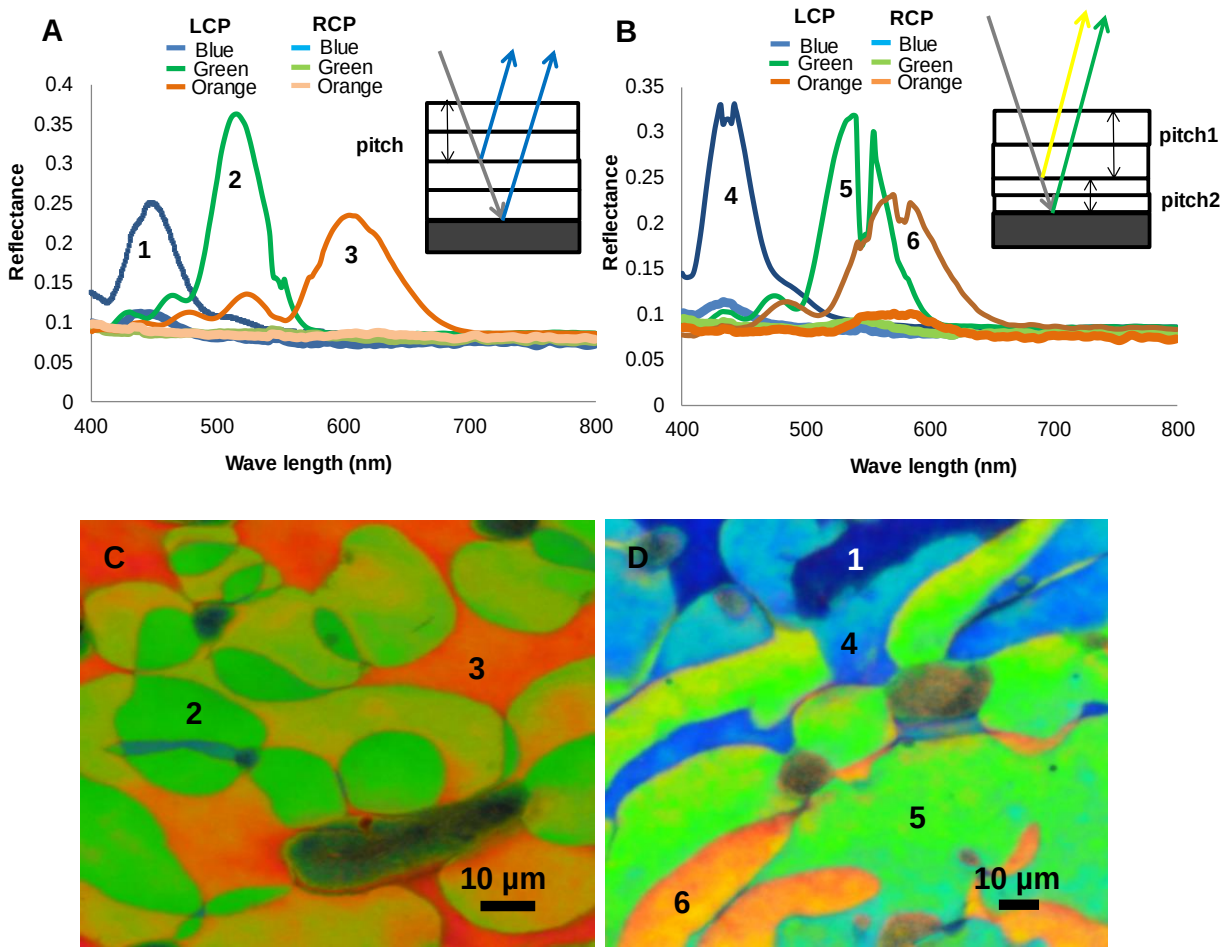

Figure 4.11. Selective reflectance spectra using circularly polarized light showing A) single-peak, and B) double-peak reflection from planar domains of CNC film using both left handed circularly polarized (LCP), and right handed circularly polarized (RCP) light, C) selective reflection micrograph under LCP illumination, D) transmission of RCP light over the same planar domains, E), F) cross polarized reflected micrographs showing selected planar domains giving reflectance spectra of both single-peak (1, 2, and 3) and double-peak (4, 5, and 6).

The pitch (P) measured based on reflectance peak (λ_{peak}) of single-spectra for blue, green, and orange planar domains were 284, 328, and 384 nm, respectively (shown in **Table 4.1**). Based on SEM measurement on the same planar domains (Figure A14) corresponding calculated pitch values were 288 ± 40, 342 ± 58, and 416 ± 38 nm,

respectively. A slight discrepancy was expected as accurate counting of chiral nematic layers (N) is challenging due to issues like wobbling of helical layers with holes and protrusions under the electron beam. However, the width of reflection spectra (**Figure 4.11A**) indicates a possible range of pitch values which would be in agreement with the SEM pitch.

Table 4.1. Measured full pitch using optical spectra and SEM. λ_{peak} is the peak wavelength, d_{SEM} film thicknesses based on SEM, N_{SEM} is the number of pseudo layers or half periods, $P_{spectra}$ is the pitch based on sepctra, and P_{SEM} is the pitch based on SEM. Errors are based on the uncertainty of half period numbers from SEM cross sections of CNC films.

Domain color	**λ_{peak} (nm)**	**d_{SEM} (nm)**	**N_{SEM}**	**$P_{spectra}$ (nm)**	**P_{SEM} (nm)**
Blue	444	1150	8 ± 1	284	288 ± 40
Green	512	1200	7 ± 1	328	342 ± 58
Orange	601	1250	6 ± 0.5	384	416 ± 38

To better understand the microstructural origin of the optical properties, perpendicular and oblique cross sections of the film were investigated by SEM. **Figure 4.12A** shows the individual chiral nematic half-pitch segments (N) in a perpendicular cross-section view of the fractured film. The thickness of each pseudo layer is half of the pitch; dividing the film thickness by total number of chiral half-pitch (N) would give the average half pitch in that planar domain. **Figure 4.12B** shows the oblique cross section (slanted to the helical axis); the parallel arc-like appearance indicates uniform planar chiral nematic ordering. These continuous stacks of nested arcs resemble the Bouligand structures of twisted plywood; that reported by Livonent *et al.* for several biological cholesteric

systems[237]. **Figure 4.12C** shows an example of a planar domain with uniform or constant pitch that resulted in single peak spectra. On the other hand, **Figure 4.12D** shows a domain with a varying pitch in the film direction (perpendicular to the film surface) which resulted in subtle color variations and double-peak spectra (**Figure 4.11B**). **Figure 4.12E** shows an example of the number of chiral nematic half-pitch segments N changing from 10 to 11, which resulted in domains with different reflectance colors. **Figure 4.12F** is from one of the films showing a tilted helix optical texture (**Figure 4.8**, spot 2) and shows a distinct tilt in the planar ordering (helix not being perpendicular to the substrate).

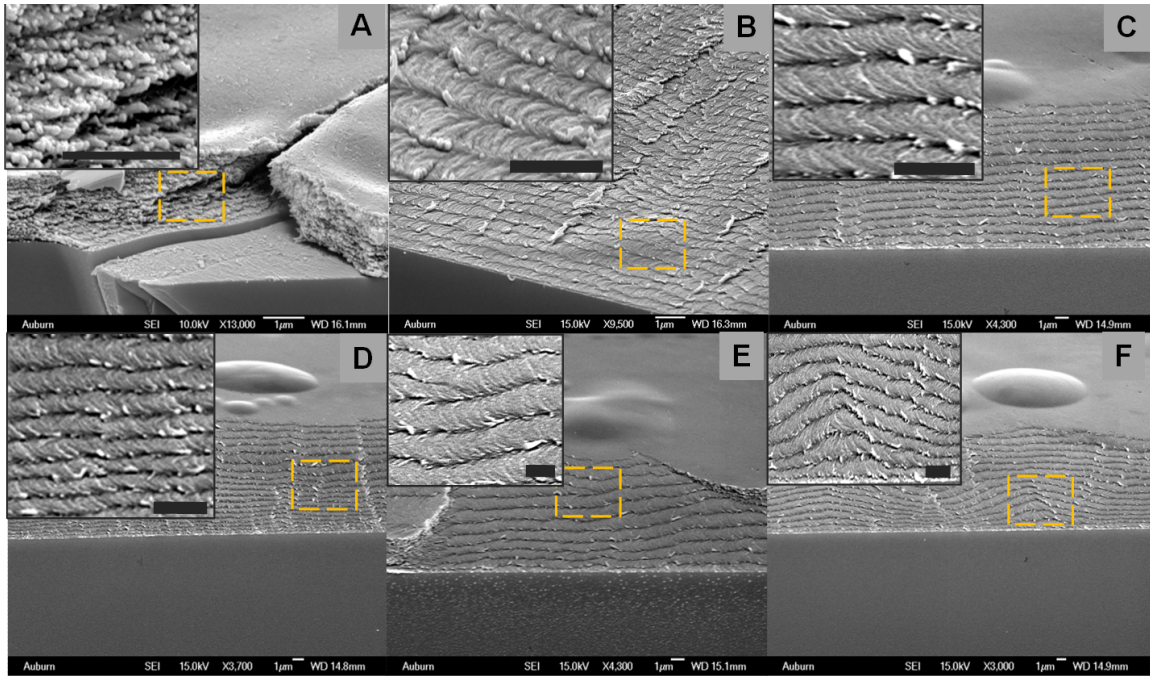

Figure 4.12. Scanning electron microscope (SEM) images of cross sections of CNC films showing A) chiral nematic layers viewed at 90° cross section, B) uniform parallel arc-like morphology of planar ordering viewed at oblique cross section, C) constant pitch and D) spatially varying pitch within a planar domain, E) line defect due to change of chiral nematic layers number, and F) tilted domain next to planar ones. Dome shaped topography on the surface of the film is attributed to beam damage. Scale bars are 1 µm.

4.4 Conclusions

In this chapter, the results of using a combination of surface anchoring, shear, and drying in a humid environment to produce photonic CNC films were discussed. The macroscopic planar ordering of the cholesteric helices in dried films exhibited broadband selective reflection spectra of polarized light. Compared to air dried CNC films, the lateral dimensions of regions of selective reflection were enhanced from a few microns[9] to millimeters in size. The interplay of slower capillary flow and orbital shear flow, in presence of surface anchoring, facilitated the perpendicular helix orientation (planar) to the film surface. SEM analysis revealed uniform planar ordering throughout the film indicated by long range arc-like structural ordering. This research also unveiled a new insight into spatially varying pitch in planar CNC films, mimicking the defect observed in the natural photonic materials cholesteric microstructure. Further investigation of the surface energy of anchor substrates may provide greater insights for planar orientation at even better length scale. Additionally, uniform planar alignment of lyotropic CNCs can be used as a versatile template for long range planar ordering of inorganic nanowires, nanorods, plasmonic nanoparticles, and nanosheets for optical applications[119,238-240].

Chapter 5 Nematic CNC Films for MEMS Fabrication

5.1 Motivation

In the last decade, there has been considerable interest in the extraction of, and potential applications for, the CNC contained within cellulosic biomass[241]. However, to date, CNC research has primarily focused on enhancing polymer mechanical properties[50,102,104] or exploiting liquid crystalline phase behavior to make optical films[9,97]. There have also been efforts to develop CNC based electroactive papers[109] and composites (with polyvinyl acetate) for implantable MEMS scale structure[6]. However, functional MEMS devices *via* aligning individual CNCs in a structural film followed by microfabrication on a test wafer have never been reported. MEMS encompass complex structures and devices that are used in sensing and actuation on micrometer scale[242]. MEMS are a key, but often hidden part that sense or control physical, chemical, and optical quantities through an electrical interface and used in numerous products in the transportation, electronic, medical, and consumer products industries[243]. Micromachining technology for MEMS was derived from integrated circuit (IC) fabrication; silicon has been the predominant material choice[244]. The current market for silicon-based microelectromechanical systems (MEMS) is $14 billion; this value is expected to grow to $20 billion by 2020, with much of the growth occurring in biomedical sensors[245]. However, for this rapidly growing market there are ongoing concerns about the use of silicon in MEMS in terms of cost, scope, and potential adverse environmental impacts. Silicon fabrication is energy intensive, requiring processing temperatures on the order of 1000 °C, and etching/releasing is performed with hazardous chemicals such as hydrofluoric acid. Furthermore, silicon is limited in terms of the range

of microstructural and chemical functionalities that can be achieved; this is particularly considered a concern for BioMEMS (MEMS based sensors with biological interfaces)[246,247]. BioMEMS have become increasingly prevalent particularly in therapeutics, diagnostics, and tissue engineering[248,249] and there is a drive to explore materials that are disposable, have readily tunable surface chemistry for binding biomolecules, and are biocompatible (for *in vivo* use). Polymer MEMS are emerging as an alternative to silicon for some applications. Polymer MEMS can have the advantages of lower cost, easier fabrication, rapid prototyping, biocompatibility, and greater ductility. However, they are typically limited in terms of mechanical properties and thermal stability[250]. Therefore, there is a need for a material that combines silicon's mechanical properties with polymer processability.

The results in this chapter show cellulose nanocrystals (CNC) as an intriguing new alternative MEMS material with the advantages of its' intriguing mechanical and optical properties. CNCs' natural abundance, renewability, biodegradability, tunable surface chemistry, and ability to be processed in aqueous solutions at near ambient conditions make them greener, lower cost alternative to silicon-based materials. Second, unlike many polymers, their intrinsic elastic modulus of approximately 150 GPa[251] is comparable to that of silicon. Unlike semi crystalline polymers, CNC does not undergo a low temperature glass transition[252]; CNC's thermal stabilities range from 190 to 300 °C depending on the surface chemistry[253]. Finally, their anisotropy and ability to be processed into highly aligned materials enable the production of MEMS with controlled anisotropic mechanical and optical properties that may not be achieved in MEMS made of traditional materials. In this work, several of the most commonly used MEMS test devices were fabricated from

aqueous cholesteric CNC dispersions made film using photolithography. Surface micromachining on aligned CNC films resulted in microdevices such as doubly clamped beam arrays (DCBs), cantilever beam arrays (CBA), residual stress testers (RSTs), and mechanical strength testers (MSTs). These devices were chosen because they are standard devices used in silicon MEMS for quality control and/or application specific functionality. For example, CBAs/DCBs are used to determine elastic modulus and as components in mass sensing applications[242,244].

5.2 Sheared CNC Films

As has been shown for fluid phase processing of other rod-like nanomaterials[254-256], the fluid phase processing using liquid crystalline dispersions results in better alignment and mechanical properties in the assembled solid material/films. However, the final structure in a film is a complex function of numerous factors including dispersion microstructures, applied shear, wet thickness, capillary effects, and microstructural relaxation time relative to the drying time. Therefore, in this chapter, the relaxation study of CNC dispersions after shear cessation will be discussed first. Next, the understanding of relaxation dynamics to obtain shear aligned CNC films will be reported for CNC MEMS fabrication.

5.2.1 Fluid phase relaxation dynamics after shear cessation

To understand the relaxation dynamics, liquid crystalline aqueous CNC dispersions (8 wt. %/ 5.14 vol. %) were sheared in a Linkam shear cell at 100 s^{-1} for 5 minutes. Next, the relaxation of CNC rods was observed using time lapse cross-polarized optical microscopy. Both 50 μm and 500 μm gaps were studied. **Figure 5.1** shows the relaxation texture of a 8

wt. % CNC dispersion in a 50 μm gap. Initially, the sheared dispersion showed a uniformly birefringent texture, indicating uniaxial rod alignment in the flow direction as shown in **Figure 5.1A**. Additional relaxation time resulted in a banded texture perpendicular to the flow direction. The banding texture began to develop at 10 minutes and was fully developed in the range of 25 - 30 minutes after shear cessation (**Figure 5.1B - D**). This type of one dimensional periodic banded texture was also reported in hydroxypropyl cellulose and poly(-γ-benzyl glutamate), by Vermant *et al*.[257] At 30 - 40 minutes, some areas appear as bright (flow aligned) and some areas appear dark (± 45° aligned to the flow direction) textures under cross-polarized light as shown in **Figure 5.1E - F**. The banded texture was originally thought to be dependent on shear rate. However, further experiments showed that if the shear rate was sufficiently high to align the rods, bands would form upon relaxation. In addition, Lonberg *et al*. utilized a magnetic field to induce rod alignment and found that bands formed upon relaxation after removal of the magnetic field. Over the course of the experimental runs, the banding texture further relaxed, though not entirely in some areas, eventually giving way to a homeotropic cholesteric texture at 70 minutes after shear cessation (**Figure 5.1H and I**). The larger image (**5.1I**) shows the recovered fingerprint texture, after high shear, given adequate relaxation time. It is important to note that at 70 minutes relaxation the helix mostly developed in the vorticity (Z) direction. However, the helix in the flow direction (X) may also be observed which can be associated with a different plane in the Y direction (shear direction or sample thickness direction). **Figure 5.2** shows that similar relaxation dynamics occurred in a 500 μm gap. Due to higher sample thickness, flow aligned sample showed uniform orange color as shown in **Figure 5.2A.**

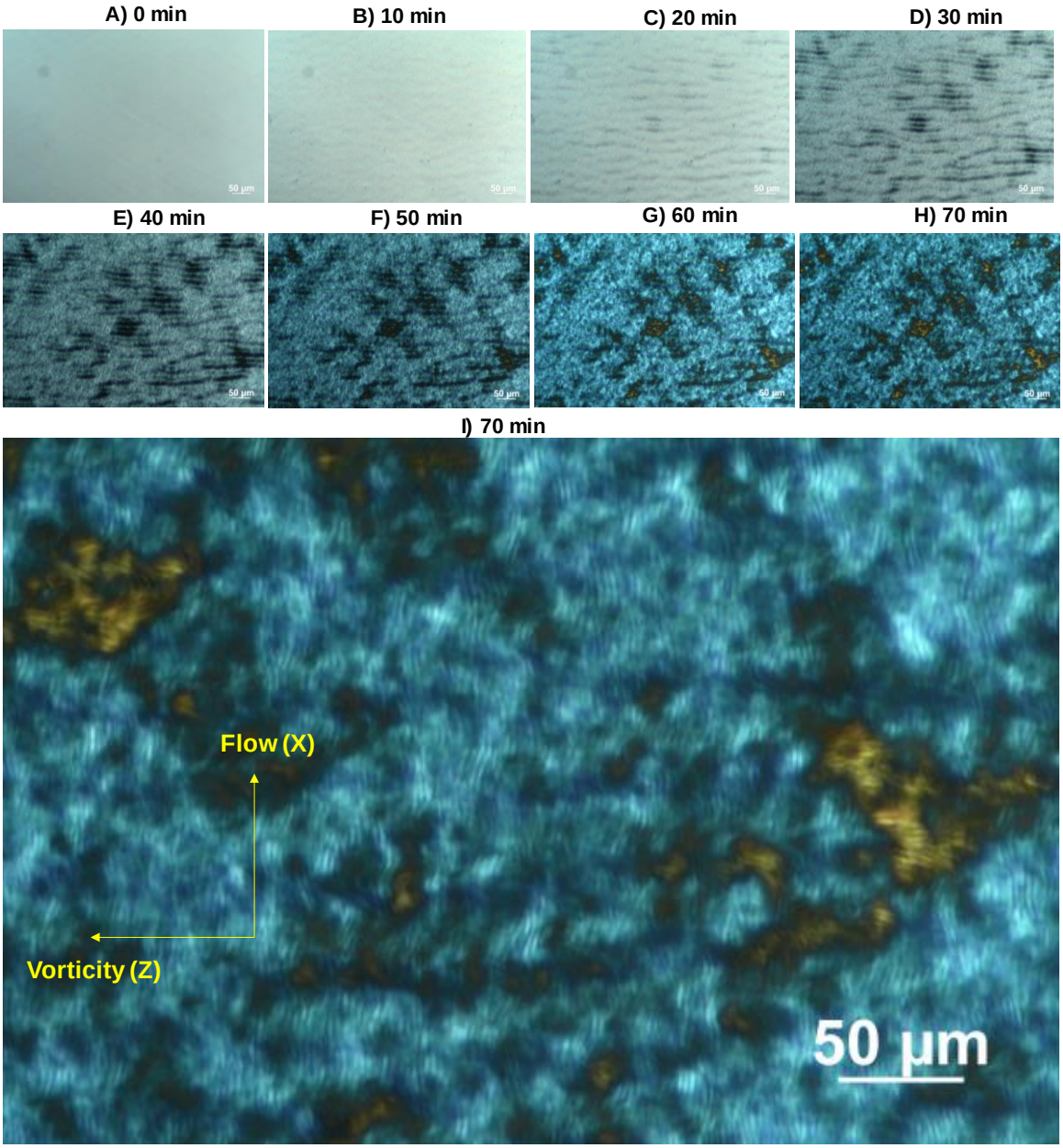

Figure 5.1. Cross-polarized transmitted light microscopic images showing the relaxation texture of 8 wt. % (5.14 vol. %) CNC dispersion after shear cessation at different times. Shear cell gap was 50 µm.

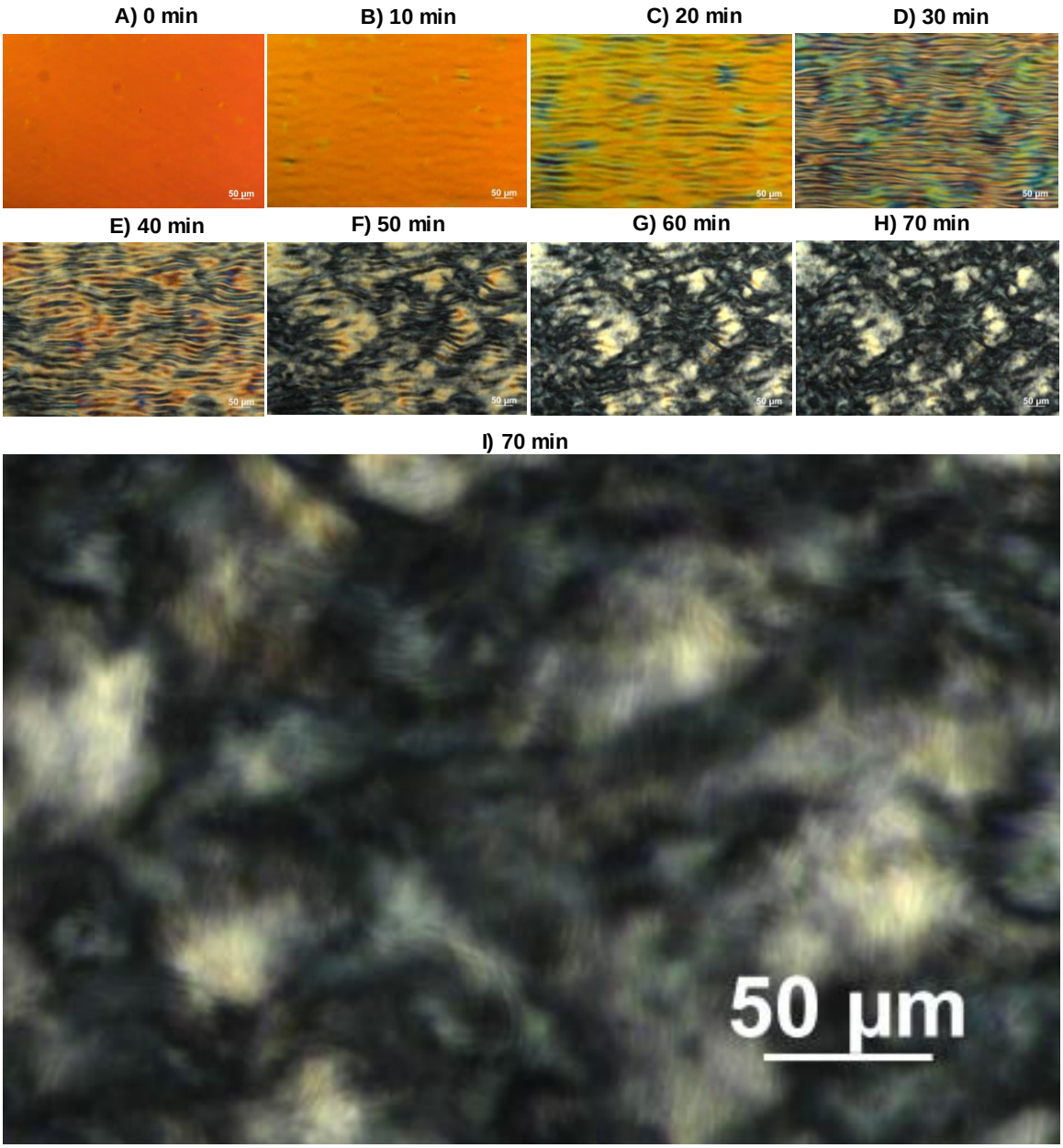

Figure 5.2. Cross-polarized transmitted light microscopic images showing the relaxation texture of 8 wt. % (5.14 vol. %) CNC dispersion after shear cessation at different times. Shear cell gap was 500 µm.

For higher gap, the change of banded textures' width was more evident than in smaller gap (**Figure 5.2B - F)**. However, the relaxed sample exhibited similar recovered microstructures at 70 minutes. **Figure 5.2I** shows the fingerprints of homeotropic

cholesteric microstructures, which were more random in 500 μm than the 50 μm gap (**Figure 5.1I**). It indicates gap height dependent relaxation which may cause different CNC microstructure configurations. This can be attributed to higher role of thermodynamic penalties associated with confinement and non-uniformity next to the boundary at smaller gap. Therefore, a sufficiently large gap can also enable planar configuration due to a decrease in the thermodynamic penalty associated with confinement while the penalty for non-uniformity near the boundary remains constant. However, the periodic banded textures were found to be independent of gap heights. Since the periodic deformation attributes a lower viscosity response compared to higher viscosity uniform slow relaxation, the banded texture appears as a result of stress relaxation. According to another explanation, the defects become highly localized when the rods are sheared and aligned with the flow direction. Therefore, Frank elastic energy stored in the defects provides the driving force for the director reorientation. Thus, a local ordering is preserved, while the global order is not. In addition to liquid crystalline CNC (8.0 wt. %/ 5.1 vol. %), a biphasic dispersion (7.0 wt. %/ 4.5 vol. %) was sheared and allowed to relax**. Figure 5.3** shows the side by side comparison of the 8.0 and 7.0 wt. % CNC dispersion during relaxation. As shown in **Figure 5.3B, D, F**, and **H**, 7 wt. % showed a quicker periodic response compared to 8.0 wt. % CNC after shear cessation. The 7.0 wt. % resulted in a fully developed banded texture within 10 minutes of relaxation which can be attributed to the sharp increase of dispersion viscosity from biphasic to liquid crystalline phase of lyotropic CNC. The relaxation dynamics may also vary with the type of counterions in the dispersion. All these factors may affect the associated electric double layers of the charged polyelectrolyte system as CNC, changing the chiral interaction and relaxation dynamics.

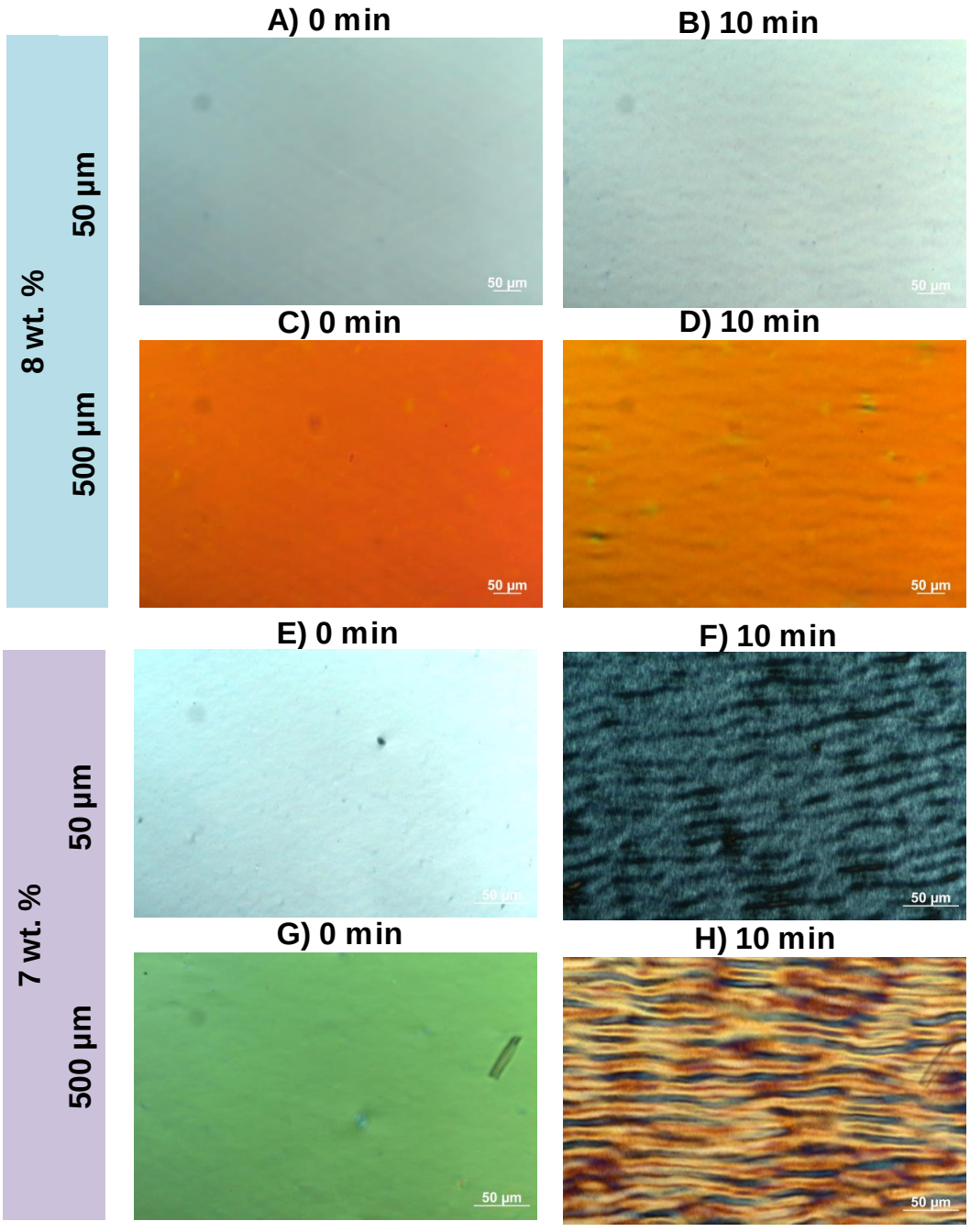

Figure 5.3. Cross-polarized transmitted light microscopic images showing the relaxation texture of A) - D) 8 wt. % (5.14 vol. %) and E) - H) 7 wt. % (4.5 vol. %) CNC dispersions after shear cessation at 0 and 10 minutes.

In an effort to further understand the microstructural response of cholesteric dispersions, a modeling study of the relaxation dynamics of CNCs' after shear cessation

was performed, in collaboration with Dr. Micah Green's group (Texas A & M). To fundamentally understand the rheo-optic experimental results, a finite element analysis was conducted using COMSOL Multiphysics. The 3D model developed by Green's group avoided the assumption of uniformity in the vorticity (normal to flow and shear) direction and allowed chiral microstructures to develop uninhibited throughout the entire system. This is in contrast to previous models that were simplified to two dimensions and restricted complex helical formations. The local representation of the microstructure was captured in the second moment of an orientation distribution function, expressed as the second order traceless tensor **Q**. Important dimensionless numbers including the ratio of inertial to elastic forces (Ericksen number) and short-range interactions to long-range elasticity (energetic dimensionless parameter) were considered to define **Q**. The microstructure relaxation with varying chiral strength and gap was investigated which provided new insight from homeotropic to planar ordering. **Figure 5.4** illustrates the 3-D simulated mesh showing the cholesteric microstructure of CNC after relaxation based on $\mathbf{Q_{22}}$ component. Here, x, y, and z are the flow, vorticity, and shear directions. As in the experiments, banded textures were also observed perpendicular to the flow direction in the simulation. The terms R, θ, and U are associated with concentration, chirality, and elastic constants of the system. From the time lapse, the real time optical contrast was also measured during relaxation to investigate the reorientation from a flow aligned state. Experimental findings complemented by simulation helped to understand the processing window to dry the flow aligned CNC and retain the microstructures.

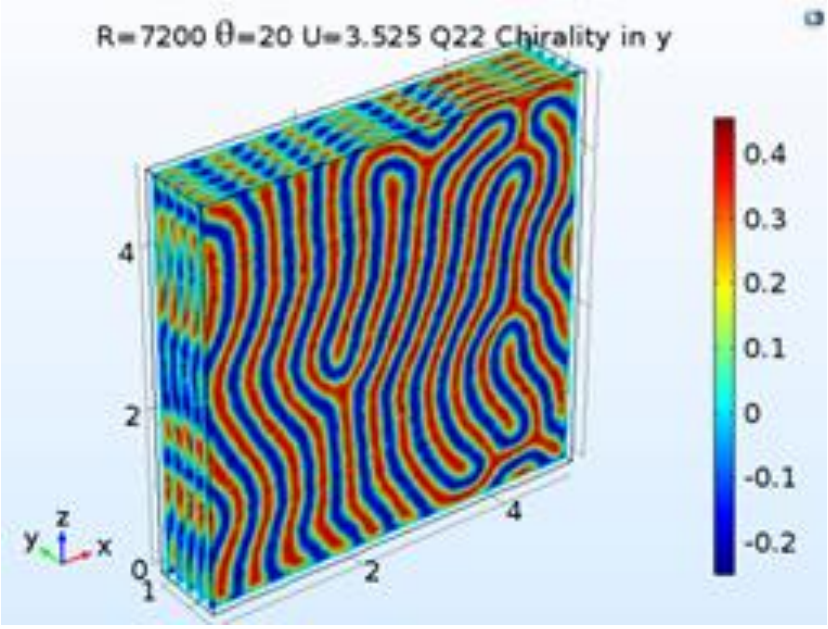

Figure 5.4. 3-D simulation based on finite element analysis showing cholesteric microstructure at equilibrium. x, y, and z are the flow, vorticity, and shear directions. R, θ, and U are parameters associated with concentration, chirality, and elastic constants of the system.

5.2.2 Directionally aligned CNC films for MEMS fabrication

Figure 5.5A shows a typical cholesteric fingerprint texture in a film produced from a 6.5 wt. % (4.2 vol. %) biphasic aqueous CNC dispersion by drop casting without applied shear. Achieving a more uniform director requires unwinding the pitch to form a nematic microstructure and solidifying the microstructure before it can relax back to a cholesteric state. **Figure 5.5B** shows the microstructure of a film produced from an 8.9 wt. % (5.6 vol. %) fully cholesteric dispersion which was sheared at 1000 s^{-1} and dried under ambient conditions. The cholesteric texture was absent, but the presence of multiple colors in this film of uniform thickness indicates a polydomain microstructure with only local ordering. Furthermore, the colloidal forces (*i.e.*, capillary stress) experienced during drying[258]

resulted in crack formation. Using a lower concentration and shear rate alleviated cracking, but a periodically banded polydomain structure formed during drying (**Figure 5.5C**). Band structures are associated with long range undulation of the director orientation[259] during relaxation as discussed before for rheo-optical experiments (**Figures 5.1 and 5.2**). The undulation can also be a result of contraction strain of sheared sample induced by stress relaxation after flow cessation[260]. This issue was resolved by faster drying right after shear at an elevated temperature of 80 °C followed by 24 hours desiccation to further insure the films were completely dry. The more uniform color of the resulting film shown in **Figure 5.5D** indicates that this method resulted in macroscopically uniform alignment. Scanning electron microscopy of the film's cross section (**Figure 5.5E**) showed that the alignment was uniaxial near the free surface, but a more chiral structure existed near the substrate. This type of structure has been attributed to the early glass transition at the liquid-vapor interface. Vitrified surface regimes help the retention of shear induced alignment of CNCs near the film's free surface, but further into the bulk, the sample remains still in liquid crystalline state[11]. This favors a dramatic decrease in transport of water to surface facilitating more time for the shear induced rods to relax back due to chiral forces waiting close to the substrate.

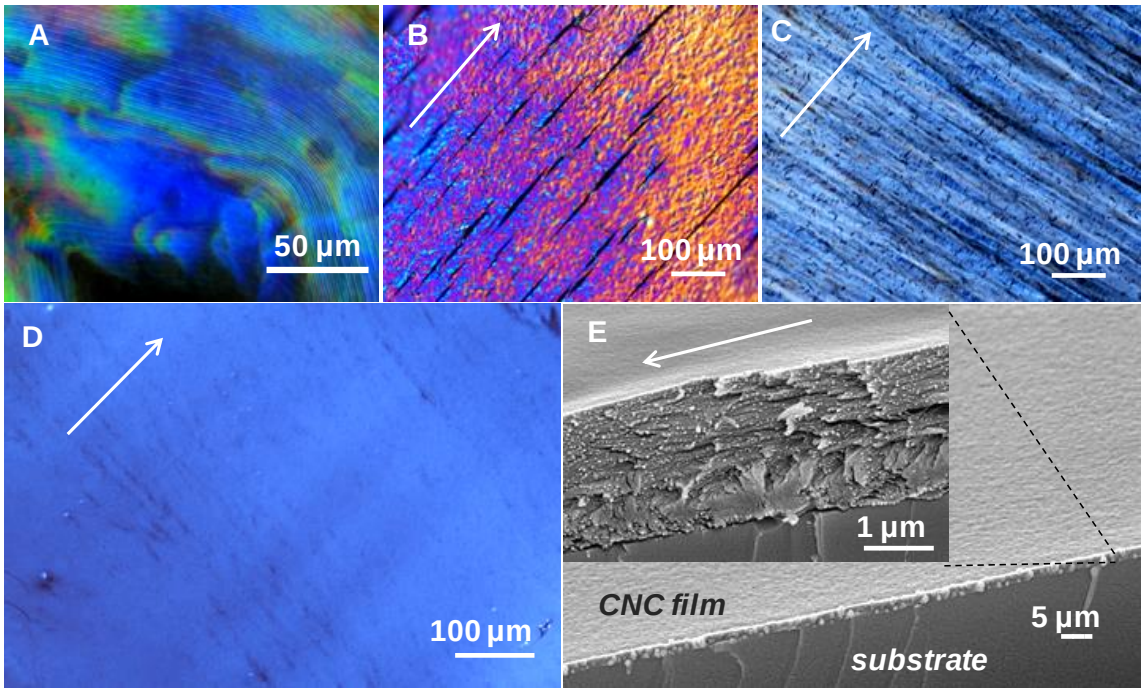

Figure 5.5. Cellulose Nanocrystal (CNC) Films. Transmitted cross-polarized and scanning electron microscopic images of dried CNC films produced from aqueous dispersions. Arrows indicate shear direction. A) The signature cholesteric texture in film cast without shear from 6.5 wt. % (4.2 vol. %) CNC. B) Crack formation along the shear direction in a film made using 8.9 wt. % (5.6 vol. %) CNC and a 1000 s^{-1} shear rate. C) The absence of cracking in the film made using 6.5 wt. % CNC and a 100 s^{-1} shear rate. D) The crack free aligned film obtained using the same process of C followed drying at 80 °C for 20 minutes followed by desiccation. E) SEM micrograph of the cross section of D, the inset shows the better uniaxial alignment of CNCs at the drying surface compared to near the substrate.

5.2.2.1 Microfabrication of CNC MEMS

The method resulting in the films shown in **Figures 5.5D** and **E** was used to make 2 and 4 µm thick CNC films (average roughness 6.34 nm, Figure A15) onto a patterned photoresist layer on a substrate. For convenience, a 100 mm diameter Si (100) wafer was used as the substrate, but a wide range of substrates are possible. The pattern on a spin coated photoresist film was created using a photo mask (Figure A16) that was designed to shape the anchor layer of the MEMS devices using Layout Systems for Individuals (LASI). The

device pattern included over 10,000 devices as shown in **Figure 5.6A**. Design of the device pattern was developed and optimized based on initial trial and error in the microfabrication[213] and material properties obtained by nanoindentation and tensile testing of similarly prepared CNC films. **Figures 5.6B - G** show the evolution of CNC MEMS devices through a lithography process, starting with a shear dried CNC film (**Figure 5.6B**) on a patterned positive photoresist (AZP4620) layer on a silicon wafer. As the aqueous CNC dispersion repels hydrophobic photoresist pattern, capacitive nitrogen plasma with optimized power and time of 90 watts and 1 minute, was applied to reduce the photoresists' static water contact angle from 53˚ to 17˚, promoting the anchoring of the CNC film to the substrate. By Physical Vapor Deposition (Ebeam-PVD) a 10 nm titanium layer was deposited on the CNC film; this changed the reflected color under cross-polarized reflected light (**Figure 5.6C**). The thin layer of titanium enhanced the next photoresist layer adhesion onto CNC film (Figure A17) as the traditional hexamethyl disilizane (HMDS) does not work as the adhesion promoter. Besides, 10 nm thick Ti/TiO_2 layer facilitates the CNC film not to disintegrate in an aqueous developer solution after patterning the second photoresist layer. **Figure 5.6D** shows the cured structural profile of MSTs after spin coating, drying, UV exposure, development of the second photoresist layer. Next, the parts of the CNC film which were not masked by the second photoresist layer were plasma etched using an inductively coupled plasma (ICP) based advanced oxide etcher (STS-AOE). In this step, to get anisotropic etching in addition to coil power, a platen power at the substrate was used[261]. That resulted in smooth side walls and precise feature size of 6 microns (lowest). To prevent the micro-crack formation and photoresist rounding problem, short plasma cycle of 20 seconds with low plasma pressure of 20 mTorr was applied. During etching

CF_4 plasma (20 sccm) was used to etch the titanium layer followed by etching of CNC film by O_2 plasma (40 sccm). **Figure 5.6E** shows the same MSTs after etching with residual photoresist on top of and beneath it. Next, the residual and anchor photoresist layers were removed by acetone wash followed by isopropyl alcohol (IPA) rinse to release and clean the devices as shown in **Figure 5.6F**; submerged devices in IPA. To overcome the surface stiction associated with micrometer feature and substrate[262] and obtain dry and ultraclean surface, CO_2 critical point drying was applied as the post release drying step (**Figure 5.6G**).

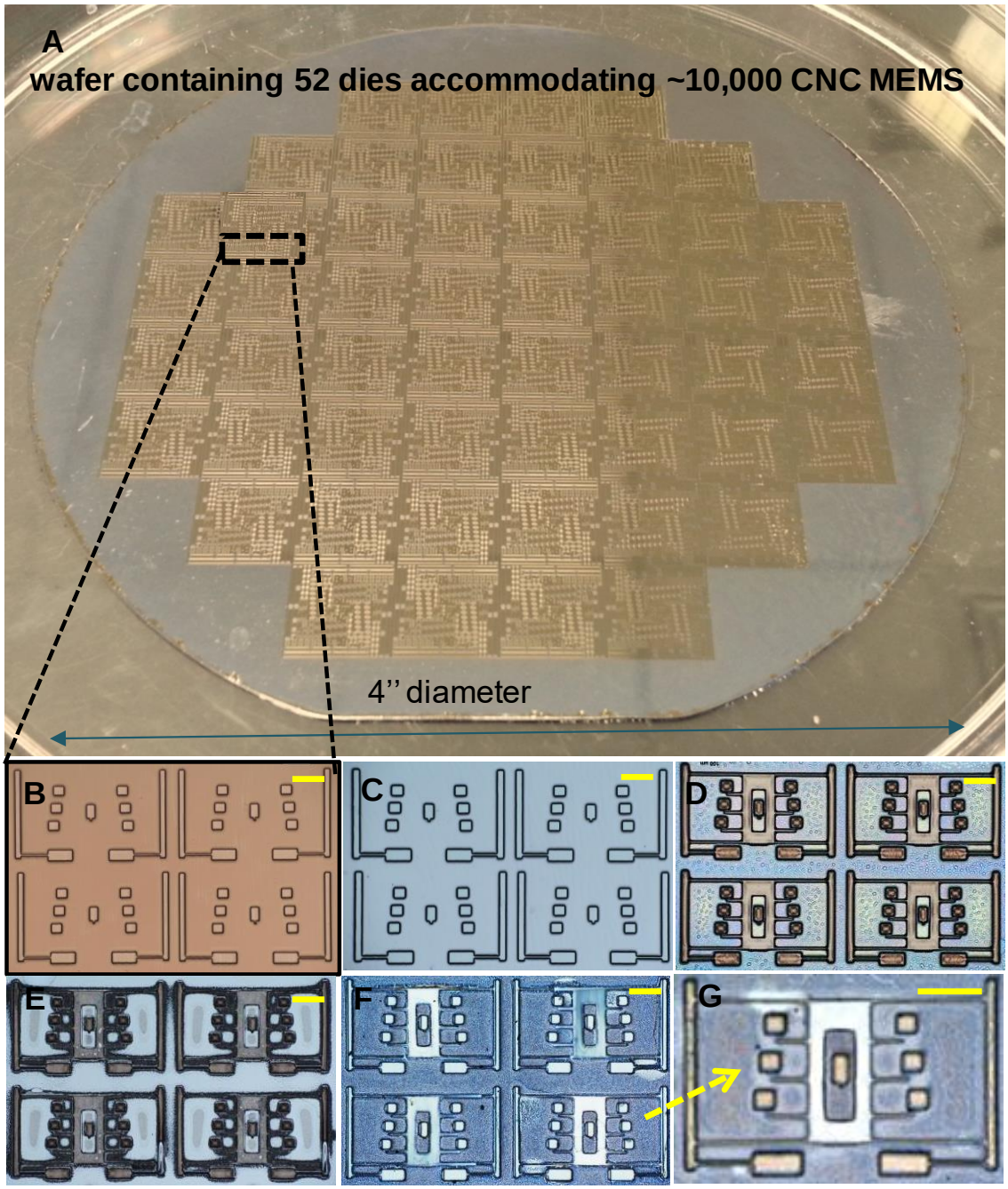

Figure 5.6. Photograph and cross-polarized reflected light optical microscopy images showing the whole substrate and steps involved in photolithographic fabrication scheme for CNC MEMS. A) A 4″ diameter wafer substrate with shear dried CNC film onto the photoresist CNC MEMS pattern on it. B) Shear aligned and dried CNC film on a patterned photoresist layer using a Si substrate. C) The same CNC film of A) after E-beam deposition of 10 nm thick Ti/TiO_2 layer. D) After creating the device pattern using a second photoresist layer achieved by photoresist coating, drying, UV exposure through an aligned

mask, and developing. E) Etched out device profiles after using inductively coupled plasma etching, white and black areas indicate the etched film and the residual photoresist on the device patterns respectively. F) Released devices after washing off the residual photoresist layers using acetone followed by IPA rinsing. G) The higher magnification image of a released MST after critical point drying. Scale bars are 100 µm.

5.2.2.2 Results

In addition to the released and dried MST (**Figure 5.6G**), the fabrication resulted in freestanding actuatable cantilever beam arrays (CBAs), doubly clamped beam arrays (DCBs), and residual stress testers (RSTs). These devices are standard tools for measuring the mechanical properties in MEMS devices. **Figure 5.7A** shows representative interferograms obtained by phase shifting interferometry (PSI) which were used to determine the height profiles of suspended beams in the CBAs. **Figure 5.7B** shows a DCB; this type of device was used for elastic modulus determination. **Figures 5.7C** and **D** show a functioning RST before and after the release; the 1.65° counter clockwise rotation after release indicates the device was freestanding and capable of detecting the compressive residual stress in the aligned CNC film.

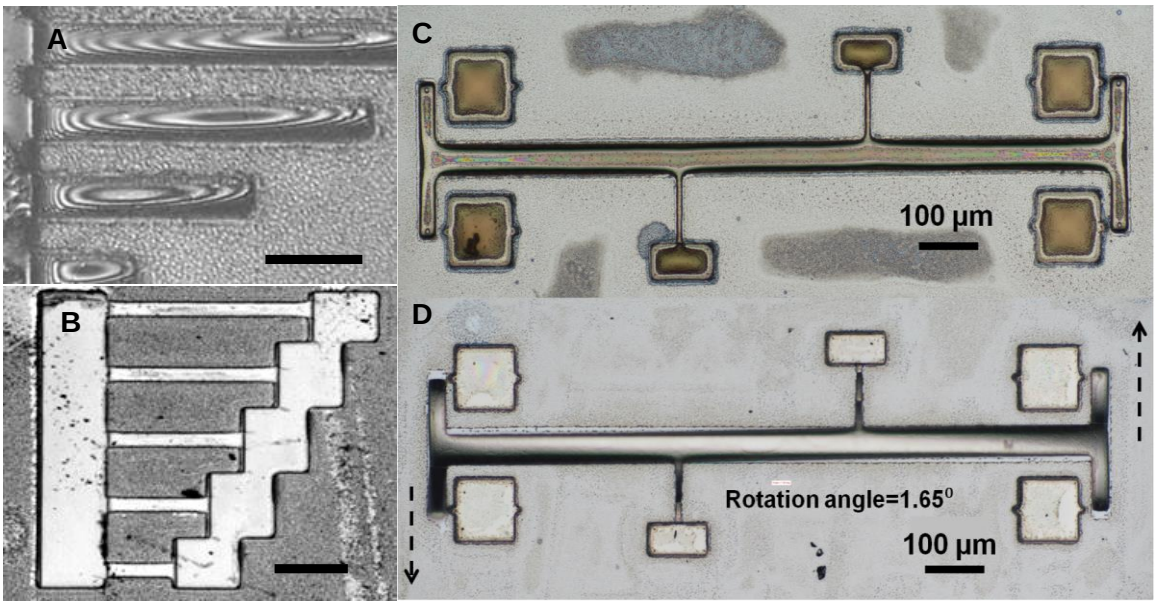

Figure 5.7. Representative micrographs of freestanding CNC MEMS after release. A) Interferograms on a cantilever beam array (CBA). B) A doubly clamped beam (DCB) array with 30 µm wide beams with lengths ranging from 100–300 µm. C) An optical micrograph showing a residual stress tester (RST) with a 300 µm distance between supporting beams connected to I-shaped beam before release. D) The same RST after release; the counterclockwise rotation is due to the compressive residual stress in the structural CNC film and indicates the device was functional and freestanding. Scale bars are 100 µm.

All these functional devices including released MSTs (shown in **Figure 5.6F**) were later used for obtaining different micromechanical properties such as elastic modulus, residual stress, fracture strength, and for electrostatic actuation. The reflected optical microscopy images in **Figure 5.8** show the effects of thickness and shear alignment on the anisotropic stress gradient in suspended cantilever beams. When the CNC were aligned parallel to long axis of the beam they exhibited significantly less curvature than when they were oriented perpendicular to the long axis. This effect was more pronounced for the 2 µm thick beams (**Figure 5.8A** and **C**) than the 4 µm beams (**Figure 5.8B** and **D**). Similarly, DCBs exhibited less curvature when CNC was aligned parallel to the beam's long axis than

aligned perpendicular to the long axis. The increased compressive (buckles upward) stress gradient caused cracking in the latter case as shown in **Figure 5.8E** and **F**. These results demonstrate that producing MEMS from liquid crystalline CNC dispersions enables creating devices with anisotropic mechanical properties, e.g., parallel/transverse elastic modulus/ compliance affecting the creep or stress relaxation[263] in devices. These directional mechanical properties can easily be tailored as a function of device thickness and the direction of applied shear. Such readily tunable anisotropic mechanical properties may not be achieved in traditional silicon and/or polymer MEMS. In addition, controlling the thickness and CNC orientation also enables tailoring device optical properties. **Figure 5.9** shows that the birefringence induced interference colors of the film/devices under cross-polarized light could be changed from blue to yellow by changing the film thickness from 2 to 4 μm. These birefringent induced tunable optical properties may create new opportunities for all pass optical filters, wavelength selective adaptive optics and phase modulators in liquid crystal MEMS technology[264,265,266].

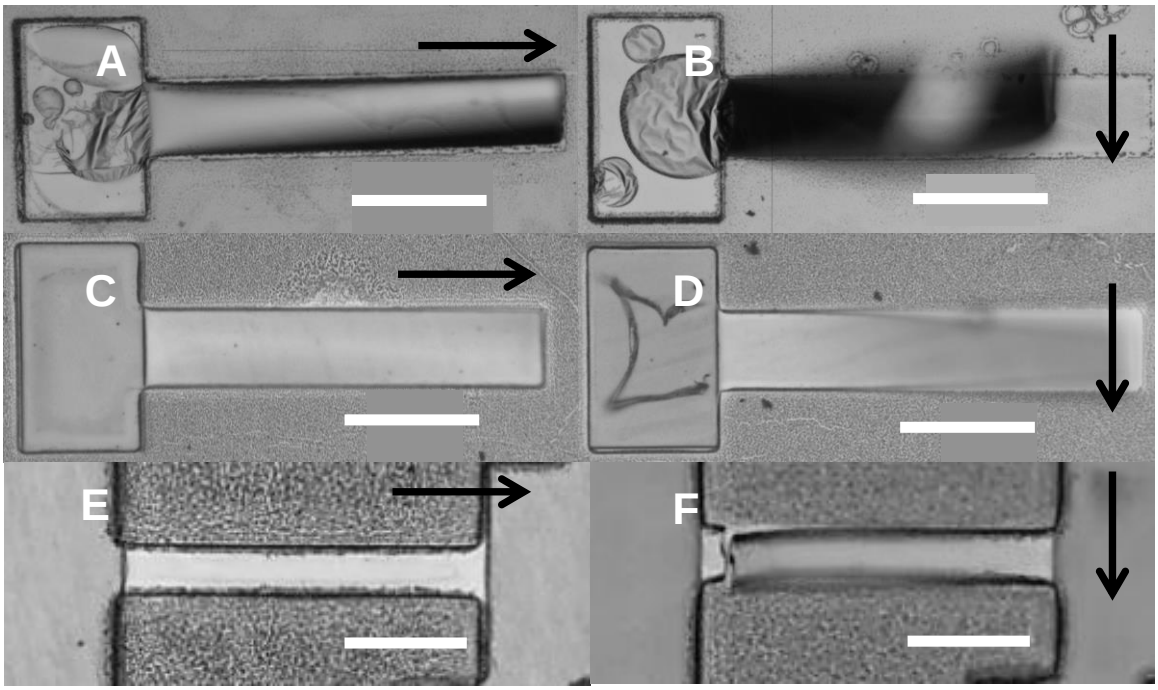

Figure 5.8. Reflected light microscopic images showing the effect of the stress gradient developed in 300 μm long CNC cantilevers and doubly clamped beams (DCBs). Arrows indicate the shear alignment direction. A) The parallel CNC alignment on 2 μm thick beam showing stress induced deflection. B) Perpendicular CNC alignment on a 2 μm thick beam, the image distortion is due to the downward beam curvature and curling of the end. C) Parallel CNC alignment on 4 μm thick beam. D) Perpendicular CNC alignment on a 4 μm thick beam. E) and F) Doubly clamped 4 μm thick, 300 μm long beams with parallel CNCs' alignment resulted in intact beams, but perpendicular CNC alignment resulted in cracking of 300 μm long beams. Scale bars are 100 μm.

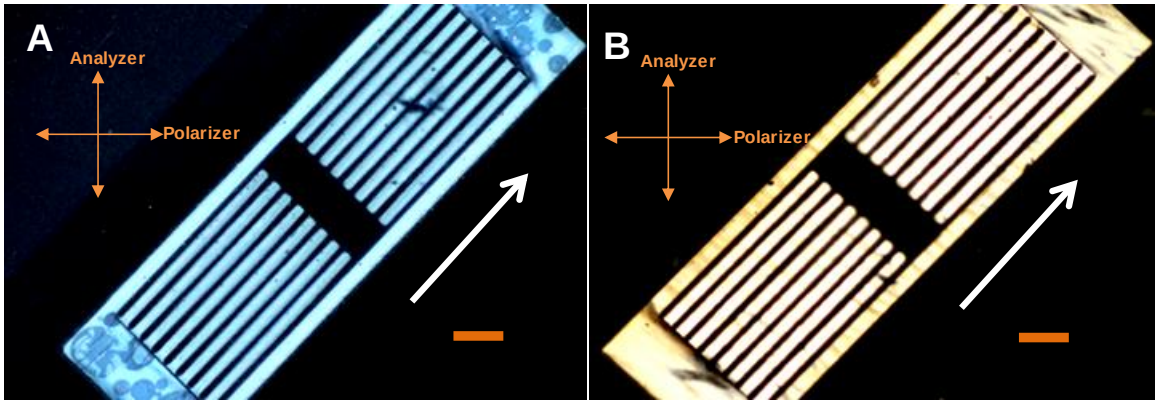

Figure 5.9. Cross-polarized reflected light microscopy images showing tunable optical properties in CNC cantilever arrays resulting from birefringence. Arrows indicate the applied shear direction A) 2 μm thick devices and B) 4 μm thick devices. Uniform colors, A) blue and B) yellow at 45° stage rotation, indicate alignment of CNC along beam long

axis. Dark spots are due to local orientation of domains in a slightly different direction. Scale bars are 50 μm.

Phase shifting interferometry (PSI) was used to determine the suspended and actuated CBAs height profiles (Figure A18). The PSI based height profile of a 300 μm long cantilever shows the freestanding microstructure with a downward arc like curvature confirming the compressive stress gradient after release. However, when sputter coating with gold plasma was done (for SEM) on the cantilevers, nature of the height profile changed (upward arc, tensile stress gradient, Figure A19) which is attributed to stress relaxation. Nevertheless, the compressive residual stresses developed in the 2 μm and 4 μm thick devices were found to be 276 ± 7 kPa and 41 ± 6 kPa respectively (for LPCVD polysilicon film 295 - 420 MPa[267]) based on the microscopically measured angle of rotation of the released RSTs (Figure A20).

Based on the linear elastic beam bending theory for DCBs, the elastic modulus of CNC MEMS was derived using point load beam bending by nanoindentation[268,269]. The longer DCBs were more compliant with the compressive stress gradient resulting in more buckling (Figure A21). Therefore, only 100 μm long DCBs were studied for nanoindentation to obtain the initial linear region of the load versus deflection curve. The slope (μN/μm) obtained from the linear region was used to determine the elastic moduli of DCBs as shown in **Figure 5.10A**; The elastic moduli obtained for both 2 and 4 μm DCBs are shown in **Table 5.1**.

Table 5.1. Tabulated micromechanical properties for CNC MEMS devices (shear alignment along long directions). Column 2, elastic modulus based on indentation was derived for 100 µm long DCBs. Column 3, residual stress was derived for RSTs with 300 µm distance between supporting beam arms. Column 4, fracture strength was derived for MST with 60 µm long and 6 µm width fracture beams. Notation; w (width), t (thickness), m (slope of force versus deflection curve), θ (angle of rotation), d (distance between supporting beams), δ_f (distance traveled by shuttle to fracture), L_c (distance between shuttle and corresponding anchored stopper). Uncertainty limits are based on maximum errors.

Micromechanical properties of CNC-MEMS	**Elastic Modulus E (GPa)**	**Residual Stress σ_R (kPa)**	**Fracture Strength σ_f (GPa)**
Equations used for calculations	$I = \frac{wt^3}{12}$ $E = \frac{mL^3}{192I}$	$\sigma_R = \frac{E\theta d}{2}$	$\sigma_f = \frac{3Ew\delta_f}{2L_c^2}$
2 µm thick devices	64 ± 44 (parallel) 17± 1.3 (perpendicular)	276 ± 7	Did not fracture
4 µm thick devices	51 ± 33 (parallel) 25 ± 8.9 (perpendicular)	41 ± 6	1.1 ± 0.3

The thickness and width of the DCBs were measured using both SEM and optical microscopy. The elastic modulus was calculated in both parallel and perpendicularly aligned CNC film to the long axis of the DCBs. Both 2 µm and 4 µm thick devices (100 µm length, 50 µm wide) were tested from eight different wafers. **Figure 5.10B** illustrates the calculated elastic modulus revealing the anisotropic mechanical property of the CNC DCBs. DCBs with parallel alignment of CNC showed higher modulus (64 ± 44 GPa and 51 ± 33 GPa for 2 and 4 µm respectively) than the perpendicular ones (17 ± 1.3 GPa and 25 ± 8.9 GPa for 2 and 4 µm respectively). The anisotropic ratios for 2 µm and 4 µm devices were 4 and 2, respectively. Though this high elastic modulus was never reported before in aligned CNC film, the anisotropic ratio is in agreement with some previous tensile testing data of thicker film (40 - 50 µm) reported by Reising *et al.* and Passantino *et al.*[103,199]. Interestingly, the 2 µm thick DCBs exhibited higher elastic modulus than 4 µm

ones in the parallel alignment case, where the perpendicular ones showed opposite trend. This behavior is attributed to the order parameter variation through the thickness of the shear aligned CNC film. Retention of shear induced alignment gets more challenging with a higher wet thickness of colloidal dispersions, and that may explain this higher mechanical property exhibited by the thinner films. **Figure 5.10C** shows the MST actuation graph for 4μm thick device showing the fracture distance of 4.82 μm for 60 μm long fracture beams on the suspended shuttle (Figure A22) while the shuttle was pushed against the stopping posts using incremental DC voltage to a piezo assisted micromanipulator. The initial low x-displacement of the shuttle (up to 10 volt) is attributed to improper contact of the probe tip with the shuttle at the initial position. Based on the distance traveled by the shuttle in *x*-direction before suspended beam fractures, the fracture strength of the actuated MSTs was 1.1 ± 0.3 GPa (for polysilicon 2.6 ± 0.4 GPa[270]). The MSTs made from 2 μm thick films were more flexible. Hence, the suspended beams did not fracture even at the maximum shuttle displacement possible for this reported design of the structure. Next, the gold sputter coated CBA actuation pad was subjected to a DC voltage while the silicon substrate was electrically grounded. Due to the buildup of capacitive charge upon applied voltage, freestanding cantilevers deflected towards the substrate as the voltage was increased (**Figure 5.10D**). The buildup of electrostatic force pulls the free end of the CBA while the elastic force restores the initial position. This shows that intrinsically dielectric CNC microstructures can even be electrically actuated by depositing a thin conductive layer of sputtered metal.

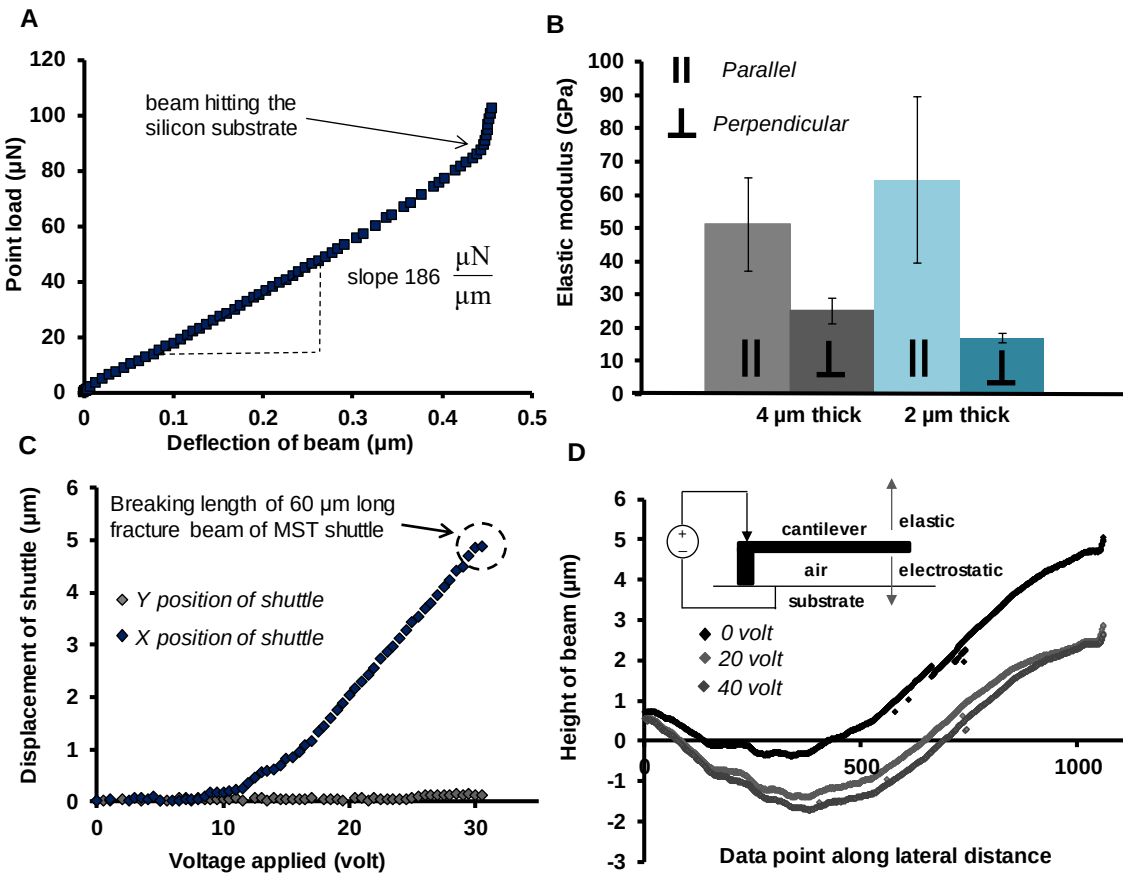

Figure 5.10. Micromechanical property analysis of CNC MEMS devices. A) Load versus deflection curve of 100 µm long, 30 µm wide and 2 µm thick DCB showing deflection distance until hits the substrate, triangle shows the selected linear region used to extract the slope needed for elastic modulus calculation following linear elastic beam theory, B) Elastic modulus of 2 µm and 4 µm thick CNC DCBs showing anisotropic mechanical properties in both parallel and perpendicular alignment direction of nanomaterials to the beams' long axis (error bars are based on standard deviation), C) Change in **X** and **Y** position of MST shuttle (4 µm thick) during mechanical actuation upon applied voltage on an open loop piezo assisted micromanipulator, the suspended shuttle was pushed towards **X** direction until 60 µm long fracture beams on both sides fractured giving the breaking length for fracture strength calculation, and D) deflection profiles of gold sputter coated CNC cantilever beam (500 µm long, 30 µm wide and 4 µm thick) due to electrostatic actuation by applying DC voltage.

5.3 Conclusions

In summary, a completely new material platform for MEMS based on CNC from woody biomass has been demonstrated and used to measure material properties of the CNC film itself. Conventional micron scale actuatable test structures have been fabricated from thin films of aligned CNC. Using those structures, an anisotropic elastic modulus (64 ± 44 GPa) that is not vastly different (*i.e.*, within an order of magnitude) from that of polycrystalline silicon[271] (164 ± 7 GPa) has been realized. Moreover, we observed that the fracture strength, stress gradient, and optical properties of the CNC film could be modulated using the CNC film processing conditions (*i.e.*, CNCs' aspect ratio and alignment), which is unlike any conventionally available MEMS materials in common use. It is known that film morphology is directly related to material properties, and we have demonstrated that the morphology of the CNC film can be exquisitely controlled. Therefore, the mechanical properties of the resulting CNC MEMS devices can be tailored to suit chosen applications. This finding may lead the way to a new paradigm in bioMEMS fabrication, for low cost and disposable POC devices based sensing for disease biomarkers[249,272].

Chapter 6 Surface Modification of CNC for Biosensing

6.1 Motivation

Recent advancements in microelectromechanical systems (MEMS) based approaches for detecting serum biomarkers have shown promising results including detection of alpha fetoproteins (AFP)[273-275], prostate specific antigens (PSA)[276-278], and carcinoembryonic antigens (CEA)[279-282] for liver, prostate, and ovarian cancer detection respectively[272]. Compared to current enzyme linked immunosorbent assays (ELISA) and fluorescence immunoassays for early stage detection, MEMS based detection may avoid the time consuming procedures, expensive instrumentation, and complicated separation and labeling steps inherent in these established methods[283-285]. Of the many types of MEMS devices, cantilever beam arrays (CBAs) are particularly promising for rapid, sensitive, and high throughput testing of multiple cancer biomarkers[284,286,287]. CBAs are extremely sensitive mass detectors; the beams can bend and undergo a change in resonance frequency as a result of the binding of biomarkers to antibodies adsorbed on the cantilever surface[272,288]. Traditional silicon-based CBAs are commercially available in many applications, but for biological testing, they suffer from limited surface tailorability, and low surface stress sensitivity (high stiffness). In addition, silicon MEMS require a rather complex, expensive, hazardous, and time consuming fabrication scheme[289-292]. In contrast, the cellulose nanocrystal (CNC) based MEMS devices (including CBAs) that have been developed in this research have much more readily controlled tailorable properties, can be produced in hours compared to days or weeks, and are fabricated using near ambient processing with relatively benign chemicals. The first successful demonstration of

functional CNC MEMS devices in this research motivated fabrication CNC MEMS-based biosensors for cancer biomarkers. The objective of this part of research was to investigate the surface chemistry of CNC to immobilize cancer specific antigens for potential application in multianalyte sensing in compared to the sensitivity and selectivity of the silicon MEMS reported in the literature on the liver, prostate, and ovarian cancer detection[293-295].

6.2 Surface Modification of CNC

Sulfuric acid hydrolysis of cellulose partially replaces the –OH groups with negative sulfate half esters ($-OSO_3^-$). Hence, rest of the surface –OH groups of CNC remain available for tunable surface chemistry. In this research, 3-aminopropyl-triethoxy silane (APTES) chemistry was used to modify the CNC surface followed by immobilization of glutaric anhydride (GA), an organo linker. The effect of silane chemistry was twofold. First, the APTES facilitated the hydrolytic stability of CNC in aqueous media which is essential for biosensing applications. Second, the $–NH_2$ functional groups attached to APTES provided the functional sites for the GA organo linkers which can eventually immobilize the antibodies. In general, the APTES reacts with an oxidized surface with free hydroxyls through S_N2 exchange by losing ethanol. The APTES monolayer formation on a substrate can be illustrated using three possible mechanisms as shown in **Figure 6.1**. According to mechanism 1, the surface attachment and condensation results in horizontal polymerization forming siloxanes with neighboring surface bonded APTES molecules. In vertical polymerization (mechanism 2), the surface bound APTES reacts with adjacent APTES molecules in the bulk solution.

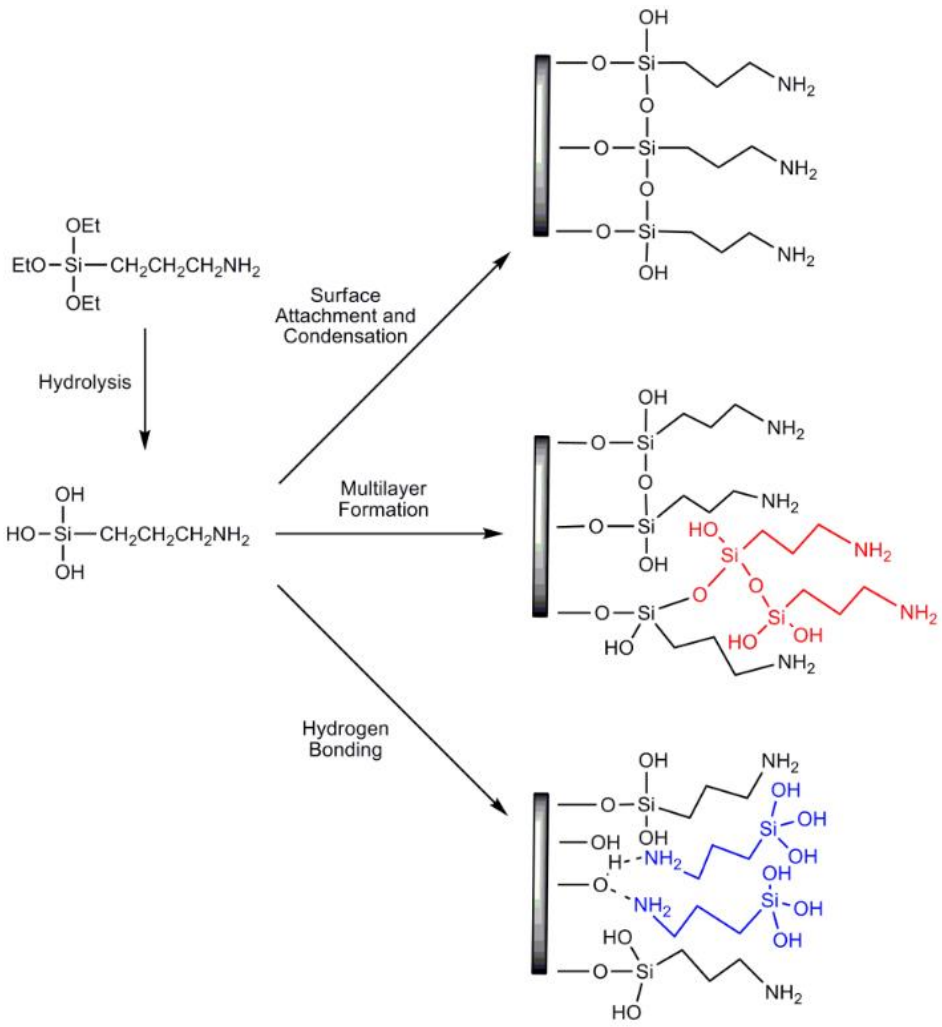

Figure 6.1. Different bonding modes of APTES on a substrate[296].

The third mechanism is the hydrogen bond formation in between –NH_2 of APTES molecules with surface –OH groups resulting in coexistence of neutral, protonated, and hydrogen bonded amines. The orientation and transformation of –NH_2 groups is a very complex process and depends on the type of substrates, solvents, and reaction conditions. For mechanism 1, the silanization is initiated *via* the hydrolysis of ethoxy terminal groups of APTES by either the moisture or water in solvents followed by condensation and polymerization near the substrate. In this study, ethanol was used as the solvent with a trace

amount of water as the catalyst. The reaction scheme that was used in this study is illustrated in **Figure 6.2**. The APTES modified CNC surface was submerged in 2 wt. % GA solution in DI water for 1 hour. The ring structure of GA opens in the presence of positive amine groups in ethanol-water mixtures forming amide bonds. The other end of the opened ring of GA contains another carbonyl group waiting for the primary amine of any antibody.

In the next step, the APTES and GA modified CNC were submerged in antibody solution in 1x phosphate buffer (PBS) at room temperature for 1 hour. After an hour, the CNC substrate was washed off using 1x PBS for three times and submerged in an antibody specific antigen solution in PBS for another hour at room temperature.

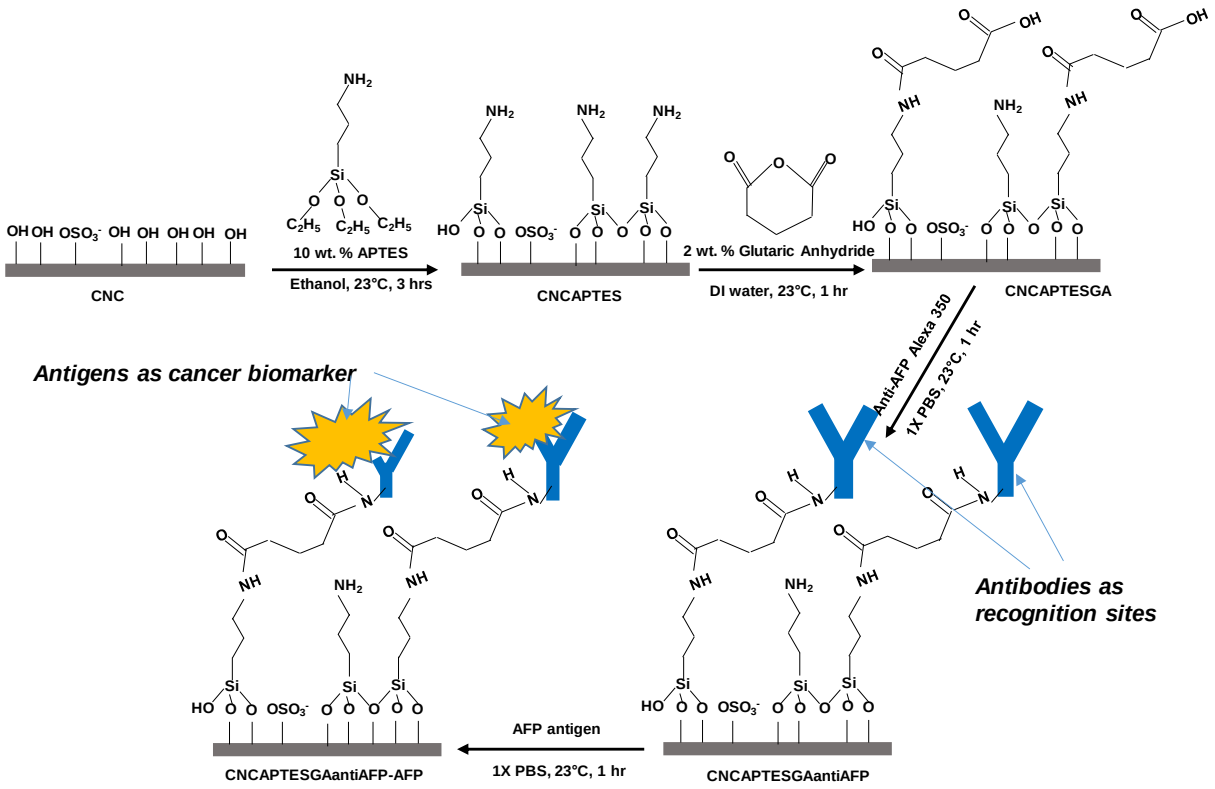

Figure 6.2. Schematic (*not according to scal*e) showing the expected APTES surface chemistry for antibody immobilization on CNC.

For the secondary immobilization of specific antibodies onto surface attached antigens/proteins, the same antibody incubation step was repeated in PBS solution. Both fluid phase and dry film surface modification schemes were approached. For the functionalization of CNC dispersions prior to film fabrication, 8 g of 12 wt. % (7.8 vol.%) sulfonated CNC was taken in a glass vial and vortex mixed with 10 g of ethanol (95% ethanol, 5% 2-propanol). After vortex mixing, the mixture was kept inside the fume hood with the cap loose. Next, 1 mL of APTES (using micropipette) was slowly added to 10 mL of ethanol (95%) in a separate glass vial. Then the mixture of ethanol, water, and CNC stock dispersion were placed inside the three-neck round bottom flask as shown in **Figure 6.3**.

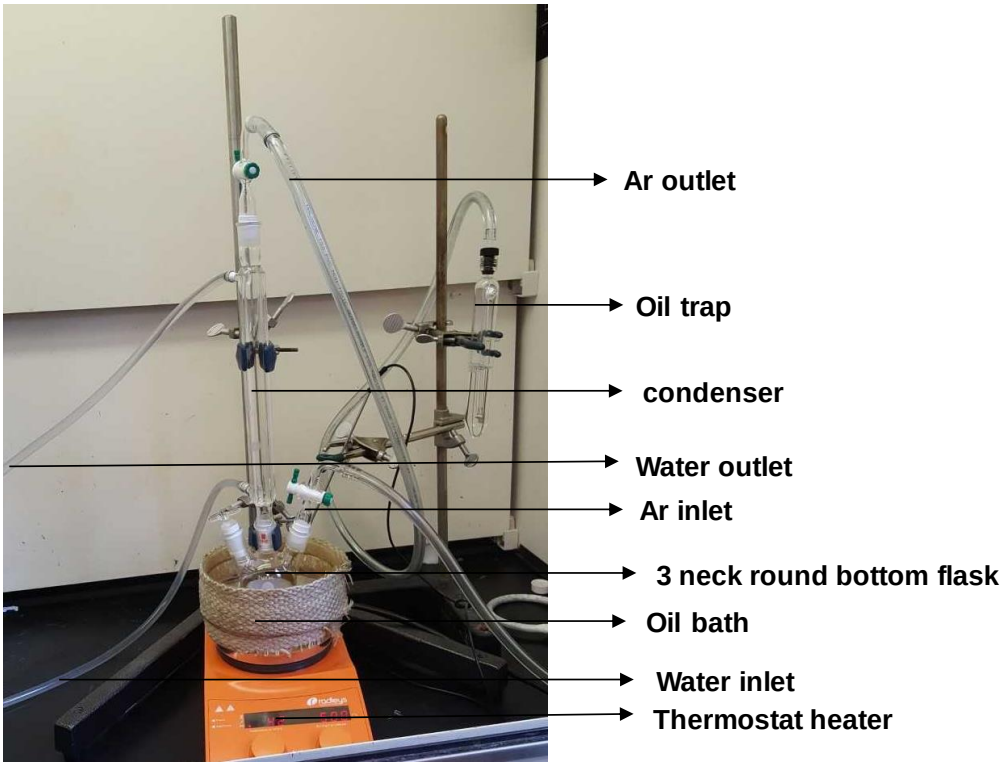

Figure 6.3. Picture showing the set up for fluid phase APTES modification of CNC dispersions.

A magnetic stirrer was placed inside the flask with the APTES and ethanol mixture. The flask was placed in an oil bath. The left neck of the flask was sealed with a glass stopcock. The middle neck was connected to the condenser. The right neck was connected to the argon gas flow outlet from the argon tank (flow should be minimum). The oil bath temperature was set at 50 ºC, and the thermal sensor probe was submerged into the oil. A magnetic stirrer was placed in the oil bath. The water flow to the condenser jacket was turned on while the temperature was raised. When the set temperature (50 ºC) was steady, the APTES in ethanol was slowly added using the left neck, and the reaction was allowed to take place for 1 hour. Then the dispersion was cooled down to room temperature and used for making sheared films.

For the post film surface modification, a range of different wt. % of APTES solutions were prepared (2 - 12 wt. %) in ethanol (95% ethanol, 5% 2-propanol). The initial water contact angles of the APTES modified films were obtained and compared with films from dispersion modified CNC. As the dispersion modified films showed excellent hydrolytic stability, the initial contact angle of that was taken as a benchmark for post film APTES modified films water contact angle. APTES ethanol solutions of different concentrations were used for different reaction times to obtain an initial water contact angle of 50°, which showed hydrolytic stability of hours in water as well. For APTES modification of the freestanding CNC cantilevers, APTES was mixed with ethanol followed by mixing on an orbital mixture for 15 minutes in a crystallization dish. A glass cover/glass Petri dish was used to cover the crystallizing dish while mixing. After 15 minutes, freestanding CNC films or CBA devices was fully submerged in ethanol APTES

solution and allowed to react at room temperature for 3 hours (keeping the glass cover on). After three hours, the APTES modified CNC cantilevers were transferred in a different crystallization dish filled with ethanol. Similarly, the APTES modified films were rinsed in ethanol for five minutes to remove all the unreacted silanes attached to the surface followed by air drying.

6.3 Results

6.3.1 Hydrolytic Stability of CNC films/CNC Cantilevers

As shown in **Figure 6.4**, the APTES modified CNC dispersion made films (**Fig. 6.4A**) remained intact after 2 hours of submersion in DI water while the regular CNC film (**Fig. 6.4B**) completely disintegrated.

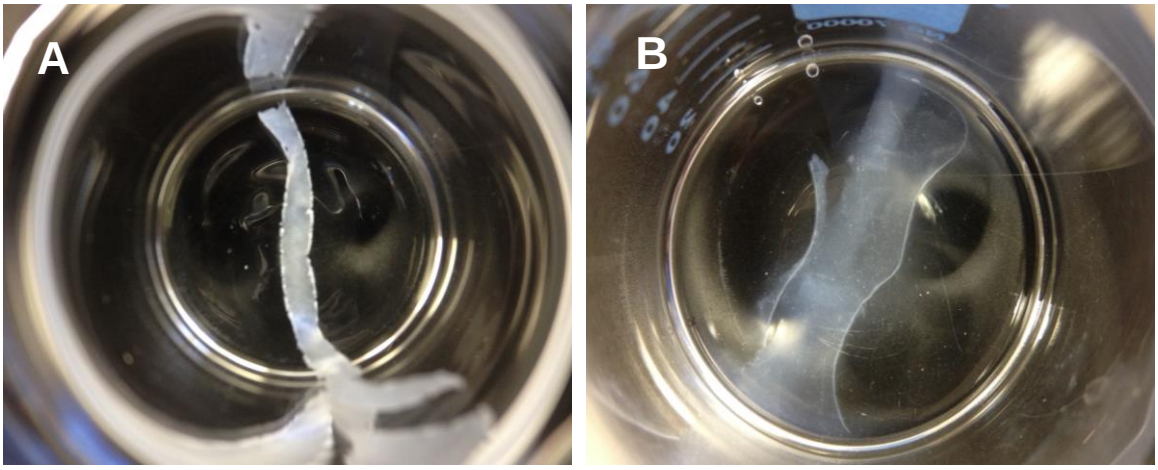

Figure 6.4. Photograph showing A) CNC film made from APTES modified dispersion and B) regular CNC film after two hours submersion in DI water.

The submersion test in water demonstrates that the APTES functionalization significantly improved hydrolytic stability. However, due to the complexity of the dispersion silane chemistry including polymerization, APTES modified CNC tend to aggregate as shown in **Figure 6.5**. However, the shear aligned CNC films made from APTES modified dispersions do not crack during drying. Therefore, CNC dispersion modified with APTES can enable fluid phase functionalization prior to MEMS fabrication.

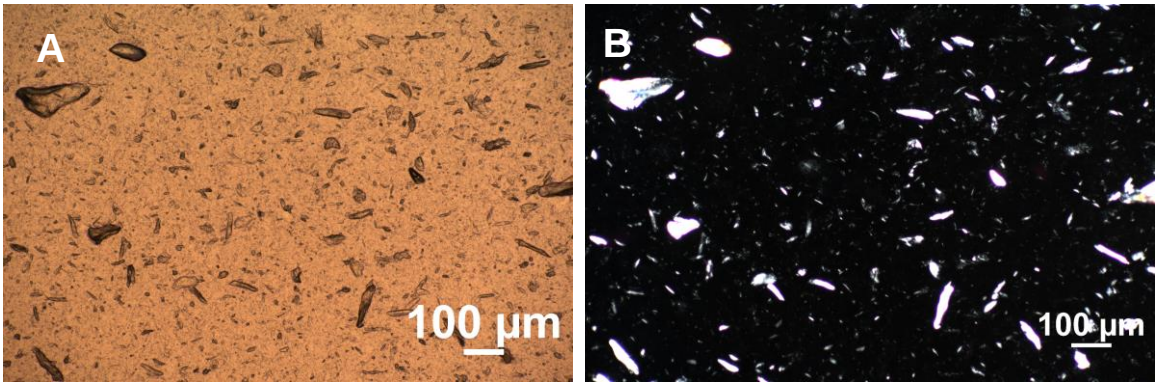

Figure 6.5. Cross-polarized A) reflected and B) transmitted light microscopic images showing sheared CNC film made from APTES modified dispersion.

These aggregates may not interfere with the uniformity of the sheared film needed for microfabrication, but the mechanical and optical anisotropy will be affected in contrast to regular CNC MEMS. More experiments for a range of CNC dispersions will need to be conducted to understand the effect of particle concentration on aggregates. Nevertheless, the post film APTES modification was also performed including fabricated devices. First, the initial water contact angle and its change over time was observed on the APTES dispersion modified films and compared with regular CNC films (**Figure 6.6A**). An initial water contact angle of about 50° was observed for the film shown in **Figure 6.4A**. Interestingly, an initial water contact angle of around 50 ° was also reported by Agarwal *et*

al., for silicon-based (Si_3N_4, SiO_2) cantilevers used for biosensing[297]. Hence, this water contact angle was considered a benchmark for the post film APTES modified films' initial water contact angles. It is essential that the films need to be hydrolytically stable. However, it is also essential not to make it truly hydrophobic (static water contact angle > 90°) since this would degrade the wetting property of the surface limiting the contacts and bindings with disease biomarkers in fluids. Therefore, the post film APTES functionalization was performed for 2 hours using different wt. % of APTES as shown in **Figure 6.6B**. Next, 10 wt. % APTES was taken as a baseline concentration to reach about 50° initial water contact angle and used for different reaction times for the surface modification. Based on the results shown in **6.6C**, a reaction time of 3 hours using 10 wt. % APTES in ethanol was finalized for post CNC films' surface modification at room temperature.

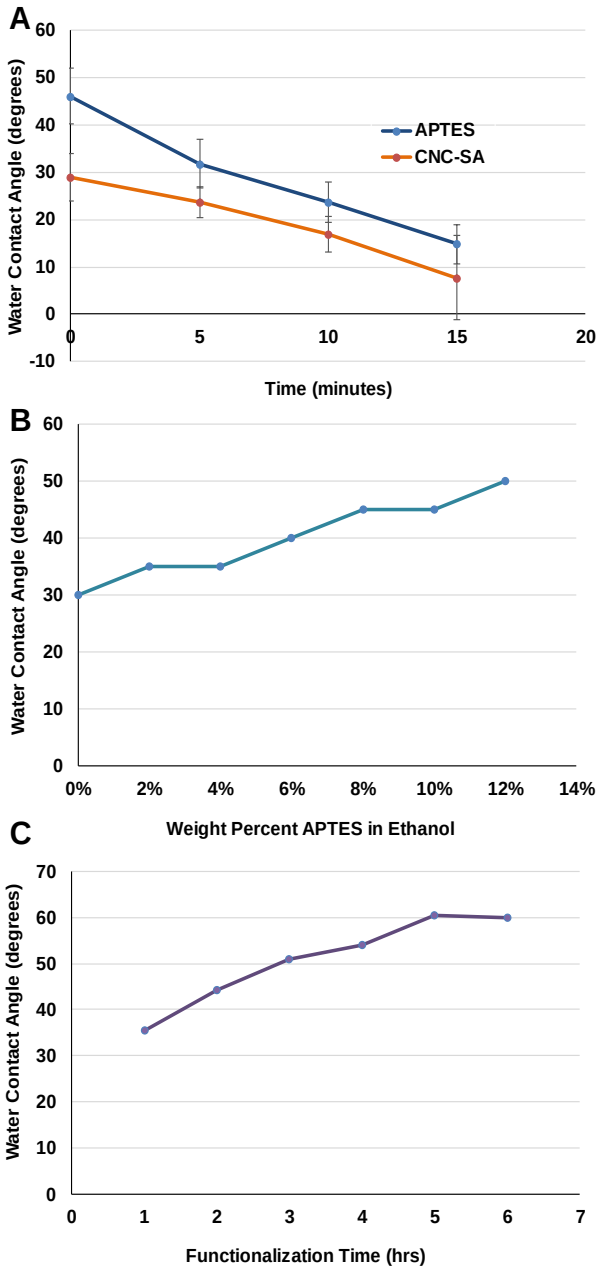

Figure 6.6. Graphs showing static water contact angles (WCA) on APTES modified CNC films. A) Water contact angle versus time for APTES modified CNC dispersion made films and regular CNC film, B) WCA after post film modification with varying APTES concentrations, and C) WCA of 10 wt.% APTES modified post CNC film with varying reaction time.

The same recipe of 10 wt. % APTES in ethanol for 3 hours of reaction time was applied to freestanding CNC MEMS. **Figure 6.7** shows the reflected optical microscopic image of a CNC CBA modified with APTES after fabrication. This array was modified in APTES ethanol followed by ethanol rinsing. Next, the array was submerged in DI water for 4 hours followed by air drying. All the cantilevers on the array were still intact as shown in **Figure 6.7**.

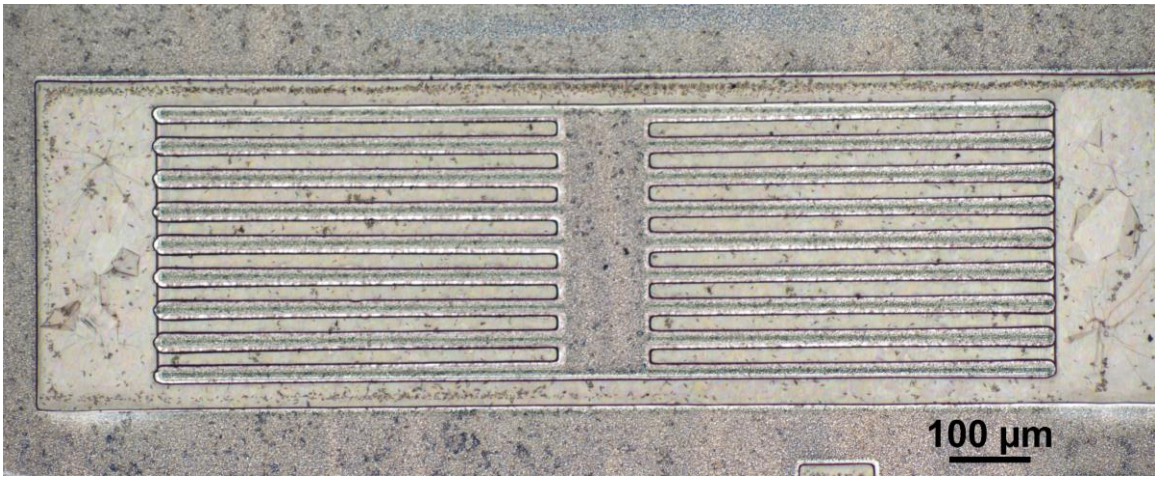

Figure 6.7. Reflected light optical microscopic image of APTES modified CNC CBA after submersion in water followed by air drying.

6.3.2 Immobilization of Primary Antibody on the APTES Modified CNC Films

The liver cancer biomarker or alpha fetoprotein (AFP) antigen was chosen for the initial immobilization effort because the results can be directly compared to other detection methods including those using silicon-based cantilever beam arrays[293,298,299]. The technique involves several steps. First, the APTES primary amine (-NH_2) was covalently modified with glutaric anhydride (GA) linker. In this reaction, one of the two GA carbonyl groups is expected to attach to the APTES –NH_2 group. Next, the AFP antibody was immobilized

by incubating the films/devices in a 0.8 μg/mL solution of AFP primary antibodies (conjugated with Alexa Fluor 488, mouse monoclonal to human IgG1, 70kDa) in 5 mL of PBS (1X, pH 7.2) for 1 hour at 22 ˚C. This step allowed the stable binding of anti AFP – NH_2 group to the remaining GA carbonyl group resulting in amide bond formation. Once the antibody was immobilized on the CNC-APTES-GA surface, the films/devices were immersed in an AFP antigen solution of 2.4 μg/mL in 5 mL PBS (1X, pH 7.2) for 1 hour at 22 ˚C. Surface and chemical characterization techniques were performed at each step of the process. Thermogravimetric analysis (up to 700 ˚C in air) indicated each step of surface modification for AFP immobilization on the APTES modified CNC films. As indicated by the thermograms in **Figure 6.8**, the pure CNC film had a steady pyrolysis (degradation starts at 260 ˚C continues up to 460 ˚C) and a residual ash content (residual mass at 700 ˚C) of 2.0 wt. %. After APTES modification, the onset of the degradation was increased to 340 ˚C. Also, the presence of functional groups caused the pyrolysis to have two distinct steps, and the ash content was 15 wt. % due to the presence of silicon. After the GA, anti AFP, and AFP antigen immobilization, pyrolysis occurred in three steps due to the thermal degradation of the biomolecules. Additional studies are needed to know if the high ash content for CNC-APTES-GA compared to the other samples is meaningful. However, as expected, the CNC film with anti-AFP showed same thermograms before and after the AFP antigen detection. Interestingly, the residual mass was found higher after the AFP antigen detection (by 5 wt. %) as shown in **Figure 6.8** (light blue compared to green).

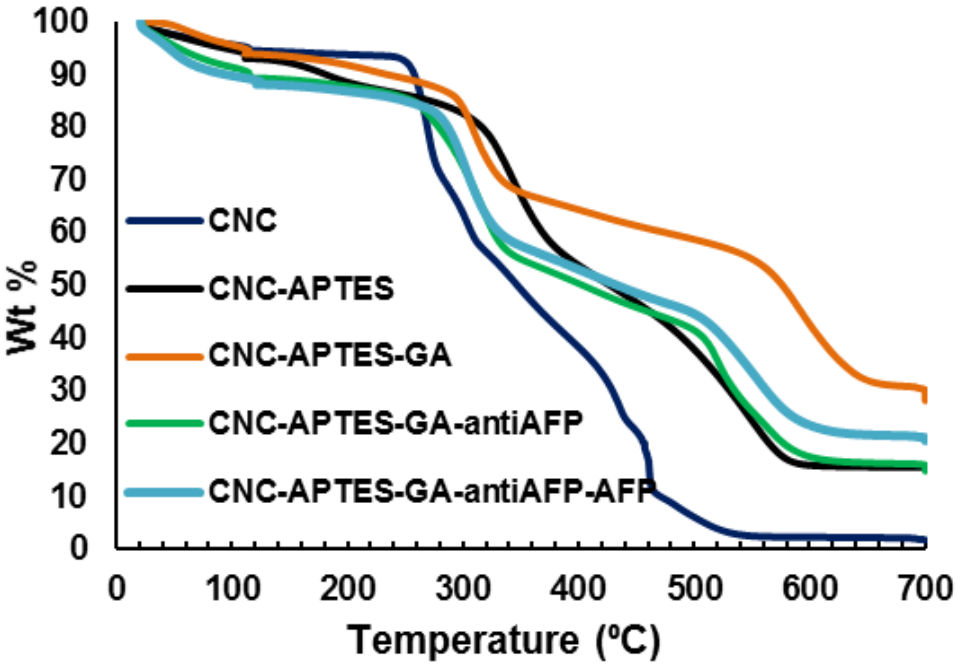

Figure 6.8. Thermograms showing thermal degradation of CNC films in the air with increasing temperature after surface modification steps using APTES (black line), APTES-GA (orange line), APTES-GA-antiAFP (green line), and APTES-GA-antiAFP-AFP (light blue line).

As the TGA analysis provided the preliminary evidence of surface immobilization, Fourier Transform Infrared Spectroscopy (FTIR) was used to further verify each attachment step (**Figure 6.9**). The initial CNC film showed a broad –OH stretch (3200 - 3600 cm^{-1}) as shown in **Figure 6.9** (dark blue). APTES functionalization (orange) resulted in the appearance of a peak corresponding to –N-H bond stretch (primary amine of organosilane). In the next step of the process, the amide bond formation of GA with the –N-H (black) resulted in this peak nearly flattening out. GA immobilization was confirmed by the presence of aldehyde (1650 - 1710 cm^{-1}) and amide peaks (1630 - 1697 cm^{-1}). After anti-AFP covalent attachment, the –N-H broad peak was recovered (green) indicating successful immobilization of the AFP antibody on CNC-APTES-GA surface. After

exposure to the AFP antigen solution, the –N-H stretch peak became sharper (3300 - 3500 cm^{-1}) which may be associated with proteins' primary amine (red).

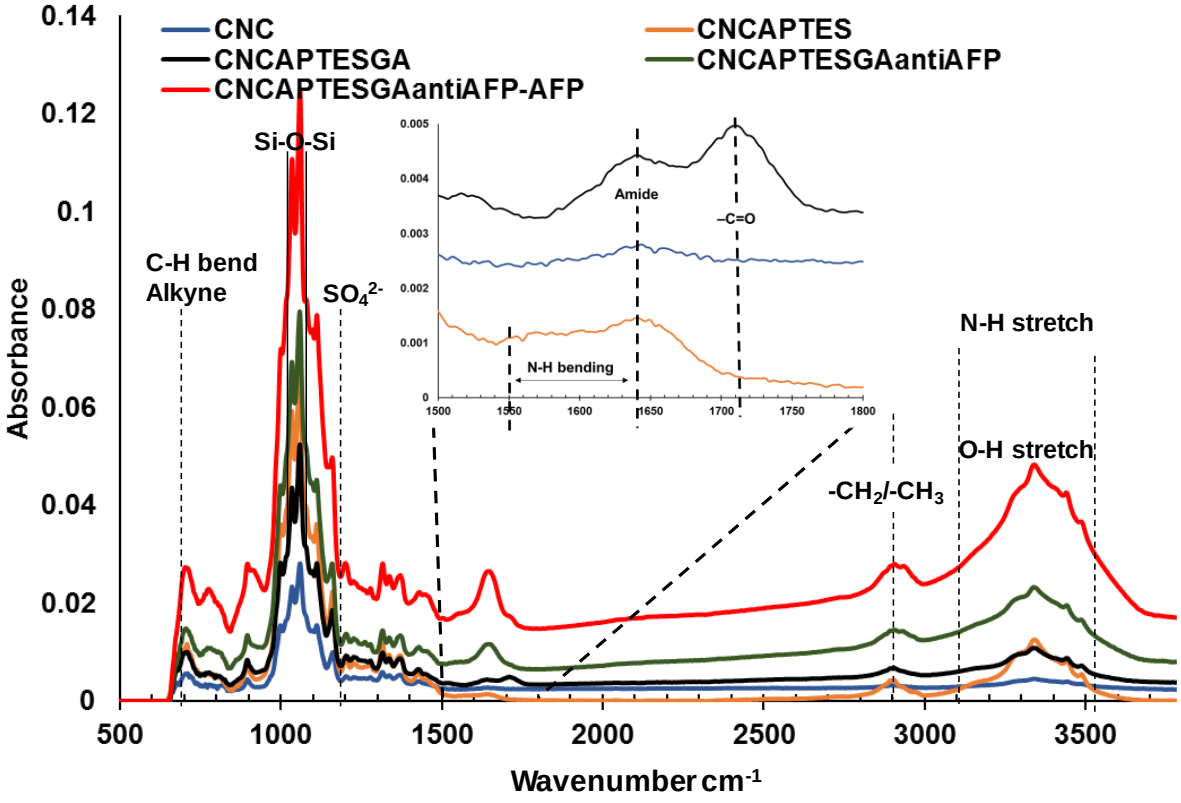

Figure 6.9. FTIR spectra showing different absorbance peaks associated with each step of surface modification of CNC films using APTES, GA, anti-AFP, and AFP antigens.

Atomic force microscopy (AFM) was used to visualize the changes in the surface resulting from each step (**Figure 6.10**). After each step of surface modification, the roughness average (R_a, roughness parameter) was obtained from the AFM height scans. The roughness average for CNC, CNC-APTES, CNC-APTES-GA, CNC-APTES-GA-antiAFP, and CNC-APTES-GA-antiAFP-AFP surfaces were 0.8, 2.3, 1.1, 0.43, and 7.1 nm, respectively. The drastic change of surface roughness after immersion in an AFP solution also suggests successful immobilization of AFP antigen (**Figure 6.10**).

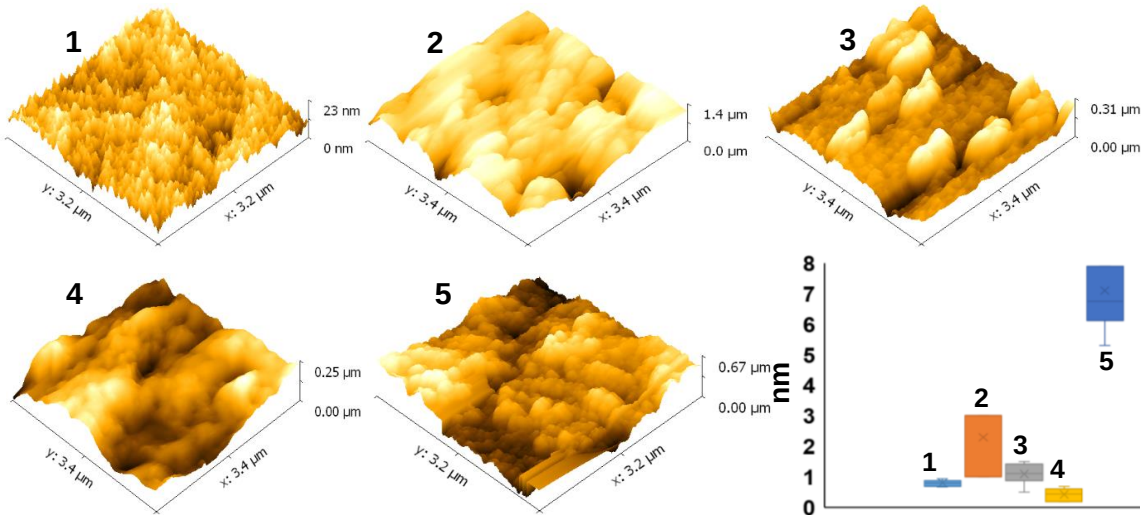

Figure 6.10. AFM height images (3D) and corresponding roughness averages after surface modification of CNC films.

Figure 6.11 A, **B**, and **C** show the fluorescence microscopy images on the anti-AFP (tagged with Alexa 350) immobilized CNC-APTES-GA film surface under 4,6-diamidino-2-phenylindole (DAPI), fluorescein isothiocyanate (FITC), and tetramethylrhodamine (TRITC) filters. The excitation and emission wavelengths for Alexa 350 fluorophores are 350 nm and 440 nm respectively. The range of emission and excitation for DAPI filter is 350 - 460 nm. Therefore, the blue fluorescence of Alexa 350 would only be visible under the DAPI filter. The uniform blue fluorescence of **Figure 6.11A** and no fluorescence on **Figures 6.11B** and **C** confirm the successful immobilization of the Alexa 350 tagged AFP antibodies on the surface modified CNC film with APTES-GA. No background fluorescence was observed under any of these three filters for CNC, CNC-APTES, and CNC-APTES-GA modified films.

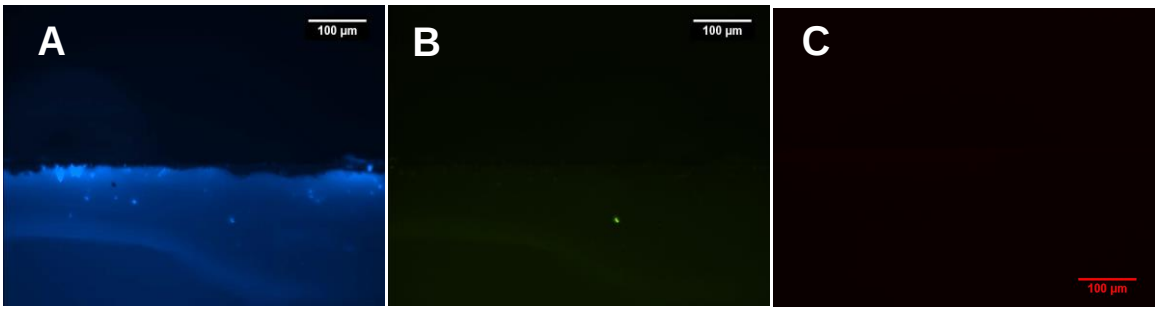

Figure 6.11. Fluorescence optical microscopic images showing the presence of Alexa 350 (blue fluorophore) tagged with AFP antibody attached to CNC-APTES-GA surface under A) DAPI, B) FITC, and C) TRITC filters.

Similarly, the same surface modification strategy was applied for immobilization of the two other cancer specific antibodies: prostate cancer specific antibodies (PSA) and ovarian cancer specific carcino embryonic antibodies (CEA). PSA and CEA antibodies were tagged with two different fluorophores, Alexa 488 (excitation 488 nm and emission 520 nm) and Alexa 555 (excitation 555 nm and emission 570 nm) respectively. The range of emission and excitation for FITC and TRITC filters are 475 - 545 nm and 517 - 605 nm respectively. Therefore, PSA and CEA antibodies tagged with green and red fluorophores were only observed under FITC and TRITC filters respectively as shown in **Figure 6.12B** and **F**. This confirms the successful immobilization of all the proposed cancer specific biomarkers on the surface modified CNC films using the same surface chemistry of APTES-GA.

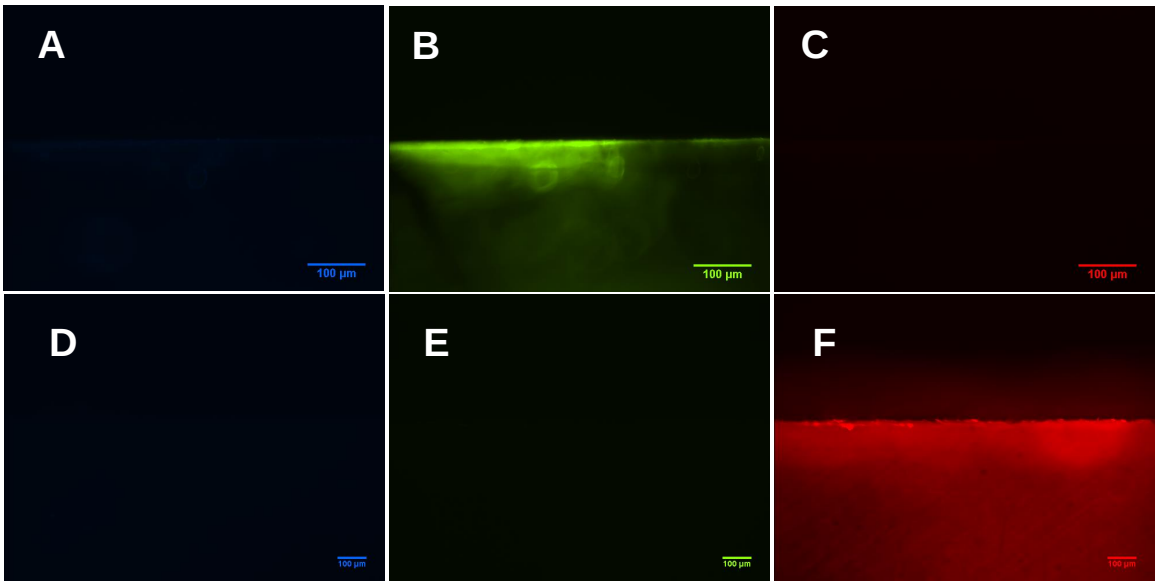

Figure 6.12. Fluorescence optical microscopic images showing the presence of Alexa 488 (green fluorophore) and Alexa 555 (red fluorophore) tagged with PSA and CEA antibodies respectively, attached to CNC-APTES-GA surface under A), D) DAPI, B), E) FITC, and C), F) TRITC filters.

6.3.3 Antigen Detection on the Antibody Immobilized CNC APTES-GA Films

After the successful immobilization of cancer specific primary antibodies on the surface modified CNC, films were exposed to antigen solutions to obtain antibody/antigen binding. AFP, PSA, and CEA antigen solutions of 2.4 µg/mL, 1.6 µg/mL, and 1.9 µg/mL concentrations (in 5 mL PBS) were used to incubate the corresponding antibody attached films at room temperature for 1 hour. To investigate the antigen attachment, a film area of approximately 20 mm x 20 mm was chosen for the surface modification and immobilization tests followed by fluorescence imaging. For each antibody, two identical films were prepared to do the analysis. One film (control) was imaged right after the antibody immobilization while the film was submerged in PBS. The same film was imaged after one hour submersion in PBS, and the average fluorescence intensities were compared

as shown in **Figure 6.13A**, **C**, and **E** for AFP, PSA, and CEA antibodies. These were considered as the control experiments. The other identical films were also imaged right after the antibody attachment and after 1 hour submersion in corresponding antigen solutions. Next, the average fluorescence intensities were compared as shown in **Figure 6.13B**, **D**, and **F** for AFP, PSA, and CEA antigens respectively.

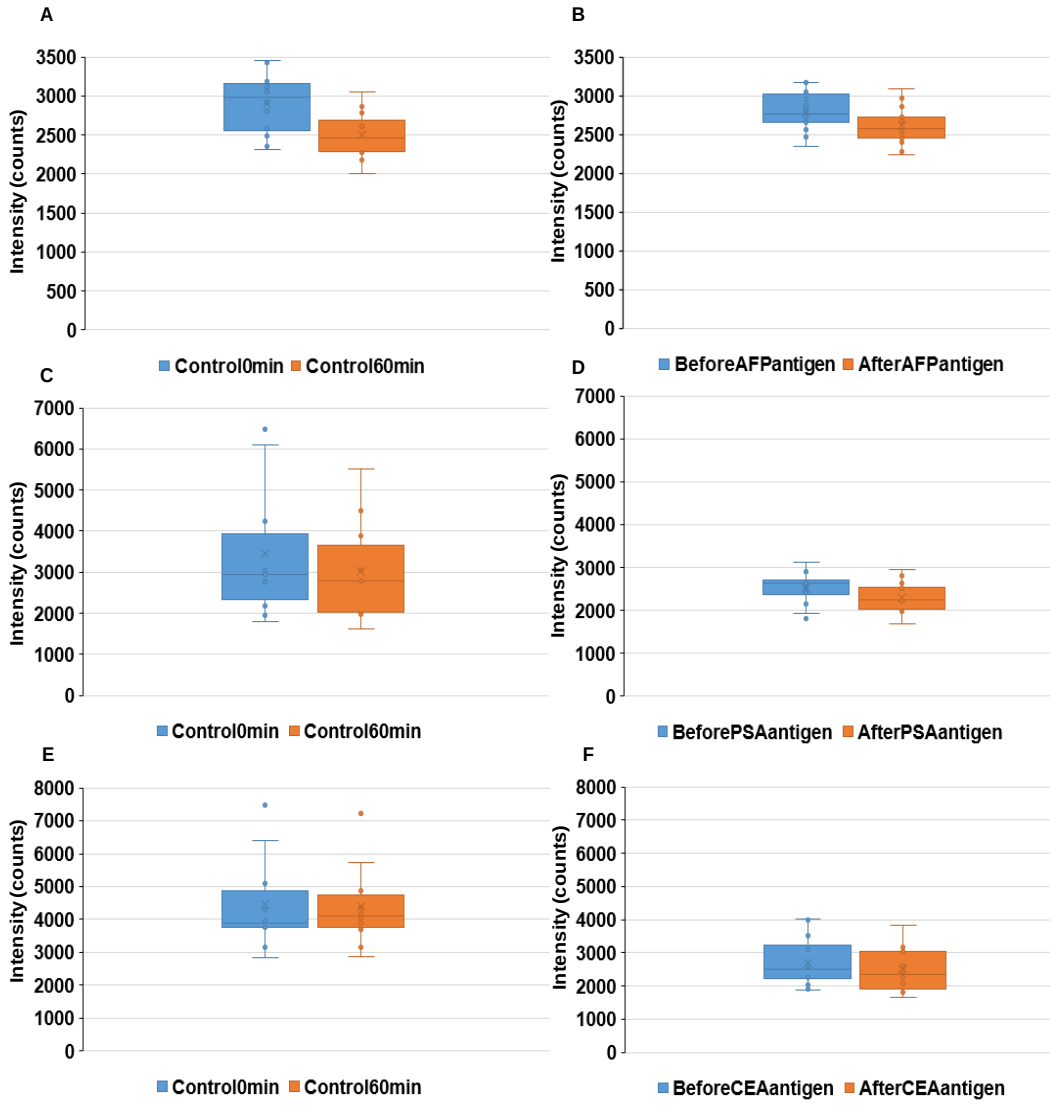

Figure 6.13. Graphs showing average intensity measured after control films fluorescence measurement for A) AFP, C) PSA, and E) CEA antibodies and after positive experiments in presence of corresponding antigen solutions of B) AFP, D) PSA, and C) CEA.

The box and whisker plots illustrated in **Figure 6.13** show the change of average intensities along with the distribution of the measured intensities across the film (16 measurements on each film). The box shows the range between 25^{th} and 75^{th} percentile and the bottom and top bars indicate the 5^{th} and 95^{th} percentiles respectively. Any measurement below or beyond this range is shown as an outlier. The mean and median values are denoted by the cross (x) and solid line respectively. Based on the observation, the decrease of average intensities was more significant in PBS as compared to the decrease in presence of antigens, especially for AFP and PSA. For CEA, the change was very negligible. This result was unexpected because more fluorescence quenching is typically expected in presence of antigen binding due to collision and non-fluorescent complex formation. In addition to fluorophore antigen interaction, other factors may also affect the quenching including antibody staining protocol, conformal dynamics of antibody immobilization on GA, different quantum yield and half-life of fluorophores molecules attached to the antibodies. Nevertheless, quenching effect with and without the presence of antigens need to be investigated with more experiments in future.

As the average intensity comparison with control films did not confirm antigen binding, the secondary attachment of antibodies to the antigens was also performed followed by fluorescence intensity measurements. **Figure 6.14** shows the results of control experiments; the measured average intensities for different antibody attached surfaces right after immobilization, after 1 hour submersion in PBS, and after 1 hour submersion in the same antibody solutions for AFP (**Figure 6.14A**), PSA (**Figure 6.14C**), and CEA (**Figure 6.14E**). Next, instead of PBS, the different antibody attached surfaces were exposed to corresponding antigen solutions followed by antibody exposures for the identical films of

CNC as shown in **Figure 6.14B**, **D**, and **F** for AFP, PSA, and CEA respectively. The side by side comparison of AFP control and AFP antigen (**Figure 6.14A and B**) showed a drastic change of average fluorescence intensity after the secondary immobilization of AFP antibodies on the attached AFP antigens compared to the secondary antibody exposure to the antibody attached surface in PBS. This confirms successful attachment of the AFP antigens on the modified CNC surface which provided more binding sites for the secondary AFP antibodies. The increase of average intensities after antigen attachment was also observed for PSA and CEA experiments (**Figure 6.14D and F**). Interestingly, a slight increase of average intensities was observed for the PSA and CEA control experiments (no antigen exposure, **Figure 6.14C and E**) as well; this is attributed to the attachment of secondary antibodies to the primarily unreacted functional groups of GA after the second exposure. Paired t test was performed to understand the significant change of intensities between control and positive experiments. The mean of differences of 15 fluorescence intensity measurements is and is not equal to zero were used as the null and alternative hypothesis for the tests. The probability values or p values were determined using 95% confidence interval (CI) limit. The p values associated with the second and third steps (PBS exposure followed by second antibody exposure) of the control experiments were 0.127, 0.747, and 0.064 for AFP, PSA, and CEA antibodies respectively. The p values associated with the second and third steps (antigen exposure followed by second antibody exposure) of the positive experiments were 0.005, 0.081, and 0.000 for AFP, PSA, and CEA antibodies respectively. These findings indicate significant change of average fluorescence intensities after the antigen immobilization compared to the PBS or control experiments.

However, the PSA associated p value were not equal or less than 0.05 within 95% CI. But, within 90% CI, PSA p value also indicated significant change of average intensities.

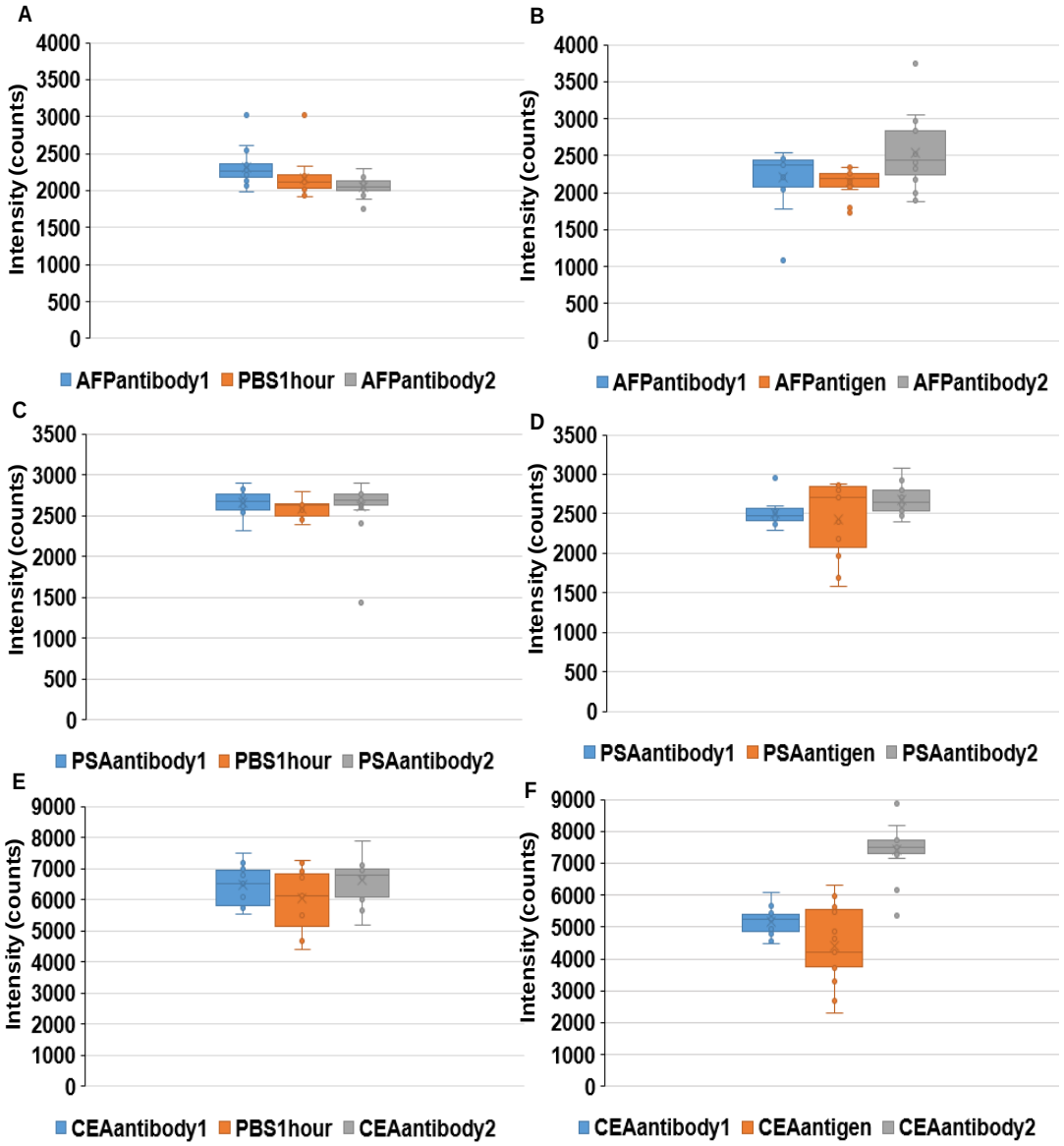

Figure 6.14. Graphs showing average intensity measured after control films fluorescence measurement for A) AFP, C) PSA, and E) CEA antibodies and after positive experiments in the presence of corresponding antigen solutions and secondary antibody exposures of B) AFP, D) PSA, and F) CEA antibodies.

6.3.4 Mass detection using cantilever beams array (CBA)

The proposed surface chemistry with APTES and GA can directly be applied to the array of CNC cantilevers. For quantitative detection of the adsorbed antigens' mass, the objective was to use the freestanding CNC cantilevers as the AFM tips before and after the biomarker exposure. The piezo-driven frequency sweep (50 - 500 kHz) on the cantilevers was applied to obtain the resonant frequency of vibration mode. The adsorbed mass of any cancer specific antigens would shift (decrease) the resonance frequency which can be correlated with the detected mass using the following equation:

$$f_R = \frac{1}{2\pi}\sqrt{\frac{k}{m^*}} \qquad 6.1$$

where f_R is the resonance frequency of the rectangular cantilever, k is the stiffness coefficient, and m^* is the effective mass of the cantilever. To test this proposed idea, the test wafers were diced into small pieces with freestanding cantilever arrays as shown in **Figure 6.15.**

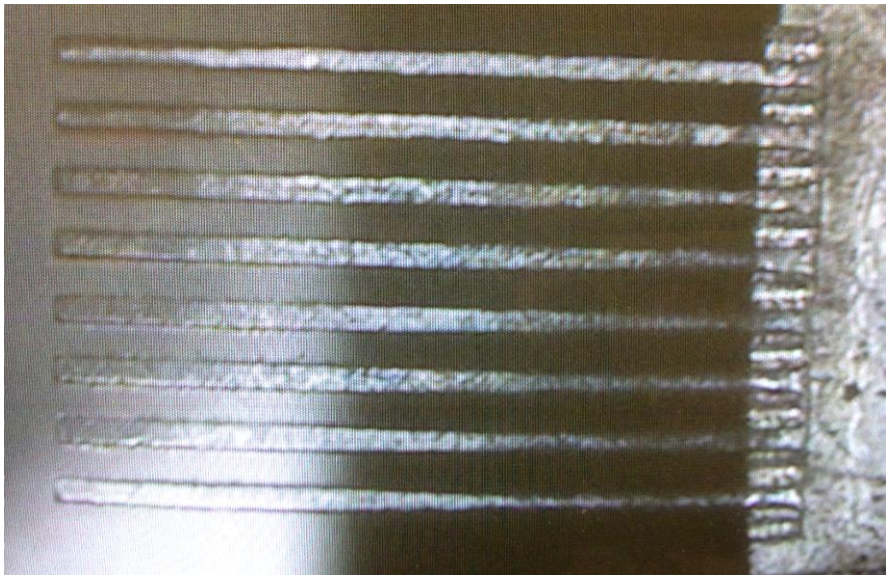

Figure 6.15. Photograph showing freestanding CNC cantilevers used as AFM tips. Beams are 500 μm long.

CNC cantilevers of different lengths were used as the AFM tips to investigate the resonance frequencies and compare them with the calculated frequencies based on the design parameters. Unfortunately, no singular peak showing consistent frequency behavior was observed as shown in **Figure 6.16**. The calculated resonant frequencies of 500 μm and 300 μm long CNC cantilevers were 7 kHz and 20 kHz respectively. However, the AFM based resonant frequencies of cantilevers with same lengths were 60 kHz and 312 kHz respectively (**Figure 6.16**). In addition, the resonance frequency was found to be sensitive to laser beam position and diameter, there were variations in day to day measurements. This variation could be attributed to poor reflectivity (CNC film is translucent) and the diffraction properties of semitransparent CNC films. More refinement with future experiments will be necessary to obtain consistent results for the quantification of antigens' mass using AFM based detection.

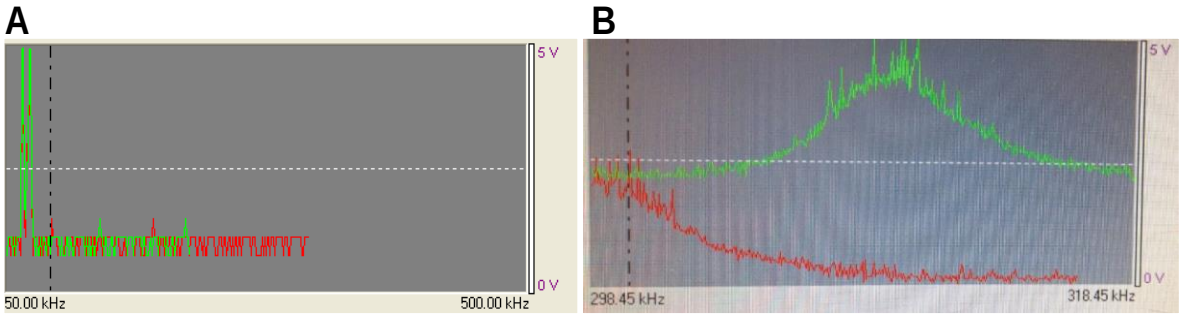

Figure 6.16. Resonance frequencies of A) 500 μm and B) 300 μm long CNC cantilevers.

In addition to an AFM based approach, the phase shifting interferometry (PSI) based height profiles were investigated on the surface modified CNC cantilevers. PSI scans were performed on the dried APTES-GA-antibody modified CNC beams; before and after the antigen exposure. As a proof of concept, the AFP antibody/antigen interaction was tested. Released and dried CNC cantilevers were modified with APTES and GA following the recipe used for fluorescence imaging. The only difference between regular CNC films and CNC cantilevers is the 10 nm titania (TiO_2) coating on the freestanding devices. However, since APTES silanization works with both hydroxyl and oxide groups, functionalization to the TiO_2 should be similar. The modified beams were exposed to 0.8 μg/mL AFP antibody solution in 5 mL PBS. Then it was rinsed in PBS and DI water, followed by air drying. Next, those beams were optically imaged and scanned with PSI to obtain the height profiles. Then the same beams were exposed to 2.4 μg/ml AFP antigen solution in 5 mL PBS followed by rinsing, drying, imaging, and additional PSI scanning. **Figure 6.17** shows the cross-polarized reflected light micrographs of the CNC cantilevers taken before and after the exposure of antigen solution. Though PBS rinsing was followed by DI water wash before drying, some salt crystals still formed on the top of the cantilevers

as shown in **Figure 6.17A** and **B**. However, the PSI height scans revealed a change of cantilever stress gradient before and after the antigen detection.

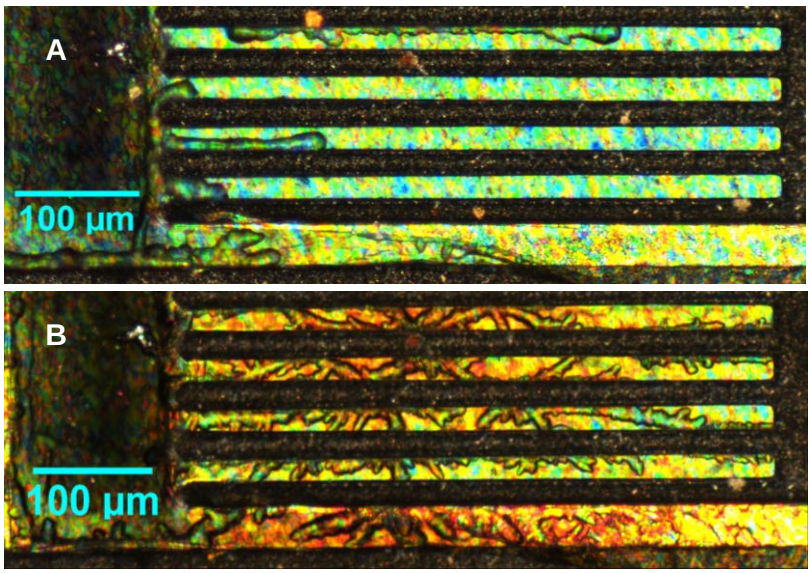

Figure 6.17. Cross-polarized reflected microscopy showing arrays of CNC cantilevers A) before and B) after the AFP antigen detection.

Figure 6.18 shows the PSI scan-based height profiles of the beams illustrated in **Figure 6.17**. The heights profiles of four APTES-GA-antiAFP modified CNC cantilevers were plotted before and after the AFP antigen exposure. As shown in **Figure 6.18**, the selected four beams on the array showed downward arc-like curvatures, indicating compressive stress gradients. However, after the AFP antigen exposure, the beams' curvatures changed to an upward-arc, indicating tensile stress gradients. This change of stress gradient can be associated with the detection of the antigens. However, the noisy profile of the surface modified beams in compared to regular CNC cantilever is attributed to not having an ultraclean substrate after series of surface modifications; this resulted in the poor nullification of the background interferograms limiting the scanning quality.

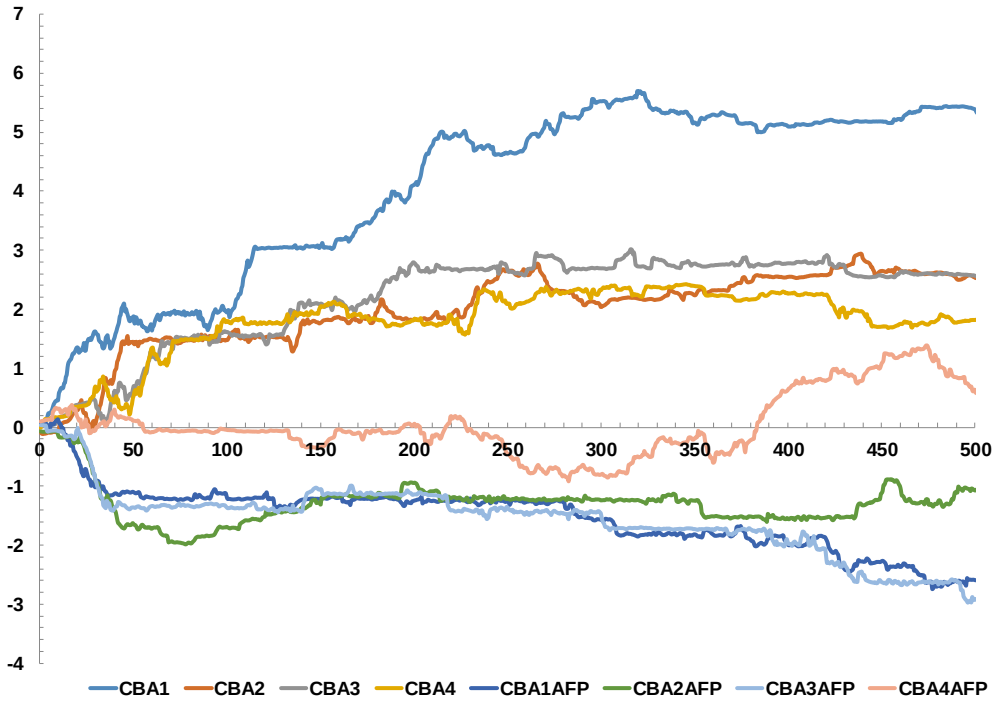

Figure 6.18. Plots showing PSI based height profiles of CNC cantilevers before (CBA1, 2, 3, 4) and after (CBA1, 2, 3,4AFP) the AFP antigen detection.

6.4 Conclusions

In this work, the tunable surface chemistry of CNC was investigated to immobilize cancer specific biomarkers. First, the disintegration problem of hydrolytic CNC films in any aqueous environment was alleviated using 3-aminopropyl-triethoxy silane (APTES) modification in ethanol. The terminal $–NH_2$ of the APTES was later used to immobilize the glutaric anhydride (GA) organolinker to bind the antibodies as well. This was followed by immobilization of three model antibodies: anti-AFP, anti-PSA, and anti-CEA. Next, the antibody immobilized CNC films were exposed to solutions of the corresponding antigens to study the biomarker sensing for cancer. To investigate the surface modifications and biomarker detections, different techniques were used including TGA, FTIR, AFM, PSI, and fluorescence imaging. In addition, the freestanding CNC cantilevers were used as the

AFM tips to study the resonance frequency for potential biosensing applications. However, the resonance frequency study was not conclusive and needs further investigations. Unfortunately, there was a random drift of resonance frequencies and interference of spurious modes in the resonance spectrum were observed. Future research can focus on several strategies for overcoming this issue. These deviations and inconsistencies are attributed to different factors including stress gradient on the devices, possible adsorption of water vapor, and diffraction of laser beams limiting the detectability of the quadrupole piezo diode. The vibration of the cantilever can excite different modes including torsional, longitudinal, lateral, and transverse. But, one type of mode shape is preferable for mass detection. The detection of the neighboring modes' amplitudes can be attributed large spot size and position of the laser spot, covering several nodes, crests, and troughs of the cantilever vibration. In addition, the coupling between the freestanding cantilever and holder can be an effective factor[300,301]. The type of drive signal (*i.e.*, white noise, chirp, etc.) and range may also affect the signal to noise ratio coupled with spurious modes[302]. The frequency range for the sweep used in this study was 50 - 500 kHz, which needs to be investigated for lower range. Also, laser beam spot size and position on the cantilevers need be studied for more consistent resonance frequency. The current fabrication involves the deposition of a 10 nm TiO_2 layer on one side of the beam. The rest of the beam stays fairly hygroscopic which may result in differential adsorption of water vapor. Stress relaxation behavior and annealing of CNC cantilevers could be considered for more investigation in this regard.

Chapter 7 Conclusions

This dissertation presented the results of interdisciplinary research on the fluid phase microstructural ordering of cellulose nanocrystals (CNC) to realize anisotropic properties in thin films. It focused on obtaining uniform CNC microstructures with planar cholesteric ordering for selective reflection and aligned nematic microstructures for use in microelectromechanical systems (MEMS). The key contributions of the optical portion of the research were new insights into importance of initial dispersion concentration, shear response, drying conditions, and surface anchoring on obtaining planar ordering of cholesteric helices in dried films. In addition, the effect of CNC dispersion microstructure and viscosity on uniform ordering during drying was explored using isotropic, biphasic, and liquid crystalline concentrations. Obtaining a fundamental understanding of the effects of these parameters on helix orientation, enabled the production of films with uniform photonic properties over significantly greater length scales than can be achieved by drop casting. SEM and spectral based cholesteric pitch also revealed new insights into planar defects, mimicking the double-peak selective reflections of natural photonic species like *lomaptera* beetles. The insights of this provide for further improving CNC films' uniformity, and for developing photonic structures from other nanomaterials.

In the second portion of the research, rheology and rheo-optics provided the understanding of unwinding the chiral microstructures of CNC dispersions. Relaxation dynamics after shear cessation were investigated through collaborative physical experiments at Auburn and three-dimensional finite element modeling by Professor

Green's group at Texas A&M. These findings enhanced understanding of the production of nematically aligned CNC films for use in MEMS fabrication.

The key contributions of the MEMS portion of the research were the first successful fabrication of free standing actuatable MEMS devices from CNC and enhanced understanding of the relationships between dispersion processing and device properties. Initial films and devices were prone to breakage. They also had poor feature resolution and were readily lifted off the substrate. Optimization of the initial dispersion concentration, surface treatment, and drying conditions eliminated the cracking issues. A novel approach of vapor deposition of a titanium layer onto the films overcame initial obstacles with poor photoresist adhesion. Anisotropic etching overcame the challenges with device fidelity. Critical point drying overcame the surface stiction and capillary induced breakage of released devices. The resulting fabrication process enabled production of several types of actuatable CNC MEMS with feature sizes as small as six microns. The fabricated devices included cantilever beam arrays, mechanical strength testers, residual strain testers, comb drive resonators, and doubly clamped beams. The devices had tunable optical and mechanical anisotropic properties. For devices made from 4 μm thick films with the CNC aligned parallel to the devices' long axes, the Young's Moduli averaged 51 GPa and the breakage strength averaged 1.1 GPa. These values are within one third of typical values for polysilicon.

To validate the concept of using CNC MEMS as biosensors, several types of CNC surface modification were investigated. First, both dispersed CNC and CNC films were functionalized with 3-aminopropyl triethoxy silane (APTES). This dramatically improved

the hydrolytic stability of CNC in an aqueous media. Next, the protocols for attaching three different model antibodies to the APTES modified CNC films were developed. Alpha fetoprotein (liver cancer), prostate specific antigens (prostate cancer), and carcinoembryonic antigen (ovarian cancer) were chosen for this research based on the availability of literature data for silicon-based MEMS detection and their relevance to early cancer detection. Thermogravimetric analysis, Fourier transformed infrared spectroscopy, atomic force microscopy, and fluorescence microscopy revealed the feasibility of achieving the required immobilization and antibody antigen binding. Preliminary research explored potential methods for quantifying detection, but further refinement will be conducted in future research.

The results and understanding of this dissertation provide the insights into fluid phase ordering of cholesteric CNC for controlled anisotropic properties in films. The processing methods studied in this research will provide the foundation for processing the large scale routes of CNC based optical, micromechanical, and inexpensive disposable biosensors in future.

References

1 Klemm, D., Heublein, B., Fink, H. P. & Bohn, A. Cellulose: fascinating biopolymer and sustainable raw material. *Angewandte Chemie International Edition* **44**, 3358-3393 (2005).

2 Wang, X., Yao, C., Wang, F. & Li, Z. Cellulose- Based Nanomaterials for Energy Applications. *Small* (2017).

3 Kim, J., Yun, S. & Ounaies, Z. Discovery of cellulose as a smart material. *Macromolecules* **39**, 4202-4206 (2006).

4 Bazhenov, V. Piezoelectric properties of wood. New York, Consultant Bureau Enterprises. *Inc., 196t* (1961).

5 Marchessault, R., Morehead, F. & Walter, N. Liquid crystal systems from fibrillar polysaccharides. *Nature* **184**, 632-633 (1959).

6 Revol, J.-F., Bradford, H., Giasson, J., Marchessault, R. & Gray, D. Helicoidal self-ordering of cellulose microfibrils in aqueous suspension. *International journal of biological macromolecules* **14**, 170-172 (1992).

7 Moon, R. J., Martini, A., Nairn, J., Simonsen, J. & Youngblood, J. Cellulose nanomaterials review: structure, properties and nanocomposites. *Chemical Society Reviews* **40**, 3941-3994 (2011).

8 Honorato Rios, C. *et al.* Equilibrium Liquid Crystal Phase Diagrams and Detection of Kinetic Arrest in Cellulose Nanocrystal Suspensions. *Frontiers in Materials* **3**, 21 (2016).

9 Dumanli, A. G. m. *et al.* Digital color in cellulose nanocrystal films. *ACS applied materials & interfaces* **6**, 12302-12306 (2014).

10 Finkelmann, H., Kim, S. T., Munoz, A., Palffy-Muhoray, P. & Taheri, B. Tunable mirrorless lasing in cholesteric liquid crystalline elastomers. *Advanced Materials* **13**, 1069-1072 (2001).

11 Lagerwall, J. P. *et al.* Cellulose nanocrystal-based materials: from liquid crystal self-assembly and glass formation to multifunctional thin films. *NPG Asia Materials* **6**, e80 (2014).

12 Brown, R. M. Cellulose structure and biosynthesis: what is in store for the 21st century? *Journal of Polymer Science Part A: Polymer Chemistry* **42**, 487-495 (2004).

13 O'sullivan, A. C. Cellulose: the structure slowly unravels. *Cellulose* **4**, 173-207 (1997).

14 Kontturi, E., Tammelin, T. & Österberg, M. Cellulose—model films and the fundamental approach. *Chemical Society Reviews* **35**, 1287-1304 (2006).

15 Rånby, B. G. Fibrous macromolecular systems. Cellulose and muscle. The colloidal properties of cellulose micelles. *Discussions of the Faraday Society* **11**, 158-164 (1951).

16 Ishikawa, A., Okano, T. & Sugiyama, J. Fine structure and tensile properties of ramie fibres in the crystalline form of cellulose I, II, IIII and IVI. *Polymer* **38**, 463-468 (1997).

17 Azizi Samir, M. A. S., Alloin, F. & Dufresne, A. Review of recent research into cellulosic whiskers, their properties and their application in nanocomposite field. *Biomacromolecules* **6**, 612-626 (2005).

18 Nishiyama, Y. Structure and properties of the cellulose microfibril. *Journal of Wood Science* **55**, 241-249 (2009).

19 Yamamoto, H. & Horii, F. CPMAS carbon-13 NMR analysis of the crystal transformation induced for Valonia cellulose by annealing at high temperatures. *Macromolecules* **26**, 1313-1317 (1993).

20 Yamamoto, H. & Horn, F. In Situ crystallization of bacterial cellulose I. Influences of polymeric additives, stirring and temperature on the formation celluloses I α and I β as revealed by cross polarization/magic angle spinning (CP/MAS) 13 C NMR spectroscopy. *Cellulose* **1**, 57-66 (1994).

21 Belton, P., Tanner, S., Cartier, N. & Chanzy, H. High-resolution solid-state carbon-13 nuclear magnetic resonance spectroscopy of tunicin, an animal cellulose. *Macromolecules* **22**, 1615-1617 (1989).

22 Nishiyama, Y., Johnson, G. P., French, A. D., Forsyth, V. T. & Langan, P. Neutron crystallography, molecular dynamics, and quantum mechanics studies of the nature of hydrogen bonding in cellulose Iβ. *Biomacromolecules* **9**, 3133-3140 (2008).

23 Hubbe, M. A., Rojas, O. J., Lucia, L. A. & Sain, M. Cellulosic nanocomposites: a review. *BioResources* **3**, 929-980 (2008).

24 Eichhorn, S. J. *et al.* current international research into cellulose nanofibres and nanocomposites. *Journal of materials science* **45**, 1 (2010).

25 Siró, I. & Plackett, D. Microfibrillated cellulose and new nanocomposite materials: a review. *Cellulose* **17**, 459-494 (2010).

26 Siqueira, G., Bras, J. & Dufresne, A. Cellulosic bionanocomposites: a review of preparation, properties and applications. *Polymers* **2**, 728-765 (2010).

27 Teeri, T. T., Brumer, H., Daniel, G. & Gatenholm, P. Biomimetic engineering of cellulose-based materials. *Trends in Biotechnology* **25**, 299-306 (2007).

28 Platikanov, D. & Exerowa, D. *Highlights in colloid science*. (John Wiley & Sons, 2009).

29 Iwamoto, S., Abe, K. & Yano, H. The effect of hemicelluloses on wood pulp nanofibrillation and nanofiber network characteristics. *Biomacromolecules* **9**, 1022-1026 (2008).

30 Habibi, Y., Lucia, L. A. & Rojas, O. J. Cellulose nanocrystals: chemistry, self-assembly, and applications. *Chemical reviews* **110**, 3479-3500 (2010).

31 Dong, X. M., Kimura, T., Revol, J.-F. & Gray, D. G. Effects of ionic strength on the isotropic-chiral nematic phase transition of suspensions of cellulose crystallites. *Langmuir* **12**, 2076-2082 (1996).

32 Marchessault, R., Morehead, F. & Koch, M. J. Some hydrodynamic properties of neutral suspensions of cellulose crystallites as related to size and shape. *Journal of Colloid Science* **16**, 327-344 (1961).

33 Orts, W., Godbout, L., Marchessault, R. & Revol, J.-F. Enhanced ordering of liquid crystalline suspensions of cellulose microfibrils: A small angle neutron scattering study. *Macromolecules* **31**, 5717-5725 (1998).

34 Araki, J., Wada, M., Kuga, S. & Okano, T. Influence of surface charge on viscosity behavior of cellulose microcrystal suspension. *Journal of wood science* **45**, 258-261 (1999).

35 Araki, J., Wada, M., Kuga, S. & Okano, T. Flow properties of microcrystalline cellulose suspension prepared by acid treatment of native cellulose. *Colloids and Surfaces A: Physicochemical and Engineering Aspects* **142**, 75-82 (1998).

36 Hamad, W. Y. & Hu, T. Q. Structure–process–yield interrelations in nanocrystalline cellulose extraction. *The Canadian Journal of Chemical Engineering* **88**, 392-402 (2010).

37 Dong, X. M., Revol, J.-F. & Gray, D. G. Effect of microcrystallite preparation conditions on the formation of colloid crystals of cellulose. *Cellulose* **5**, 19-32 (1998).

38 Beck-Candanedo, S., Roman, M. & Gray, D. G. Effect of reaction conditions on the properties and behavior of wood cellulose nanocrystal suspensions. *Biomacromolecules* **6**, 1048-1054 (2005).

39 Filson, P. B. & Dawson-Andoh, B. E. Sono-chemical preparation of cellulose nanocrystals from lignocellulose derived materials. *Bioresource Technology* **100**, 2259-2264 (2009).

40 Ranby, B. G. Aqueous colloidal solutions of cellulose micelles. *Acta Chemica Scandinavica* **3**, 649-650 (1949).

41 Rånby, B. & Ribi, E. Über den feinbau der zellulose. *Cellular and Molecular Life Sciences* **6**, 12-14 (1950).

42 Araki, J., Wada, M., Kuga, S. & Okano, T. Birefringent glassy phase of a cellulose microcrystal suspension. *Langmuir* **16**, 2413-2415 (2000).

43 Habibi, Y. *et al.* Bionanocomposites based on poly (ε-caprolactone)-grafted cellulose nanocrystals by ring-opening polymerization. *Journal of Materials Chemistry* **18**, 5002-5010 (2008).

44 Habibi, Y. & Dufresne, A. Highly filled bionanocomposites from functionalized polysaccharide nanocrystals. *Biomacromolecules* **9**, 1974-1980 (2008).

45 Habibi, Y., Foulon, L., Aguié-Béghin, V., Molinari, M. & Douillard, R. Langmuir–Blodgett films of cellulose nanocrystals: Preparation and characterization. *Journal of Colloid and Interface Science* **316**, 388-397 (2007).

46 Cao, X., Chen, Y., Chang, P. R., Stumborg, M. & Huneault, M. A. Green composites reinforced with hemp nanocrystals in plasticized starch. *Journal of Applied Polymer Science* **109**, 3804-3810 (2008).

47 Cao, X., Chen, Y., Chang, P., Muir, A. & Falk, G. Starch-based nanocomposites reinforced with flax cellulose nanocrystals. *Express Polym Lett* **2**, 502-510 (2008).

48 Cao, X., Dong, H. & Li, C. M. New nanocomposite materials reinforced with flax cellulose nanocrystals in waterborne polyurethane. *Biomacromolecules* **8**, 899-904 (2007).

49 Helbert, W., Cavaille, J. & Dufresne, A. Thermoplastic nanocomposites filled with wheat straw cellulose whiskers. Part I: processing and mechanical behavior. *Polymer composites* **17**, 604-611 (1996).

50 Grunert, M. & Winter, W. T. Nanocomposites of cellulose acetate butyrate reinforced with cellulose nanocrystals. *Journal of Polymers and the Environment* **10**, 27-30 (2002).

51 Araki, J. & Kuga, S. Effect of trace electrolyte on liquid crystal type of cellulose microcrystals. *Langmuir* **17**, 4493-4496 (2001).

52 Hirai, A., Inui, O., Horii, F. & Tsuji, M. Phase separation behavior in aqueous suspensions of bacterial cellulose nanocrystals prepared by sulfuric acid treatment. *Langmuir* **25**, 497-502 (2008).

53 Angles, M. N. & Dufresne, A. Plasticized starch/tunicin whiskers nanocomposites. 1. Structural analysis. *Macromolecules* **33**, 8344-8353 (2000).

54 de Souza Lima, M. M. & Borsali, R. Static and dynamic light scattering from polyelectrolyte microcrystal cellulose. *Langmuir* **18**, 992-996 (2002).

55 Angles, M. N. & Dufresne, A. Plasticized starch/tunicin whiskers nanocomposite materials. 2. Mechanical behavior. *Macromolecules* **34**, 2921-2931 (2001).

56 Heux, L., Chauve, G. & Bonini, C. Nonflocculating and chiral-nematic self-ordering of cellulose microcrystals suspensions in nonpolar solvents. *Langmuir* **16**, 8210-8212 (2000).

57 Heux, L. & Bonini, C. Microfibrilated and/or microcrystalline dispersion, in particular of cellulose, in an organic solvent. U.S. Patent No. 6,967,027 (2005).

58 Bonini, C. *et al.* Rodlike cellulose whiskers coated with surfactant: a small-angle neutron scattering characterization. *Langmuir* **18**, 3311-3314 (2002).

59 Rojas, O. J., Montero, G. A. & Habibi, Y. Electrospun nanocomposites from polystyrene loaded with cellulose nanowhiskers. *Journal of Applied Polymer Science* **113**, 927-935 (2009).

60 Bondeson, D. & Oksman, K. Dispersion and characteristics of surfactant modified cellulose whiskers nanocomposites. *Composite Interfaces* **14**, 617-630 (2007).

61 Kim, J. *et al.* Dispersion of cellulose crystallites by nonionic surfactants in a hydrophobic polymer matrix. *Polymer Engineering & Science* **49**, 2054-2061 (2009).

62 Araki, J., Wada, M. & Kuga, S. Steric stabilization of a cellulose microcrystal suspension by poly (ethylene glycol) grafting. *Langmuir* **17**, 21-27 (2001).

63 Habibi, Y., Chanzy, H. & Vignon, M. R. TEMPO-mediated surface oxidation of cellulose whiskers. *Cellulose* **13**, 679-687 (2006).

64 Montanari, S., Roumani, M., Heux, L. & Vignon, M. R. Topochemistry of carboxylated cellulose nanocrystals resulting from TEMPO-mediated oxidation. *Macromolecules* **38**, 1665-1671 (2005).

65 Hasani, M., Cranston, E. D., Westman, G. & Gray, D. G. Cationic surface functionalization of cellulose nanocrystals. *Soft matter* **4**, 2238-2244 (2008).

66 Siqueira, G., Bras, J. & Dufresne, A. Cellulose whiskers versus microfibrils: influence of the nature of the nanoparticle and its surface functionalization on the thermal and mechanical properties of nanocomposites. *Biomacromolecules* **10**, 425-432 (2008).

67 de Menezes, A. J., Siqueira, G., Curvelo, A. A. & Dufresne, A. Extrusion and characterization of functionalized cellulose whiskers reinforced polyethylene nanocomposites. *Polymer* **50**, 4552-4563 (2009).

68 Braun, B. & Dorgan, J. R. Single-step method for the isolation and surface functionalization of cellulosic nanowhiskers. *Biomacromolecules* **10**, 334-341 (2008).

69 Sobkowicz, M. J., Braun, B. & Dorgan, J. R. Decorating in green: surface esterification of carbon and cellulosic nanoparticles. *Green Chemistry* **11**, 680-682 (2009).

70 Yuan, H., Nishiyama, Y., Wada, M. & Kuga, S. Surface acylation of cellulose whiskers by drying aqueous emulsion. *Biomacromolecules* **7**, 696-700 (2006).

71 Goussé, C., Chanzy, H., Excoffier, G., Soubeyrand, L. & Fleury, E. Stable suspensions of partially silylated cellulose whiskers dispersed in organic solvents. *Polymer* **43**, 2645-2651 (2002).

72 Orelma, H., Filpponen, I., Johansson, L.-S., Laine, J. & Rojas, O. J. Modification of cellulose films by adsorption of CMC and chitosan for controlled attachment of biomolecules. *Biomacromolecules* **12**, 4311-4318 (2011).

73 Orelma, H., Teerinen, T., Johansson, L.-S., Holappa, S. & Laine, J. CMC-modified cellulose biointerface for antibody conjugation. *Biomacromolecules* **13**, 1051-1058 (2012).

74 Habibi, Y., Hoeger, I., Kelley, S. S. & Rojas, O. J. Development of Langmuir−Schaeffer Cellulose Nanocrystal Monolayers and Their Interfacial Behaviors. *Langmuir* **26**, 990-1001 (2009).

75 Rondeau-Mouro, C. *et al.* Structural features and potential texturising properties of lemon and maize cellulose microfibrils. *Carbohydrate Polymers* **53**, 241-252 (2003).

76 Elazzouzi-Hafraoui, S. *et al.* The shape and size distribution of crystalline nanoparticles prepared by acid hydrolysis of native cellulose. *Biomacromolecules* **9**, 57-65 (2007).

77 Tokoh, C., Takabe, K., Fujita, M. & Saiki, H. Cellulose synthesized by Acetobacter xylinum in the presence of acetyl glucomannan. *Cellulose* **5**, 249-261 (1998).

78 Terech, P., Chazeau, L. & Cavaille, J. A small-angle scattering study of cellulose whiskers in aqueous suspensions. *Macromolecules* **32**, 1872-1875 (1999).

79 Dufresne, A., Cavaille, J.-Y. & Vignon, M. R. Mechanical behavior of sheets prepared from sugar beet cellulose microfibrils. *Journal of applied polymer science* **64**, 1185-1194 (1997).

80 Saito, T., Kimura, S., Nishiyama, Y. & Isogai, A. Cellulose nanofibers prepared by TEMPO-mediated oxidation of native cellulose. *Biomacromolecules* **8**, 2485-2491 (2007).

81 Hanley, S. J., Revol, J.-F., Godbout, L. & Gray, D. G. Atomic force microscopy and transmission electron microscopy of cellulose from Micrasterias denticulata; evidence for a chiral helical microfibril twist. *Cellulose* **4**, 209-220 (1997).

82 Ifuku, S. *et al.* Surface modification of bacterial cellulose nanofibers for property enhancement of optically transparent composites: dependence on acetyl-group DS. *Biomacromolecules* **8**, 1973-1978 (2007).

83 Lagerwall, J. P. & Scalia, G. A new era for liquid crystal research: applications of liquid crystals in soft matter nano-, bio-and microtechnology. *Current Applied Physics* **12**, 1387-1412 (2012).

84 Klemm, D. *et al.* Nanocelluloses: A new family of nature- based materials. *Angewandte Chemie International Edition* **50**, 5438-5466 (2011).

85 Park, J. H. *et al.* Macroscopic Control of Helix Orientation in Films Dried from Cholesteric Liquid- Crystalline Cellulose Nanocrystal Suspensions. *ChemPhysChem* **15**, 1477-1484 (2014).

86 Majoinen, J., Kontturi, E., Ikkala, O. & Gray, D. G. SEM imaging of chiral nematic films cast from cellulose nanocrystal suspensions. *Cellulose* **19**, 1599-1605 (2012).

87 Roman, M. & Gray, D. G. Parabolic focal conics in self-assembled solid films of cellulose nanocrystals. *Langmuir* **21**, 5555-5561 (2005).

88 Beck, S., Bouchard, J. & Berry, R. Controlling the reflection wavelength of iridescent solid films of nanocrystalline cellulose. *Biomacromolecules* **12**, 167-172 (2010).

89 Mosser, G., Anglo, A., Helary, C., Bouligand, Y. & Giraud-Guille, M.-M. Dense tissue-like collagen matrices formed in cell-free conditions. *Matrix Biology* **25**, 3-13 (2006).

90 Shopsowitz, K. E., Qi, H., Hamad, W. Y. & MacLachlan, M. J. Free-standing mesoporous silica films with tunable chiral nematic structures. *Nature* **468**, 422-425 (2010).

91 Kelly, J. A., Shopsowitz, K. E., Ahn, J. M., Hamad, W. Y. & MacLachlan, M. J. Chiral nematic stained glass: controlling the optical properties of nanocrystalline cellulose-templated materials. *Langmuir* **28**, 17256-17262 (2012).

92 Shopsowitz, K. E., Stahl, A., Hamad, W. Y. & MacLachlan, M. J. Hard templating of nanocrystalline titanium dioxide with chiral nematic ordering. *Angewandte Chemie International Edition* **51**, 6886-6890 (2012).

93 Shopsowitz, K. E., Hamad, W. Y. & MacLachlan, M. J. Flexible and iridescent chiral nematic mesoporous organosilica films. *Journal of the American Chemical Society* **134**, 867-870 (2012).

94 Shopsowitz, K. E., Hamad, W. Y. & MacLachlan, M. J. Chiral nematic mesoporous carbon derived from nanocrystalline cellulose. *Angewandte Chemie International Edition* **50**, 10991-10995 (2011).

95 Qi, H., Roy, X., Shopsowitz, K. E., Hui, J. K. H. & MacLachlan, M. J. Liquid-crystal templating in ammonia: a facile route to micro- and mesoporous metal nitride/carbon composites. *Angewandte Chemie International Edition* **49**, 9740-9743 (2010).

96 Palffy-Muhoray, P., Cao, W., Moreira, M., Taheri, B. & Munoz, A. Photonics and lasing in liquid crystal materials. *Philosophical Transactions of the Royal Society of London A: Mathematical, Physical and Engineering Sciences* **364**, 2747-2761 (2006).

97 Zhang, Y. P., Chodavarapu, V. P., Kirk, A. G. & Andrews, M. P. Structured color humidity indicator from reversible pitch tuning in self-assembled nanocrystalline cellulose films. *Sensors and Actuators B: Chemical* **176**, 692-697 (2013).

98 Beck, S., Bouchard, J., Chauve, G. & Berry, R. Controlled production of patterns in iridescent solid films of cellulose nanocrystals. *Cellulose* **20**, 1401-1411 (2013).

99 Zhang, Y. P., Chodavarapu, V. P., Kirk, A. G. & Andrews, M. P. Nanocrystalline cellulose for covert optical encryption. *Journal of Nanophotonics* **6**, 063516-063511-063516-063519 (2012).

100 Querejeta-Fernández, A. *et al.* Circular dichroism of chiral nematic films of cellulose nanocrystals loaded with plasmonic nanoparticles. *ACS nano* **9**, 10377-10385 (2015).

101 Beck, S., Bouchard, J. & Berry, R. Dispersibility in water of dried nanocrystalline cellulose. *Biomacromolecules* **13**, 1486-1494 (2012).

102 Choi, Y. & Simonsen, J. Cellulose nanocrystal-filled carboxymethyl cellulose nanocomposites. *Journal of nanoscience and nanotechnology* **6**, 633-639 (2006).

103 Passantino, J. M., Haywood, A. D., Goswami, J. & Davis, V. A. Effects of Polymer Additives and Dispersion State on the Mechanical Properties of Cellulose Nanocrystal Films. *Macromolecular Materials and Engineering* **302** (2017).

104 Roman, M. & Winter, W. T. Cellulose nanocrystlas for thermoplastic reinforcement: effect of filler surface chemistry on composite properties in Cellulose Nanocomposites. Chapter 8. *ACS Publications*, 99-113 (2006).

105 La Mantia, F. & Morreale, M. Green composites: A brief review. *Composites Part A: Applied Science and Manufacturing* **42**, 579-588 (2011).

106 Faruk, O., Bledzki, A. K., Fink, H.-P. & Sain, M. Biocomposites reinforced with natural fibers: 2000–2010. *Progress in polymer science* **37**, 1552-1596 (2012).

107 Hess-Dunning, A. E. *et al.* Microscale characterization of a mechanically adaptive polymer nanocomposite with cotton-derived cellulose nanocrystals for implantable bioMEMS. *Journal of Microelectromechanical Systems* **23**, 774-784 (2014).

108 Yan, C. *et al.* Highly stretchable piezoresistive graphene–nanocellulose nanopaper for strain sensors. *Advanced materials* **26**, 2022-2027 (2014).

109 Zhai, L., Mun, S., Gao, X., Kim, J. & Kim, J. Cellulose electro-active paper fabricated by facile solvent exchange pretreatment and its physical and electromechanical properties. *Cellulose* **22**, 927-933, doi:10.1007/s10570-015-0553-y (2015).

110 Yang, X., Shi, K., Zhitomirsky, I. & Cranston, E. D. Cellulose nanocrystal aerogels as universal 3D lightweight substrates for supercapacitor materials. *Advanced Materials* **27**, 6104-6109 (2015).

111 Nyström, G. *et al.* Self-assembled three-dimensional and compressible interdigitated thin-film supercapacitors and batteries. *Nature communications* **6** (2015).

112 Yang, X. & Cranston, E. D. Chemically cross-linked cellulose nanocrystal aerogels with shape recovery and superabsorbent properties. *Chemistry of Materials* **26**, 6016-6025 (2014).

113 Leung, A. C., Lam, E., Chong, J., Hrapovic, S. & Luong, J. H. Reinforced plastics and aerogels by nanocrystalline cellulose. *Journal of nanoparticle research* **15**, 1636 (2013).

114 Onsager, L. The effects of shape on the interaction of colloidal particles. *Annals of the New York Academy of Sciences* **51**, 627-659 (1949).

115 Flory, P. J. Theory of crystallization in copolymers. *Transactions of the Faraday Society* **51**, 848-857 (1955).

116 Sluckin, T. J., Dunmur, D. A. & Stegemeyer, H. Crystals that flow. *Liquid Crystals Series Taylor & Francis: London* (2004).

117 Bawden, F., Pirie, N., Bernal, J. & Fankuchen, I. Liquid crystalline substances from virus-infected plants. *Nature* **138**, 1051 (1936).

118 Burchill, P. J. Chemical characterization of Kevlar-49. *Journal of Materials Science* **13**, 2275-2276 (1978).

119 Davis, V. A. Liquid crystalline assembly of nanocylinders. *Journal of materials research* **26**, 140-153 (2011).

120 Donald, A. M., Windle, A. H. & Hanna, S. *Liquid crystalline polymers*. (Cambridge University Press, 2006).

121 Doi, M. & Edwards, S. F. *The theory of polymer dynamics*. Vol. 73 (oxford university press, 1988).

122 Doi, M. & Edwards, S. The theory of polymer dynamics. 1986. *Claredon, Oxford. ISBN 0-19-852033* **6** (1986).

123 Rai, P. K. *et al.* Isotropic− Nematic Phase Transition of Single-Walled Carbon Nanotubes in Strong Acids. *Journal of the American Chemical Society* **128**, 591-595 (2006).

124 Ureña-Benavides, E. E., Ao, G., Davis, V. A. & Kitchens, C. L. Rheology and phase behavior of lyotropic cellulose nanocrystal suspensions. *Macromolecules* **44**, 8990-8998 (2011).

125 Larson, R. G. *The structure and rheology of complex fluids*. Vol. 150 (Oxford university press New York, 1999).

126 Frenkel, D. Structure of hard-core models for liquid crystals. *The Journal of Physical Chemistry* **92**, 3280-3284 (1988).

127 Green, M. J., Parra-Vasquez, A. N. G., Behabtu, N. & Pasquali, M. Modeling the phase behavior of polydisperse rigid rods with attractive interactions with applications to single-walled carbon nanotubes in superacids. *The Journal of chemical physics* **131**, 084901 (2009).

128 Khokhlov, A. & Semenov, A. On the theory of liquid-crystalline ordering of polymer chains with limited flexibility. *Journal of Statistical Physics* **38**, 161-182 (1985).

129 Stroobants, A., Lekkerkerker, H. & Odijk, T. Effect of electrostatic interaction on the liquid crystal phase transition in solutions of rodlike polyelectrolytes. *Macromolecules* **19**, 2232-2238 (1986).

130 Odijk, T. Theory of lyotropic polymer liquid crystals. *Macromolecules* **19**, 2313-2329 (1986).

131 Hanson, E. & Shen, Y. Refractive indices and optical anisotropy of homologous liquid crystals. *Molecular crystals and liquid crystals* **36**, 193-207 (1976).

132 Klemm, D., Philipp, B., Heinze, U. & Wagenknecht, W. Activated cellulose. *Comprehensive cellulose chemistry* **1**, 152-154 (1998).

133 Wu, S. T., Efron, U. & Hess, L. D. Birefringence measurements of liquid crystals. *Applied optics* **23**, 3911-3915 (1984).

134 Viale, S., Jager, W. F. & Picken, S. J. Synthesis and characterization of a water-soluble rigid-rod polymer. *Polymer* **44**, 7843-7850 (2003).

135 Michel-Lévy, M. & Lacroix, A. Minéralogie sur nouveau gisemant de dumortiérite. *CR Acad Sci Paris* **106**, 1546-1548 (1888).

136 Baek, S. G., Magda, J., Larson, R. & Hudson, S. Rheological differences among liquid- crystalline polymers. II. Disappearance of negative N 1 in densely packed lyotropes and thermotropes. *Journal of Rheology* **38**, 1473-1503 (1994).

137 Hongladarom, K., Secakusuma, V. & Burghardt, W. Relation between molecular orientation and rheology in lyotropic hydroxypropylcellulose solutions. *Journal of Rheology* **38**, 1505-1523 (1994).

138 Walker, L. M., Wagner, N. J., Larson, R. G., Mirau, P. A. & Moldenaers, P. The rheology of highly concentrated PBLG solutions. *Journal of Rheology* **39**, 925-952 (1995).

139 Larson, R. & Mead, D. Time and Shear- Rate Scaling Laws for Liquid Crystal Polymers. *Journal of Rheology* **33**, 1251-1281 (1989).

140 Baek, S. G., Magda, J. & Larson, R. Rheological differences among liquid-crystalline polymers. I. The first and second normal stress differences of PBG solutions. *Journal of Rheology* **37**, 1201-1224 (1993).

141 Hongladarom, K. & Burghardt, W. Molecular alignment of polymer liquid crystals in shear flows. 2. Transient flow behavior in poly (benzyl glutamate) solutions. *Macromolecules* **26**, 785-794 (1993).

142 Hermans, J. The viscosity of concentrated solutions of rigid rodlike molecules (poly-γ-benzyl-l-glutamate in m-cresol). *Journal of Colloid Science* **17**, 638-648 (1962).

143 Papkov, S., Kulichikhin, V., Kalmykova, V. & Malkin, A. Y. Rheological properties of anisotropic poly (para- benzamide) solutions. *Journal of Polymer Science Part B: Polymer Physics* **12**, 1753-1770 (1974).

144 Kiss, G. & Porter, R. S. in *Journal of Polymer Science: Polymer Symposia*. 193-211 (Wiley Online Library).

145 Aharoni, S. M. Rigid backbone polymers, XVII: Solution viscosity of polydisperse systems. *Polymer* **21**, 1413-1422 (1980).

146 Ao, G. *Liquid Crystalline Phase Behavior and Fiber Spinning of Double-Stranded DNA Stabilized Single-Walled Carbon Nanotube Dispersions*, Auburn University, (2012).

147 Kiss, G., Orrell, T. & Porter, R. S. Rheology and rheo-optics of anisotropic poly-β-benzyl-aspartate gel. *Rheologica Acta* **18**, 657-661 (1979).

148 Onogi, S. & Asada, T. Rheology and rheo-optics of polymer liquid crystals in *Rheology*. Springer, Boston, 127-147 (1980).

149 Pochon, M. Origine et évolution des sols du Haut-Jura suisse. (1978).

150 Kiss, G. Rheology and rheo-optics of concentrated solutions of helical polypeptides. University of Massachusetts Amherst (1979).

151 Wissbrun, K. F. Observations on the melt rheology of thermotropic aromatic polyesters. *Polymer International* **12**, 163-169 (1980).

152 Shirnarnura, K., White, J. & Fellers, J. Hydroxypropylcellulose, A Thermotropic Liquid Crystal. *Univ. of Tenn. PATRA Report* (1980).

153 Wissbrun, K. F. Rheology of rod- like polymers in the liquid crystalline state. *Journal of Rheology* **25**, 619-662 (1981).

154 Fishers, J. & Fredrickson, A. Interfacial effects on the viscosity of a nematic mesophase. *Molecular Crystals and Liquid Crystals* **8**, 267-284 (1969).

155 Tseng, H., Silver, D. L. & Finlayson, B. A. Application of the continuum theory to nematic liquid crystals. *The Physics of fluids* **15**, 1213-1222 (1972).

156 Horn, R. G. & Kleman, M. in *Annales de physique.* 229-234 (EDP Sciences).

157 Nielsen, L. E. *Polymer rheology*. (M. Dekker, 1977).

158 Kulichikhin, V. *et al.* Orientational structure formation in lyotropic, liquid crystals of poly-p-benzamide. *Polymer Science USSR* **18**, 3031-3043 (1976).

159 Onogi, Y., White, J. L. & Fellers, J. F. Rheo-optics of shear and elongational flow of liquid cystalline polymer solutions: hydroxypropyl cellulose/water and poly-p-phenylene terephthalamide/sulfuric acid. *Journal of Non-Newtonian Fluid Mechanics* **7**, 121-151 (1980).

160 Cogswell, F. N. On the formation of a low viscosity state in stiff chain polymers. *Polymer International* **12**, 170-173 (1980).

161 Davis, V. A. *et al.* Phase behavior and rheology of SWNTs in superacids. *Macromolecules* **37**, 154-160 (2004).

162 Haywood, A. D. *et al.* New insights into the flow and microstructural relaxation behavior of biphasic cellulose nanocrystal dispersions from RheoSANS. *Soft matter* **13**, 8451-8462 (2017).

163 Romo-Uribe, A. & Windle, A. "Log-Rolling" Alignment in Main-Chain Thermotropic Liquid Crystalline Polymer Melts under Shear: An In-Situ WAXS Study. *Macromolecules* **29**, 6246-6255 (1996).

164 Quijada-Garrido, I., Siebert, H., Becker, P., Friedrich, C. & Schmidt, C. Transient rheological behavior of tumbling side-chain liquid crystal polymers and determination of their λ parameters. *Rheologica Acta* **38**, 495-502 (1999).

165 Echeverria, C., Almeida, P. L., Aguilar Gutierrez, O. F., Rey, A. D. & Godinho, M. H. Two negative minima of the first normal stress difference in a cellulose- based cholesteric liquid crystal: Helix uncoiling. *Journal of Polymer Science Part B: Polymer Physics* **55**, 821-830 (2017).

166 Ciferri, A. *Liquid crystallinity in polymers*. (VCH Publishers, 1991).

167 Marrucci, G. Rheology of nematic polymers. *Liquid Crystallinity in Polymers: Principles and Fundamental Properties, A. Ciferri, ed* (1991).

168 Grizzuti, N., Cavella, S. & Cicarelli, P. Transient and steady- state rheology of a liquid crystalline hydroxypropylcellulose solution. *Journal of Rheology* **34**, 1293-1310 (1990).

169 Moldenaers, P. & Mewis, J. Transient behavior of liquid crystalline solutions of poly (benzylglutamate). *Journal of Rheology* **30**, 567-584 (1986).

170 Marrucci, G. Dynamics of entanglements: A nonlinear model consistent with the Cox-Merz rule. *Journal of non-newtonian fluid mechanics* **62**, 279-289 (1996).

171 Ianniruberto, G. & Marrucci, G. On compatibility of the Cox-Merz rule with the model of Doi and Edwards. *Journal of Non-Newtonian fluid mechanics* **65**, 241-246 (1996).

172 Mead, D., Larson, R. & Doi, M. A molecular theory for fast flows of entangled polymers. *Macromolecules* **31**, 7895-7914 (1998).

173 Mead, D. W. Analytic derivation of the Cox–Merz rule using the MLD "toy" model for polydisperse linear polymers. *Rheologica Acta* **50**, 837-866 (2011).

174 Sakamoto, K., MacKnight, W. J. & Porter, R. S. Dynamic and steady- shear melt rheology of and ethylene- methacrylic acid copolymer and its salts. *Journal of Polymer Science Part B: Polymer Physics* **8**, 277-287 (1970).

175 Earnest, T. & MacKnight, W. Effect of hydrogen bonding and ionic aggregation on the melt rheology of an ethylene–methacrylic acid copolymer and its sodium salt. *Journal of Polymer Science Part B: Polymer Physics* **16**, 143-157 (1978).

176 Honorato-Rios, C. *et al.* Equilibrium liquid crystal phase diagrams and detection of kinetic arrest in cellulose nanocrystal suspensions. *Frontiers in Materials* **3**, 21 (2016).

177 Leong, Y. & Ong, B. Critical zeta potential and the Hamaker constant of oxides in water. *Powder Technology* **134**, 249-254 (2003).

178 Wang, S. C. & Wei, W. C. J. Electrokinetic properties of nanosized SiC particles in highly concentrated electrolyte solutions. *Journal of the American Ceramic Society* **84**, 1411-1414 (2001).

179 Lin, N. & Dufresne, A. Surface chemistry, morphological analysis and properties of cellulose nanocrystals with gradiented sulfation degrees. *Nanoscale* **6**, 5384-5393 (2014).

180 Zhong, L., Fu, S., Peng, X., Zhan, H. & Sun, R. Colloidal stability of negatively charged cellulose nanocrystalline in aqueous systems. *Carbohydrate Polymers* **90**, 644-649 (2012).

181 de Souza Lima, M. M. & Borsali, R. Rodlike cellulose microcrystals: structure, properties, and applications. *Macromolecular Rapid Communications* **25**, 771-787 (2004).

182 Dong, X. M. & Gray, D. G. Effect of counterions on ordered phase formation in suspensions of charged rodlike cellulose crystallites. *Langmuir* **13**, 2404-2409 (1997).

183 Boluk, Y., Lahiji, R., Zhao, L. & McDermott, M. T. Suspension viscosities and shape parameter of cellulose nanocrystals (CNC). *Colloids and Surfaces A: Physicochemical and Engineering Aspects* **377**, 297-303 (2011).

184 Beck, S. & Bouchard, J. Auto-catalyzed acidic desulfation of cellulose nanocrystals. *Nordic Pulp & Paper Research Journal* **29**, 6-14 (2014).

185 Shafiei Sabet, S. *Shear rheology of cellulose nanocrystal (CNC) aqueous suspensions*, University of British Columbia, (2013).

186 Straley, J. P. Theory of piezoelectricity in nematic liquid crystals, and of the cholesteric ordering. *Physical Review A* **14**, 1835 (1976).

187 Haywood, A. Flow-Directed Assembly of Cellulose Nanocrystal Dispersions with Ordered Film Applications. (2016).

188 Shafiei-Sabet, S., Hamad, W. Y. & Hatzikiriakos, S. G. Rheology of nanocrystalline cellulose aqueous suspensions. *Langmuir* **28**, 17124-17133 (2012).

189 Bercea, M. & Navard, P. Shear dynamics of aqueous suspensions of cellulose whiskers. *Macromolecules* **33**, 6011-6016 (2000).

190 Conway, B. & Dobry-Duclaux, A. in *Rheology, Volume 3* 83-120 (Elsevier, 1960).

191 Mewis, J. & Spaull, A. Rheology of concentrated dispersions. *Advances in Colloid and interface Science* **6**, 173-200 (1976).

192 Mewis, J. Thixotropy-a general review. *Journal of Non-Newtonian Fluid Mechanics* **6**, 1-20 (1979).

193 Russel, W. B. Bulk stresses due to deformation of the electrical double layer around a charged sphere. *Journal of Fluid Mechanics* **85**, 673-683 (1978).

194 Wierenga, A. M., Philipse, A. P. & Reitsma, E. M. Decay of flow birefringence in dispersions of charged colloidal rods: Effect of double-layer interactions. *Langmuir* **13**, 6947-6950 (1997).

195 Ebeling, T. *et al.* Shear-induced orientation phenomena in suspensions of cellulose microcrystals, revealed by small angle X-ray scattering. *Langmuir* **15**, 6123-6126 (1999).

196 Haywood, A. D. & Davis, V. A. Effects of liquid crystalline and shear alignment on the optical properties of cellulose nanocrystal films. *Cellulose* **24**, 705-716 (2017).

197 Geng, Y., Almeida, P. L., Feio, G. M., Figueirinhas, J. o. L. & Godinho, M. H. Water-based cellulose liquid crystal system investigated by rheo-NMR. *Macromolecules* **46**, 4296-4302 (2013).

198 Pan, J., Hamad, W. & Straus, S. K. Parameters affecting the chiral nematic phase of nanocrystalline cellulose films. *Macromolecules* **43**, 3851-3858 (2010).

199 Reising, A. B., Moon, R. J. & Youngblood, J. P. Effect of particle alignment on mechanical properties of neat cellulose nanocrystal films. (2012).

200 Habibi, Y., Heim, T. & Douillard, R. AC electric field- assisted assembly and alignment of cellulose nanocrystals. *Journal of Polymer Science Part B: Polymer Physics* **46**, 1430-1436 (2008).

201 Csoka, L., Hoeger, I. C., Peralta, P., Peszlen, I. & Rojas, O. J. Dielectrophoresis of cellulose nanocrystals and alignment in ultrathin films by electric field-assisted shear assembly. *Journal of colloid and interface science* **363**, 206-212 (2011).

202 Tashiro, K. & Kobayashi, M. Theoretical evaluation of three-dimensional elastic constants of native and regenerated celluloses: role of hydrogen bonds. *Polymer* **32**, 1516-1526 (1991).

203 Rusli, R. & Eichhorn, S. J. Determination of the stiffness of cellulose nanowhiskers and the fiber-matrix interface in a nanocomposite using Raman spectroscopy. *Applied Physics Letters* **93**, 033111 (2008).

204 Hoeger, I., Rojas, O. J., Efimenko, K., Velev, O. D. & Kelley, S. S. Ultrathin film coatings of aligned cellulose nanocrystals from a convective-shear assembly system and their surface mechanical properties. *Soft Matter* **7**, 1957-1967 (2011).

205 Giasson, J. La lecture. *De la théorie à la pratique* **1** (1995).

206 Klemm, D., Philipp, B., Heinze, T., Heinze, U. & Wagenknecht, W. *General considerations on structure and reactivity of cellulose: section 2.1–2.1. 4*. (Wiley Online Library, 2004).

207 Shrestha, S., Diaz, J. A., Ghanbari, S. & Youngblood, J. P. Hygroscopic Swelling Determination of Cellulose Nanocrystal (CNC) Films by Polarized Light Microscopy Digital Image Correlation. *Biomacromolecules* **18**, 1482-1490 (2017).

208 Kern, W. The evolution of silicon wafer cleaning technology. *Journal of the Electrochemical Society* **137**, 1887-1892 (1990).

209 Howe, R. T. Surface micromachining for microsensors and microactuators. *Journal of Vacuum Science & Technology B: Microelectronics Processing and Phenomena* **6**, 1809-1813 (1988).

210 Legtenberg, R., Jansen, H., De Boer, M. & Elwenspoek, M. Anisotropic reactive ion etching of silicon using SF 6/O 2/CHF 3 gas mixtures. *Journal of the electrochemical society* **142**, 2020-2028 (1995).

211 Anguita, J. & Briones, F. HF/H2O vapor etching of SiO2 sacrificial layer for large-area surface-micromachined membranes. *Sensors and Actuators A: Physical* **64**, 247-251 (1998).

212 Svetovoy, V., Berenschot, J. W. & Elwenspoek, M. C. Precise test of the diffusion-controlled wet isotropic etching of silicon via circular mask openings. *Journal of The Electrochemical Society* **153**, C641-C647 (2006).

213 Ansari, N. M. A. *Understanding the effect of surface topography on stiction and friction in MEMS*, Auburn University, (2011).

214 Mulhem, G. T. in *The 7th International Conference on Sensors and Actuators.* 296-299.

215 Kwok, D. Y. & Neumann, A. W. Contact angle measurement and contact angle interpretation. *Advances in colloid and interface science* **81**, 167-249 (1999).

216 Sinclair, M. B., de Boer, M. P. & Corwin, A. D. Long-working-distance incoherent-light interference microscope. *Applied optics* **44**, 7714-7721 (2005).

217 Dong, X. M. & Gray, D. G. Induced circular dichroism of isotropic and magnetically-oriented chiral nematic suspensions of cellulose crystallites. *Langmuir* **13**, 3029-3034 (1997).

218 Dierking, I. *Textures of liquid crystals*. (John Wiley & Sons, 2003).

219 de Vries, H. Rotatory power and other optical properties of certain liquid crystals. *Acta Crystallographica* **4**, 219-226 (1951).

220 John, W. S., Fritz, W., Lu, Z. & Yang, D.-K. Bragg reflection from cholesteric liquid crystals. *Physical Review E* **51**, 1191 (1995).

221 Gray, D. G. Recent advances in chiral nematic structure and iridescent color of cellulose nanocrystal films. *Nanomaterials* **6**, 213 (2016).

222 Kopp, V. I. & Genack, A. Z. Twist defect in chiral photonic structures. *Physical review letters* **89**, 033901 (2002).

223 Carter, I., Weir, K., McCall, M. & Parker, A. Variation in the circularly polarized light reflection of Lomaptera (Scarabaeidae) beetles. *Journal of The Royal Society Interface* **13**, 20160015 (2016).

224 Vignolini, S. *et al.* Pointillist structural color in Pollia fruit. *Proceedings of the National Academy of Sciences* **109**, 15712-15715 (2012).

225 Wang, P. X., Hamad, W. Y. & MacLachlan, M. J. Structure and transformation of tactoids in cellulose nanocrystal suspensions. *Nature communications* **7** (2016).

226 Mu, X. & Gray, D. G. Droplets of cellulose nanocrystal suspensions on drying give iridescent 3-D “coffee-stain” rings. *Cellulose* **22**, 1103-1107 (2015).

227 Dierking, I. Chiral liquid crystals: Structures, phases, effects. *Symmetry* **6**, 444-472 (2014).

228 Zapotocky, M., Ramos, L., Poulin, P., Lubensky, T. & Weitz, D. Particle-stabilized defect gel in cholesteric liquid crystals. *Science* **283**, 209-212 (1999).

229 Huang, C.-Y., Stott, J. J. & Petschek, R. G. Routes to self-assembling stable photonic band-gap phases in emulsions of chiral nematics with isotropic fluids. *Physical review letters* **80**, 5603 (1998).

230 Deegan, R. D. *et al.* Capillary flow as the cause of ring stains from dried liquid drops. *Nature* **389**, 827-829 (1997).

231 Gençer, A., Schütz, C. & Thielemans, W. Influence of the Particle Concentration and Marangoni Flow on the Formation of Cellulose Nanocrystal Films. *Langmuir* **33**, 228-234 (2016).

232 Zola, R. S., Evangelista, L., Yang, Y.-C. & Yang, D.-K. Surface induced phase separation and pattern formation at the isotropic interface in chiral nematic liquid crystals. *Physical review letters* **110**, 057801 (2013).

233 Chen, J.-Y. & Chen, L.-W. Twist defect in chiral photonic structures with spatially varying pitch. *Journal of Physics D: Applied Physics* **38**, 1118 (2005).

234 Ličen, M. *et al.* Correlation between structural properties and iridescent colors of cellulose nanocrystalline films. *Cellulose* **23**, 3601-3609 (2016).

235 Yang, Y.-C. *et al.* Photonic defect modes of cholesteric liquid crystals. *Physical Review E* **60**, 6852 (1999).

236 Hodgkinson, I. J., Wu, Q. H., Thorn, K. E., Lakhtakia, A. & McCall, M. W. Spacerless circular-polarization spectral-hole filters using chiral sculptured thin films: theory and experiment. *Optics Communications* **184**, 57-66 (2000).

237 Livolant, F., Giraud, M. & Bouligand, Y. Goniometric effect observed in sections of twisted fibrous materials. *Biologie Cellulaire* **31**, 159 (1978).

238 Lagerwall, J. *et al.* Nanotube alignment using lyotropic liquid crystals. *Advanced materials* **19**, 359-364 (2007).

239 Hamley, I. Nanotechnology with soft materials. *Angewandte Chemie International Edition* **42**, 1692-1712 (2003).

240 Dierking, I., Scalia, G., Morales, P. & LeClere, D. Aligning and reorienting carbon nanotubes with nematic liquid crystals. *Advanced materials* **16**, 865-869 (2004).

241 Brinchi, L., Cotana, F., Fortunati, E. & Kenny, J. Production of nanocrystalline cellulose from lignocellulosic biomass: technology and applications. *Carbohydrate Polymers* **94**, 154-169 (2013).

242 Judy, J. W. Microelectromechanical systems (MEMS): fabrication, design and applications. *Smart materials and Structures* **10**, 1115 (2001).

243 Fischer, A. C. *et al.* Integrating MEMS and ICs. *Microsystems & Nanoengineering* **1**, 15005 (2015).

244 Wang, X., Engel, J. & Liu, C. Liquid crystal polymer (LCP) for MEMS: processes and applications. *Journal of Micromechanics and Microengineering* **13**, 628 (2003).

245 Yole Development. Status of the MEMS Industry 2015. (Villeurbanne, France 2015).

246 Liu, C. Recent developments in polymer MEMS. *Advanced Materials* **19**, 3783-3790 (2007).

247 Hess-Dunning, A. E. *et al.* Microscale Characterization of a Mechanically Adaptive Polymer Nanocomposite With Cotton-Derived Cellulose Nanocrystals for Implantable BioMEMS. *Microelectromechanical Systems, Journal of* **23**, 774-784 (2014).

248 Grayson, A. R. *et al.* A BioMEMS review: MEMS technology for physiologically integrated devices. *Proceedings of the IEEE* **92**, 6-21 (2004).

249 Bashir, R. BioMEMS: state-of-the-art in detection, opportunities and prospects. *Advanced drug delivery reviews* **56**, 1565-1586 (2004).

250 Zhao, J., Sheadel, D. A. & Xue, W. Surface treatment of polymers for the fabrication of all-polymer MEMS devices. *Sensors and Actuators A: Physical* **187**, 43-49 (2012).

251 Iwamoto, S., Kai, W., Isogai, A. & Iwata, T. Elastic modulus of single cellulose microfibrils from tunicate measured by atomic force microscopy. *Biomacromolecules* **10**, 2571-2576 (2009).

252 Lu, P. & Hsieh, Y.-L. Preparation and properties of cellulose nanocrystals: Rods, spheres, and network. *Carbohydrate Polymers* **82**, 329-336 (2010).

253 Camarero Espinosa, S., Kuhnt, T., Foster, E. J. & Weder, C. Isolation of Thermally Stable Cellulose Nanocrystals by Phosphoric Acid Hydrolysis. *Biomacromolecules* **14**, 1223-1230 (2013).

254 Ericson, L. *et al.* Macroscopic, neat, single-walled carbon nanotube fibers. *Science* **305**, 1447-1450 (2004).

255 Davis, V. A. *et al.* True solutions of single-walled carbon nanotubes for assembly into macroscopic materials. *Nature Nanotechnology* **4**, 830-834 (2009).

256 Xu, T. & Davis, V. A. Liquid Crystalline Phase Behavior of Silica Nanorods in Dimethyl Sulfoxide and Water. *Langmuir* **30**, 4806-4813, doi:10.1021/la405013h (2014).

257 Vermant, J., Moldenaers, P., Mewis, J. & Picken, S. Band formation upon cessation of flow in liquid- crystalline polymers. *Journal of rheology* **38**, 1571-1589 (1994).

258 Singh, K. B., Bhosale, L. R. & Tirumkudulu, M. S. Cracking in drying colloidal films of flocculated dispersions. *Langmuir* **25**, 4284-4287 (2009).

259 Godinho, M., Fonseca, J., Ribeiro, A., Melo, L. & Brogueira, P. Atomic force microscopy study of hydroxypropylcellulose films prepared from liquid crystalline aqueous solutions. *Macromolecules* **35**, 5932-5936 (2002).

260 Fernandes, S. N. *et al.* Structural color and iridescence in transparent sheared cellulosic films. *Macromolecular Chemistry and Physics* **214**, 25-32 (2013).

261 Perry, A. & Boswell, R. Fast anisotropic etching of silicon in an inductively coupled plasma reactor. *Applied physics letters* **55**, 148-150 (1989).

262 Jafri, I. H., Busta, H. & Walsh, S. T. in *Symposium on Micromachining and Microfabrication.* 51-58 (International Society for Optics and Photonics).

263 Landel, R. F. & Nielsen, L. E. *Mechanical Properties of Polymers and Composites, Second Edition*. (Taylor & Francis, 1993).

264 Madsen, C. *et al.* A tunable dispersion compensating MEMS all-pass filter. *IEEE Photonics technology letters* **12**, 651-653 (2000).

265 Dayton, D. *et al.* Demonstration of new technology MEMS and liquid crystal adaptive optics on bright astronomical objects and satellites. *Optics express* **10**, 1508-1519 (2002).

266 Restaino, S. R. *et al.* in *Proc. Soc. Phot. Opt. Instrum. Eng.* 776-781.

267 Maier-Schneider, D., Köprülülü, A., Holm, S. B. & Obermeier, E. Elastic properties and microstructure of LPCVD polysilicon films. *Journal of Micromechanics and Microengineering* **6**, 436 (1996).

268 Pruessner, M. W. *et al.* Mechanical property measurement of InP-based MEMS for optical communications. *Sensors and Actuators A: Physical* **105**, 190-200 (2003).

269 Li, X., Bhushan, B., Takashima, K., Baek, C.-W. & Kim, Y.-K. Mechanical characterization of micro/nanoscale structures for MEMS/NEMS applications using nanoindentation techniques. *Ultramicroscopy* **97**, 481-494 (2003).

270 Jonestt, P., Johnsontt, G. & Howe, R. in *MRS proceedings.* 197 (Cambridge Univ Press).

271 Cho, S. & Chasiotis, I. Elastic properties and representative volume element of polycrystalline silicon for MEMS. *Experimental Mechanics* **47**, 37-49 (2007).

272 Tothill, I. E. in *Seminars in cell & developmental biology.* 55-62 (Elsevier).

273 Kojima, K. *et al.* Electrochemical protein chip with arrayed immunosensors with antibodies immobilized in a plasma-polymerized film. *Analytical chemistry* **75**, 1116-1122 (2003).

274 Guan, J.-G., Miao, Y.-Q. & Chen, J.-R. Prussian blue modified amperometric FIA biosensor: one-step immunoassay for α-fetoprotein. *Biosensors and Bioelectronics* **19**, 789-794 (2004).

275 Wilson, M. S. Electrochemical immunosensors for the simultaneous detection of two tumor markers. *Analytical chemistry* **77**, 1496-1502 (2005).

276 Meyerhoff, M. E., Duan, C. & Meusel, M. Novel nonseparation sandwich-type electrochemical enzyme immunoassay system for detecting marker proteins in undiluted blood. *Clinical chemistry* **41**, 1378-1384 (1995).

277 Sarkar, P., Pal, P. S., Ghosh, D., Setford, S. J. & Tothill, I. E. Amperometric biosensors for detection of the prostate cancer marker (PSA). *International journal of pharmaceutics* **238**, 1-9 (2002).

278 Fernández-Sánchez, C., McNeil, C. J., Rawson, K. & Nilsson, O. Disposable noncompetitive immunosensor for free and total prostate-specific antigen based on capacitance measurement. *Analytical chemistry* **76**, 5649-5656 (2004).

279 Zhu, Q., Chai, Y.-Q., Yuan, R., Wang, N. & Li, X.-L. Development of a biosensor for the detection of carcinoembryonic antigen using faradic impedance spectroscopy. *Chemistry Letters* **34**, 1682-1683 (2005).

280 Dai, Z., Chen, J., Yan, F. & Ju, H. Electrochemical sensor for immunoassay of carcinoembryonic antigen based on thionine monolayer modified gold electrode. *Cancer detection and prevention* **29**, 233-240 (2005).

281 Tan, F., Yan, F. & Ju, H. A designer ormosil gel for preparation of sensitive immunosensor for carcinoembryonic antigen based on simple direct electron transfer. *Electrochemistry communications* **8**, 1835-1839 (2006).

282 Lin, J., Yan, F. & Ju, H. Noncompetitive enzyme immunoassay for carcinoembryonic antigen by flow injection chemiluminescence. *Clinica chimica acta* **341**, 109-115 (2004).

283 Joo, J., Kwon, D., Yim, C. & Jeon, S. Highly sensitive diagnostic assay for the detection of protein biomarkers using microresonators and multifunctional nanoparticles. *ACS nano* **6**, 4375-4381 (2012).

284 Bhalerao, K. D., Lee, S. C., Soboyejo, W. O. & Soboyejo, A. B. A folic acid-based functionalized surface for biosensor systems. *Journal of Materials Science: Materials in Medicine* **18**, 3-8 (2007).

285 Peng, J., Feng, L. N., Ren, Z. J., Jiang, L. P. & Zhu, J. J. Synthesis of Silver Nanoparticle–Hollow Titanium Phosphate Sphere Hybrid as a Label for Ultrasensitive Electrochemical Detection of Human Interleukin- 6. *Small* **7**, 2921-2928 (2011).

286 Ferrari, M. Cancer nanotechnology: opportunities and challenges. *Nature Reviews Cancer* **5**, 161-171 (2005).

287 Wu, J., Fu, Z., Yan, F. & Ju, H. Biomedical and clinical applications of immunoassays and immunosensors for tumor markers. *TrAC Trends in Analytical Chemistry* **26**, 679-688 (2007).

288 Hansen, K. M. & Thundat, T. Microcantilever biosensors. *Methods* **37**, 57-64 (2005).

289 Fritz, J. Cantilever biosensors. *Analyst* **133**, 855-863 (2008).

290 Boisen, A., Dohn, S., Keller, S. S., Schmid, S. & Tenje, M. Cantilever-like micromechanical sensors. *Reports on Progress in Physics* **74**, 036101 (2011).

291 Calleja, M. *et al.* Highly sensitive polymer-based cantilever-sensors for DNA detection. *Ultramicroscopy* **105**, 215-222 (2005).

292 Calleja, M., Tamayo, J., Nordström, M. & Boisen, A. Low-noise polymeric nanomechanical biosensors. *Applied Physics Letters* **88**, 113901 (2006).

293 Shuaipeng, W., Jingjing, W., Yinfang, Z., Jinling, Y. & Fuhua, Y. Cantilever with immobilized antibody for liver cancer biomarker detection. *Journal of Semiconductors* **35**, 104008 (2014).

294 Pan, X. Q. & Lee, R. J. In vivo antitumor activity of folate receptor-targeted liposomal daunorubicin in a murine leukemia model. *Anticancer research* **25**, 343-346 (2005).

295 Malhotra, R., Patel, V., Vaqué, J. P., Gutkind, J. S. & Rusling, J. F. Ultrasensitive electrochemical immunosensor for oral cancer biomarker IL-6 using carbon nanotube forest electrodes and multilabel amplification. *Analytical chemistry* **82**, 3118-3123 (2010).

296 Vashist, S. K., Lam, E., Hrapovic, S., Male, K. B. & Luong, J. H. Immobilization of antibodies and enzymes on 3-aminopropyltriethoxysilane-functionalized bioanalytical platforms for biosensors and diagnostics. *Chemical reviews* **114**, 11083-11130 (2014).

297 Agarwal, D. K., Maheshwari, N., Mukherji, S. & Rao, V. R. Asymmetric immobilization of antibodies on a piezo-resistive micro-cantilever surface. *RSC Advances* **6**, 17606-17616 (2016).

298 Wang, S., Wang, J., Zhu, Y., Yang, J. & Yang, F. A new device for liver cancer biomarker detection with high accuracy. *Sensing and Bio-Sensing Research* **4**, 40-45 (2015).

299 Wang, J. Development of Microcantilever Sensors for Liver Cancer Detection. *Adv Cancer Prev* **1**, 2 (2016).

300 Rabe, U. *et al.* Influence of the cantilever holder on the vibrations of AFM cantilevers. *Nanotechnology* **18**, 044008 (2006).

301 Tsuji, T., Kobari, K., Ide, S. & Yamanaka, K. Suppression of spurious vibration of cantilever in atomic force microscopy by enhancement of bending rigidity of cantilever chip substrate. *Review of Scientific Instruments* **78**, 103703 (2007).

302 Kathel, G. *et al.* Measurement and reliability issues in resonant mode cantilever for bio-sensing application in fluid medium. *Journal of Micromechanics and Microengineering* **26**, 095007 (2016).

Appendix

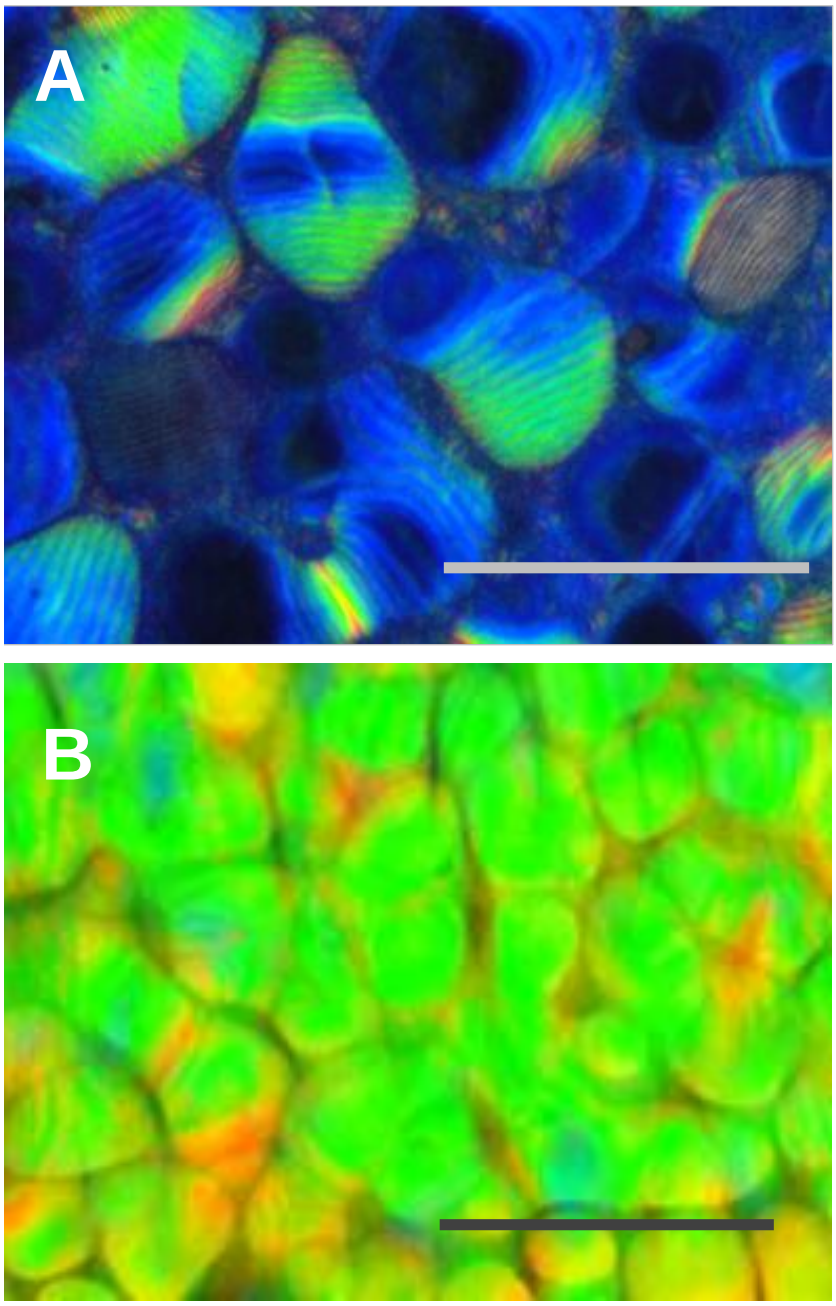

Figure A1. Cross-polarized reflected micrographs showing the effect of surface anchoring on planar orientation, CNC film dried in water vapor saturated environment assisted by orbital shear with a cover slip (A) off and (B) on during drying. Scale bars are 100 µm.

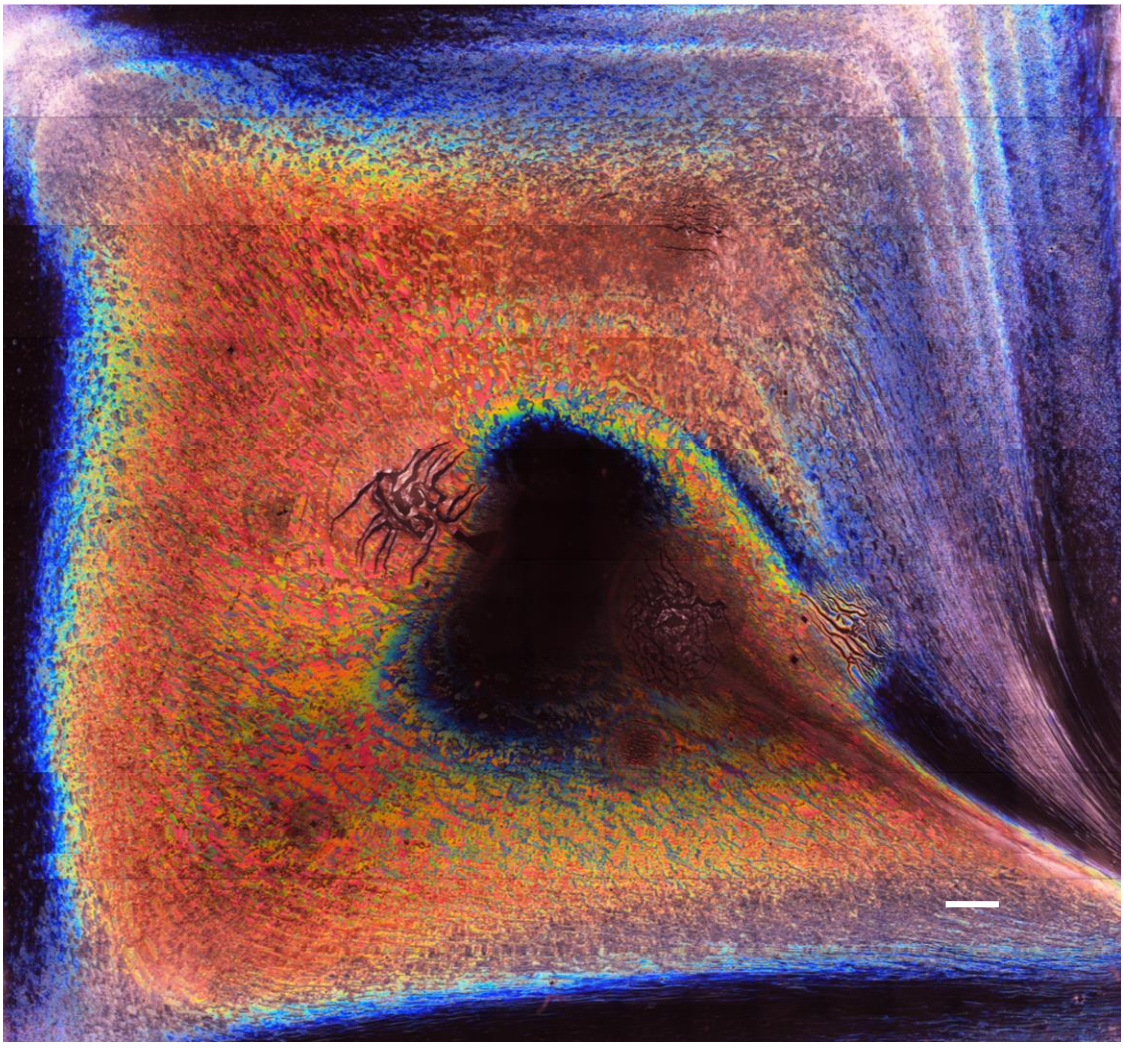

Figure A2. Cross polarized reflected light microscopic image of CNC film using 6.5 wt. % CNC dispersion fabricated using surface anchoring, orbital shear, and water vapor saturated environment). Scale bar is 1 mm.

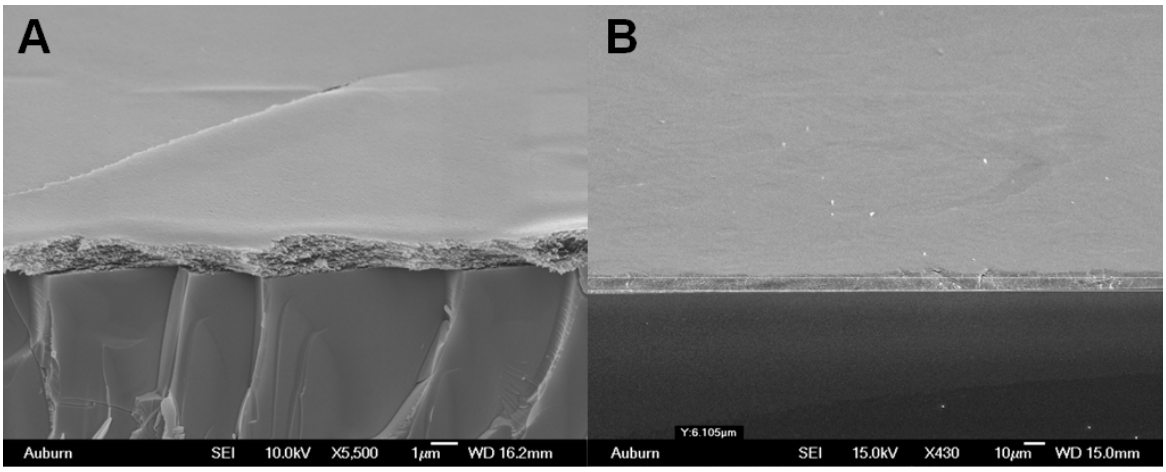

Figure A3. Scanning electron micrographs showing planar film thicknesses, (A) close to film center, thickness approximately 1 μm (B) close to film edge, thickness approximately 10 μm.

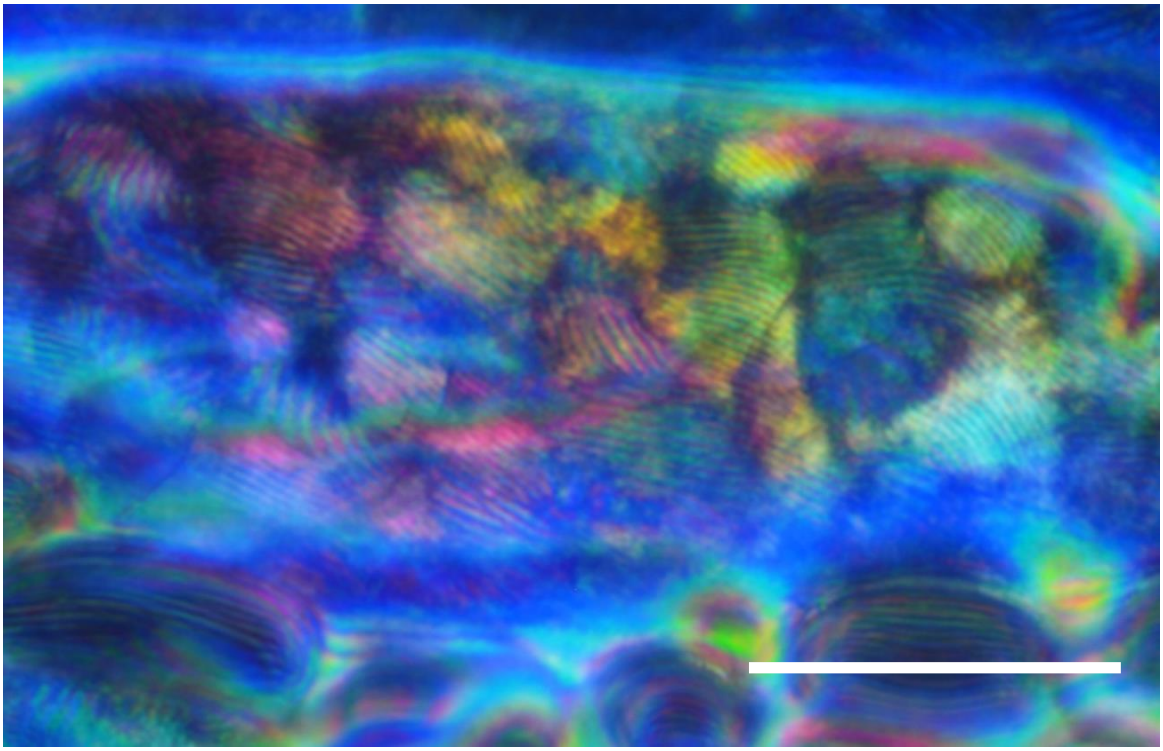

Figure A4. Cross polarized reflected light microscopic image showing focal conic and homeotropic texture. Scale bar is 100 μm.

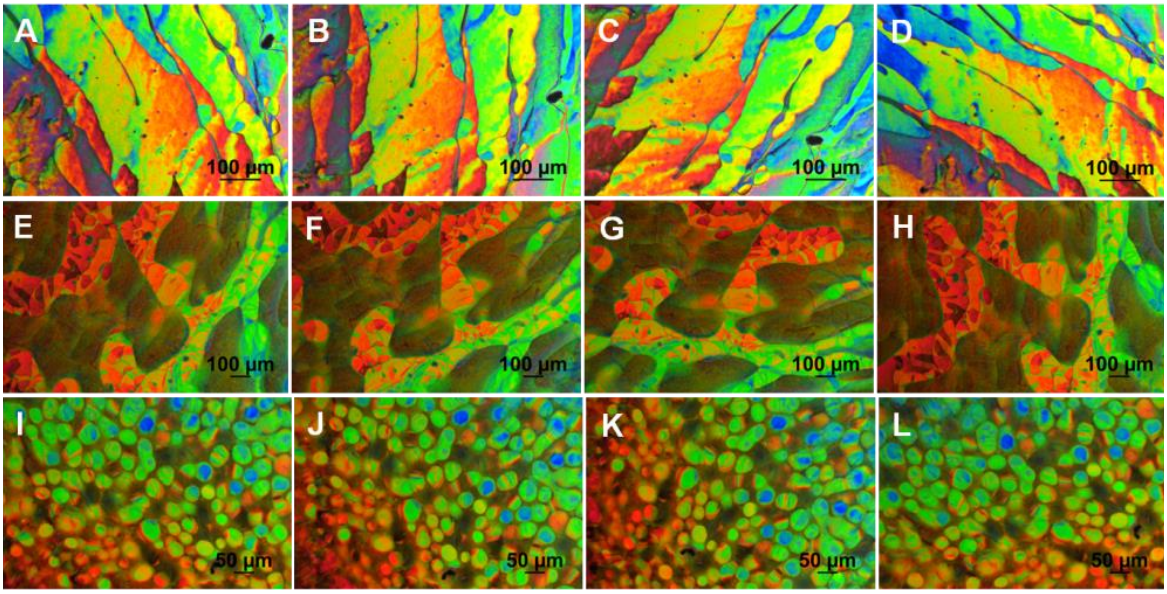

Figure A5. Cross polarized reflected light micrographs showing no change of planar domains colors (no birefringence associated with homeotropic optical axis to the film is present) upon stage rotation (A) 0º, (B) 30º, (C) 60º, and (D) 90^0 for domains from Region 1 (using 6.5 wt. % dispersion), (E) 0º, (F) 30º, (G) 60º, and (H) 90^0 for domains from Region 3 (using 6.5 wt. % dispersion), and (I) 0º, (J) 30º, (K) 60º, and (L) 90^0 for domains found using 2 wt. % dispersion. Scale bars are 100 µm in A – H and 50 µm in I – L.

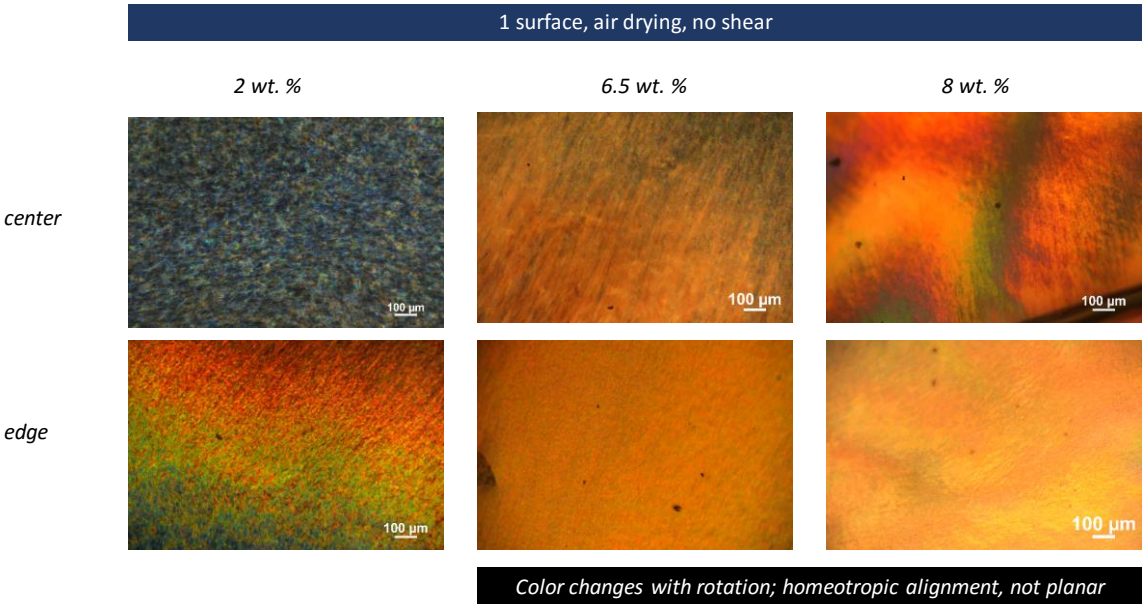

Figure A6. Cross-polarized reflected right microscopic images showing CNC films obtained using 2.0 wt. %, 6.5 wt. %, and 8.0 wt. % aqueous dispersions using 1 surface anchoring, dried in air with no shear.

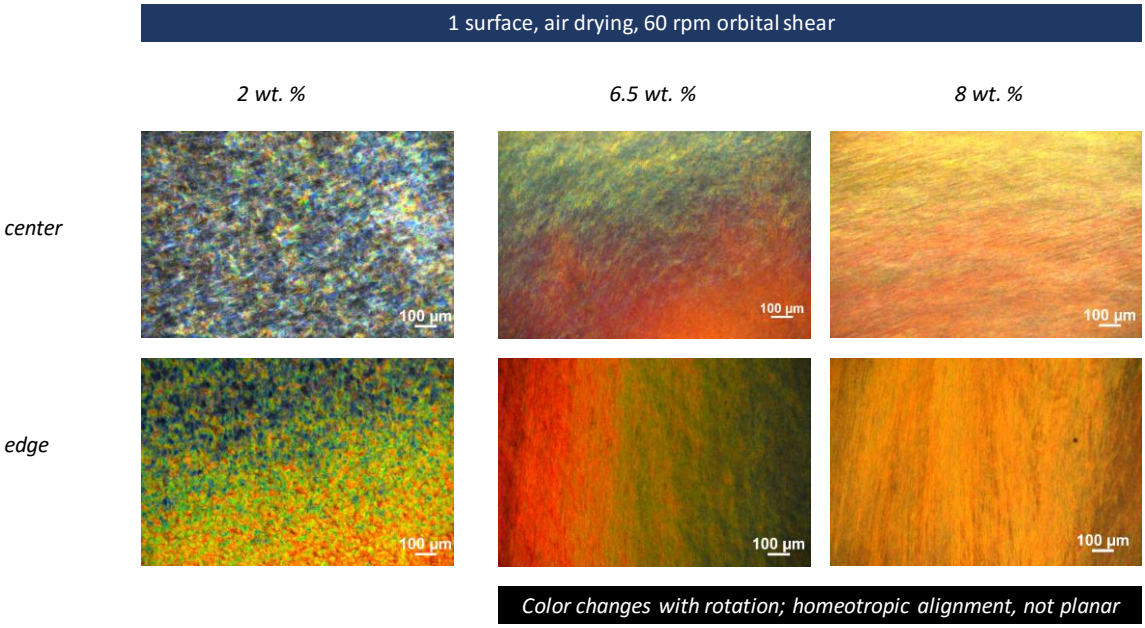

Figure A7. Cross-polarized reflected right microscopic images showing CNC films obtained using 2.0 wt. %, 6.5 wt. %, and 8.0 wt. % aqueous dispersions using one surface anchoring, dried in air with 60 rpm orbital shear.

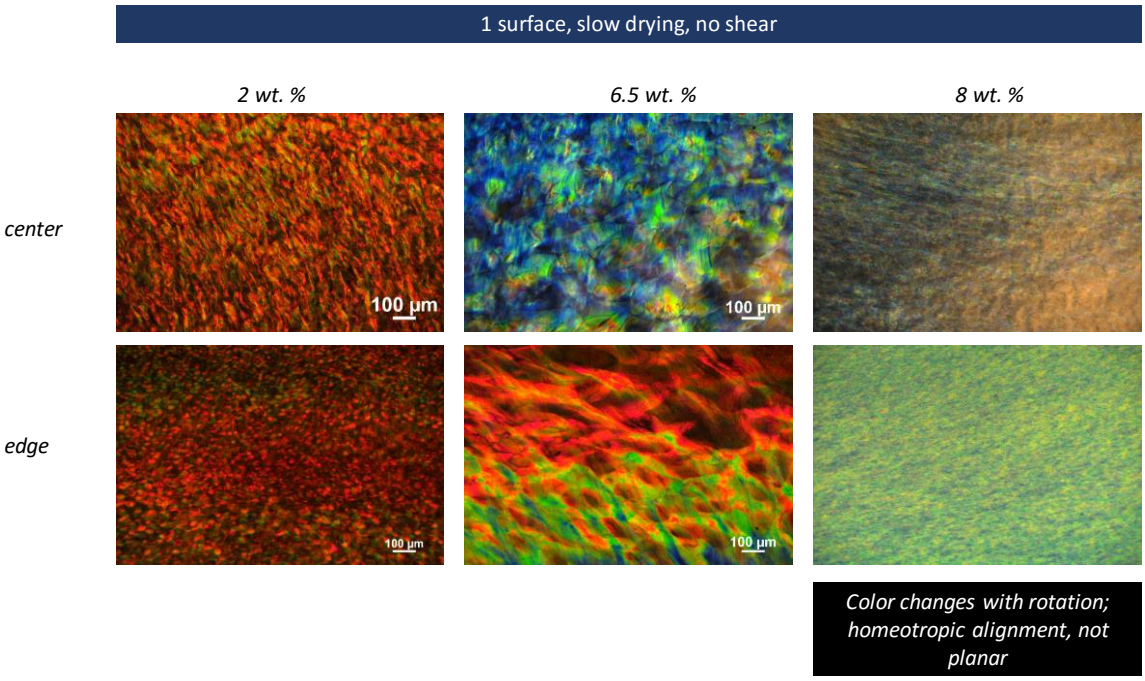

Figure A8. Cross-polarized reflected right microscopic images showing CNC films obtained using 2.0 wt. %, 6.5 wt. %, and 8.0 wt. % aqueous dispersions using one surface anchoring, dried in humid environment with no shear.

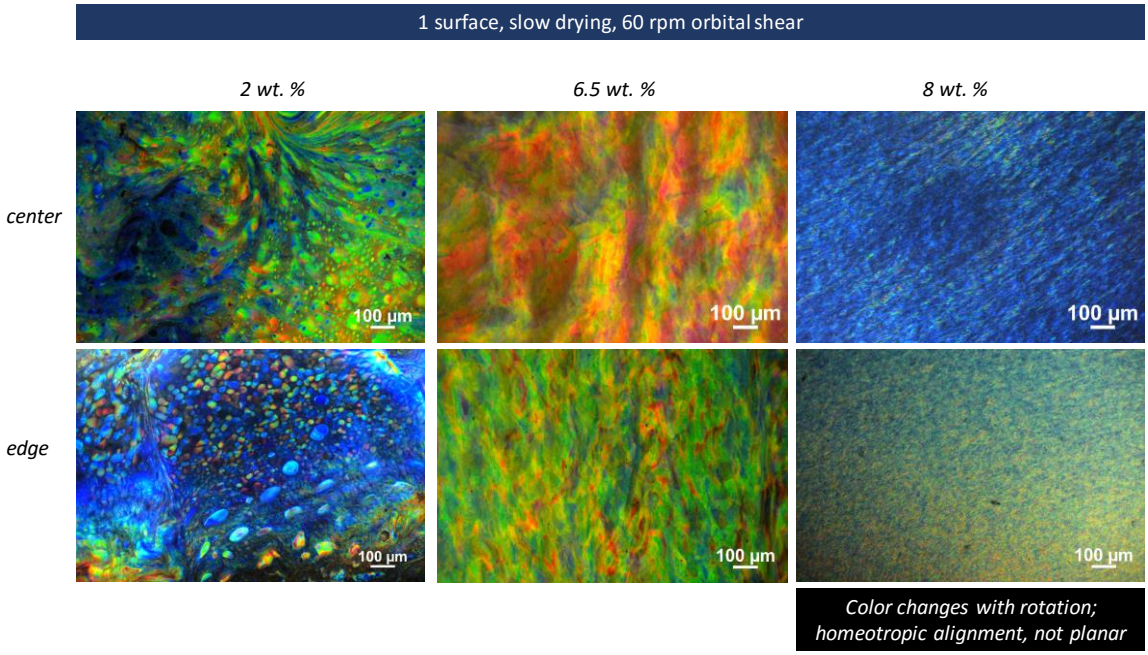

Figure A9. Cross-polarized reflected right microscopic images showing CNC films obtained using 2.0 wt. %, 6.5 wt. %, and 8.0 wt. % aqueous dispersions using one surface anchoring, dried in humid environment with 60 rpm orbital shear.

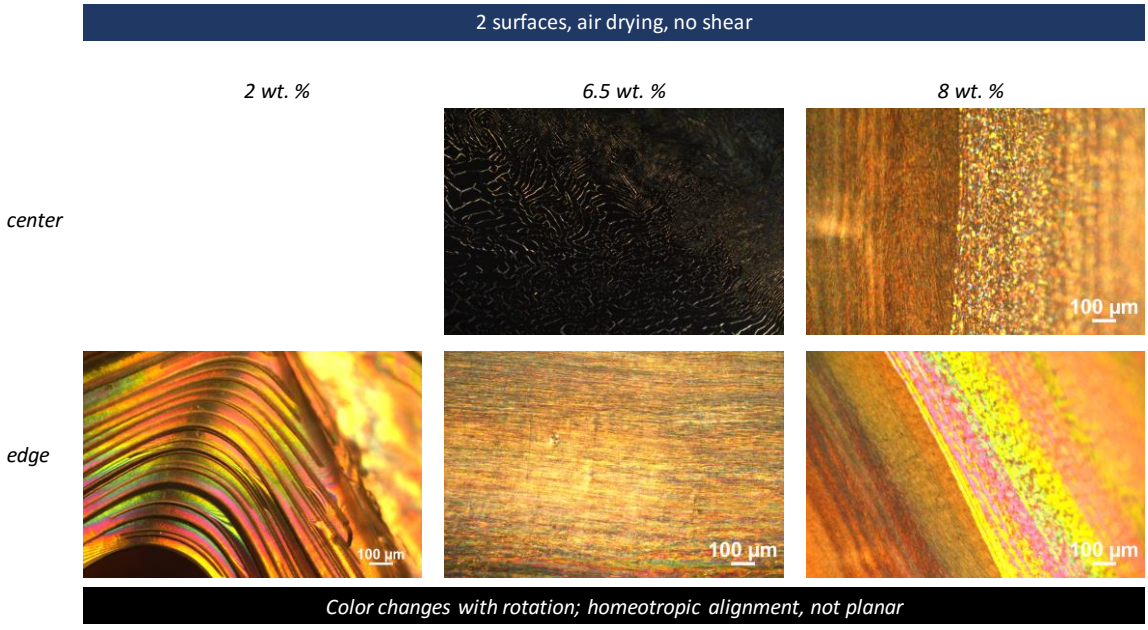

Figure A10. Cross-polarized reflected right microscopic images showing CNC films obtained using 2.0 wt. %, 6.5 wt. %, and 8.0 wt. % aqueous dispersions using two surface anchoring, dried in air with no shear.

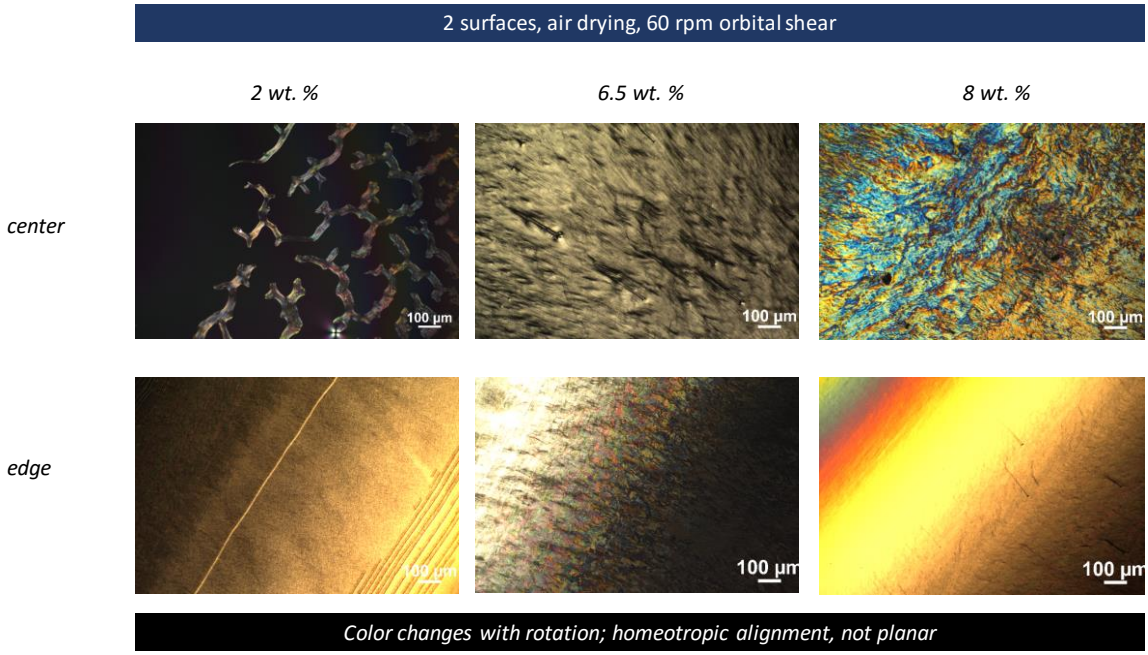

Figure A11. Cross-polarized reflected right microscopic images showing CNC films obtained using 2.0 wt. %, 6.5 wt. %, and 8.0 wt. % aqueous dispersions using two surface anchoring, dried in air with 60 rpm orbital shear.

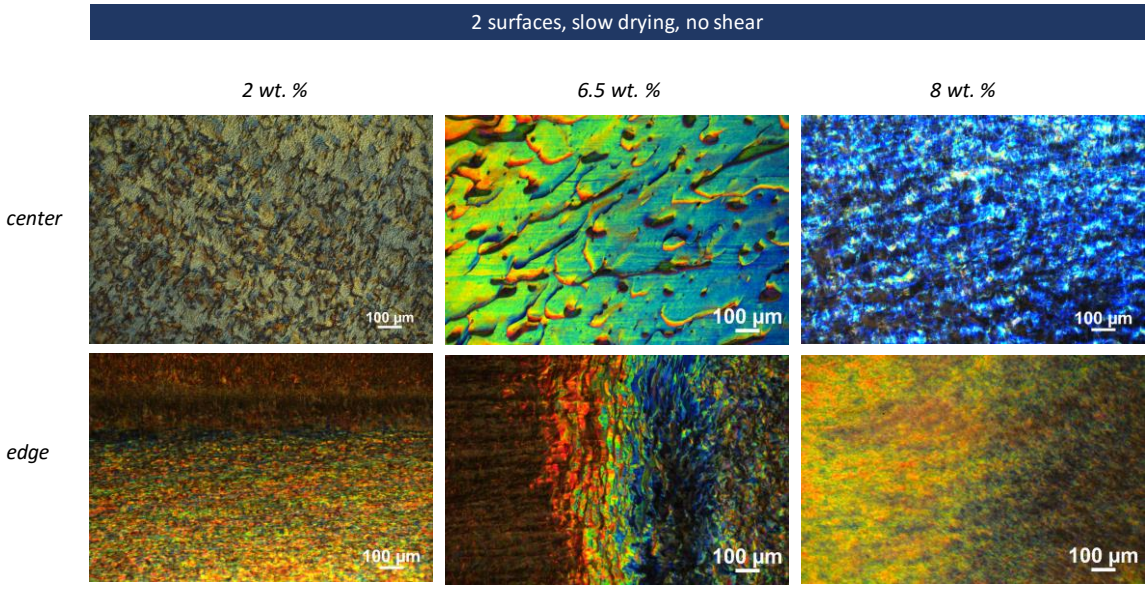

Figure A12. Cross-polarized reflected right microscopic images showing CNC films obtained using 2.0 wt. %, 6.5 wt. %, and 8.0 wt. % aqueous dispersions using two surface anchoring, dried in humid environment with no shear.

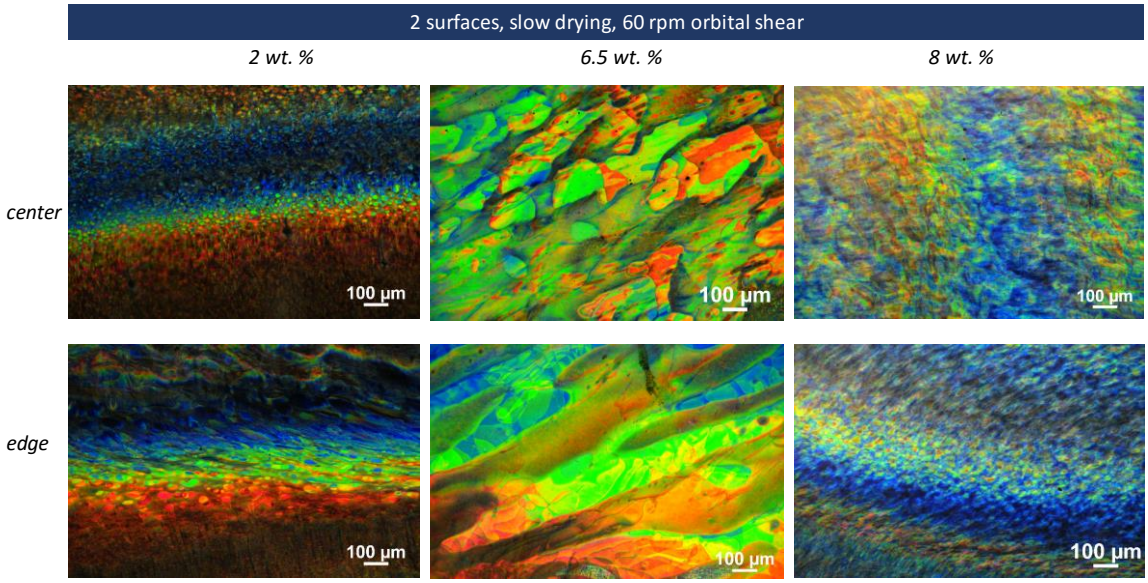

Figure A13. Cross-polarized reflected right microscopic images showing CNC films obtained using 2.0 wt. %, 6.5 wt. %, and 8.0 wt. % aqueous dispersions using two surface anchoring, dried in humid environment with 60 rpm orbital shear.

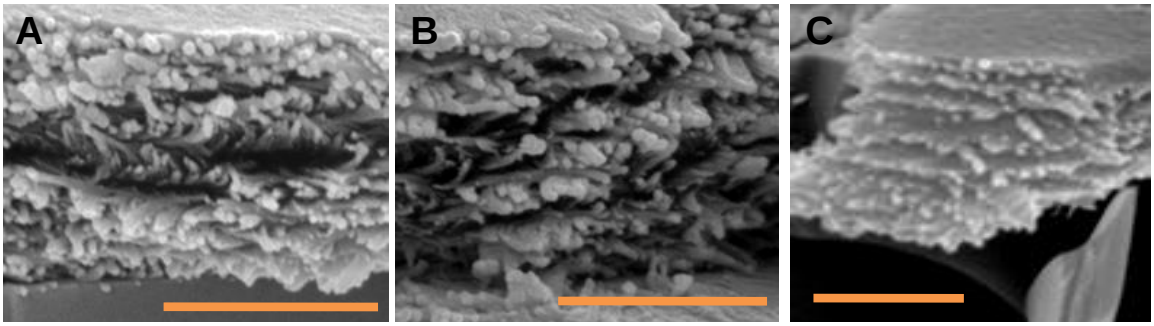

Figure A14. SEM for pitch calculation in Table S1 for (a) blue, (b) green, and (c) orange domains. Scale bars are 1 µm.

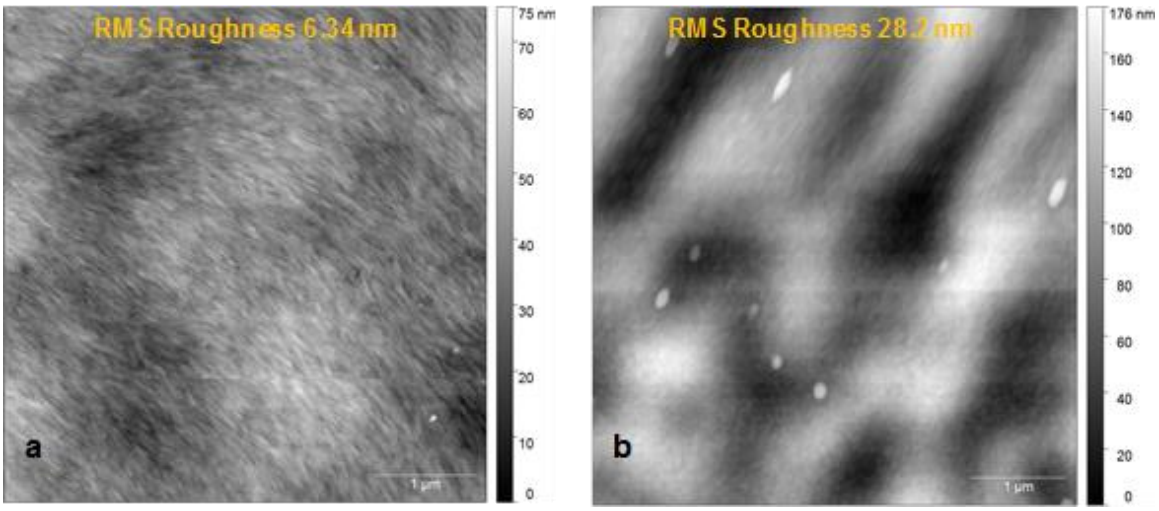

Figure A15. AFM scan of sheared film of (A) CNC and (B) 10 nm Ti/TiO_2 coated CNC.

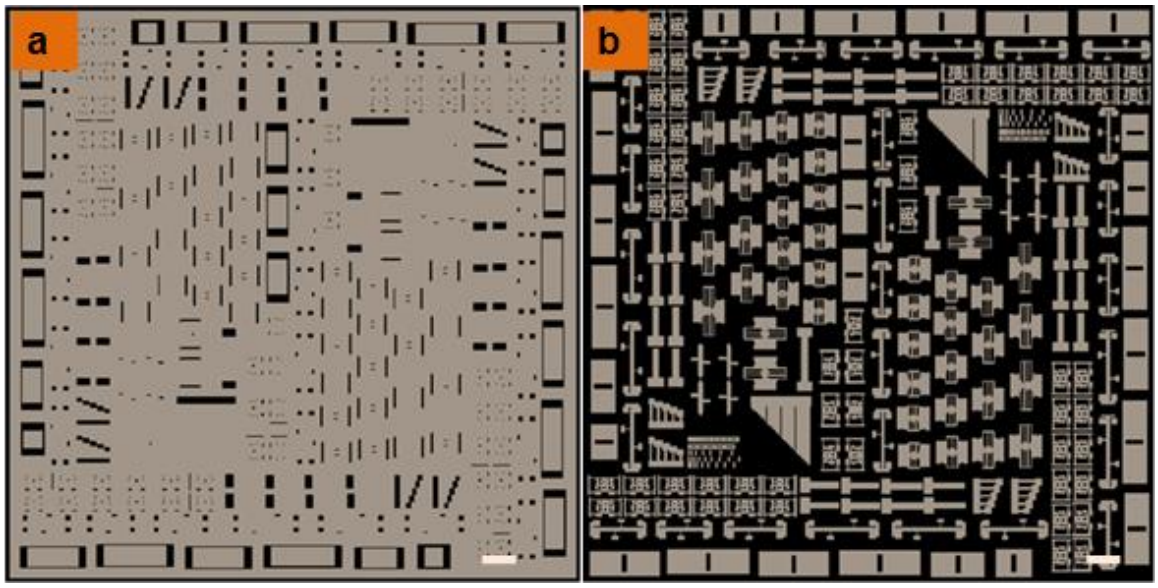

Figure A16. LASI based design of CNC-MEMS showing (a) anchor and (b) device layer masks. Scale bars are 300 µm. Black represents the open areas to be UV exposed.

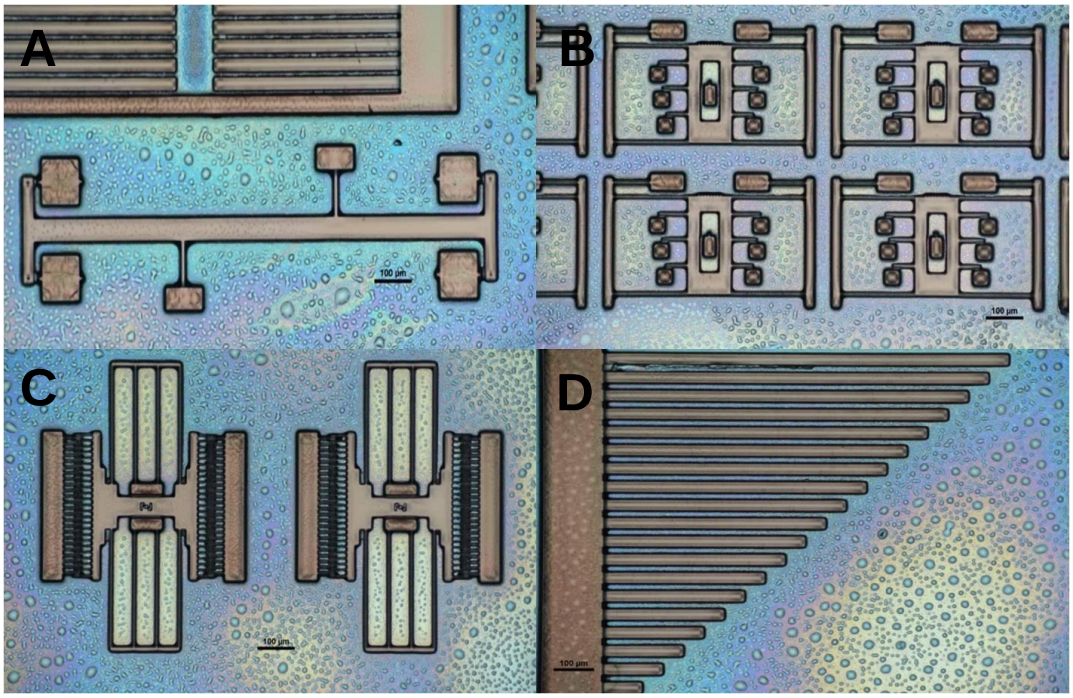

Figure A17. Cross-polarized reflected light microscopic images showing second photoresist pattern of CNC MEMS devices on 10 nm titania coated shear aligned CNC films.

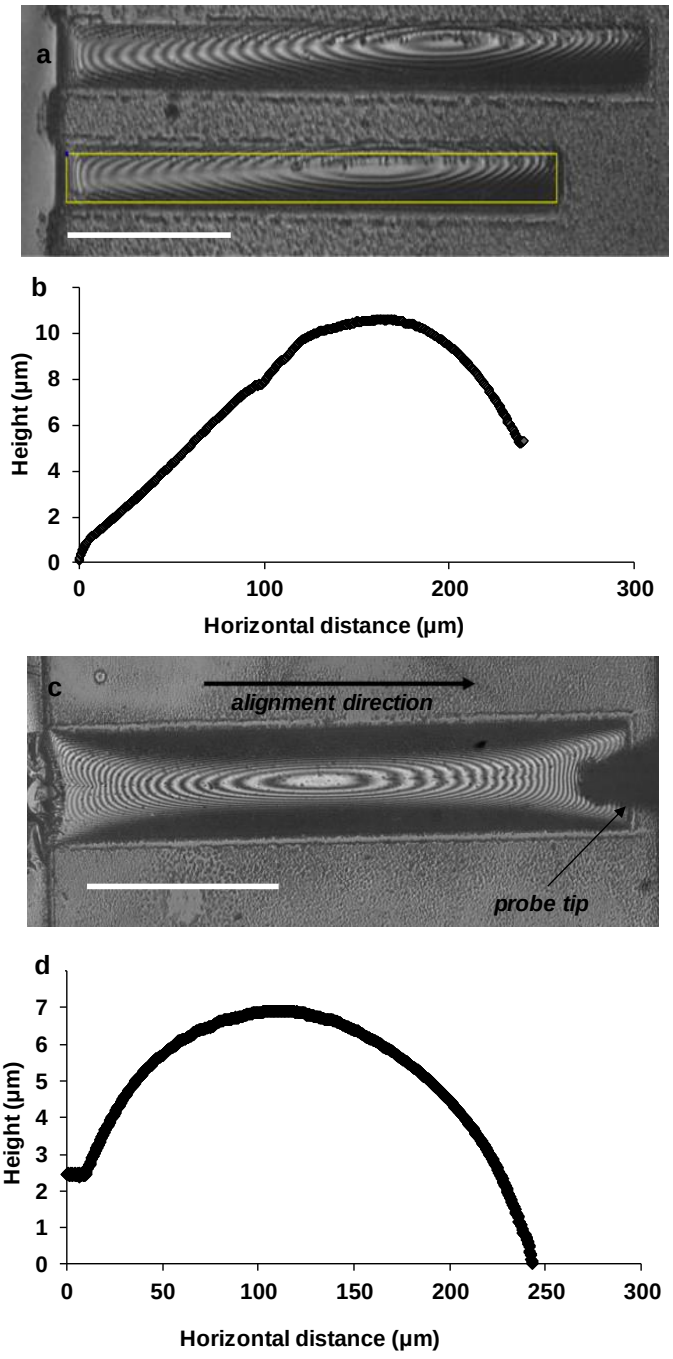

Figure A18. a) Phase shifting interferograms (PSI) on freestanding CNC cantilevers, used for determination of b) height profile (exhibits downward arc meaning compressive stress gradient). The yellow box indicates the scanning region. c) A cantilever free end mechanically actuated using a probe tip connected to a module. d) The PSI based height profile of that mechanically clamped beam in (c) showing robustness. Scale bars are 100 µm.

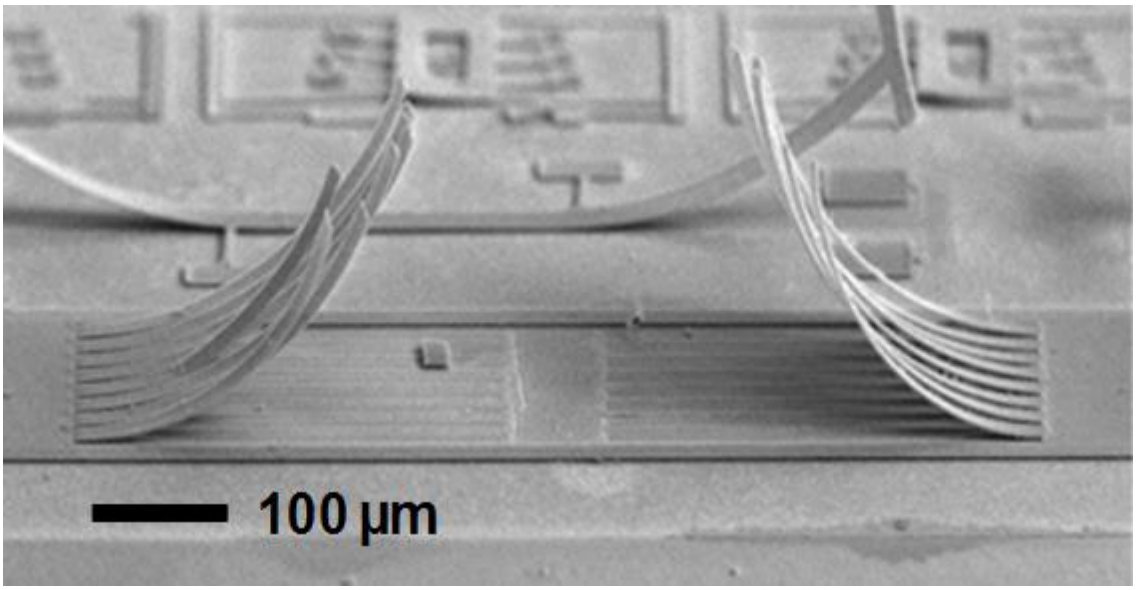

Figure A19. SEM image of gold sputter coated cantilevers showing an upward arc array, indicating the transition to a tensile stress gradient which is attributed to stress relaxation.

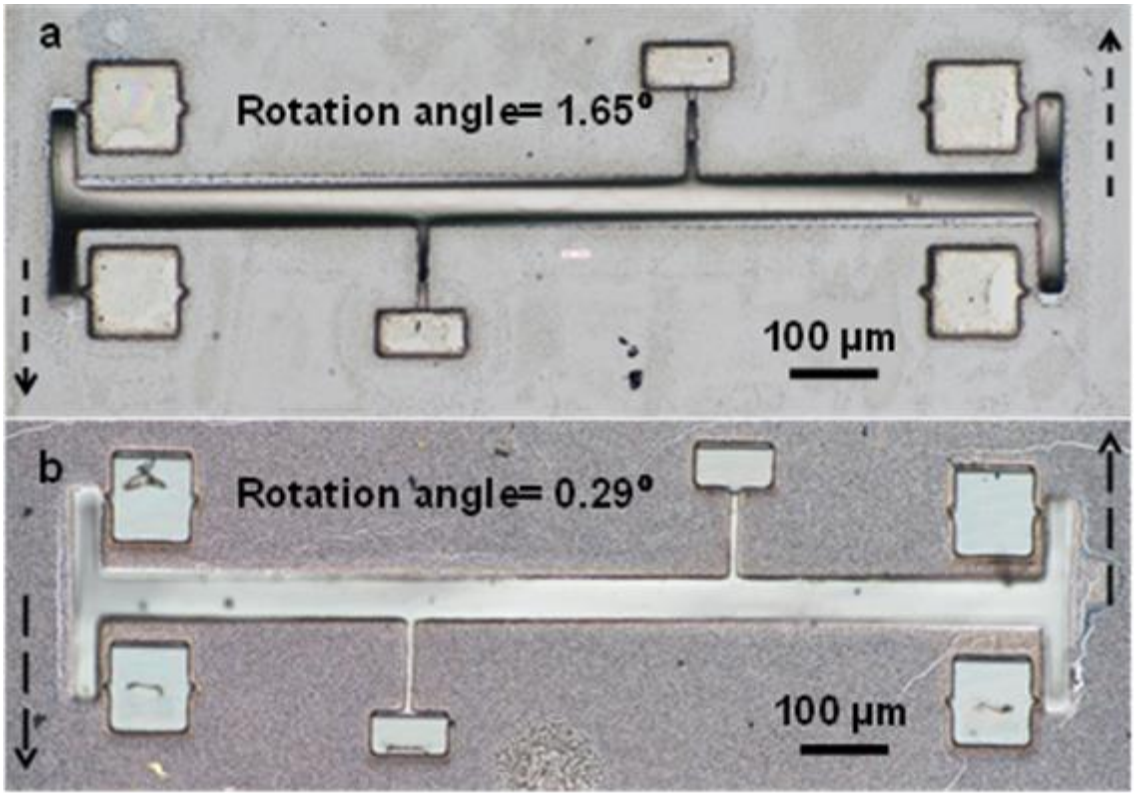

Figure A20. Reflectance micrograph showing thickness dependent compressive residual stress developed in CNC-RSTs. Counterclockwise rotation in (A) 2 µm and (B) 4 µm thick RSTs with a lever arm of 300 µm; I shaped beam is along the shear alignment direction of individual nanocrystals.

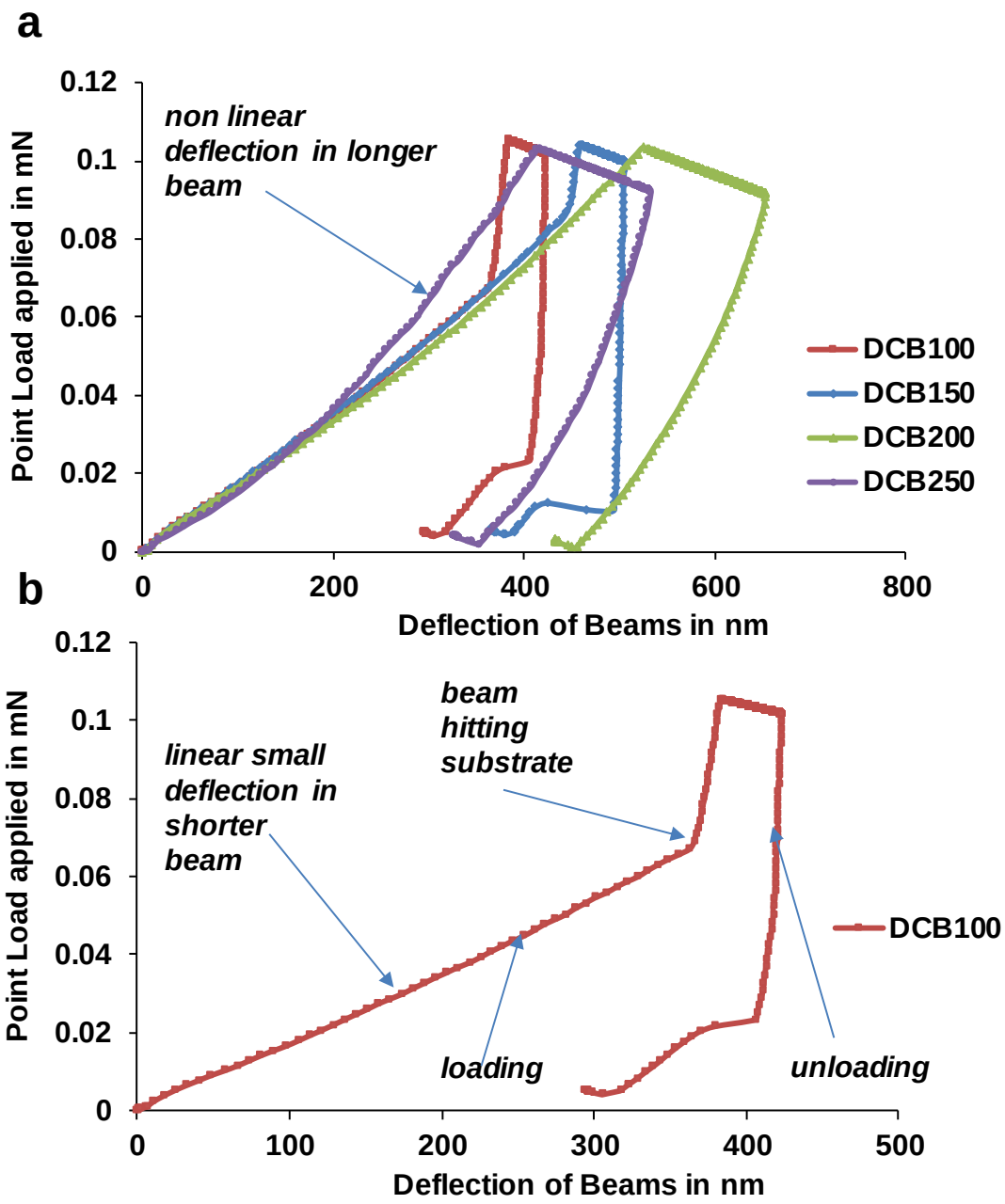

Figure A21. a) Load versus deflection curves of CNC DCBs obtained by point load nanoindentation. The longer beams are more compliant to buckling resulting in nonlinear deflection while subjected to load. In contrast b) the shorter beam (100 μm) exhibits a linear bending profile showing the drastic change of load while beam hits the wafer substrate. The slope obtained from this linear bending region was used to obtain the elastic moduli.

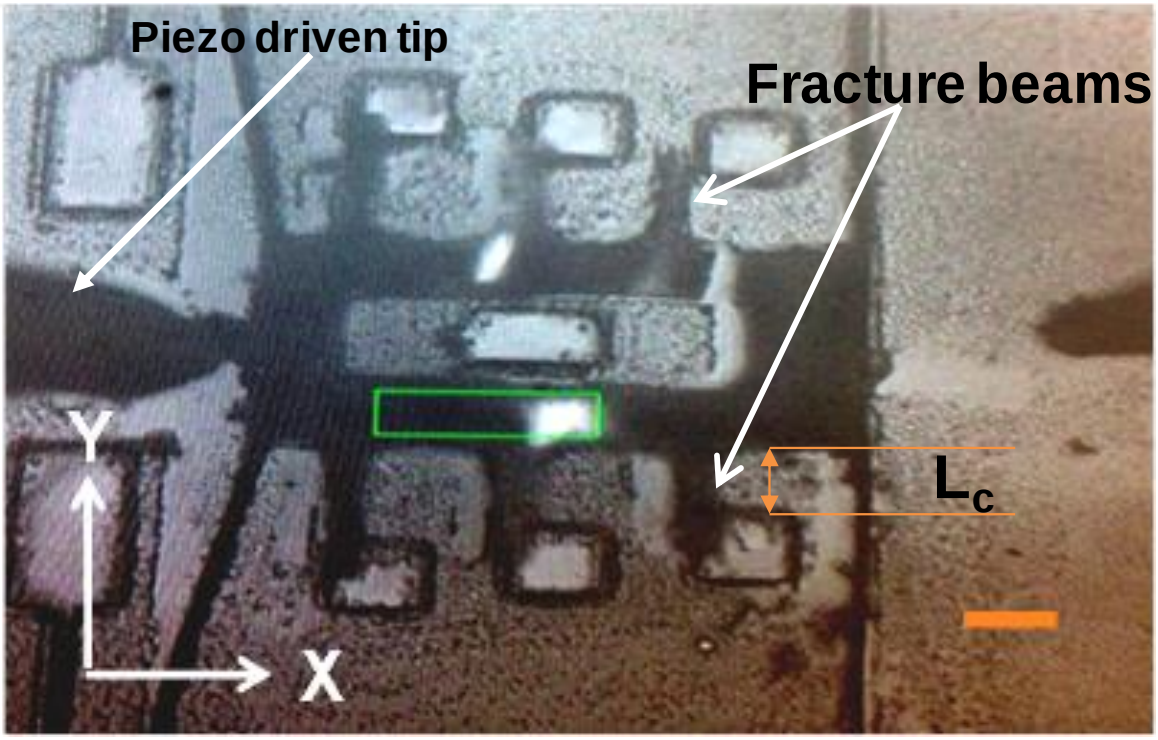

Figure A22. Microscopy image showing the direction of actuation of MST shuttle using an open loop piezo assisted micromanipulator (on the left), applying DC voltage; scale bar is 50 μm. The fracture distance and distance between stopping post and shuttle (L_c) were used to obtain fracture strength of MSTs.